

MICRO-VESSEL MODELS FOR DRUG
SCREENING AND DISEASE MODELING

ADVANCING MICRO-VESSEL MODELS FOR
HIGH-THROUGHPUT PRE-CLINICAL DRUG SCREENING AND
PHYSIOLOGICAL DISEASE MODELING

By DAWN SONG YI LIN, B.A.Sc., Hons

A Thesis Submitted to the School of Graduate Studies in Partial
Fulfillment of the Requirements for
the Degree Doctor of Philosophy

McMaster University © Copyright by Dawn Song Yi Lin, May 2024

McMaster University

DOCTOR OF PHILOSOPHY (2024)

Hamilton, Ontario, Canada (Chemical Engineering)

TITLE: Advancing micro-vessel models for high-throughput pre-clinical drug screening and physiological disease modeling

AUTHOR: Dawn Song Yi Lin
B.A.Sc., Hons (Mechanical Engineering),
University of Toronto, Toronto, Canada

SUPERVISOR: Professor Dr. Boyang Zhang

NUMBER OF PAGES: xxxvii, 214

Lay Abstract

In clinical trials, a staggering 90% of drugs fail during testing in people. Traditional preclinical drug screening methods rely on culturing human cells on flat surfaces or using animal models, both fraught with limitations such as lacking structural complexity or having DNA differences from humans. Addressing this issue could notably reduce efforts and costs.

This thesis is dedicated to advancing preclinical drug testing through micro-vessel models. It focuses on constructing 3D vessels using human cells, offering a more accurate representation of human physiology. Two models are discussed: one with self-assembled vessels featuring complex structures, and another emphasizing sacrificial materials to design simpler vascular shapes, ensuring consistency in testing.

By leveraging these innovative models, researchers can subject various drugs to micro-vessels constructed in vitro, enabling them to predict their effects in humans. This approach has the potential to transform drug testing methodologies, moving towards the utilization of artificial human organ models.

Abstract

Conventional pre-clinical drug screening, reliant on 2D cell cultures and animal studies, faces challenges—the former lacks biological complexity, and the latter lacks predictability due to differences between animals and humans from genetic to functional levels. Organ-on-chip technologies have evolved to bridge the gap between preclinical and clinical trials, necessitating human cells for precise predictions of human responses. Considering the significance of the vascular system in various diseases, incorporating vascular units into organ-on-chip devices is critical.

For effective drug discovery using vessels-on-chips, achieving high-throughput and consistency between samples is crucial. However, many vessels-on-chips are manually handled during preparation and data collection, reducing throughput and increasing sample-to-sample variations. The conventional closed microfluidic chip format further impedes accessibility, hindering automation. This thesis focuses on two high-throughput micro-vessel models replicating vascular functions under perfusion in a 384-well plate format. These open-top models allow automated preparation and examination, enhancing efficiency in compound screening.

The first model features a self-assembled perfusable micro-vascular network on a 384-well plate, co-culturing endothelial cells (EC) with stromal cells in a hydrogel.

Automated using a robotic system and a fluorescent plate reader, it supports organ-specific functions and enables nanoparticle transport to target tissues. Utilized for testing cancer therapeutic drugs, it demonstrates dose-related responses in vascular permeability and architectures.

The second model is dedicated to crafting micro-vessels of consistent quality for biological testing and disease modeling. It employs a sacrificial material for pre-designed tubular shapes for EC seeding. The integration of automated processes and a straight channel design minimizes sample discrepancies. Furthermore, a tri-culture system enhances barrier integrity, enabling effective drug screening that distinguishes between vasculotoxic and non-vasculotoxic agents with notable sensitivity and specificity.

Looking ahead, there is potential to further refine these models to encompass a broader range of vascular diseases, which could lead to novel insights and therapeutic targets.

To my father and mother

Acknowledgements

Little did I know how much I would gain from the past five years as a PhD candidate, a journey that extended far beyond acquiring knowledge and building skills. The process instilled in me a humility from accepting failure, despite my best efforts in brainstorming, planning, and conducting experiments. It also pleasantly surprised me with unexpected rewards in the form of financial support, academic recognition, and most importantly, invaluable mentorship and companionship.

My journey would not have begun without my advisor, Dr. Boyang Zhang, who saw potential in me to complete such a prestigious degree. Five years ago, as a mechanical engineering student nearing graduation, I was uncertain about pursuing a career aligned with my passion for healthcare. Dr. Zhang guided me towards a fruitful path that would gradually equip me to contribute to the healthcare field. He mentored me to be a better learner, encouraged curiosity, taught me not to fear failure, and instilled discipline in every task, no matter how small. Without Dr. Zhang's continuous devotion to my research and personal development, I would not have reached my capacity to conduct the work presented in this thesis. For this, I owe him my deep gratitude.

I would also like to express my gratitude to the members of my supervisory committee: Dr. Carlos Filipe and Dr. Katrina Choe, who encouraged me to trust in the

process. They held me accountable, helping me to reach every significant milestone during my PhD, from the comprehensive exam to the impending defense day.

My sincere appreciation also extends to all BZhang Lab members, every past summer student, undergraduate volunteer, and graduate student, who graced me with their generous help, companionship, and timely guidance. Special thanks go to Shrvanthi, Luis, and Feng for lifting me from the depths of experimental failures; to Sonya, Alex, and Andrew for their cheerful spirits and deep biological insight; to Kimia, Nicky, Sara and Mathiew for their warm smiles and willingness to help others; to Mandeep, Brenda, Hanieh, Rhiannon, Sarah, Anushree, Manvir, and Albert for enabling me to be a more helpful mentor and for sharing their wisdom.

I must also convey my gratitude to my mentors who introduced me to tissue engineering before my PhD. Dr. Milica Radisic opened this door when I was a second-year undergraduate student at the University of Toronto. She offered me a work-study position in her lab, where I had the chance to assist Dr. Boyang Zhang during his time there. The invaluable experience I gained in Dr. Radisic's lab later led me to Dr. Jeffrey Karp and Dr. Yuhan Lee at Harvard Medical School. They offered me a one-year opportunity to spend my co-op year in Boston, working on biomaterial research, which completely shifted my career path away from mechanical engineering in the automotive industry to a life-changing trajectory. I am deeply thankful to Dr. Radisic, Dr. Karp, and Dr. Lee for providing opportunities to work on eye-opening projects and for being inspirational role models.

I must also acknowledge my friends outside of the lab, who have been a continuous support, making this journey less solitary. My heartfelt thanks to the Cephas fellowship at Hamilton Chinese Alliance Church, Auntie Liming, Uncle Peter, Claire,

Yilin, Xiangyi, Xiaoqian, Peter, Michael, Steven, Cindy, Viola, Xudi, Ada, Ruth, Shin, Xudong, Kevin, Jacki , and Jiawei for helping me stay socially active despite weekend lab work and for keeping me in their prayers. To my friends afar in China and Korea, CQ and Ashley, and to my Toronto friends, Keyue, Peri, and Danniell, I am grateful for their remembrance and for nurturing our friendship despite the distance.

My pursuit of a PhD would not have been possible without the devotion of my parents, Phillip and Yan. I thank them for their care and mental support, for uplifting me, and for standing by me when I felt drained. My father's perseverance will always be my strength to face life's challenges, and my mother's commitment to serving those in need will continually remind me to look beyond my own interests. I also want to thank my grandparents, who believed in me even before my earliest memories began.

Lastly, I cannot conclude these acknowledgments without giving ultimate thanks to my God, who sent His son, Jesus Christ, to die on the cross for my sin, so that I may live through His resurrection, and who gives my life a purpose worth pursuing. May my life be a small story about a big God.

致謝

過去五年作為博士生的旅程裡，我的收穫遠遠超出了知識和技能的領域。這個旅程讓我更加謙卑——謙卑去接受失敗，即便是在我精心策劃和努力實驗之後。除了學習接受失敗，這份旅程也帶給了我許許多多的驚喜，從經濟支持、學術認可，到最重要的——寶貴的指導和陪伴。

五年前，我還是一個雖然對醫療行業保有熱情，但是對下一步舉棋不定、即將畢業的本科生。如果沒有我的導師張博洋教授在那時相信我有完成這樣一個富有挑戰的學位的潛力，我的博士旅程也許根本不會開始。張教授不僅引導我走上一條逐步裝備我來為醫療領域做出貢獻的道路，他也指導我成為一個更好的學習者：保持好奇心，不畏懼失敗，在最小的任務中追求卓越。如果沒有張教授對我的研究項目和個人發展持續地投入和指導，我今天一定無法呈現出在這份畢業論文中所體現的能力。我衷心地感激他。

我還想向我的指導委員會成員表示感謝：他們是Carlos Filipe教授和Katrina Choe教授，他們鼓勵我要專注和享受這個旅程。他們也幫助我，確保我在博士生期間按時達到每一個重要的里程碑，包括從博士資格綜合考試到即將到來的答辯日。

我也要向所有張教授實驗室的成員，無論是以往的暑期學生、本科志願者還是研究生表示衷心的感謝，他們慷慨地向我提供幫助、陪伴和及時的指導。我要特別感謝Shravanthi、Luis和張逢在我陷入實驗失敗的低谷中的時候安慰、振作我；感謝Sonya、Alex和Andrew向我們所有人傳遞他們愉悅的情緒也分享他們深入的生物學見解；感謝Kimia、Nicky、Sara和Mathiew對我們大家時常展露的熱情微笑和他們出於樂意的幫助；感謝Mandeep、Brenda、Hanieh、Rhiannon、Sarah、Anushree、Manvir和Albert教我如何成為一名能更有效助人的指導者，也感謝他們與我並分享他們的智慧。

我也要感謝在我攻讀博士學位之前就介紹我進入生物工程領域的導師們。當我還是多倫多大學二年級的本科生時，Milica Radisic教授為我開啓了這扇門。她在她的實驗室向我提供了一個工讀職位，使我有機會來協助當時在Radisic教授實驗室進行研究工作的我現在的導師，張博洋教授。我在Radisic教授實驗室獲得的寶貴經驗，後來幫助我有機會為在哈佛醫學院的Jeffrey Karp教授和Yuhan Lee教授工作。他們為我提供了一年的機會，在波士頓從事生物材料研究來豐富我的本科學習，這個經歷完全改變了我的志向，使我從原先的志願成為一名汽車行業的機械工程師轉向一條不同的軌跡。我非常感謝Radisic教授、Karp教授和Lee教授向我提供了寶貴的研究機會，他們每個人也成為了我人生路上不可替代的榜樣。

我也要感謝實驗室外的朋友們，他們一直給予我支持，讓這段旅程並不孤單。衷心感謝海明頓華人宣教會法團契裡的莉明姊、Uncle Peter、Claire、藝琳、相宜、小倩、Peter、Michael、Steven、Cindy、Viola、徐迪、Ada、仁慈、Shin、旭東、Kevin、Jacki和Jiawei，即便我週末時常需要進行實驗室工作，他們也一直鼓勵我保持社交，時常邀請我參與不同的活動，並且他們還常常為我祈禱。我也要感謝遠在中國和韓國的朋友CQ和Ashley，以及在多倫多的朋友Keyue、Peri和Danniel，感謝他們在距離遙遠的情況下珍惜和維繫我們的友誼。

如果沒有我的父親Phillip和母親Yan的奉獻，我追求博士學位的道路是不可能開始和完成的。我感謝他們給我在日常起居和心靈上的支持，感謝他們在我感到筋疲力盡時陪伴著我。我父親的毅力將永遠作為我面對生活困難時的力量，而我母親對有需要幫助的人的憐憫將時時提醒我凡事不能只看自己的益處。我也要感謝我的爺爺、奶奶、姥爺和姥姥，感謝他們在我能夠記事以先就相信了我可以。

最後，我要將一切的感謝獻給我的神，他派遣他的獨生子耶穌基督為我的罪而死在十字架上，使我得以藉著他的復活如今也活著——祂賦予了我的生命一個值得追求的意義。願我的人生最後成為一篇關於一位偉大真神的小小故事。

Table of Contents

Lay Abstract	iii
Abstract	iv
Acknowledgements	vii
List of Figures	xix
List of Tables	xxx
Definitions, and Abbreviations	xxxix
Declaration of Academic Achievement	xxxvii
1 Introduction	1
Modeling organ-specific vasculature with organ-on-a-chip devices	2
Abstract	2
1.1 Introduction	3
1.2 Engineering Approaches in Building Blood Vessels In Vitro	8
1.2.1 Blood vessel in a channel	8

1.2.2	Blood vessel on a membrane	11
1.2.3	Blood vessel in hydrogels	12
1.2.4	Blood vessel in a multi-well plate	14
1.2.5	Blood vessel explants	15
1.2.6	Blood vessel in a scaffold	16
1.3	Organ-Specific Vasculature-on-a-Chip	17
1.3.1	Cardiac vasculature-on-a-chip	18
1.3.2	Liver vasculature-on-a-chip	21
1.3.3	Pulmonary vasculature-on-a-chip	22
1.3.4	Kidney vasculature-on-a-chip	23
1.3.5	BBB-on-a-chip	25
1.4	Future Challenges in Device Development	27
1.4.1	The challenge of material selection in device development	27
1.4.2	The challenge of clinically relevant cell sources	28
1.4.3	The challenge of sensor integration and device operation	29
1.5	Conclusions	29
	Competing Interests	30
	Acknowledgments	30
2	IFlowPlate™ - Vascularization for Supporting Tissue Functions	31
	From model system to therapy: scalable production of perfusable vascularized liver spheroids in “open-top” 384-well plate	32
	Abstract	32
2.1	Introduction	34

2.2	Materials and Methods	36
2.2.1	Plate fabrication	36
2.2.2	Cell culture	37
2.2.3	Gel casting and cell seeding	38
2.2.4	Functional assays	39
2.2.5	Immunofluorescent staining and TEM imaging	40
2.2.6	Albumin assay	41
2.2.7	Sample size and statistical analysis	41
2.3	Results	42
2.3.1	IFlowPlate™ operation and culture of perfusable microvascular bed	42
2.3.2	Angiogenesis assay on IFlowPlate™	45
2.3.3	Culture of vascularized liver spheroids on IFlowPlate™	46
2.4	Discussion	51
2.5	Conclusions	53
	Competing Interests	53
	Acknowledgments	53
3	IFlowPlate™ - Microvascular Array for Drug Screening	54
	Robot-assisted fabrication of microvascular networks: enhancing high-throughput screening for chemotherapy drugs	55
	Abstract	55
3.1	Introduction	56
3.2	Materials and Methods	58

3.2.1	Cell culture	58
3.2.2	Vascular networks formation	58
3.2.3	Purfusion and permeability assay	60
3.2.4	Treatments	62
3.2.5	Imaging analysis	62
3.2.6	Statistical analysis	62
3.3	Results	64
3.3.1	Automated high-throughput microvascular network assay setup	64
3.3.2	Structural analyses of the microvascular networks	67
3.3.3	Testing chemotherapy drugs using the vasculature assay on IFlowPlate™	70
3.4	Discussion	77
3.5	Conclusions	80
	Competing Interests	80
	Acknowledgments	81
4	AngioPlate™ - Predesigned Vessels	82
	Subtractive manufacturing with swelling induced stochastic folding of sacrificial materials for fabricating complex perfusable tissues in multi-well plates	83
	Abstract	84
4.1	Introduction	84
4.2	Materials and Methods	87
4.2.1	AngioPlate™ fabrication	87

4.2.2	Cell culture	88
4.2.3	Hydrogel casting and device operation	88
4.2.4	Vascular variability, permeability, and drug testing	90
4.2.5	Immunostaining and histology	90
4.2.6	Statistical analysis	91
4.3	Results	92
4.4	Discussion	97
4.5	Conclusions	101
	Competing Interests	101
	Acknowledgments	101
5	AngioPlate™ - Vessel Arrays for Drug Screening	103
	High-throughput modeling of vascular responses in human microvessel arrays using AngioPlate™	104
	Abstract	104
5.1	Introduction	105
5.2	Materials and Methods	108
5.2.1	Cell culture	108
5.2.2	Hydrogel casting	109
5.2.3	Vessels formation	111
5.2.4	Permeability assay	112
5.2.5	Treatments	113
5.2.6	Cytokine analysis	114
5.2.7	Immunofluorescent staining and TEM imaging	115

5.2.8	Imaging analysis	116
5.2.9	Statistical analysis	116
5.3	Results	117
5.3.1	Co-culture with stromal cells improves vascular barrier function	119
5.3.2	Different co-cultures of stromal cells and HUVECs exhibited distinctive cytokine patterns	124
5.3.3	Modeling pathophysiological microvessels with biological com- pounds	128
5.3.4	Screening chemotherapy drugs and demonstrating vascular dose- dependent responses	135
5.3.5	Organ-specific microvessels reveal the distinctive patterns in cytokines and recovery	139
5.4	Discussion	145
5.5	Conclusions	152
	Competing Interests	153
	Acknowledgments	153
6	Conclusions and Recommendations for Future Work	155
6.1	Comparison of IFlowPlate™ and AngioPlate™	157
6.1.1	IFlowPlate™: flexibility and dynamism in vascular modeling .	157
6.1.2	AngioPlate™: precision and reproducibility in high-throughput settings	158
6.1.3	Choosing between IFlowPlate™ and AngioPlate™	159
6.2	Future Work	159

6.2.1	IFlowPlate™: advanced vascularized tumor models and organ-specific vascular mechanisms	160
6.2.2	AngioPlate™: organ-specific drug efficacy and mechanical actuation for disease modeling	161
	Bibliography	163
	A Supplemental Information for Chapter 2	194
	B Supplemental Information for Chapter 3	196
	C Supplemental Information for Chapter 4	200
	D Supplemental Information for Chapter 5	204

List of Figures

1.1	Value proposition of advanced in vitro models, organ-on-a-chip. . . .	5
1.2	The rise in academic publishing in the field of organ-on-a-chip. The keywords ‘organ-on-a-chip’ or ‘organ-on-a-chip AND vascular’ were searched in Google Scholar. The number of publications found from the search for each corresponding year was plotted from 2008 to 2017. The rise in publications on the topic of organ-on-a-chip exemplifies the increasing activity in the field. Vasculature has been mentioned in nearly two-thirds of all organ-on-a-chip publications, indicating the prevalence and importance of this biological component in organ-on-a-chip models.	8
1.3	Selected examples of various approaches to create a blood vessel-on-a-chip as an in vitro model for drug discovery. (a) Human umbilical vein endothelial cells cultured on the inner luminal surface of a PDMS microchannel with a cross-section of $30 \times 30 \mu\text{m}$. Reproduced from [1]. CC BY 4.0. (b) Human trophoblasts and endothelial cells cultured on two sides of a PDMS membrane and stained for E-cadherin (red) and VE-cadherin (green), respectively. Reproduced from [2] with permission of The Royal Society of Chemistry. (continued)	10

1.4	Selected examples of in vitro models with organ-specific vasculatures (heart, liver, lung, kidney, and brain) for drug discovery. (continued)	20
2.1	Abstract for Chapter 2	33
2.2	IFlowPlate™ operation and interstitial flow in hydrogel. (a, b) Image and illustration of IFlowPlate™ containing an array of three-well perfusion units connected with microchannels. Scale bar, 3 mm. (c) Illustration of vascularized hepatic spheroids in IFlowPlate™. Blood vessels are shown in red while hepatic spheroids are shown in green. (d) Distribution of color dye in fibrin gel over time under either interstitial flow or passive diffusion in IFlowPlate™. White dotted lines outline the edge of the well. Scale bar, 3 mm.	43
2.3	Culture of perfusable microvascular bed on IFlowPlate™. (continued)	44
2.4	Angiogenesis assay on IFlowPlate™. (a) Illustration of the experimental setup for the angiogenesis assay. (b) Fluorescent image of GFP-endothelial cell sprouting into fibrin gel with or without fibroblasts (FBs). Scale bar, 100 μ m. (c) Quantification of the length of vessel sprouts in fibrin gel with or without fibroblasts. NS indicates no sprouting. * indicates $p < 0.05$. $n = 3$	46
2.5	Culture of vascularized liver spheroids on IFlowPlate™. (continued) .	47

2.6	Nanoparticle and nutrient delivery to liver spheroids on IFlowPlate. (a) Illustration of intravascular nanoparticle deliver to liver spheroids. (b) Bright-field and fluorescent time-lapse images of nanoparticles (1 μ m, green) perfused from the vasculature and then leaked into the liver spheroid. Red arrows label the particle exiting the vessel and entering the liver spheroid. White arrows label a cluster of particles accumulating inside the spheroid. Scale bar, 200 μ m. (c) Fluorescent images of wells seeding with microvasculature (GFP, green), fibroblasts, and different numbers of liver spheroids (labeled with cell-tracker red) on day 6. Liver spheroids also contain GFP-endothelial cells (green). The final images are stitched from multiple images. High-magnification images are derived from areas labeled with dotted white boxes. Scale bar, 1 mm. (d) Quantification of albumin secretion from spheroids cultured with or without vasculature and perfusion. n = 4. * indicates p < 0.05. (e) Image of extracted vascularized hepatic tissue that can be used for implantation. The ruler shown is in mm scale.	50
3.1	Automated procedures for building human microvascular networks on IFlowPlate™(continued)	66
3.2	Structural analyses of microvascular networks. (continued)	69

3.3	Figure 3. 3. Screening chemotherapy drug bortezomib on IFlowPlate™. (a) Representative images of microvascular networks before and after 72 h bortezomib treatment at various concentrations. n = 4 for the vehicle group and n = 5 for the rest groups. (b) Graph quantifying diffused dextran during the 1-hour permeability assay in μ g, percentage change of perfusable networks, and percentage change of GFP signal ratio. n = 4 for the vehicle group and n = 5 for the other groups. (c) The heat map visualizes the GFP signal measurements of the middle wells containing microvascular networks.(continued)	73
3.4	Figure 3. 4. Screening chemotherapy drug vincristine on IFlowPlate™. (a) Representative images of microvascular networks before and after 72 h vincristine treatment at various concentrations. n = 5 for each group. (b) Graph quantifying percentage change of perfusable networks and percentage change of GFP signal ratio. n = 5 for each group. (c) The heat map visualizes the GFP signal measurements of the middle wells containing microvascular networks. (continued) . . .	76
4.1	Subtractive manufacturing with swelling induced stochastic folding of sacrificial materials for fabricating complex perfusable tissues. (a) Image of encapsulated alginate fiber networks in a 384-well plate. (b) Schematic on the use of AngioPlate™, which includes gel casting, folding of the alginate network in the hydrogel, and degradation of the sacrificial alginate template. (c) Illustration of a generic bifurcating network design. (continued)	86

4.2 Vasculature in AngioPlate™ device. (a) 3D volumetric rendering of confocal z-stack images of a vascular network populated with human umbilical cord vein endothelial cells. View from xz-plane is maximum projection. Cells were stained for CD31 (green) and DAPI (blue). Scale bar, 500 μ m. (b) Fluorescent images of vascular networks perfused with 70 kDa fluorescein-dextran (green) with or without the presence of endothelial cells and/or Triton™ X-100 treatments. Scale bar, 2 mm. (c) Quantification of dextran (70 kDa) diffusion rates of the vascular networks in response to no treatment, Triton™ X-100 (positive control), and drug treatments, n = 3. Statistical significance was determined using one-way ANOVA. * $p \leq 0.05$ ** $p \leq 0.01$ *** $p \leq 0.001$. ns indicates not significantly different. (d-f) Fluorescent image of a vascular network stained for laminin (green), F-actin (red), CD31(red), extracellular vWF (green), and DAPI (blue). Scale bar, 100 μ m. g, Transmission electron microscope image of endothelium on a vessel wall showing the tight junction between two adjacent endothelial cells. Scale bar, 1 μ m. 96

5.1	AngioPlate™for building human microvessels assay. (a) A schematic overview of vascular assays building on AngioPlate™. Samples such as drugs, inflammatory cytokines, and pathogenic agents can be screened on AngioPlate™through the vessels. Each AngioPlate™contains 128 sets of tissue culture units available for building vessels. Each tissue culture unit consists of one inlet well, one middle well, and one outlet well. One channel connects the inlet and middle wells in the same tissue culture unit, while another channel connects the middle and outlet wells. Additionally, a gelatin fiber served as the sacrificial material is placed in the center of the tissue culture unit, crossing the inlet, middle, and outlet wells. Various human vessel assays can be built on AngioPlate™using human organ-specific stromal cells and ECs, such as lung and liver-specific vessels. (continued)	118
5.2	Establishment of mature microvessels with stromal cells. (continued)	122
5.3	Cytokine analysis reveals the influence of stromal cells on vascular maturation. (continued)	127
5.4	Development of microvessels that mimic pathological conditions using biological substances. (continued)	134

5.5	Capturing dose-dependent responses of chemotherapy drugs using microvessels assay on AngioPlate™. (a) Visualization of the dextran diffusion across various doses for bortezomib, vincristine, paclitaxel, axitinib, bleomycin, mitomycin, sorafenib, amifostine, imatinib, tamoxifen. (b) Categorization of the chemotherapy drugs tested based on their known effects on microvessels and captured impacts. (c-l) Quantification of the transportation rate for microvessels under the influence of (c) bortezomib, n = 17 in total; (d) vincristine, n = 14 in total; (e) paclitaxel, n = 12 in total; (f) axitinib, n = 11 in total; (g) bleomycin, n = 9 in total; (h) mitomycin, n = 11 in total; (i) sorafenib, n = 13 in total; (j) amifostine, n = 10 in total; (k) imatinib, n = 13 in total; (l) tamoxifen, n = 13 in total. The active C_{max} concentration for each drug is labeled.	138
5.6	Building organ-specific microvessels and modeling organ-specific vascular responses. (continued)	143
A.1	Fluorescent images of GFP-endothelial cells (green) self-assemble into microvascular networks at different initial cell seeding densities. Scale bar, 3mm.	195
B.1	Fluorescent images taken with the FITC filter and 4X objective of self-assembled microvascular networks with and without fibroblasts on day 1, day 3, and day 7.	198

B.2	The flowchart describing the major processes in code to control the robotic handling system for preparing microvascular networks on IFlow-Plate™. Created in Lucid (lucid.co)	199
C.1	Step-by-step fabrication of AngioPlate-384™. First, using standard photolithography, we fabricated a PDMS mold with various patterns connected to an inlet and outlet well. The mold was then capped onto a polystyrene sheet to form an array of micro-channel networks. The networks were loaded with 3 wt.% alginate solution. Next, the entire mold was immersed in a calcium bath (1 mM), where calcium ions gradually diffused from the inlet and outlet wells into the alginate solution within the network, cross-linking the alginate overnight. With this approach, we were able to pattern 128 independent alginate fiber networks in the format of a 384-well plate. PEGDM solution was injected into the channels in the same way to encapsulate the alginate fiber to facilitate alginate release and to create the inlet/outlet channels. Finally, the polystyrene sheet patterned with alginate and PEGDM was assembled onto the base of a bottomless 384-well plate, encasing and sealing the alginate networks with a high-viscosity PDMS glue.	201

C.2	Optimization of hydrogel matrix cross-linking condition for network formation. Fluorescent images of networks perfused with 1 μ m fluorescent particles (green) under various gelling conditions in both the collagen-based gel and fibrin-based gel. Red boxes label the good conditions that resulted in the formation of complete perfusable networks. Scale bar, 2mm.	202
C.3	Structural variation of vasculature in AngioPlate™. (a) Brightfield time-lapse images of networks seeded with human endothelial cells. Scale bar 1mm. (b) Quantification of variation in vasculature structure. n=12. (c) Variation in the network structures from 12 different wells. Scale bar 1mm.	203
D.1	Illustration of vessel development on AngioPlate™. Hydrogel casting and sacrificial material removal are performed on day 0. Stromal cells are cultured from day 0 to day 4 for maturation, and ECs are seeded on day 4 and cultured until day 14 for further vascular maturation. Treatments and data collection occur from day 14 to day 17. Created with BioRender.com.	208
D.2	Brightfield images of vessels built with different stromal cell conditions on day 4, day 11, and 18 (continued)	209

D.3	DAPI analyses of vessels cultured with different stromal cell conditions.	
	(a) Visualization of the DAPI from vessel images and quantification demonstrated as polar histogram for each nuclei identified from each vessel. Three vessels from each condition were used: vessels built with HUVECs (vessel 1: n = 141, vessel 2: n = 84, vessel 3: n = 111), HUVECs with FBs (vessel 1: n = 136, vessel 2: n = 142, vessel 3: n = 69), HUVECs with PCs (vessel 1: n = 127, vessel 2: n = 155, vessel 3: n = 93), and HUVECs with PCs and FBs (vessel 1: n = 101, vessel 2: n = 93, vessel 3: n = 101). (b) The average circularity of the nuclei identified in each vessel for vessels built with HUVECs only, with HUVECs and FBs, with HUVECs and PCs, and with HUVECs, PCs, and FBs. n = 3. (c) The fraction of cells that are aligned with the flow direction, having DAPI centre line direction within 10° away from the vessel centre line. The fraction of aligned cells for each condition was compared to the HUVECs only group (n = 3) : HUVECs with FBs (** P = 0.0033, n = 3); HUVECs with PCs (* P = 0.0104, n = 3); HUVECs with PCs and FBs (n = 3).	210
D.4	(a, b) Quantification of TRITC 65-85 kDa (a) and FITC 4 kDa (b) dextran diffusion in the vessels on day 11 and day 18 for conditions developed without cells, with HUVECs, with FBs, with HUVECs and FBs, with PCs, with HUVECs and PCs, with PCs and FBs, and with HUVECs, PCs, and FBs.	211
D.5	(a-c) Measurements of differential concentrations of cytokines between the control group (n = 6) and the IFN γ group (n = 3). (continued) .	212

D.6	(a-c) Brightfield images of vessels taken with 4x objectives and enlarged regions for vessels built with different organ specific cells on day 4, day 10, and day 16: (a) HUVECs and Lung FBs; (b) liver ECs and liver FBs; (c) lung ECs and lung FBs.	214
D.7	The illustration of the sterile reagents and devices loading locations on the robotic handling system.	215
D.8	The flowchart describing the major processes in code to control the robotic handling system for preparing vessels on AngioPlate™. Created in Lucid (lucid.co)	216

List of Tables

1.1	Representative contributions to the modeling of vascular physiology from organ-on-a-chip devices with a vascular component.	6
4.1	List of antibodies used and their catalog numbers	91
B.1	Reagents for establishing different numbers of columns using the NIMBUS system	197
D.1	Cell suspension preparation for setting up different experimental manually	205
D.2	Reagents preparation for setting up various number of columns using the NIMBUS system	206
D.3	Compounds' catalog numbers and stock concentrations	207

Definitions, and Abbreviations

Definitions

Angiogenesis Angiogenesis is the physiological process through which new blood vessels form from pre-existing vessels. This complex, multi-step process is vital for growth, development, and wound healing in the body.

Array An array in the context of scientific research and laboratory terminology is an orderly arrangement of samples where specific reactions can take place or be measured. It allows for systematic analysis and is often used to conduct multiple experiments simultaneously.

Assay An assay is a laboratory procedure that measures the presence, quantity, or functional activity of a target entity, which can be a drug, biochemical substance, or a cell in an organism or organic sample. Assays are used for a variety of purposes, such as disease diagnosis, detecting the concentration of a particular molecule (like glucose in blood), determining the effects of a drug, or measuring the purity of a substance.

Cytokine Cytokines are a broad category of small proteins that are important

in cell signaling. They are released by cells and have a specific effect on the interactions and communications between cells.

High-throughput

High-throughput refers to techniques and processes that allow for the rapid and simultaneous analysis of a large number of samples or the testing of multiple variables with minimal manual intervention.

Organ-on-a-chip

An organ-on-a-chip is a microfluidic cell culture device created with the intent to mimic complex biological functions of an organ in a small-scale, controlled environment. This technology leverages advances in microfabrication, tissue engineering, and microfluidics to create three-dimensional models of human organs on a chip – essentially, miniaturized versions of full-scale organs.

Perfusability In tissue engineering and vascular research, perfusability is defined as the capability of a synthetic or engineered vessel to support the flow of blood or a blood-mimicking fluid through it under physiological conditions.

Permeability In vascular engineering, permeability refers to the capacity of blood components, nutrients, and other molecules to pass through the endothelial layer lining the blood vessels. The design of vascular

grafts or synthetic vessels aims to replicate this selective permeability, thereby maintaining physiological functions such as nutrient delivery and waste removal. This approach also supports proper cellular communication and homeostasis.

Stromal cells Stromal cells are a type of connective tissue cells found in various organs and tissues throughout the body. They play a fundamental role in supporting the structure and function of the specific tissue in which they reside.

Vascularization

Vascularization in tissue engineering refers to the formation of functional blood vessels within engineered tissues. It is a critical process for providing nutrients, oxygen, and waste removal to sustain living cells, especially in thicker tissue constructs where diffusion alone is insufficient for cell survival.

Abbreviations

IL-1RA Interleukin-1 Receptor Antagonist

BMP-9 Bone Morphogenetic Protein 9

DAPI 4',6-Diamidino-2-Phenylindole

EC Endothelial Cell

EGF Epidermal Growth Factor

F-actin	Filamentous Actin
FB	Fibroblast
FGF-1	Fibroblast Growth Factor 1
FGF-2	Fibroblast Growth Factor 2
FITC	Fluorescein Isothiocyanate
G-CSF	Granulocyte-Colony Stimulating Factor
GM-CSF	Granulocyte-Macrophage Colony-Stimulating Factor
HB-EGF	Heparin-Binding Epidermal Growth Factor
HepG2	Hepatocellular Carcinoma Cell Line
HGF	Hepatocyte Growth Factor
HUVEC	Human Umbilical Vein Endothelial Cells
IFNγ	Interferon Gamma
IL-1β	Interleukin-1 Beta
IL-10	Interleukin-10
IL-12(p40)	40 kDa Subunit of IL-12
IL-12(p70)	70 kDa Subunit of IL-12
IL-13	Interleukin-13
IL-2	Interleukin-2

IL-4	Interleukin-4
IL-5	Interleukin-5
IL-6	Interleukin-6
IL-8	Interleukin-8
LPS	Lipopolysaccharide
MCP-1	Monocyte Chemoattractant Protein-1
PC	Pericyte
PLGF	Placental Growth Factor
Poly(I:C)	Polyinosinic:Polycytidylic Acid
SEM	Scanning Electron Microscopy
TEM	Transmission Electron Microscopy
TGFβ	Transforming Growth Factor Beta
TNFα	Tumor Necrosis Factor Alpha
TRITC	Tetramethylrhodamine Isothiocyanate
VEGF-A	Vascular Endothelial Growth Factor A
VEGF-C	Vascular Endothelial Growth Factor C
VEGF-D	Vascular Endothelial Growth Factor D

Declaration of Academic Achievement

This Ph.D. thesis has been prepared as a sandwich thesis containing work previously published or prepared for publishing, as listed below.

Chapter 1: Lin, D. S. Y., Guo, F., & Zhang, B. (2019). Modeling organ-specific vasculature with organ-on-a-chip devices. *Nanotechnology*, 30(2), 024002.

DOI 10.1088/1361-6528/aae7de

Chapter 2: Lin, D. S. Y., Rajasekar, S., Marway, M. K., & Zhang, B. (2020). From model system to therapy: scalable production of perfusable vascularized liver spheroids in "open-top" 384-well plate. *ACS Biomaterials Science & Engineering*, 7(7), 2964-2972. DOI 10.1021/acsbiomaterials.0c00236

Chapter 3: Lin, D. S. Y., Anvari, N., Rajasekar, S., & Zhang, B. (2024). Robot-assisted fabrication of microvascular networks: enhancing high-throughput screening for chemotherapy drugs. (*Manuscript in preparation.*)

Chapter 4: Rajasekar, S.*, Lin, D. S. Y.*, Zhang, F.*, Sotra, A., Boshart, A., Clotet-Freixas, S., Liu, A., Hirota, J. A., Ogawa, S., Konvalinka, A., & Zhang, B. (2022). Subtractive manufacturing with swelling induced stochastic folding of sacrificial materials for fabricating complex perfusable tissues in multi-well plates. *Lab on*

a Chip, 22(10), 1929-1942. (* *These authors contributed equally to the work.*) DOI:
10.1039/d1lc01141c

Chapter 5: Lin, D. S. Y., Hashemi, H., Chakravarty, A., Jozani, K., Bonanno, J., Anvari, N., Rajasekar, S., Zhang, F., & Zhang, B. (2024). High-throughput modeling of vascular responses in human microvessel arrays using AngioPlate™ (*Manuscript in preparation.*)

Chapter 1

Introduction

The content of this chapter is a second revision of the manuscript text for publication under the following citation:

- Lin, D. S. Y., Guo, F., & Zhang, B. (2019). Modeling organ-specific vasculature with organ-on-a-chip devices. *Nanotechnology*, 30(2), 024002.

(Requested permission to reprint.)

Copyright © Institute of Physics and IOP Publishing Limited 2019.

DOI 10.1088/1361-6528/aae7de

Modeling organ-specific vasculature with organ-on-a-chip devices

Author contributions

D.S.Y.L. wrote and edited the manuscript. F.G. edited the manuscript. B.Z. wrote and edited the manuscript, and supervised the work.

Abstract

Organ-on-a-chip devices, also known as microphysiological systems, have gained significant attention in recent years. Recent advances in tissue engineering and microfabrication have enabled these devices to provide more precise control over cellular microenvironments to mimic the tissue-level or organ-level function of the human body. These more complex tissue models can provide either an improvement in the functional expression and maturation of cells or an avenue to probe biological

events and function that would otherwise be difficult to visualize and mechanistically study. This high-value information, when complemented with the existing gold standards of cell-based assays and animal models, could potentially lead to more informed decision-making in drug development. A prevalent biological component in many organ-on-a-chip devices is an engineered vascular interface that is present in almost all organs of the human body. The vasculature and the vascular interface are particularly susceptible to biomechanical forces; they function as the conduits for inter-cellular and inter-organ interactions and regulate drug transport. In this review, we examine the various approaches taken to model the human vasculature with an emphasis on the engineering of organ-specific vasculatures and discuss various challenges and opportunities ahead as the field advances.

Keywords: organ-on-a-chip, vascularization, microfluidics, microfabrication

1.1 Introduction

The rising cost of drug development is a major healthcare issue. Despite the increasing expenditures invested in drug development, the number of drugs approved annually has been decreasing over the past 20 years [3]. This trend is at least in part due to the lack of tools to dissect and predict the effects of drugs prior to clinical trials. Existing clinical models, such as cell-based assays in the monolayer culture format, can be powerful tools because of their low costs and high-throughput capability, and they will be irreplaceable as initial screening tools. However, it is clear that cell-based assay, even complemented with animal testing, falls short in accurately predicting the effects of drugs as the success rate from Phase I clinical trial to market approval is

only 9.6% [4]. More advanced tissue model that provides a physiologicalrelevant microenvironment could drive more matured expression of cellular functions or provide a way to model and probe complex biological events that would otherwise be impossible to dissect or even observe in either monolayer culture or animal tests. Built on this principle, organ-on-a-chip technology emerged from the advancement in microfabrication and tissue engineering. Such platforms could provide high-value data that would otherwise be difficult to acquire in the existing drug discovery pipeline. However different models will offer different types of high-value data. Therefore, the utility of organ-on-a-chip devices will vary based on the specific biological question.

For instance, in a lung-on-a-chip device, Ingber’s group demonstrated neutrophil transendothelial migration in response to bacterial infection followed by phagocytosis in real time, which is a very complex biological event that would otherwise be difficult to observe directly during pulmonary inflammation and infection [5]. In a liver-on-a-chip device, Bhatia’s group showed robust functional improvement in gene expression profiles, phase I/II metabolism, canalicular transport of primary hepatocytes under patterned co-culture of hepatocytes and stromal cells compared to standard monolayer culture [6]. In one case, the organ-on-a-chip device offered a new capability to observe biological events, while in the other case, the organ-on-a-chip device offered more matured cellular functions that could alter the results of drug response (Figure 1.1, Table 1.1). Organ-on-a-chip technology clearly presents an enormous potential. However, translation of this technology will require further refinement in the manufacturing and engineering to address issues in usability, robustness, material

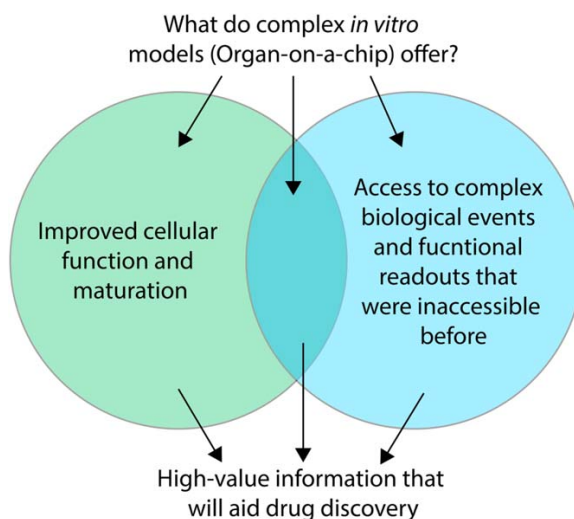


Figure 1.1: Value proposition of advanced in vitro models, organ-on-a-chip.

compatibility, and end-point analysis. More importantly, extensive biological validation will be expected to justify the additional costs and lower experimental throughputs. Overcoming these barriers to adoption will require collective efforts from the scientific community. In order to move the technology forward, this community will include not only bioengineers but also clinicians and biologists. Nonetheless, success in this endeavor will lead to enormous economic values as many major organ-on-a-chip companies are starting to explore and expand this market space: US company Organovo (market cap \$389 M) endeavors to bioprint liver organoids for drug testing; Wyss Institute startup Emulate raised \$45 M to develop lung and gut organ-on-a-chip platforms [3].

A common component of many organ-on-a-chip devices is the blood vessels or the vascular interfaces, which are so prevalent in almost every organ in the body (Figure 1.2). In this review, we specifically focus on the vasculature which functions

Table 1.1: Representative contributions to the modeling of vascular physiology from organ-on-a-chip devices with a vascular component.

Improved functions	Value added capabilities	References
Mechanical cyclic stretch shows exacerbated nanoparticle infiltration of the vascular-alveolar barrier, more closely resembles the physiological response in vivo	Visualizing neutrophil transendothelial migration in response to bacterial infection	[5]
	Observation of cell-free layer under physiological perfusion of blood in engineered microcapillaries	[1]
	Observation of vascular architecture-dependent VWF assembly after vessel injury	[7]
	Visualizing the process of thrombosis that involves collagen I deposition in blood clots by fibroblasts	[8]
	Visualizing cancer cell extravasation from engineered microcapillaries	[9]
Improved response to known anti-cancer drugs compared to cell-based assays (e.g., mitomycin C, gemcitabine, and vorinostat, etc)	Visualizing vessel regression and inhibition of tumor growth in response to anti-cancer drugs	[10]
	Visualizing vessel dilation and contraction in response to chemical stimuli	[11]
Improved function of hepatocytes in the presence of vasculature (e.g., cytochrome P450 expression, albumin/urea secretion, etc)		[12]
Reduced vascular permeability in blood–brain-barrier with direct neurovascular contact		[13]

as both the conduit and the barrier for inter-cellular interaction, inter-organ interactions, and drug delivery. Correctly incorporating a perfusable vascular component in an in vitro model is a critical aspect of the organ-on-a-chip technology that differs from the conventional monolayer cell culture. Blood vessels are anatomically unique in the sense that they experience a multitude of mechanical factors in their environment. Environmental factors, such as mechanical shear stress, cyclic stretching, flow pattern, and geometrical constraints, have been shown to have profound effects on the permeability, surface activity, and remodeling capabilities of blood vessels. Many engineering approaches have been developed to model the vasculature, but capturing all facets of the vascular physiology in a single model still remains a challenge. Furthermore, blood vessels develop different architectures, flow patterns, anatomical structures, and morphologies in different organs or even in different parts of an organ. These organ-specific differences in the vasculature are closely linked to the specific function of an organ, hence it remains to be seen if reproducing these organ-specific characteristics would lead to improved biological functions and specification as well as capture unique organ-specific biological events (e.g., the presence of tissue-specific oxygen gradients and drug delivery). So far only a few organ-on-a-chip devices have attempted to capture the organ-specific hallmarks of a vasculature while the majority of studies have incorporated the vascular component with only generic functionalities. In this review, we discuss the current state-of-the-art technologies in the modeling of blood vessels with organ-on-a-chip devices and present a unique focus on the modeling of organ-specific vasculature. Lastly, we discuss future challenges in device development and the path to commercialization.

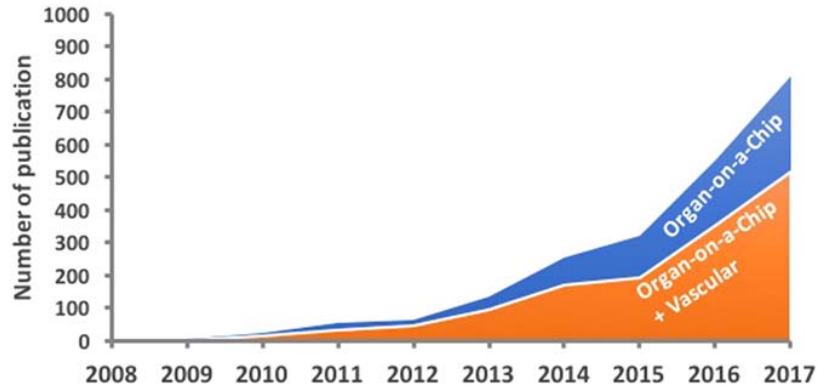


Figure 1.2: The rise in academic publishing in the field of organ-on-a-chip. The keywords ‘organ-on-a-chip’ or ‘organ-on-a-chip AND vascular’ were searched in Google Scholar. The number of publications found from the search for each corresponding year was plotted from 2008 to 2017. The rise in publications on the topic of organ-on-a-chip exemplifies the increasing activity in the field. Vasculature has been mentioned in nearly two-thirds of all organ-on-a-chip publications, indicating the prevalence and importance of this biological component in organ-on-a-chip models.

1.2 Engineering Approaches in Building Blood Vessels In Vitro

1.2.1 Blood vessel in a channel

Advances in soft-lithography allow us to easily construct optically transparent microfluidic devices containing microchannels in which human endothelial cells can be coated on the inner luminal surface to mimic an artificial blood vessel or a blood vessel network. Within these devices, the microenvironment of the endothelial cells can be fine-tuned by controlling fluid-induced shear stress and geometrical constraints, etc [14, 15]. The effects of fluid-induced shear stress on endothelial cell alignment and elongation, and on the secretion of angiogenic growth factors, etc have been widely demonstrated. Fluid shear forces imposed on the apical surface of endothelial cells

are transmitted to the intracellular cytoskeleton through transmembrane mechanosensors, leading to endothelial cells' morphological adaptation [16]. These microfluidic devices also facilitated the study of the interaction between the circulating cells in the blood and the endothelium. A recent study used a simple microfluidic channel coated with a layer of endothelial cells to examine the role of a glycosaminoglycan-rich layer (presented on the surface of the endothelium) in regulating the surface interaction with blood cells (Figure 1.3(a)) [1]. This device offers an important capability to closely examine the distribution of red blood cells (e.g., observation of cell-free-layer) under physiological perfusion inside micro-capillary mimics (Table 1.1).

In this case, however, microfabrication yielded microchannels with a square cross-section. Although this does not limit endothelial coverage, it presents a geometrical configuration that deviates from the physiological condition. This issue can be resolved with additional modification steps, including sequentially injecting a silicone oligomer solution and air through the micro-channels to produce a circular cross-section [17]. The macro-architecture of the vascular network can also play a role in regulating the interaction between the endothelium and the circulating cells [18–21]. Microfluidic devices can be used to recapitulate parts of the physiological microcirculation captured from clinical images. The role of bifurcations, tortuosities, and cross-sectional changes of the microfluidic network in the preferential adhesion of circulating cells or drug carriers can be studied on such systems to offer new biological insights [20, 22]. Although growing endothelial cells in microfluidic channels can provide robust control of the vascular structure, vascular permeability is an important parameter that cannot be easily probed in such systems. To overcome this issue,

the vascular channels and the parenchymal space can be compartmentalized and connected through permeable barriers composed of channel walls with micro-gaps. This configuration allows diffusion of biomolecules across the vascular barrier to enable the interaction between the endothelium and the parenchymal tissue [23–27].

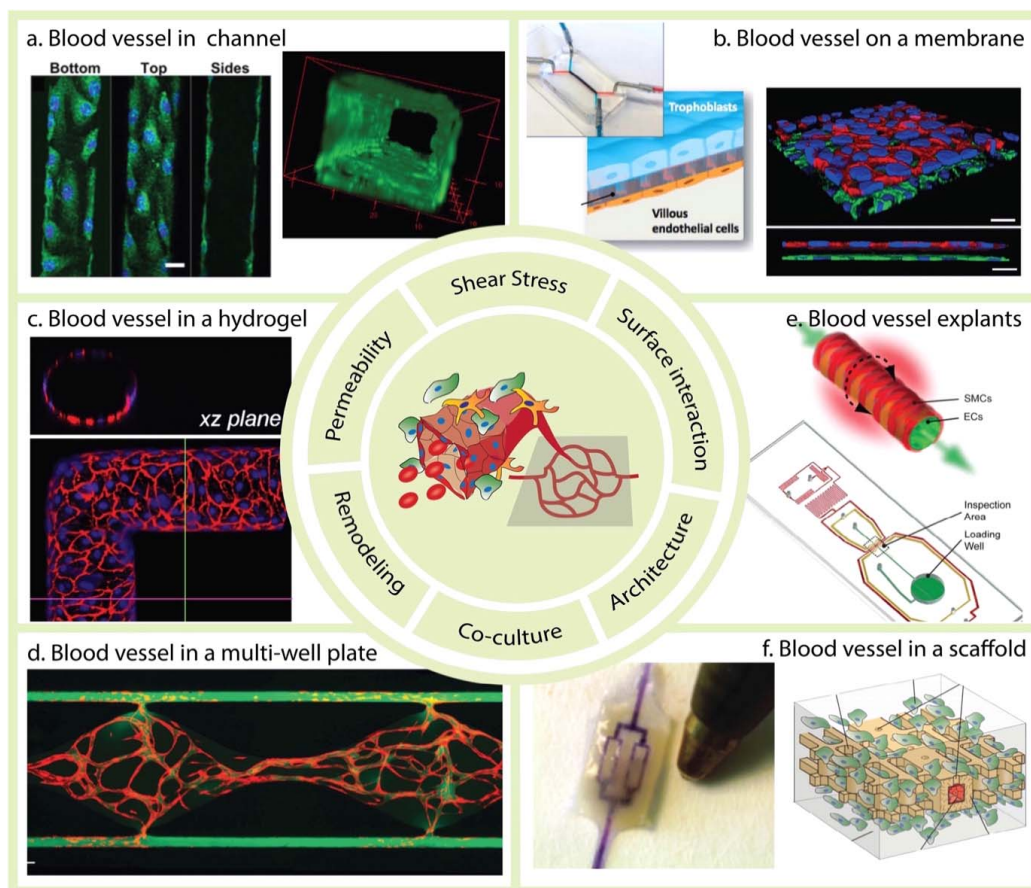


Figure 1.3: Selected examples of various approaches to create a blood vessel-on-a-chip as an in vitro model for drug discovery. (a) Human umbilical vein endothelial cells cultured on the inner luminal surface of a PDMS microchannel with a cross-section of $30 \times 30 \mu\text{m}$. Reproduced from [1]. CC BY 4.0. (b) Human trophoblasts and endothelial cells cultured on two sides of a PDMS membrane and stained for E-cadherin (red) and VE-cadherin (green), respectively. Reproduced from [2] with permission of The Royal Society of Chemistry. (continued)

Figure 1.3: (continued) (c) Human endothelial cells cultured on the inner luminal surface of a microchannel (100 μ m in diameter) embedded inside a collagen I hydrogel matrix and stained for CD31 (red). Reproduced with permission from [28]. (d) Human endothelial colony-forming cell-derived endothelial cells (red) isolated from cord blood formed vascular networks perfused with 70 kDa FITC-dextran (green). Reproduced from [10] with permission of The Royal Society of Chemistry. (e) Illustration of the integration of isolated mouse arteries and microfluidic devices to control and visualize vessel dilation and constriction. Reproduced from [11] with permission of The Royal Society of Chemistry. (f) An engineered AngioChip hepatic tissue with a built-in branched vasculature perfused with a blue dye next to the tip of a ball-point pen to show the scale. [29] 2016 Copyright © Springer Nature.

1.2.2 Blood vessel on a membrane

Another way of looking at the vasculature is to zoom in on the vascular interface at where the endothelium can be viewed as a flat cell monolayer. In this format, a number of organ-specific vascular interfaces have been developed (Figure 1.3(b)). Donald Ingber et al. demonstrated an in vitro model that can capture the organ-level functionality (e.g., breathing) of the human lung [5]. This breakthrough involved the culture of endothelial cells and lung epithelial cells on opposite sides of an elastic membrane that was subjected to both fluid-induced shear stress and cyclic stretching, thus mimicking the dilation of the lung alveoli. This platform captured many aspects of the vascular physiology, including the transendothelial migration of circulating immune cells followed by phagocytosis under physiological flow, which would otherwise be impossible to model on a 2D monolayer culture (Table 1.1). The significance of being able to track and visualize these types of complex biological events is that as we look at disease and drug treatments (e.g., inflammatory disease or drugs) we will be able to precisely determine which step breaks down in this sequence of biological processes instead of solely relying on end results. This will not only allow us to gain

confidence in the understanding of a disease but also the mechanism of action of a drug. In this study, the significance of cyclic mechanical strain was also highlighted with the demonstration of elevated nanoparticle uptake across the vascular-epithelial barrier, which is in agreement with animal studies. Building on this seminal work, the Ingber group and others have developed a series of biological models: placenta-on-a-chip [30, 2] glomerulus-on-a-chip [31], blood–brain barrier (BBB)-on-a-chip [32], vessel-on-a-chip [33], blinking eye-on-a-chip [34], and cancer-on-a-chip [35], etc. This expansion of membrane-based devices is a clear indication of the potential to replicate a diverse set of biological environments. To further enable multi-organ integration by potentially linking these individual organ models together with a continuous vascular interface, endothelialized elastomeric tubing was also developed to facilitate the connections [36].

1.2.3 Blood vessel in hydrogels

One important concern, however, in regenerating the vascular interface with a membrane-based approach is the membrane itself. The elastic membrane, with a thickness of around $10\ \mu\text{m}$, is an artificial barrier in between the endothelium and the underlying parenchymal tissue or epithelial cells. However, the basement membrane that separates the endothelium from the parenchymal tissues, which the elastic membrane mimics, has a thickness of no more than $100\ \text{nm}$ in vivo. Although patterned micro-holes on elastic membranes allow cell migration and molecular diffusion, direct intercellular contact or vascular remodeling can be difficult to establish. This limitation can be overcome with compatible natural hydrogel matrices. Recent advances in hydrogel molding techniques have enabled the fabrication of hollow channels within

a soft hydrogel using 3D printing of sacrificial materials [37], soft-lithography [28], etc. (Figure 1.3(c)). Culturing endothelial cells within these micro-channels, which are surrounded by compatible hydrogels embedded with parenchymal or stromal cells, allowing close contact between the endothelium and the parenchymal tissues to establish a more realistic vascular interface [28, 38]. In addition, the mechanical stiffness of the hydrogel matrix can be fine-tuned to better model the physiological conditions compared to synthetic materials such as polydimethylsiloxanes (PDMS) and polystyrenes. Within the hydrogel matrices, endothelial cells can readily modify the microenvironment to form circular vessels or vascular branching through angiogenic sprouting [28, 39, 40]. Enabling biological remodeling is as important as controlling the initial biological structure. This type of platform could help visualize and study transient cellular events (e.g., vascular sprouting, regression, and rearrangement) that would only happen during tissue growth and remodeling.

Moreover, the emergence of 3D printing and microfabrication makes it feasible to construct complex 3D vasculatures, opening the gateway to engineering large vascularized tissues as well as examining complex blood flow dynamics in 3D [39, 7, 41–44]. For instance, after vessel injury, the endothelium becomes activated and starts to secrete von Willebrand factors (vWF). Secreted vWF quickly assemble into thick bundles or complex meshes. Using a microfabricated vascular model, the study found high shear stress, sharp geometrical turn, and smaller vessel diameter all induce more vWF assembly [7]. VWF assembly is an important step in the initiation of microvascular thrombosis because the presence of vWF bundles binds platelets, leukocytes, and erythrocytes as well as obstructs blood flow [7] (Table 1.1). This study highlights the significant role of vascular architecture in disease modeling. In a different study,

the complex interaction among the endothelium, blood, thrombi, and stromal cells in post-thrombotic remodeling was captured in a simple bifurcated vessel that was 3D printed to model thrombosis on-a-chip [8]. By incorporating fibroblasts, endothelium, and blood clots, the study demonstrated the deposition of type I collagen in the blood clot by fibroblasts, which resembles the fibrosis remodeling process in vivo (Table 1.1).

1.2.4 Blood vessel in a multi-well plate

To simplify and accelerate commercial translation, organ-on-a-chip devices would also benefit by adapting the model from a microfluidic setup to a conventional multi-well plate format, which is widely used in the pharmaceutical industry for drug screening. MIMETAS, an organ-on-a-chip company based in Leiden, Netherlands, is leading this effort with their proprietary phase-guided hydrogel patterning technique. On their commercialized microfluidic titer plate, an array of hydrogel-liquid interfaces can be rapidly created in a multi-well plate format with this technique. Endothelial cells [45], intestinal epithelial cells [46], kidney proximal tubular cells [47], and other parenchymal tissues [48–50] have been cultured in this format under perfusion. In contrast to other blood vessel on-a-chip technologies based in microfluidic devices, MIMETAS' OrganoPlate® provides high-throughput experimentation (e.g., 96 vessels in a single plate) with the use of simple gravity-driven flow that requires no bulky external pumps and is highly scalable. However, this platform thus far is limited to modeling tubular vessels without any branched vascular structures. The native vasculature is dynamic and constantly evolves through remodeling and rearrangement, especially in response to disease or tissue regeneration. Based on the intrinsic tendency of

endothelial cells to self-assemble into a rudimentary vascular network, a perfusable vascular bed can be engineered in a hydrogel given the right experimental conditions. Several different microfluidic devices have been developed to facilitate anastomoses or the connection of self-assembled microvascular networks with microfluidic perfusion circuits at pre-established hydrogel-liquid interfaces to establish perfusion [51–55]. Without physical constraint on the self-assembled microvessels within the hydrogel, dynamic vascular events, such as angiogenesis and vessel regression, can be studied and visualized in response to drug stimuli under perfusion. This capability is powerful as traditionally only simple cellular functions, such as endothelial cell migration, can be studied in a 2D transwell system while more complex vascular remodeling events have to be studied on animals with cranial windows. Organ-on-a-chip platforms based on this principle have also been productized in the multi-well plate format (Figure 1.3(d)) [10, 56, 9, 57]. In this format, a panel of FDA-approved anti-cancer compounds with different anti-tumor and anti-vessel effects were tested on an array of vascularized tumor models. The platform successfully captured the anti-vascular effects of linifanib, axitinib, and sorafenib and the anti-tumor effects of mitomycin C, gemcitabine, vorinostat, and tamoxifen, while monolayer cell assay failed to capture the anti-tumor effects of mitomycin C, gemcitabine, and vorinostat at the same dosage (Table 1.1).

1.2.5 Blood vessel explants

Another important aspect of the vascular physiology is the smooth muscle cells. Many clinical drugs target smooth muscle cells to modulate vessel dilation and contraction.

But incorporating smooth muscles in a blood vessel-on-a-chip model has been challenging, partly due to the complexity involved in reproducing the circumferential alignment and concentric geometry of the smooth muscles. Nonetheless, microfluidic chips have been developed to study explanted small arteries and veins [11, 58], where the vascular explants can be loaded, cultured, and stimulated with drugs inside the chip (Figure 1.3(e)). In this format, vessel dilation and contraction in response to drug stimuli can be visualized in real time. The core of this technology is in the controlled manipulation of organ explants and engineered tissues. Therefore, this technology can potentially be integrated with organoid technology and tissue engineering that seek to provide sophisticated human tissue substitutes. For example, stem cell-derived organoids, although structurally sophisticated, may benefit from the dynamic perfusion offered by this type of microfluidic platforms.

1.2.6 Blood vessel in a scaffold

Many vascular models were developed separately from the parenchymal tissues (e.g., liver, cardiac, and skeletal muscles) [28, 59], whereas many parenchymal tissues have been developed in the absence of vasculature [60–62]. There is often a technical gap between these two types of models. However, placing a perfusable vascular interface within a 3D functional tissue is a critical step toward high-fidelity organ models. Recently, we engineered functional heart muscles and liver tissues with a built-in stable vasculature using a microfabricated bio-scaffold (Figure 1.3(f)) [29]. The vascular interface supported by the elastomeric polymer is both permeable and mechanically stable to withstand extensive parenchyma remodeling without collapsing. This feature allows us to effectively place a perfusable vasculature inside a functional tissue

with high cell density. Vascular sprouting from the predefined vessel network is also possible. It is important to note that vascular remodeling/sprouting and mass transport in a hydrogel are very different from that of a dense tissue [63]. Therefore, establishing perfusable vasculature within a dense functional tissue at a physiological cell density (10^8 cells cm^{-3}) is a challenge and a physiological hallmark that should not be overlooked.

1.3 Organ-Specific Vasculature-on-a-Chip

The interactions of blood flow, vessel architecture, endothelium, and parenchymal tissues vary drastically from organ to organ. These differences largely arise from the anatomical and functional differences between the vasculatures in different organs. For instance, the endothelium from different organs displays different morphologies. One of the classifications of the vascular system, developed by Majno in 1965, categorized the vascular endothelium into three major groups based on their characteristics of the endothelial lining and the basement membrane: type I vessels have continuous endothelial lining (e.g., skeletal muscle, brain, myocardium, lung, skin); type II vessels have continuous endothelial lining but with fenestrations (e.g., endocrine glands, kidney); type III vessels have discontinuous endothelial lining (e.g., liver, spleen) [64, 65]. These morphological differences impart the vasculature with widely different permeability and barrier functions. In addition, the parenchymal tissue structures provide important physical cues to the development of the vascular networks. For instance, the microvasculature in muscles develops along the muscle fiber whereas the vasculature in kidney glomeruli forms spherical clusters, a striking contrast as a result of different developmental processes [65, 66]. Therefore, to correctly model drug delivery

or biological interactions in these organ-specific microenvironments, it is essential to recapitulate the organ-specific vascular architectures and morphologies.

1.3.1 Cardiac vasculature-on-a-chip

For a typical human at rest, the blood is pumped through the heart at a rate of 6 liters per minute. To support this mechanical demand, the heart develops a muscular wall that is supported by nutrients delivered through a dense vascular network [67]. In fact, in the myocardium, each cardiomyocyte is located no further than approximately 20 μm away from a capillary. The average diameter of capillaries in the adult human is 8 μm [68], and the density of capillaries in the myocardium is around 2000 capillaries mm^{-2} . To reproduce this highly organized and dense vasculature, Thomas Eschenhagen et al. developed a 3D microvessel system with a high vascular density (lumina diameter of 6–8 μm , intervessel distances of 20–60 μm) in a strip of cardiac muscle [69]. A dense capillary network can also be induced with an explanted artery or vein on micropatterned substrates that contain a thymosin β 4-hydrogel in the presence of soluble vascular endothelial growth factor. Cardiomyocytes can be seeded on top of the established vascular bed, which can then be perfused to study the impact of the capillaries on the functions of the adjacent myocardial cells (Figure 1.4(a)). Radisic et al. used the same scheme integrated with cellular processes and lumen propagation to engineer endothelial cell proliferation and capillary outgrowth [70]. Even though the study reproduced aligned blood vessel structures, the model only included a single layer of vascular network physically separated from the cardiomyocyte layer. To establish a multi-layer vessel network, a continuously

extruded hydrogel tube that mimics blood vessels can be 3D printed into a 3D lattice matrix, which can be subsequently populated with cardiomyocytes [71]. This approach, although scalable, cannot provide branched vascular structures due to limitation in the 3D extrusion process. Alternatively, we have engineered a 3D branching vasculature with a 3D stamped polymer scaffold that can be populated with a variety of parenchymal cells (e.g., cardiomyocytes and hepatocytes). Different from soft hydrogel materials, the polymer scaffold can provide sufficient mechanical support to the built-in vasculature to support a contractile cardiac muscle [29]. This platform would allow us to deliver drugs indirectly to a beating cardiac muscle through the vasculature barrier, mimicking the actual physiological condition. In a different study that delivered drugs to an engineered liver tissue through a built-in vascular interface using a liver-on-a-chip device, the results showed a delayed drug response in the presence of the vascular barrier [72]. This study indicates that to better understand the rate of tissue response to drugs, the vascular barrier is a critical parameter to consider even for small molecule drugs.

The endothelium that lines the vascular system has been shown to play a key role in controlling cardiac functions. Regulation of the subjacent cardiomyocytes was first described for the endocardial endothelium, and further established for the vascular endothelium in the myocardial capillaries [73]. While both endothelia have similar impacts on cardiac functions and growth, possibly as autocrine or paracrine modulators, it has been shown that each undertakes different paths in terms of signal processing. In addition, they differ in developmental and morphological features. Past developments in heart-on-a-chip models have focused mainly on the myocardial capillaries, while the endocardial endothelium has yet to be incorporated. The endocardial endothelium

plays a critical role in the embryonic development of myocardial cells through the neuregulin growth factor signaling pathway. The endocardial endothelium controls trabeculation of the heart by releasing neuregulins as a paracrine [74]. The modulation of the development of myocardial cells, executed by the myocardial capillaries, occurs much later compared to the endocardial endothelium. These physiological differences can potentially inspire the development of a heart-on-a-chip device with a built-in vascular component. Therefore, to accurately replicate the cardiac physiological environment, specific models that include the endothelium at different regions of the heart need to be developed in the future.

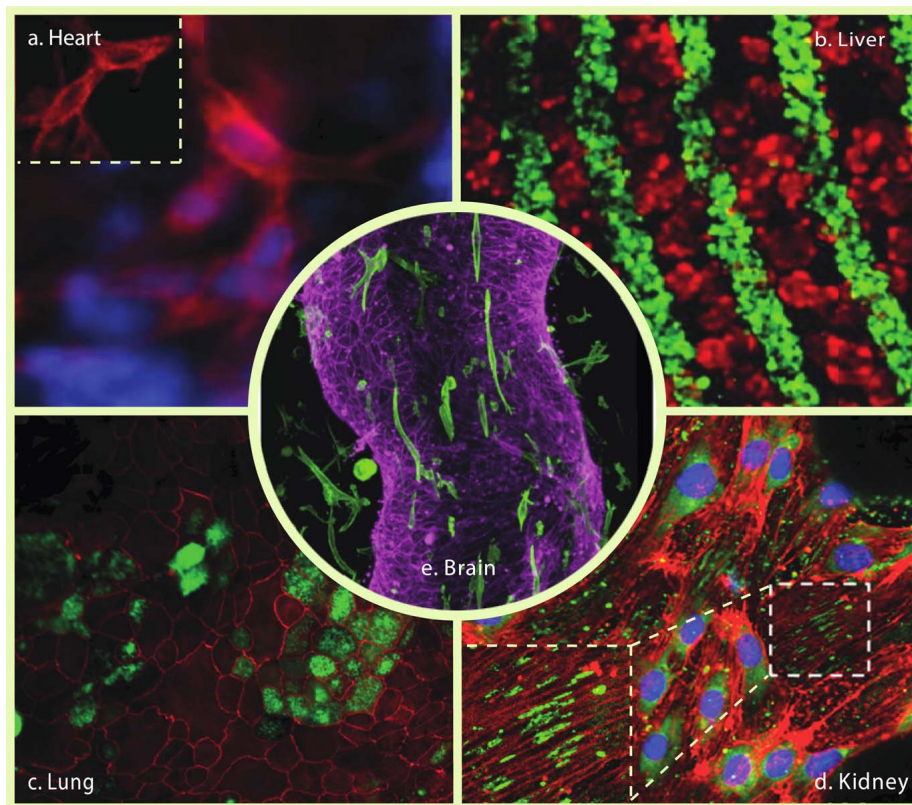


Figure 1.4: Selected examples of in vitro models with organ-specific vasculatures (heart, liver, lung, kidney, and brain) for drug discovery. (continued)

Figure 1.4: (continued) (a) High magnification image of troponin T immunostained (red) sections of engineered cardiac tissue cultured on top of a Tb4 gel embedded with capillaries, where the cell nuclei are stained with Hoechst dye (blue). Reproduced with permission from [70]. (b) Liver endothelial cells (green) patterned in fibrin hydrogel and integrated with hepatic aggregates (red) to form free-standing liver tissue seeds. From [75]. Reprinted with permission from AAAS. (c) Human airway epithelial cells (Calu-3) cultured on suspended hydrogel and stained with goblet cell marker MUC5AC (green) and ZO-1 tight junctions (red). Reproduced from [76] with permission of The Royal Society of Chemistry. (d) An engineered human kidney microvessel at a junction of a vessel network stained for F-actin (red) and plasmalemma vesicle-associated protein-1 (green). Reproduced with permission from [40]. Copyright © 2016 by the American Society of Nephrology. (e) An engineered brain microvessel composed of human endothelial cells (stained for VE-Cadherin, Magenta) and surrounded by brain astrocytes (stained for F-actin, green). Reproduced from [77]. CC BY 4.0.

1.3.2 Liver vasculature-on-a-chip

The hepatic sinusoids and the hepatocytes are the fundamental units that enable the liver to perform metabolism, store glycogen, synthesize proteins, and carry out detoxification. Hepatocytes are responsible for metabolic reactions and require organized vascular and stromal support [78, 79]. The highly organized hepatic sinusoids are open pore capillaries that have a discontinuous endothelium [80]. This feature of the liver endothelium, together with the presence of the perisinusoidal space (the space of Disse), underlies the efficient mass transport between the blood and the hepatic tissues [78]. To reproduce this intricate tissue organization, multiple types of cells need to be fabricated in an orderly fashion. An InVERT (Intaglio-Void/Embed-Relief Topographic) molding technique was developed by Stevens et al. to create an organized hepatic environment with compartments containing different cells in vitro (Figure 1.4(b)) [12, 75]. Endothelial/ stromal cells and induced pluripotent stem

cell (iPSC)-derived hepatocyte-like cells were patterned in PDMS topographic substrates and then transferred into a 3D hydrogel, yielding an engineered tissue with pre-defined microscale architectures. A rudimentary vasculature, for instance, can be patterned into a lattice matrix surrounding isolated islands of hepatocytes. However, with this approach the fabricated vascular system lacks perfusion *in vitro*. Liver-specific vasculature can also be engineered using a decellularized liver matrix. Uygun et al. have successfully built a transplantable recellularized liver graft that can carry out cytochrome P450 expression, albumin secretion, and urea synthesis [81]. The preserved vascular architecture in the liver matrices can be perfused and reendothelialized. Decellularized scaffolds can provide direct access to the high-level biological architectures of an organ, which are still largely missing in organ-on-a-chip models. Even though decellularized matrices are generally used for *in vivo* implantation, they can still play an essential role in an *in vitro* model when used as miniaturized scaffolds or processed hydrogels to overcome the issue of mass production and the high-throughput experimentation required in drug testing applications.

1.3.3 Pulmonary vasculature-on-a-chip

The minimal functional units for carrying out gas exchange in the lung are the alveoli, which are spherical capsules that have an average diameter of 0.2 mm. A group of alveoli are bundled together around an alveolar duct that has a luminal diameter of 0.3 mm [82]. Around the alveoli, a vascular-ductal complex is formed to facilitate the exchange of oxygen and carbon dioxide between the blood and the air. This blood-air interface, lined with alveolar epithelium and capillary endothelium, can be as thin as 0.5 μm and it directly regulates pulmonary permeability [83]. Moreover,

this barrier also needs to withstand mechanical changes in the microenvironment such as transmural pressure. To reproduce this organ-level physiological function, the Ingber group has developed a lung-on-a-chip device that can be populated with human alveolar epithelial cells and human pulmonary microvascular endothelial cells on two sides of an elastic membrane to mimic the alveolar wall [5, 84]. However, in the native lung, instead of an elastic membrane, type I and IV collagen provide the necessary strength to the barrier between the alveolar epithelium and the capillary endothelium. The collagen layer is also an essential component that regulates the rate of oxygen diffusion in vivo [85]. Therefore, to better mimic this physiological environment, a recent advance in microfabrication was able to successfully replace the synthetic elastic membrane with a natural collagen membrane (Figure 1.4(c)) [76]. Thus far, these devices are designed to recapitulate the alveolar interface in a plane. Future development is needed to capture the organ-specific 3D architecture of the alveolar vascular-ductal complex. For instance, in chronic obstructive pulmonary disease, the merging of smaller alveoli to form fewer larger alveoli, trapping of air sacs, clogging due to the accumulation of mucus, and collapsing of the alveoli are examples of lung damage that will only manifest through the organ-specific architecture of the lung.

1.3.4 Kidney vasculature-on-a-chip

Nephrons are the minimal functional units in the kidney that filter and reabsorb extracellular fluid. To perform this demanding task, there are about 1.25×10^6 nephrons in each functioning adult kidney [86]. The main components in a nephron are Bowman's capsule, the proximal tubule, the loop of Henle, the distal tubule, and

the collecting tubule, all of which are surrounded and supported by a dense network of capillaries. This highly organized microvasculature uses up to approximately 20%–25% of the total cardiac output [87]. The glomerulus, which carries out the first round of blood filtration, is composed of an aggregate of microvessels that are surrounded by a layer of podocytes responsible for the selective permeation of a variety of molecules across this barrier. Musah et al. developed a glomerulus-on-a-chip device to recapitulate the kidney filtration function in the glomerulus using human iPSC-derived podocytes along with glomerular endothelial cells [88]. When treated with biochemical insults, the model can mimic physiological podocyte injury. A similar membrane-based glomerulus-on-a-chip device, developed by Zhou et al., used mouse glomerular endothelial cells and podocytes to study hypertensive nephropathy resulting from mechanical impacts [31]. Another platform, developed by Wang et al., used explanted glomeruli from rat kidneys in a microfluidic perfusion platform to model diabetic nephropathy by introducing a high glucose medium [89]. Thus far, the focus of these models has been the vascular interface. However, the glomerular vessels have a very unique convoluted 3D architecture that likely plays a key role in blood filtration. For instance, glomerulosclerosis can lead to the widespread collapse of glomerular capillary loops, which will drastically reduce renal function. Modeling this process could require this tissue-level 3D vascular architecture which is yet to be replicated in an organ-on-a-chip system.

To replicate the anatomy of the peritubular capillaries around the kidney tubules, collagen gel can be fabricated with soft-lithography to generate a 3D microvasculature populated with primary human kidney peritubular microvascular endothelial cells (Figure 1.4(d)). In this system, the presence of endothelial fenestration and

the variation in barrier permeability can be visualized over the entire vascular network [40]. To replicate the convoluted proximal tubular architecture, hollow channels of pre-designed architecture can be fabricated in a hydrogel with 3D printing of sacrificial materials. The open lumen can be populated with primary human proximal tubule cells [90]. In this perfusable microenvironment, the tubular cells showed remarkable improvements in cell morphology (e.g., polarization, columnar shape, increase in microvilli length and density, etc.), as well as in the dose dependent response to Cyclosporine A (nephrotoxin). To reproduce the entire renal tubule and vascular complex in future development, kidney-specific micro-vasculatures will need to be combined with region-specific networks that mimic the proximal convoluted tubule, the loop of Henle and the proximal straight tubule, which collectively contributes to the entire process of filtrate reabsorption.

1.3.5 BBB-on-a-chip

The endothelium of cerebral blood vessels, along with neurons, astrocytes, and oligodendrocytes, form the BBB, which is the minimal functional unit that regulates the material exchange between the blood and the brain [91]. Wang et al. developed a microfluidic BBB model for drug permeability screening by culturing hiPSC-derived cerebral vascular endothelial cells and primary rat astrocytes on each side of a porous membrane to mimic the BBB interface. Incorporated with transendothelial electrical resistance sensors, this model can track transendothelial permeability in real time [92]. Even though the porous membrane permits biochemical interaction and crosstalk between the astrocytes and the endothelium, it has been shown that astrocyte end-feet, which physically extend to the cerebral endothelial cells, and pericytes play a key

role in maintaining the barrier tightness and permeability [93]. In addition, astrocytes have a group of receptors relevant to the innate immune responses [94], while pericytes participate in immune responses by releasing mediators such as nitric oxide and cytokines [95].

To allow the direct physical interaction between the endothelium and the astrocytes/pericytes, Herland et al. developed a 3D model by culturing primary human brain microvascular endothelial cells in a hollow cylindrical channel within a collagen hydrogel embedded with pericytes or astrocytes (Figure 1.4(e)). Following inflammatory stimulation with $\text{TNF-}\alpha$, the neuroinflammatory response from the 3D BBB-on-a-chip model showed a more robust cytokine release profile than the transwell system [77]. Another 3D BBB model with a vascular network in the presence of neural cells was developed by Bang et al. This platform can supply the endothelial cells and the neural cells with different media, such as endothelial growth medium and neurobasal medium, respectively. Synaptic structural features and astrocytic contact with the vascular network can also be readily established [13]. Potentially due to the higher degree of neurovascular interfacing and the presence of synapses on this platform, a low vascular network permeability, comparable to values reported in vivo, was successfully achieved (Table 1.1). The importance of establishing direct neurovascular contact in enhancing vessel barrier function is a direct evidence of the utility of organ-on-a-chip devices in improving tissue-level function and maturation compared to traditional cell-based assays.

1.4 Future Challenges in Device Development

1.4.1 The challenge of material selection in device development

The use of PDMS as an easily moldable material has accelerated the field of organ-on-a-chip and microfluidics in general by providing a means for rapid device prototyping. Its biocompatibility, optical transparency, elasticity, and gas permeability are desirable parameters for cell cultures. However, its hydrophobicity renders it a drug-absorbing material, especially to small hydrophobic drugs, which complicates its use in drug testing. This is especially true for small hydrophobic drugs used in microfluidic channels with a large surface-to-volume ratio. In this case, surface drug absorption can significantly alter the drug concentration in the solution. For experiments requiring long-term drug exposure, the presence of PDMS can alter the drug concentration [96], even in devices with a low surface-to-volume ratio. As many organ-on-a-chip prototypes move toward commercialization, adapting industrial manufacturing methods with non-absorbent hard plastics, such as polystyrene, becomes essential. Using polystyrene in the prototyping stage can be costly because expensive industrial equipment, such as hot embosser and injection molding system, are required to mold polystyrene. However, this issue can be circumvented by the solvent casting of polystyrene with the use of proper solvent (e.g., gamma-butyrolactone (GBL)) [97]. On the other hand, for devices that require an elastic material, several alternative elastomers show minimal drug absorption while preserving many desirable characteristics of PDMS are available, such as styrene-ethylene/butylene-styrene

(SEBS) block copolymer [98–100] and polyurethane [101]. For drug testing applications, it is crucial to make this transition, especially for blood vessel models that require accurate modeling of mass transport.

1.4.2 The challenge of clinically relevant cell sources

Human umbilical vein endothelial cells (HUVECs) are commonly used as a general source of human endothelial cells in many organ-on-a-chip models. However, the organ-specific origin of the endothelial cells can have a profound effect on the biological model [65, 66]. For instance, HUVECs lack the fenestrations present in the microvascular endothelial cells, which is important in the modeling of hepatic sinusoids. Therefore, the choice of endothelial cells will depend on the specific model and the corresponding parenchymal tissues. It remains to be seen if the finely controlled microenvironments offered by the organ-on-a-chip devices can alter the identity of endothelial cells or induce the organ-specific differentiation of endothelial progenitor cells. But prior to that, accurate modeling of organ-specific vasculature will still depend on the availability of specialized endothelial cell sources. Advances in stem biology and primary tissue isolation techniques will provide us with increasingly specialized endothelial cell populations, such as the BBB endothelial cells [102] and the kidney peritubular microvascular endothelial cells [40], which are urgently needed to further advance this field.

1.4.3 The challenge of sensor integration and device operation

As tissue models become more realistic, experimental readouts can also increase in complexity. Recent advances in tissue clearing techniques have made it feasible to visualize cells deep within a solid organ or even a whole animal [103, 104]. Tissue clearing procedures may become routine for visualizing built-in vasculature in engineered biological models. Built-in electronic sensors may also provide real-time functional readouts on tissue health and conditions [105–107]. This is especially critical if the experimental throughputs of an organ-on-a-chip device are to be increased. Furthermore, device standardization is another important aspect [108]. Ultimately, organ-on-a-chip devices will be operated by non-experts. Therefore, minimizing the learning curve required in device operation will help accelerate device translation. Some organ-on-a-chip companies have approached this issue by adapting their device to the standard multiwell plate format, which can be operated with standard pipetting techniques and is accessible to biologists (e.g., devices from MIMETAS [50], AIM Biotech [109], 4Design Biosciences [54], and AlveoliX [110]). Meanwhile, others are building integrated systems to automate the operation of organ-on-a-chip devices without compromising the complexity of the device itself (e.g., devices from Emulate [5], Quorum Technology [58], and Nortis [111].)

1.5 Conclusions

The specific benefit of organ-on-a-chip devices, especially in modeling blood vessels will depend on the specific biological questions we seek to answer. For instance,

specific organ models will be required to model organ-specific vascular physiology. Considering the multitude of biological factors in the vascular environment that are uniquely present in different human organs, the current ‘gold standards’ of generalized 2D cell culture and animal models are simply inadequate. Pharmaceutical companies are cautiously optimistic about this technology. By actively collaborating with academic labs, they hope to shape the technology early on in this emerging field to enhance their technical competitiveness in drug development.

Competing Interests

B.Z. is a co-founder of TARA Biosystems Inc. and holds equity in the company.

Acknowledgments

We thank Beezly Groh for help with the editing of this manuscript. This work was funded by the NSERC Discovery Grant to B.Z.

Chapter 2

IFlowPlate™ - Vascularization for Supporting Tissue Functions

The content of this chapter is a second revision of the manuscript text for publication under the following citation:

- Lin, D. S. Y., Rajasekar, S., Marway, M. K., & Zhang, B. (2020). From model system to therapy: scalable production of perfusable vascularized liver spheroids in "open-top" 384-well plate. *ACS Biomaterials Science & Engineering*, 7(7), 2964-2972.

(Obtained permission to reprint.)

Copyright © 2021, American Chemical Society

DOI 10.1021/acsbiomaterials.0c00236

From model system to therapy: scalable production of perfusable vascularized liver spheroids in “open-top” 384-well plate

Author contributions

D.S.Y.L. performed the experiments, analyzed the results, and prepared the manuscript. S.R. performed the initial proof-of-concept study. M.K.M. performed the albumin ELISA assay. B.Z. envisioned the concept, supervised the work, and edited the manuscript.

Abstract

Vasculature is a key component of many biological tissues and helps to regulate a wide range of biological processes. Modeling vascular networks or the vascular interface in

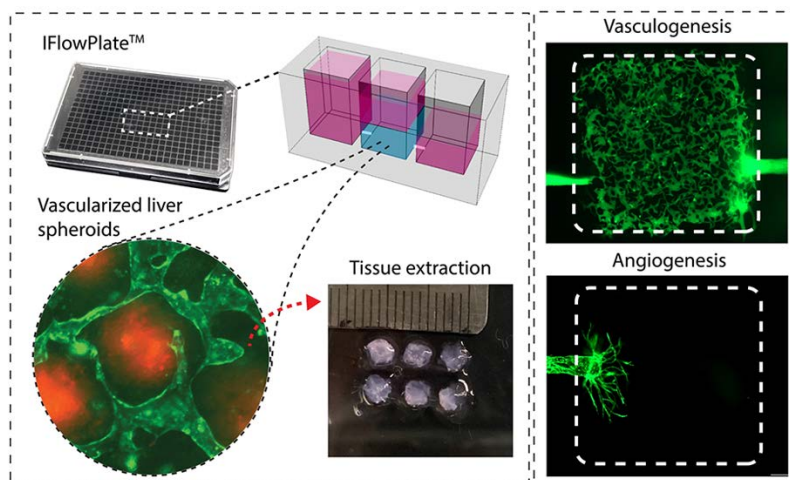


Figure 2.1: Abstract for Chapter 2

organ-on-a-chip systems is an essential aspect of this technology. In many organ-on-a-chip devices, however, the engineered vasculatures are usually designed to be encapsulated inside closed microfluidic channels, making it difficult to physically access or extract the tissues for downstream applications and analysis. One unexploited benefit of tissue extraction is the potential of vascularizing, perfusing, and maturing the tissue in well-controlled, organ-on-a-chip microenvironments and then subsequently extracting that product for *in vivo* therapeutic implantation. Moreover, for both modeling and therapeutic applications, the scalability of the tissue production process is important. Here we demonstrate the scalable production of perfusable and extractable vascularized tissues in an “open-top” 384-well plate (referred to as IFlow-Plate™), showing that this system could be used to examine nanoparticle delivery to targeted tissues through the microvascular network and to model vascular angiogenesis. Furthermore, tissue spheroids, such as hepatic spheroids, can be vascularized in a scalable manner and then subsequently extracted for *in vivo* implantation. This

simple multiple-well plate platform could not only improve the experimental throughputs of organ-on-a-chip systems but could potentially help expand the application of model systems to regenerative therapy.

Keywords: tissue spheroids, vasculature, liver, organ-on-a-chip, hydrogel, angiogenesis

2.1 Introduction

Blood vessels play vital roles in organ function and development. Our vascular systems not only supply tissues with oxygen and nutrients but also participate in many biological processes, such as transporting immune cells in an inflammatory response, trafficking cancer cells in tumor metastasis, establishing biochemical gradients, improving parenchymal tissue survival and function through paracrine signaling, repairing tissues through angiogenesis, etc. The incorporation of vascular networks in biological models is integral to accurately model human diseases as well as to maintain proper tissue function in vitro. Microphysiological systems, also known as organ-on-a-chip, have been developed to model various cellular microenvironments in the human body [112]. For instance, Huh et al. developed lung alveoli-on-a-chip, lung airway-on-a-chip, and placenta-on-a-chip, etc [113–115]. These organ chips consist of multilayer microfluidic channels separated by a porous membrane which is lined with epithelial cells and human endothelial cells to model the epithelium and vascular interface of various organs. Some of these membrane-based systems have also been scaled up to a well-plate format [116]. The membrane-based vascular barrier is advantageous for tracking drug and biomolecular transports, immune cell extravasation, as well as simulating blood circulation. To directly shape blood vessel networks inside hydrogels,

hydrogel patterning or 3D printing has been used [117–120]. These systems provide well-controlled vessel structures, but vessel sizes are usually over 100 μm [121].

Other microfluidic systems have also been developed to culture smaller microvascular networks to study angiogenesis, vasculogenesis, and various vascular events by taking advantage of the ability of endothelial cells to self-assemble into a microvascular network given the right conditions [122]. This type of system allows intimate contact between the endothelial cells and other stromal and parenchymal cells. It is particularly useful for studying the remodeling process of blood vessels in response to chemical gradients, fluid flow, and drug treatments [123–127]. However, these self-assembled vascular networks are often constrained inside a closed or semi-closed microfluidic channel that limits their physical integration with other larger tissue models [128, 129]. Even though vasculature is an essential biological component, models of the vascular network alone have limited biological significance and applications.

To overcome the challenge of integrating vasculature into other parenchymal tissue models, we sought solutions outside of the traditional microfluidics setup, which inevitably contains closed channels or membranes that would present unnecessary physical constraints. Instead, we used the conventional 384-well plate with open wells, which is widely used in biological research, as our starting point. We customized the 384-well plate (referred to as IFlowPlate™) with a simple modification so that an array of up to 128 perfusable vascular networks can be formed, connected, and perfused inside these open wells. The formed vascular barrier guides fluid perfusion in the vascular lumen from an inlet to an outlet well while the interstitial space outside of the vascular network can be accessed from the center well. Without the physical constraints of a microfluidic channel, microtissue spheroids of various sizes

and quantities can be incorporated and vascularized by a microvascular bed spanning over an area of 3.4×3.4 mm. The “open-top” well design not only facilitates tissue seeding but also allows future tissue extraction for either downstream analysis or implantation - an important feature that could potentially help expand the application of microphysiological systems to regenerative therapies.

2.2 Materials and Methods

2.2.1 Plate fabrication

The IFlowPlate™ platform consists of two components: a 384-well bottomless plate (82051544, Greiner Bio- One), and a 813- μ m-thick, 7.5 mm \times 11.4 mm polystyrene sheet (V16013, Jerry’s Artarama) as the bottom. To embed an array of microchannels inside the plate, we patterned a sacrificial material, poly(ethylene glycol) dimethyl ether (PEGDM, M2000, 445908- 50G, Sigma-Aldrich) onto the polystyrene sheet. First, a polydimethylsiloxane (PDMS, Sylgard 184, 4019862, The Dow Chemical Company) mold containing the patterned microchannels were made using the standard lithography technique. The PDMS mold had a base-to-catalyst-mix ratio of 30:1 and was allowed to cure overnight at 47.5 °C to ensure complete curing while keeping the PDMS mold soft. The PDMS mold was then capped onto a plasma-treated polystyrene sheet. Next, PEGDM pellets were melted at 65 °C and injected into the microchannels with a syringe. The injected PEGDM fluid was allowed to solidify at 4 °C; the PDMS mold was then slowly peeled off from the polystyrene sheet, leaving behind the patterned PEGDM features on the polystyrene sheet.

To bond the patterned polystyrene sheet with the 384-well bottomless plate, we

used a PDMS glue (Sylgard 186, 2137054, The Dow Chemical Company). Before bonding, the bottom side of the bottomless plate was plasma-treated for 90 s. This plasma treatment step is important to ensure the PDMS glue applied will spread easily and evenly across the plate surface. Otherwise, the glue sealing will be uneven. 5g of the PDMS glue (base-to-catalyst-mix ratio of 10:1) was first spread onto a glass slide, and the glass slide was then used to stamp the PDMS glue onto the bottom of the bottomless plate. The polystyrene sheet containing the PEGDM features (with a cross-sectional area of $150 \times 300 \mu\text{m}$) was then pressed onto the well plate to seal the bottom. The two components were held together by metal clips overnight before the PDMS cured. The metal clips were removed and the plate was packaged in a sealed plastic bag and gamma-ray sterilized at the irradiation facility at McMaster University. Prior to use, $90 \mu\text{L}$ of sterile distilled water was added to each well of the plate and then the plate was incubated overnight at 37°C , followed by using 5% CO_2 to wash off the PEGDM features and prime the device for cell seeding.

2.2.2 Cell culture

Human umbilical vein endothelial cells (GFP-HUVECs) tagged with green fluorescent proteins were purchased from Angio-Proteomie (CAP-0001GFP). The GFP-HUVECs were cultured in an endothelial cell growth medium (ECGM2, C-22011, Promo Cell). Normal human primary lung fibroblasts and hepatocellular carcinoma cells (HepG2s) were purchased from the American Type Culture Collection (ATCC, CRL-10741). The fibroblasts were cultured in a Dulbecco's modified Eagle's medium (DMEM, 319005-CL, Wisent Bioproducts) containing 10% fetal bovine serum (FBS, 098150, Wisent Bioproducts). The HepG2s were cultured in an Eagle's minimum essential

medium (EMEM, 302003, ATCC) containing 10% FBS. Cells between passages 3 and 4 were used in all experiments. To track the hepatocytes, we stained the cells with CellTracker Red CMTPX (C34552, Thermo Fisher Scientific) following the supplier's instructions. Aggrewell800 plates (STEMCELL technologies) were used to prepare the liver spheroids according to the supplier's instructions. The plates were treated with an anti-adherence rinsing solution (07010, STEMCELL technologies) to prevent cell attachment. 1100 cells were added per well. The cells were allowed to form aggregates for 6 days in the Aggrewell800 plate before seeding into the IFlowPlate™. EMEM and ECGM2 media at a ratio of 1:1 (v/v) were used as the coculture media for the vascularized spheroid culture.

2.2.3 Gel casting and cell seeding

For gel casting, 25 μ L of fibrin gel (10 mg/mL, F38791G, Sigma-Aldrich) with GFP-HUVECs at a seeding density of 35 M cells/mL and thrombin (0.25U/mL, T6884100UN, Sigma-Aldrich) were cast in each center well. For vascularized spheroids, 2030 spheroids were used per 25 μ L of fibrin gel. After casting, the gel was allowed to cross-link for 25 min at room temperature. It is important to note here that the fibrin gel we used was very sticky. They strongly adhered to the well plate. In addition, we plasma-treated the entire plate prior to packaging the plates. Plasma treatments helped activate the plate surface and make the plate even more adhesive. We did not observe any delamination between the fibrin gel and the well surface except when we manually tried to remove the fibrin gel from the well plate. After the gel crosslinked, the coculture media were supplemented with 20 μ g/mL aprotinin (616370100MG-M, Sigma-Aldrich) and added to the inlet, outlet, and center wells at volumes of 80, 80,

and 40 μL , respectively. The IFlowPlate™ was then placed on a perfusion rocker with the stage tilt at a 30° angle and the tilt direction programmed to change every 15 min. Media in the inlet, outlet, and center wells were changed daily. The inlet/outlet channel size, the tilting angle of the stage, and the frequency of tilting are parameters that could be further optimized to better control the perfusion condition. When designing the system, the inlet and outlet channels should be small enough to provide enough resistance to prevent the gel solution from entering the channel during casting but also large enough to allow sufficient fluid flow under a pressure gradient. The tilt angle could be adjusted to control the flow rate. The frequency of the tilt direction change should be set to avoid abrupt changes in the flow rate over time. The tilt angle and the frequency of the tilt direction change synergistically determined the flow rate.

2.2.4 Functional assays

To confirm the perfusability of the self-assembled vasculature, we used fluorescein isothiocyanate-dextran (2 mg/mL, average Mw 70,000, 46945100MG-F, Sigma-Aldrich) in DPBS. On day 6 after cell seeding, all the media in the wells were aspirated. 60 μL of media was added to the center well. No media were added to the outlet well, and 90 μL of the dextran solution was added to the inlet well. The vasculature was imaged immediately using a Cytation5 multimode reader. To visualize the flow inside the vasculature and the vascularized spheroids in the IFlowPlate, we added 90 μL of fluorescent particle solution (1.0 μm , amine-modified polystyrene, L10301 ML, Sigma-Aldrich), diluted at a ratio of 1:250 in D-PBS, to the inlet wells. Fluorescent and brightfield videos were captured using the Cytation5 multimode reader

and a Nikon tissue culture microscope. Iterative calculations of the cross-correlation between the two images' interrogation windows were conducted to determine the particle displacement. For the angiogenesis assay, we seeded 90 μ L of GFP-endothelial cells suspension (0.6 M cells/mL) in the inlet wells. During seeding, the plate was tilted at 30° for 10 min to allow more cells to settle into the inlet channel. 25 μ L of Fibrin gels with or without fibroblasts (0.5 M cells/mL) were cast in the center wells. ECGM2 medium was added to all three wells and changed every day. The IFlowPlate™ was then placed on the rocker for perfusion. Fluorescent images were taken with a Cytation5 multimode reader to track vascular sprouting every 3 days.

2.2.5 Immunofluorescent staining and TEM imaging

To assess the morphology of the assembled vasculature, the tissue samples were fixed in 10% formalin (HT5011284L, Sigma-Aldrich) 8 days after seeding and then blocked with 5% normal goat serum (NS02L-1 ML, Sigma-Aldrich). The tissues were then immunostained for F-actin (phalloidin-iFlour 594 conjugate, 20553300, Cedarlane Laboratories) and DAPI (D95425MG, Sigma-Aldrich) following standard procedures. Finally, the tissues were imaged with a confocal microscope (Nikon A1 confocal with ECLIPSE Ti microscope). Transmission electron microscopy (TEM) images were taken to capture the morphologies of the vascular networks and the liver spheroids formed. The samples were picked out from the IFlowPlate™ using a tweezer and sent to the Faculty of Health Sciences EM Facility at McMaster University for processing. Specifically, the samples were rinsed two times in phosphate buffer solution after fixing in 1osmium tetroxide in 0.1 M phosphate buffer for 1 h. Next, the samples were dehydrated through a graded ethanol series (50, 70, 70, 95, 95, 100, and 100%).

Final dehydration was done in 100(PO). The samples were then slowly infiltrated with Spurr's resin through a graded series (2:1 PO:Spurr's, 1:1 PO:Spurr's, 1:2 PO:Spurr's, 100% Spurr's, 100% Spurr's, 100% Spurr's) with rotation of the samples in between solution changes. The samples were then transferred to an embedding mold filled with fresh 100% Spurr's resin and polymerized overnight in a 60 °C oven. Thin sections were cut on a Leica UCT ultramicrotome and placed onto a Cu grid. The sections were poststained with uranyl acetate and lead citrate. The processed sections were imaged at the Canadian Centre for Electron Microscopy (CCEM).

2.2.6 Albumin assay

For the static liver spheroids-only group, the liver spheroids were cultured in a standard 384-well plate without perfusion. All media were collected and changed daily. For the perfusable liver spheroids with vasculature group, liver spheroids were cultured in the IFlowPlate™ in the presence of endothelial cells. All media were collected and changed from the inlet, outlet, and center wells daily. Quantification of secreted albumin in collected culture was conducted using an Albumin Human ELISA kit (50140096, Cayman Chemical Co) according to the manufacturer's protocol, and the data were normalized to the number of hepatocytes.

2.2.7 Sample size and statistical analysis

Normality and equality of variance were tested using SigmaPlot. One-way ANOVA in conjunction with Tukey's test at $p < 0.05$ and a power greater than 0.90 was used to determine the statistical significance. Means and standard deviation were plotted in all graphs. * denotes significant differences with $p < 0.05$.

2.3 Results

2.3.1 IFlowPlate™ operation and culture of perfusable microvascular bed

We developed a customized 384-well plate (IFlowPlate™) embedded with microchannels that connect three adjacent wells to form an array of 128 individually perfusable units (Figure 2.2(a, b)). Natural hydrogel, such as fibrin gel, seeded with human endothelial cells and fibroblasts can be cast into the the center well, whereas the other two wells function as inlet- and outlet-reservoirs for perfusion (Figure 2.2(c)). A gelliquid interface forms in between the center well and the inlet/outlet channels. Perfusion is established with gravity by tilting the plate at a 30° angle, with the direction of the tilt being alternated every 15 min to maintain perfusion. Interstitial flow was first established through the porous fibrin gel, which allows rapid mass transport through the hydrogel as shown by the diffusion of color dyes from the inlet and outlet (Figure 2.2(d)). In comparison, without a pressure head driven by gravity, passive diffusion alone led to much slower mass transport through the hydrogel with no discernible gradient established in 30 min (Figure 2.2(d)).

When the fibrin gel was embedded with endothelial cells (GFP-human umbilical cord vein endothelial cells, GFP-HUVECs), the cells can self-assemble into a perfusable microvascular network that will connect to the inlet and outlet channels. Therefore, the initial interstitial flow through the hydrogel will be gradually redirected through the vascular network after the vascular connection is established as early as 5 days after cell seeding. We found the endothelial cells can self-assemble

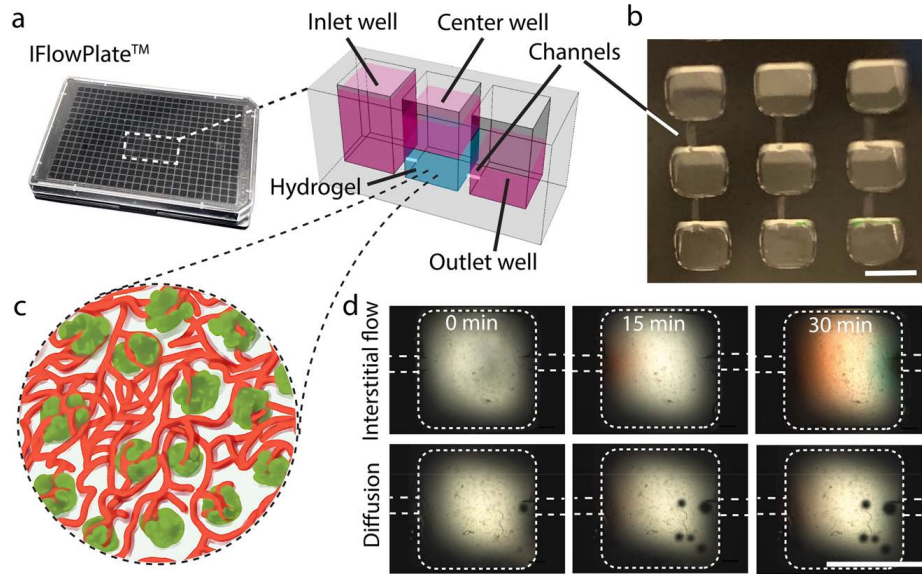


Figure 2.2: IFlowPlate™ operation and interstitial flow in hydrogel. (a, b) Image and illustration of IFlowPlate™ containing an array of three-well perfusion units connected with microchannels. Scale bar, 3 mm. (c) Illustration of vascularized hepatic spheroids in IFlowPlate™. Blood vessels are shown in red while hepatic spheroids are shown in green. (d) Distribution of color dye in fibrin gel over time under either interstitial flow or passive diffusion in IFlowPlate™. White dotted lines outline the edge of the well. Scale bar, 3 mm.

into a perfusable microvasculature, with or without the presence of fibroblasts, emulating the vasculogenesis process (Figure 2.3(a, b)). The density of endothelial cells seeding is crucial to forming a connected vessel network, and we found a seeding density of 35 million/mL was adequate for vessel connection (Supplementary Figure A.1). The fibrin gelation time, controlled by the final concentration of thrombin in the gel mixture (0.25 U/mL), was sufficiently slow so that the gel could be cast into a large number of wells before gelation to facilitate high-throughput tissue production and screening. The self-assembled vessels had a diameter between 10 and 80 μm , similar to native capillary vessels [130]. It was observed that fibroblasts were always

located outside of the microvasculature and some wrapped around the microvasculature from the exterior vessel surface. It was determined that the addition of aprotinin (1% (v/v)) in the culture media is necessary to prevent fibrin gel degradation over time [131]. The resulting endothelial cells formed a tight vascular barrier that can confine large fluorescent proteins (70 kDa dextran) in the luminal space with minimal leakage over time (Figure 2.3(c)). Microparticles can also be perfused through the network (Supplementary Video A.1).

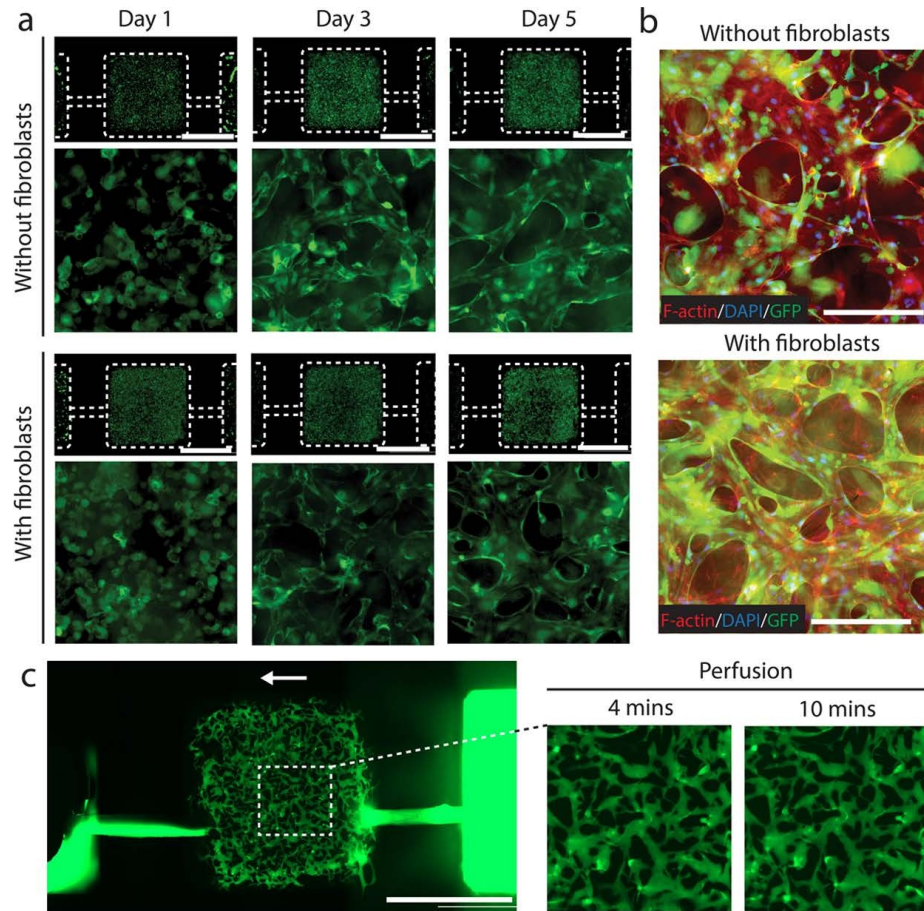


Figure 2.3: Culture of perfusable microvascular bed on IFlowPlate™. (continued)

Figure 2.3: (continued) (a) Fluorescent images of GFP-HUVECs (green) assemble into a microvascular network over time with or without the presence of fibroblasts. Images are stitched from multiple images. Dotted white lines outline the edge of the wells and the microchannel. Scale bar, 2 mm. (b) Confocal image of the microvascular network with or without fibroblasts on day 5 stained for F-actin (red), GFP (green), and DAPI (blue). Scale bar, 200 μ m. (c) Perfusion of fluorescent 70 kDa dextran (green) from the inlet well, through the microvascular bed, to the outlet well. Images are stitched from multiple images. The white arrow indicates the flow direction. Scale bar, 3 mm. High-magnification fluorescent images of the microvascular network perfused with the dextran over time.

2.3.2 Angiogenesis assay on IFlowPlate™

Even though the presence of fibroblasts did not make a significant difference in the vasculogenesis process, vascular sprouting in angiogenesis appeared to be guided by the presence of fibroblasts. To study angiogenesis, endothelial cells can be seeded inside the inlet channel against the gel liquid interface located between the center well and the inlet channel (Figure 2.4(a)). When fibroblasts were present inside the gel in the center well, endothelial cells were able to sprout into the gel toward the fibroblasts (Figure 2.4(b)). However, without fibroblasts, minimal sprouting was observed. We did not see the effect of fibroblasts on vasculogenesis likely because endothelial cells intrinsically have the ability to self-assemble. However, directional angiogenesis will require guidance from fibroblasts. This is consistent with previous findings using conventional microfluidic devices which showed the presence of fibroblasts helps to facilitate angiogenic sprouting [123, 132]. The extent of sprouting can be quantified and can be used as an assay for screening pro- or antiangiogenic drugs on this high-throughput platform (Figure 2.4(c)).

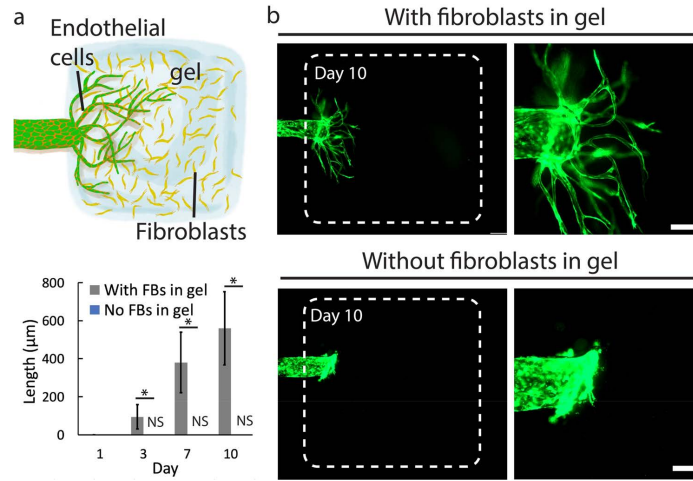


Figure 2.4: Angiogenesis assay on IFlowPlate™. (a) Illustration of the experimental setup for the angiogenesis assay. (b) Fluorescent image of GFP-endothelial cell sprouting into fibrin gel with or without fibroblasts (FBs). Scale bar, 100 μm . (c) Quantification of the length of vessel sprouts in fibrin gel with or without fibroblasts. NS indicates no sprouting. * indicates $p < 0.05$. $n = 3$.

2.3.3 Culture of vascularized liver spheroids on IFlowPlate™

To integrate this vascular network with larger solid tissues, we fabricated liver spheroids with a diameter of around 200-300 μm by aggregating hepatocytes (HepG2), endothelial cells (GFP-HUVECs), and fibroblasts in an array of funnel-shaped microwells (Figure 2.5(a)). These spheroids were then mixed with endothelial cells and fibroblasts in fibrin and cast into the IFlowPlate™. Endothelial cells inside the spheroids were able to self-assemble within the spheroids while the endothelial cells outside of the spheroids formed a microvascular network around the spheroids. In some cases, the endothelial cells were able to form microvessels that penetrate through the tissue spheroids (Figure 2.5(b, c)). Around the spheroids, microvascular remodeling was also visible, where small changes in the vascular network structure can be seen and

tracked daily. The vascular network around the spheroids is also perfusable, indicating that nutrients and oxygen can be delivered with convective flow directly to the spheroids after the vasculature is established on day 6 (Figure 2.5(e)). Taking advantage of the fact that tissues can be physically extracted for downstream analysis, we imaged sections of the extracted tissues with transmission electron microscopy (TEM) and found cross-sections of microvessels with tight intercellular junctions between the endothelial cells (Figure 2.5(d)). In the application of drug testing, other downstream analyses, such as histology sectioning, transcriptome, and proteomic assays could also be performed on the extracted tissues in the future.

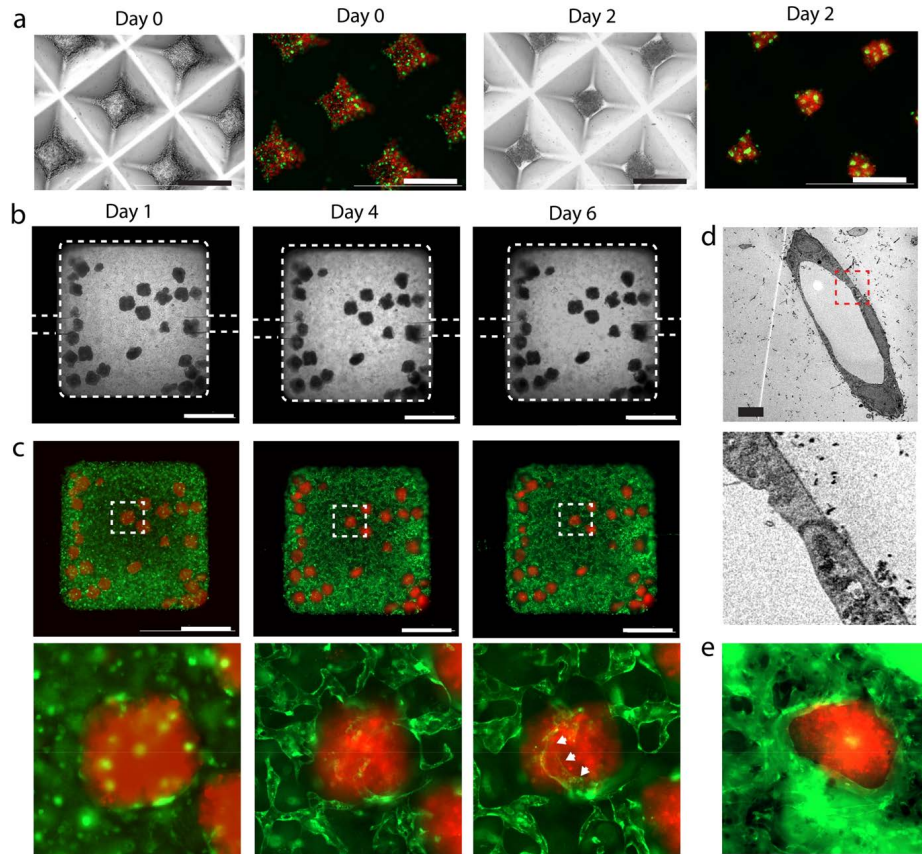


Figure 2.5: Culture of vascularized liver spheroids on IFlowPlate™. (continued)

Figure 2.5: (continued) (a) Bright-field and fluorescent images of liver spheroids cultured in microwells over 2 days prior to seeding into IFlowPlate. Hepatic spheroids containing hepatocytes labeled with red cells tracker (red), GFP-endothelial cells (green) and fibroblasts. Scale bar, 500 μ m. (b) Bright-field images of well seeded with microvasculature, fibroblasts, and liver spheroids over time. Dotted white lines outline the edge of the wells and the microchannel. Scale bar, 1 mm. (c) Fluorescent images of corresponding wells seeding with microvasculature (GFP, green), fibroblasts, and liver spheroids (labeled with cell-tracker red) over time. Liver spheroids also contain GFP-endothelial cells (green). Images are stitched from multiple images. High-magnification images were derived from areas labeled with dotted white boxes. White arrows label the microvessels that penetrate the liver spheroid. Scale bar, 1 mm. (d) TEM of a cross-section of a self-assembled microcapillary vessel. Scale bar, 5 μ m. (e) Perfusion of fluorescent 70 kDa dextran (green) through the microvascular network around the hepatic spheroid, indicating a perfusable vascular network is established in proximity to the liver cells.

We also delivered GFP-nanoparticles through the established microvasculature and found that the particles tend to leak out from the vessels in the region around the spheroids (Figure 2.6(a, b) and Supplementary Video A.2). Some particles were able to enter the tissue spheroids and accumulate inside the spheroid. These observations could be due to the growth of the hepatic spheroids, which then cause structural changes in the nearby vessels. This delivery process can easily be visualized on the platform and could be used to model drug delivery to target tissues or tumor microenvironment. Because of the size of the well and the limited amounts of culture media in the three-well perfusion unit, there is an upper limit on the number of tissue spheroids this system can support. We found that at least 30 spheroids can be maintained within one well (Figure 2.6(c)). However, when more than 60 spheroids are present, the lack of nutrients and oxygen led to the deterioration of the vascular network without which the rate of mass transport inside the hydrogel was slowed down

even further. At a density of 90 spheroids per well, microvasculature was visible only in the peripheral of the well and failed to form in between the spheroids. We thus chose to apply 30 spheroids per well as the optimized liver spheroid seeding density which could change depending on the metabolic rate of the specific tissue spheroids. Furthermore, we found that perfusion and the presence of vasculature significantly improved the production of albumin from the hepatic spheroids on day 2 (Figure 2.6(d)). The production of albumin plateaued after that, consistent with previous findings [133]. In this demonstration, we used a liver cell line (HepG2) that has been conditioned to in vitro culture and expansion. Freshly isolated primary liver cells, however, could potentially show more significant functional improvement in the presence of vasculature as previously demonstrated [134]. Finally, we demonstrated that vascularized tissues can be physically extracted from the well plate for implantation (Figure 2.6(e)). Studies are currently underway to validate whether pre-vascular assembly and perfusion in vitro could accelerate vascular connection and maturation, thus improving parenchymal tissue survival and post-implantation in animal models.

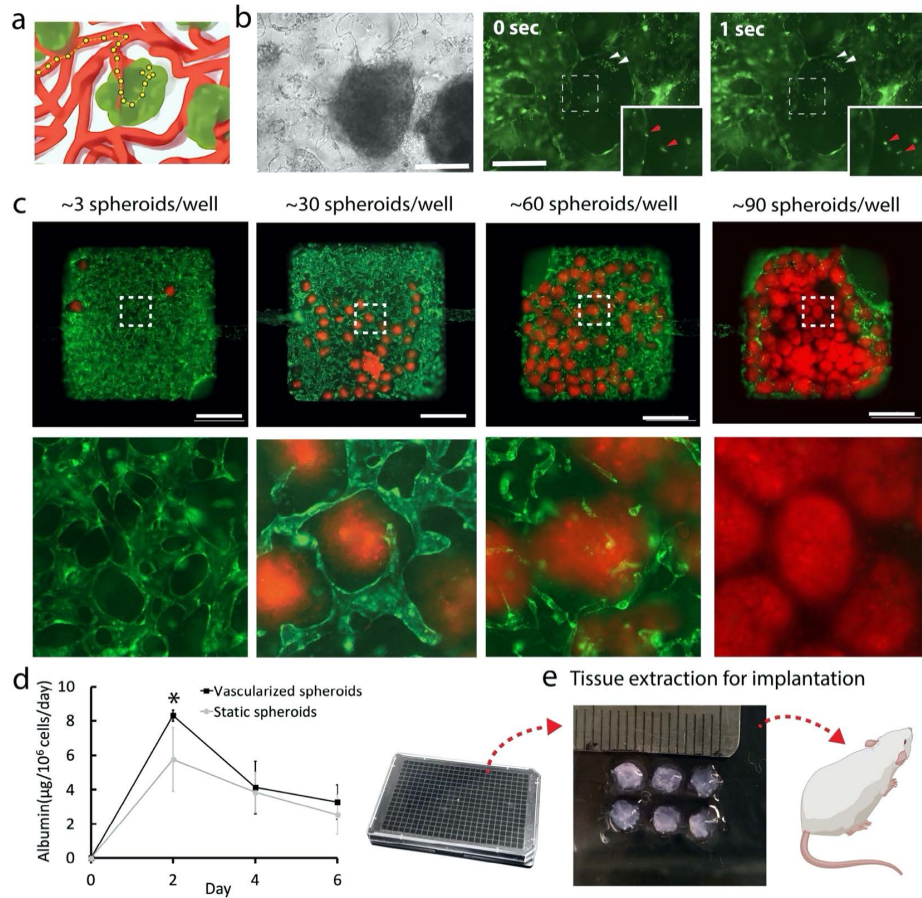


Figure 2.6: Nanoparticle and nutrient delivery to liver spheroids on IFlowPlate. (a) Illustration of intravascular nanoparticle delivery to liver spheroids. (b) Bright-field and fluorescent time-lapse images of nanoparticles ($1 \mu\text{m}$, green) perfused from the vasculature and then leaked into the liver spheroid. Red arrows label the particle exiting the vessel and entering the liver spheroid. White arrows label a cluster of particles accumulating inside the spheroid. Scale bar, $200 \mu\text{m}$. (c) Fluorescent images of wells seeding with microvasculature (GFP, green), fibroblasts, and different numbers of liver spheroids (labeled with cell-tracker red) on day 6. Liver spheroids also contain GFP-endothelial cells (green). The final images are stitched from multiple images. High-magnification images are derived from areas labeled with dotted white boxes. Scale bar, 1mm . (d) Quantification of albumin secretion from spheroids cultured with or without vasculature and perfusion. $n = 4$. * indicates $p < 0.05$. (e) Image of extracted vascularized hepatic tissue that can be used for implantation. The ruler shown is in mm scale.

2.4 Discussion

We developed a platform that allows easy integration of microvasculature with solid tissue spheroids to build complex tissues. The platform is based on the conventional 384-well plate, which is the gold standard in biological research, easy to use, and can be operated with just simple pipetting techniques. The same platform can potentially be applied to building other vascularized tissues such as vascularized tumor spheroids, adipose tissues, organoids, etc. In the current configuration, endothelial cells embedded inside the gel could potentially connect to the top surface of the gel. However, this problem could be solved by casting a second layer of fibrin gel that is free of cells. The second layer of fibrin gel will serve as a barrier to prevent these open connections. Because the luminal space of the vasculature can be compartmentalized from the parenchymal space outside the vasculature, different culture media or stimuli could be applied from the center well and the inlet/outlet wells to facilitate multicellular coculture. Furthermore, inside the 3D gel, fibroblasts and other stromal cells can also closely associate and interact with the parenchymal tissues and the microvasculature. These intercellular interactions play an important role in the study of diseases such as fibrosis, edema, and thrombosis, etc. In future studies, epithelial cells could also be added onto the hydrogel surface over the microvascular bed. For instance, if used to model the interface of the lung epithelium or the human skin, culture media in the center well could be removed to create an air/liquid interface. Nutrients can be supplied to the epithelium layer through the underlying perfusable microvascular network.

One novel feature of this system is that the entire tissue, including the microvasculature, can be extracted from the center well in its entirety for downstream analyses,

as well as for implantation. This allows for the tissue to first be matured in vitro under vascular perfusion and then implanted in vivo. Implantation of an already perfused microvascular network could potentially accelerate vascular integration and perfusion in vivo. Accelerating vascular connection upon tissue implantation is critically important to ensuring tissue survival in regenerative medicine [135]. Previously, patterned vasculature has been shown to improve vascular integration in vivo but has not been pre-perfused in vitro prior to implantation [134]. Other systems designed for the culture of perfusable microvasculature in vitro do not allow for easy tissue extraction for implantation [128]. To the best of our knowledge, this is the first system that allows microvascular perfusion in vitro followed by the complete removal of the vascularized tissue for implantation on a scalable platform. The ability to produce large quantities of these vascularized tissues in the format of a 384-well plate is another important feature that could find application in high-throughput drug discovery or regenerative therapy with a modular tissue engineering approach [136].

In future studies, the fibrin-based hydrogel matrix could be replaced with organ-specific decellularized matrices [137]. When combined with organ-specific endothelial cells, a more organ-specific microvascular environment could be established [138]. The inclusion of stromal cells, such as pericytes or smooth muscle cells, in addition to fibroblasts, will also further enhance vessel maturation and stability. To improve the liver model, Kupffer cells that are responsible for regulating inflammation and fibrosis could be included in the liver spheroids for disease modeling [139]. The current design relies on duo-directional fluid flow to maintain perfusion. However, if the unidirectional flow is needed, the platform could be adapted based on a recently published strategy that can achieve unidirectional perfusion with gravity-driven flow [140].

2.5 Conclusions

In conclusion, we have established a simple-to-use microphysiological system in the format of conventional 384-well plates that enables the scalable production of perfusable vascularized liver spheroids. By growing tissues in this dynamic, vascularized, and perfusable microenvironment with an “open-top” well design, tissue spheroids can be matured in vitro and used for either high-throughput drug screening or extracted for in vivo implantation. With this platform, a microphysiological system that provides a highly controlled microenvironment to guide tissue maturation could be applied to tissue transplantation therapy, leading to the convergence of microphysiological systems with regenerative medicine.

Competing Interests

The authors declare the following competing financial interest(s): DSYL, SR, and BZ are inventors of a provisional patent filed based on this work.

Acknowledgments

We thank Matthew Smith for editing the manuscript. This work was funded by the National Sciences and Engineering Research Council of Canada (NSERC) Discovery Grant (RGPIN-05500-2018) and Canadian Institute of Health Research (CIHR) Project Grant (PJT-166052) to BZ.

Chapter 3

IFlowPlate™ - Microvascular Array for Drug Screening

The content of this chapter is a second revision of the manuscript text for publication under the following citation:

- Lin, D. S. Y., Anvari, N., Rajasekar, S., & Zhang, B. (2024). Robot-assisted fabrication of microvascular networks: enhancing high-throughput screening for chemotherapy drugs.

(Manuscript in preparation.)

Robot-assisted fabrication of microvascular networks: enhancing high-throughput screening for chemotherapy drugs

Author contributions

D.S.Y.L. and B.Z. designed the experiments. D.S.Y.L. performed the experiments and analyzed the data. N.A. performed imaging analysis and PCA. S.R. provided technical support. D.S.Y.L. and B.Z. interpreted the data. D.S.Y.L. wrote the manuscript. B.Z. supervised all aspects of the work.

Abstract

Recent advancements in organ-on-chip technology have substantially enhanced drug screening capabilities, particularly in evaluating the complex vascular interactions

of chemotherapeutic agents. Utilizing the IFlowPlate™, a customized 384-well device, our study investigates the vascular toxicities of bortezomib and vincristine—two chemotherapeutics known for their efficacy against various cancers and their potential vascular side effects. By integrating a robotic handling system with the REAVER image-analysis program, we achieve high consistency and precision in the preparation and analysis of arrays of self-assembled microvascular networks. This setup effectively mimics dynamic vascular architectures, incorporating critical physiological factors such as interstitial flow and cell-to-cell crosstalk, thus replicating *in vivo* conditions more accurately. Our findings reveal dose-dependent toxicities and emphasize the utility of microvascular networks in bridging the gap between preclinical screenings and clinical realities. This approach enhances drug evaluation strategies and optimizes therapeutic outcomes by providing a more accurate prediction of chemotherapeutic impacts on vascular health.

3.1 Introduction

Recent advances in organ-on-chip technology have significantly enhanced the capabilities of drug screening, particularly in understanding the complex interactions between chemotherapeutic agents and vascular systems [141–143]. The development of high-throughput vessel assays [144], represents a critical step forward in mimicking human vascular responses under controlled laboratory conditions. These models provide a valuable platform for assessing the vascular toxicity of cancer treatment drugs, which is crucial for optimizing therapeutic strategies and minimizing adverse effects.

Our study utilizes the previously developed IFlowPlate™ [145, 146], a customized

384-well device, which allows for the preparation and analysis of up to 128 self-assembled microvascular network sets per device. This setup significantly enhances our ability to conduct large-scale drug screening efficiently. By leveraging the precision of advanced robotics [147, 148] integrated with the REAVER image-analysis program [149], we have achieved high consistency and reliability in sample preparation and data collection. This integration is pivotal in ensuring the quality of the microvascular networks, which are essential for accurate drug toxicity assessment. In this study, we focus on the vascular toxicities of bortezomib and vincristine, two widely used chemotherapeutic agents known for their efficacy in treating various cancers but also associated with potential vascular side effects. The strategic design of our assay closely mirrors the dynamic nature of vascular architecture, accommodating factors such as the presence of interstitial flow [150] and cell-to-cell crosstalks [151], both of which significantly influence vascular responses under chemotherapeutic stress. These elements are critical in the context of drug administration, as they closely replicate the in vivo environment, enhancing the relevance of our findings.

This study is designed not only to delineate the dose-dependent vascular toxicities elicited by these drugs but also to assess the translational potential of using microvascular networks as reliable models for preclinical compound screening. Through this approach, we aim to bridge the gap between in vitro findings and clinical expectations, providing a more accurate prediction of chemotherapeutic impacts on vascular health.

3.2 Materials and Methods

3.2.1 Cell culture

Original vials of GFP Expressing Human Umbilical Vein Endothelial Cells (GFP-HUVECs, Angio-Proteomie, CAP-0001GFP) at passage 3 (P3) and Human Primary Lung Fibroblasts (Lung FBs, ATCC, PCS-201-013) at P2 were acquired. GFP-HUVECs were cultured in T75 flasks (CELLSTART, 82050-856) precoated with a 0.2% w/v gelatin (Sigma-Aldrich, G9391) solution in PBS (Gibco, 14190144) for 20 minutes at 37 °C with 5% CO₂. Lung FBs were cultured in T75 flasks. GFP-HUVECs were cultured in Endothelial Cell Growth Medium2 (ECGM2, PromoCell, C-22011) and Lung FBs were cultured in Dulbecco's Modified Eagle Medium (DMEM, Gibco, 11995065) supplemented with 10% FBS, 1% HEPES (Gibco, 15630106), 1% Penicillin-Streptomycin (Pen-Strep, Wisent Inc., 450-201 EL). Harvesting of GFP-HUVECs and FBs as conducted using Trypsin-EDTA (0.05%, Gibco, 25300054). Working cell banks were established by expanding GFP-HUVECs and Lung FBs to P7. Subsequently, GFP-HUVECs and Lung FBs were resuspended in a freezing medium comprising 5% DMSO (Sigma-Aldrich, D2650), 20% FBS, and 75% culture media to achieve a concentration of 7×10^5 cells/mL. Cell suspensions were aliquoted into cryogenic vials (VWR, 66008-751) at 1 mL each. Fresh frozen vials were sourced from the working cell banks for each experimental iteration.

3.2.2 Vascular networks formation

The methodology for manually preparing human microvascular networks on IFlow-Plate™ has been previously described [145, 146]. To automate the development of

microvascular networks on IFlowPlate™ using a robotic handling system (Hamilton Company, NIMBUS4), on day 0, GFP-HUVECs and Lung FBs, nearing confluence in T75 flasks, were harvested, counted, and 0.5625 and 0.1125 million cells of each type, respectively, were placed into autoclaved 2.0 mL microcentrifuge tubes (VWR, 10025-738) for centrifugation. Following centrifugation, the supernatant was aspirated, and 62.5 μ L of PBS was added to resuspend the cell pellet. The required number of microcentrifuge tubes for various experimental setups is outlined in Supplementary Table B.1. Additionally, four 2.0 mL tubes containing 20 mg/mL Fibrinogen (Sigma-Aldrich, F3879), four 2.0 mL tubes of 1.5 U/mL Thrombin (Sigma-Aldrich, T6884, stock solution at 10 U/mL, resuspended in 0.1% w/v BSA (Sigma-Aldrich, A9418) in PBS), and four 15 mL falcon tubes of water were prepared and positioned in the robotic handling system as specified in Supplementary Table B.1 and Figure 3.1(d). After ensuring that all tubes and plates were positioned correctly in their designated spots, the software automated the process of mixing and casting the hydrogel. The flowchart illustrating the programming code is provided in Supplementary Figure B.2. While the IFlowPlate™ was left to incubate for 30 mins on a flat surface at RT, the Thrombin and Fibrinogen present in the hydrogel underwent crosslinking, resulting in the formation of the Fibrin gel, with GFP-HUVECs and Lung FBs suspended within its matrices. To enhance cell survival within the channels connecting the inlet and outlet wells to the central wells, a coating medium of ECGM2 supplemented with 1 mg/ml Fibrinogen, 0.1 U/ml Thrombin, and 20 μ g/ml aprotinin was prepared. After 30 mins of hydrogel crosslinking, the water in the inlet and outlet wells was removed, 100 μ l of the coating medium was added to each inlet and outlet well, and 40 μ l added to the middle wells. The plate was then placed on a leveled surface at 37 °C with 5%

CO₂ overnight for incubation. On day 1, the coating medium was removed from all wells, and 50 μ l of ECGM2 supplemented with 20 μ g/mL aprotinin was added into the inlet and outlet wells, and 80 μ l to the middle wells. The discrepancy in total volume between the side wells and the middle wells was intended to aid in the removal of bubbles from the channels. Subsequently, the device was placed on a rocker at 37 °C with 5% CO₂ overnight. On day 2, GFP-HUVECs, nearing confluence, were harvested, counted, and placed in a 50 mL falcon tube to undergo centrifugation and be adjusted to a concentration of 5×10^5 cells/mL in ECGM2 supplemented with 20 μ g/mL aprotinin. The media were removed from all wells, and 120 μ L of the GFP-HUVECs suspension was introduced into both the inlet and outlet wells. This was followed by a 2-h incubation at 37 °C with 5% CO₂ on a leveled surface, facilitating the attachment of GFP-HUVECs within the channels. After this period, 40 μ L of ECGM2 supplemented with 20 μ g/mL aprotinin was dispensed to the middle wells. Following this, the device was cultured at 37°C with 5% CO₂ on a rocker to facilitate the formation of self-assembled microvascular networks. ECGM2 supplemented with 20 μ g/mL aprotinin was replenished daily by adding 90 μ L to the inlet and outlet wells and 50 μ L to the middle wells. The quality of the vessels was assessed from day 7 onwards for further investigation.

3.2.3 Perfusion and permeability assay

To evaluate the barrier function of the vessels, a perfusion medium containing 1 mg/mL of 65-85 kDa TRITC dextran (Sigma-Aldrich, T1162) in ECGM2 was utilized. A standard curve was established by serial dilution of 65-85 kDa TRITC dextran and 4 kDa FITC dextran (Sigma-Aldrich, 46944) in media, consisting of concentrations

of 1 mg/mL, 0.1 mg/mL, 0.01 mg/mL, 0.001 mg/mL, 0.0001 mg/mL and 0 mg/mL for each dextran. 100 μ L of each concentration was added three times, with 100 μ L added to the inlet well, 100 μ L added to the middle well, and another 100 μ L added to the outlet well. Following this, the media were removed from the inlet and outlet wells, and 90 μ L of perfusion medium was added to the inlet wells. Upon switching to the permeability medium, the IFlowPlate™ was placed into a plate reader (Agilent, BioTek Cytation 5) for intensity measurement. A two-wavelength reading was established with excitation at 544 nm and emission at 570 nm for TRITC and at 491 nm and 516 nm for FITC. Fluorescent intensities of all sample wells were collected at $t = 0$ and $t = 60$ mins. During the 60 mins of perfusion with the perfusion medium, the IFlowPlate™ was incubated at 37 °C with CO₂, on a leveled surface. After the fluorescent reading at $t = 60$ mins, fluorescent imaging was conducted using TRITC and FITC filters and the 4X objective with the same plate reader to determine if the microvascular network was perfusable and to obtain qualitative visual data. A microvascular network is deemed perfusable when the perfusion medium is observed to reach the outlet well by traveling through the lumen of the microvascular network. Subsequently, the perfusion medium was aspirated, and all sample wells were washed twice with ECGM2, using 90 μ L of medium for the inlet and outlet wells, and 50 μ L of medium for the middle wells. ECGM2 supplemented with 20 μ g/mL aprotinin was added back to all sample wells if continued culture was required. The standard curve was not aspirated if further permeability testing was to be conducted on the same plate. Data analysis was performed using Microsoft Excel, GraphPad Prism 10.2.1, and Fiji 2 software.

3.2.4 Treatments

Bortezomib and vincristine doses, sourced from NIH (Approved Oncology Drugs Set X, plates 4893-4894), were prepared at concentrations of 1, 0.1, 0.01, 0.001, and 0 μ M in ECGM2 supplemented with 20 μ g/mL aprotinin. To mimic the intravenous administration of chemotherapy drugs, we added the treatment media to the inlet and outlet only, with normal media added to the middle well. A vehicle medium was created by incorporating 0.01% DMSO into the culture media. Quality control involved conducting permeability tests for these treatments on day 7. Treatments were administered from day 10 to day 13. Fresh media were prepared on day 9 and refreshed daily.

3.2.5 Imaging analysis

GFP intensities of the microvascular networks were normalized using the FITC standard curve and were further analyzed using GraphPad Prism 10.2.1. The GFP signal ratio was calculated as the 72 h GFP signal divided by the 0 h GFP signal of the same well. The image-analysis program Rapid Editable Analysis of Vessel Elements Routine (REAVER) [149] was utilized to analyze microvascular structures. Data collected using REAVER were imported into GraphPad Prism 10.2.1 for further analysis.

3.2.6 Statistical analysis

To determine EC₅₀, a nonlinear regression, log(inhibitor) vs. normalized response with variable slope, was used on normalized raw data. The data were represented by their mean and standard deviation (SD). Shapiro-Wilk normality testing was conducted on all datasets. For more than two groups analyses, if all groups within

the data passed the normality test, we assumed a Gaussian distribution and applied ANOVA; otherwise, a nonparametric test was utilized. Equal SDs were presumed if the ratio between the largest and smallest SDs among the tested groups was 4; otherwise, equal SDs were not presumed. In cases where the data were assumed to follow a Gaussian distribution with equal SDs, statistical significance was evaluated using ordinary one-way ANOVA followed by Fisher's LSD test. If the data were assumed to follow a Gaussian distribution but did not have equal SDs, statistical significance was assessed using Brown-Forsythe and Welch ANOVA tests, followed by Dunnett's T3 multiple comparisons test. For datasets not assumed to follow a Gaussian distribution, statistical significance was assessed using the Kruskal-Wallis test, followed by Dunn's multiple comparisons test. For two-group analyses, if the data passed a normality test and both groups had equal standard deviations, an unpaired t-test was conducted. If the data passed a normality test but unequal standard deviations were observed, an unpaired t-test with Welch's correction was performed. If the data could not be assumed to follow a Gaussian distribution, a Mann-Whitney test was used. Significance levels were denoted as ns for not significant, * for $P < 0.05$, ** for $P < 0.01$, *** for $P < 0.001$, and **** for $P < 0.0001$. Analysis was conducted using GraphPad Prism 10.2.1 software. Principal Component Analysis (PCA) was implemented for the vessel morphological features extracted from the REAVER software for different doses of drugs. Raw data were standardized to have a mean of 0 and a standard deviation of 1. PCA was applied based on parallel analysis.

3.3 Results

3.3.1 Automated high-throughput microvascular network assay setup

We utilized a previously developed customized 384-well device, IFlowPlate™, for building an automated high-throughput microvascular network assay [145, 146]. In total, 128 sets of microvascular networks can be prepared on one device. In each tissue culture unit, three wells are interconnected by two channels. The inlet and outlet wells serve mainly as media reservoirs, while the middle wells are for growing the major microvascular network (Figure 3.1(a)). Based on our pre-existing protocol [145, 146], we chose a HUVECs to FBs ratio of 5:1 to proceed (Supplementary Figure B.1), and we integrated a robotic handling system into our hydrogel casting process. Reagents including distilled water, cell suspension, Fibrinogen, and Thrombin and tools including the 300 μ L tips and the IFlowPlate™ were loaded into the robotic handling system to prepare high-throughput microvascular network assay (Figure 3.1(b-d)). The program coordinating the robotic handling system has been optimized to achieve consistent hydrogel mixing and casting between tissues (Supplementary Figure B.2). A timeline is designed for various compound screenings to standardize the usage of the high-throughput microvascular network assay (Figure 3.1(e)). On day 0, hydrogel containing ECs and FBs was cast into the middle well, and on day 2, ECs were added to the inlet and outlet wells and to the channels connecting the middle wells to the outer wells. The high-throughput microvascular networks were examined on day 7 to perform quality control, and only perfusable microvascular networks were selected to be used as a compound screening assay from day 10 to day 13. The

treatment was started on day 10 and continued until day 13. Before and after the compound introduction, the microvascular networks were examined for perfusability and GFP-HUVECs' fluorescent signal. Microvascular structures and permeability collected on day 13 were also analyzed. All data collected were incorporated into the interpretation of the compounds' impacts on the microvascular networks (Figure 3.1(e)).

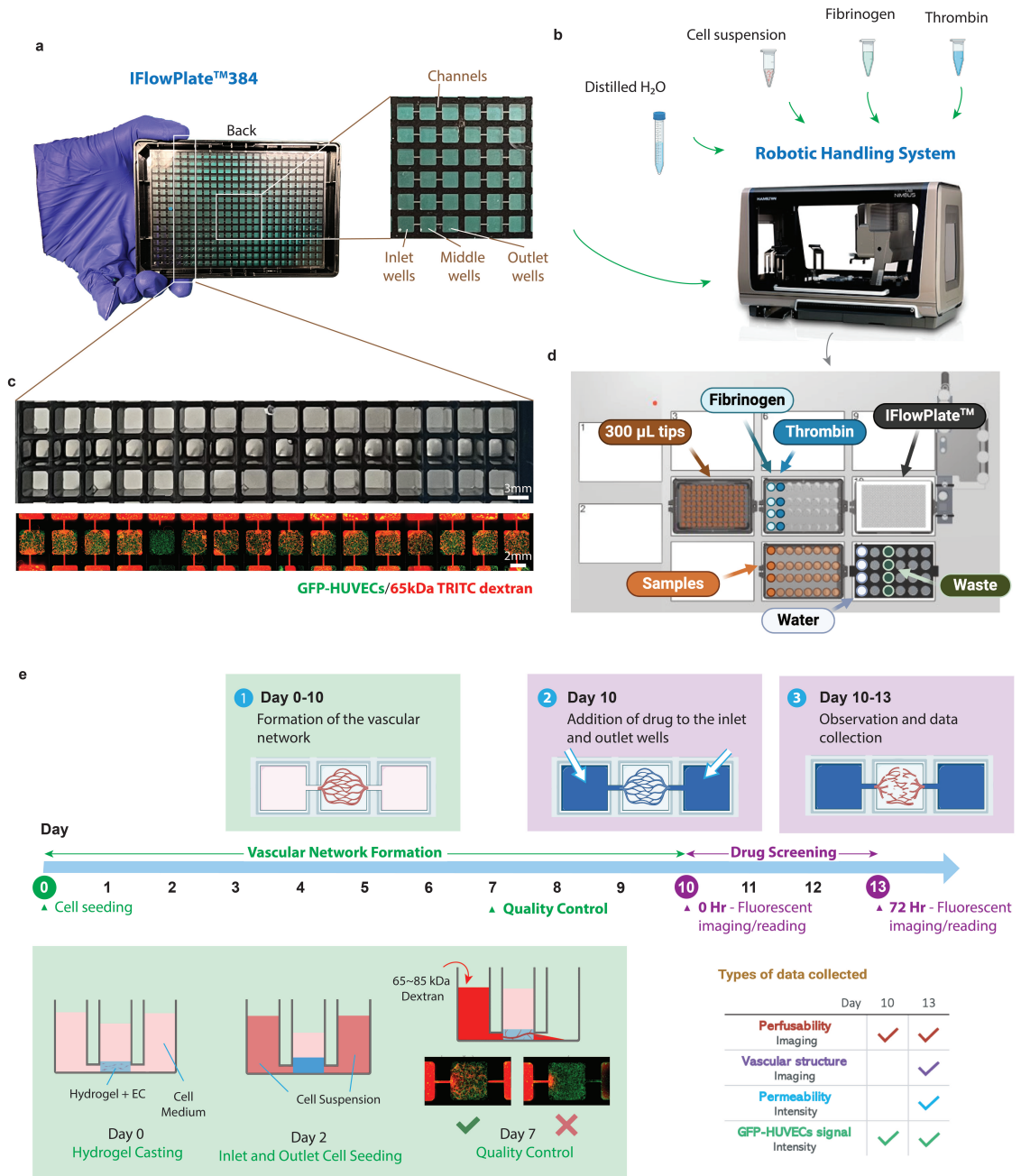


Figure 3.1: Automated procedures for building human microvascular networks on IFlowPlate™ (continued)

Figure 3.1: (continued) (a) The IFlowPlate™ consists of 128 sets of tissue culture units, each comprising an inlet well, a middle well, and an outlet well connected by two channels. One channel connects the inlet and middle wells, while the other connects the middle and outlet wells. (b) A schematic overview of the robotic handling system and the reagents involved. Created with BioRender.com. (c) Pictures of the microvascular networks prepared by the robotic handling system. The top image shows 16 tissue culture units with hydrogel cast into the middle well, captured under ambient light. The bottom image, captured with the FITC filter for GFP-HUVECs and the TRITC filter for the 65-85 kDa dextran, shows the microvascular networks in the same 16 tissue culture units. (d) A layout overview of the reagents and devices setup inside the robotic handling. Created with BioRender.com. (e) Standardized timeline and procedure for utilizing the built microvascular networks for screening various compounds. On day 0, hydrogel containing ECs and FBs is cast into the middle well. On day 2, extra ECs are seeded into the inlet and outlet wells. On day 7, quality control is conducted to check for vascular network formation and perfusability. From day 10 to day 13, the microvascular networks are treated with various compounds to study their impact on vascular function and architecture. Perfusability data and GFP-HUVECs florescent intensity are collected before and after treatment, while vascular structure and permeability data are collected on day 13 after treatment. Created with BioRender.com.

3.3.2 Structural analyses of the microvascular networks

Vessels can undergo various mechanisms to adapt their architectures to the needs present in the microenvironment. Researchers have grouped the commonly observed vascular mechanisms into four categories [152]. The fusion describes when two nearby vascular branches merge into one vessel. The intussusception describes a process contrary to the fusion, which is when one vessel splits into two branches. Sprouting is a process when a new vessel grows out side-way from an existing vessel. Lastly, regression happens when a vascular branch retracts back to the vessel from which it originally grew out (Figure 3.2(a)). The four vascular mechanisms can affect nine vascular structural parameters, including vessel area fraction, vessel length, vessel length

density, number of branchpoints, number of segments, mean segment length, mean segment diameter, mean tortuosity, and complexity (Figure 3.2(b)). We adopt these parameters to describe the microvascular architecture based on the image-processing program, REAVER, developed by Peirce's group [149].

When conducting quality control on the vessels prepared by hand and the vessels prepared by the robotic handling system, we noticed that the morphologies of the microvascular networks formed were similar and the network became perfusable by day 10 of culturing (Figure 3.2(c, d)). By utilizing REAVER, we can identify microvascular networks' vessels, their branchpoints, and the segments between the branchpoints (Figure 3.2(e)). Based on the analyzed data from the vessels prepared manually or by the robotic handling system on both day 3 and day 7, we observed that there was no significant difference between the microvascular development between the manual and the robotic groups regarding the vascular architectural parameters, except for the vessel area fraction, which showed a 0.91-fold decrease on day 3 and a 1.13-fold increase on day 7 when comparing the robotic group to the manual group (Figure 3.2(f-n)). In sum, the robotic handling system can replace manual hydrogel preparation to re-produce similar and consistent microvascular networks.

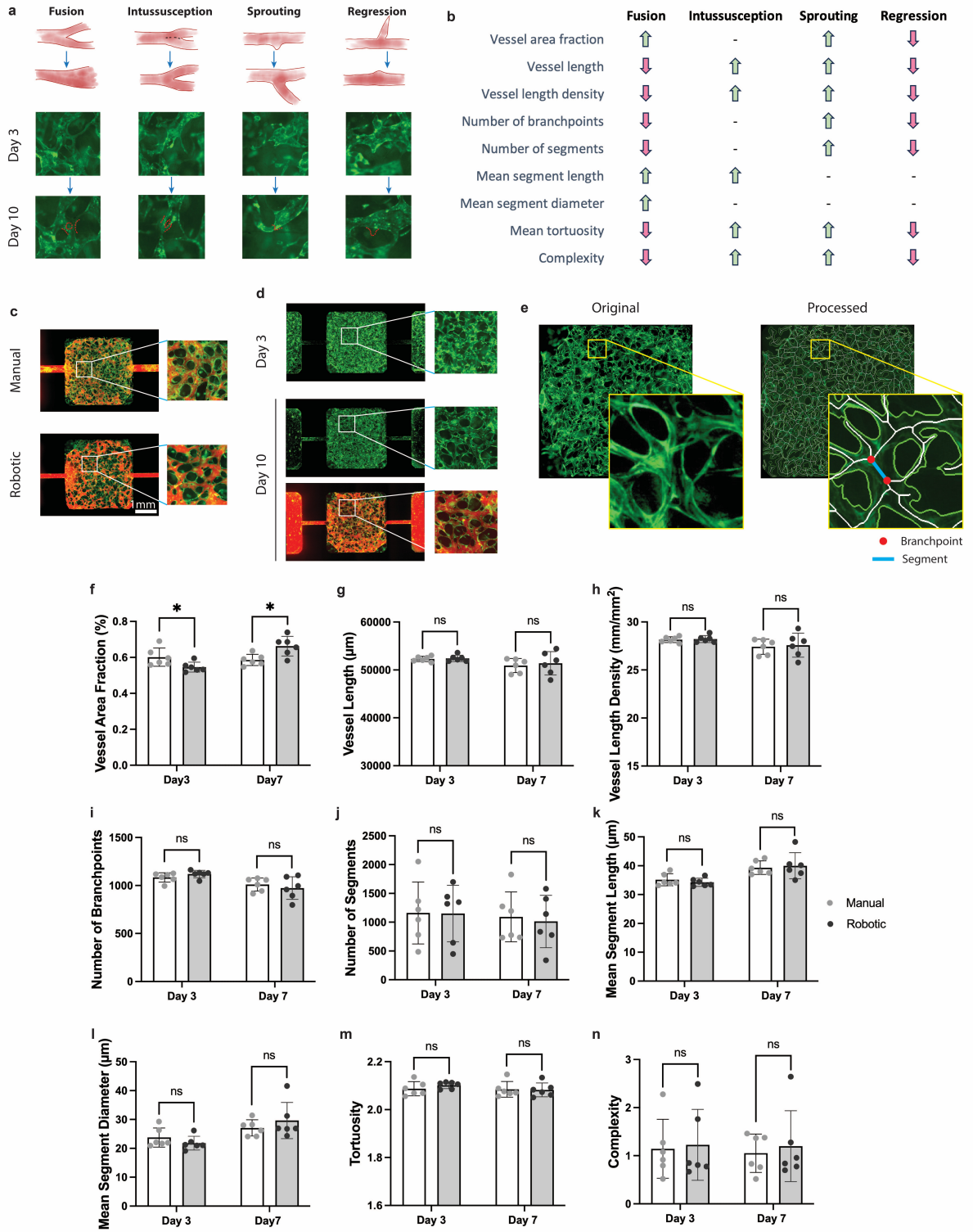


Figure 3.2: Structural analyses of microvascular networks. (continued)

Figure 3.2: (continued) (a) Illustrations depict four major vascular mechanisms adapted from Udan et al. (2013) [152], along with example images captured regarding each mechanism of the microvascular networks on IFlowPlate™. (b) A list of vascular parameters and how they can be affected by the four major vascular mechanisms. (c) Representative images of microvascular networks prepared manually and automatically on day 7, showing GFP-HUVECs in green and perfusion medium containing TRITC 65-85 kDa dextran in red. (d) Representative images of microvascular network formed on day 3 and day 10. (e) Representative images of the original GFP image of the microvascular network in the middle well of IFlowPlate™ imported into REAVER [149] and the processed image output via REAVER. Green lines outline the vessels, red dots indicate the branchpoints, and the blue bar labels the segment element found between the branchpoints. (f-n) Structural analyses of the microvascular network built manually and automatically using REAVER on day 3 and day 10 for (f) the vessel area fraction (Day 3: * P = 0.0400, Day 10: * P = 0.0133) ; (g) the vessel length; (h) the vessel length density; (i) the number of branchpoints; (j) the number of segments; (k) the mean segment length; (l) the mean segment diameter; (m) the tortuosity; (n) the complexity. n = 6 for each condition.

3.3.3 Testing chemotherapy drugs using the vasculature assay on IFlowPlate™

We then used the microvascular networks to test for chemotherapy drug impact. The first drug we selected for screening was bortezomib. As a proteasome inhibitor, bortezomib has been reported to be vascular-toxic in various studies [153, 142]. We investigated the effect that bortezomib exerted on the microvascular networks after 72 hr of treatment, on day 13, with doses of 1, 0.1, 0.01, 0.001, and 0 μ M and compared the results to the 0 hr data. The doses applied bracketed the C_{max} found in the literature [154]. Fluorescent images were taken with the TRITC filter for visualizing 65 86 kDa dextran and the FITC filter for GFP-HUVECs 1 h after the addition of

the perfusion medium into the networks, showing that the microvascular networks remained perfusable for the vehicle group and the lowest doses, while starting from dose 0.01 μM and up the microvascular networks became non-perfusable (Figure 3.3(a)). A heat map containing each middle well’s signal from the GFP-HUVECs was constructed based on 0 h and 72 h after treatment with doses. There were significant GFP signal drops, indicating HUVEC apoptosis, in the groups with the two highest doses, 0.1 and 1 μM (Figure 3.3(c)). Additionally, we also calculated the mass of diffused dextran across the vascular lumen into the interstitial space. The percentage of the perfusable networks, the middle well GFP signal ratio, and the diffused dextran mass were plotted in the same graph to capture the different facets of the effect that bortezomib exerted on the microvascular networks. We also calculated EC50s for the perfusability and GFP signal results to demonstrate the half-maximal effective concentration of bortezomib to induce total non-perfusability ($EC50_{Perfusability} = 8.68 \times 10^{-9}\text{M}$) and loss of GFP signal in the microvascular networks ($EC50_{GFP} = 8.66 \times 10^{-8}\text{M}$) (Figure 3.3(b)). Bortezomib’s EC50s related to different protease activities and cell growth were previously reported to be between 0.05 nM to 0.7 μM [155–157]. The EC50s we detected using the microvascular networks on IFlowPlate™ agree with the effective concentration range determined previously. We analyzed images of the GFP-microvascular networks using REAVER to assess structural features at each dose. Nine vascular parameters were investigated, including vessel area fraction, vessel length, vessel length density, branchpoints, segments, mean segment length, mean segment diameter, mean tortuosity, and complexity (Figure 3.3 (d-l)). Bortezomib exhibited significant dose-dependent variations compared to the vehicle group in five vascular parameters. Specifically, at concentrations of 0.01 μM and 0.1 μM ,

bortezomib resulted in a 1.28-fold and 1.27-fold increase in the vessel area fraction, respectively (Figure 3.3 (d)). Conversely, the vessel length decreased by about 0.91-fold at 0.01 μM , and the vessel length density decreased by about the same factor at this concentration (Figure 3.3 (e, f)). the segment diameter demonstrated a 1.55-fold increase at 0.001 μM and a 1.59-fold increase at 0.01 μM (Figure 3.3 (j)). Additionally, the tortuosity increased by approximately 1.02-fold at both 0.1 μM and 1 μM (Figure 3.3 (k)).

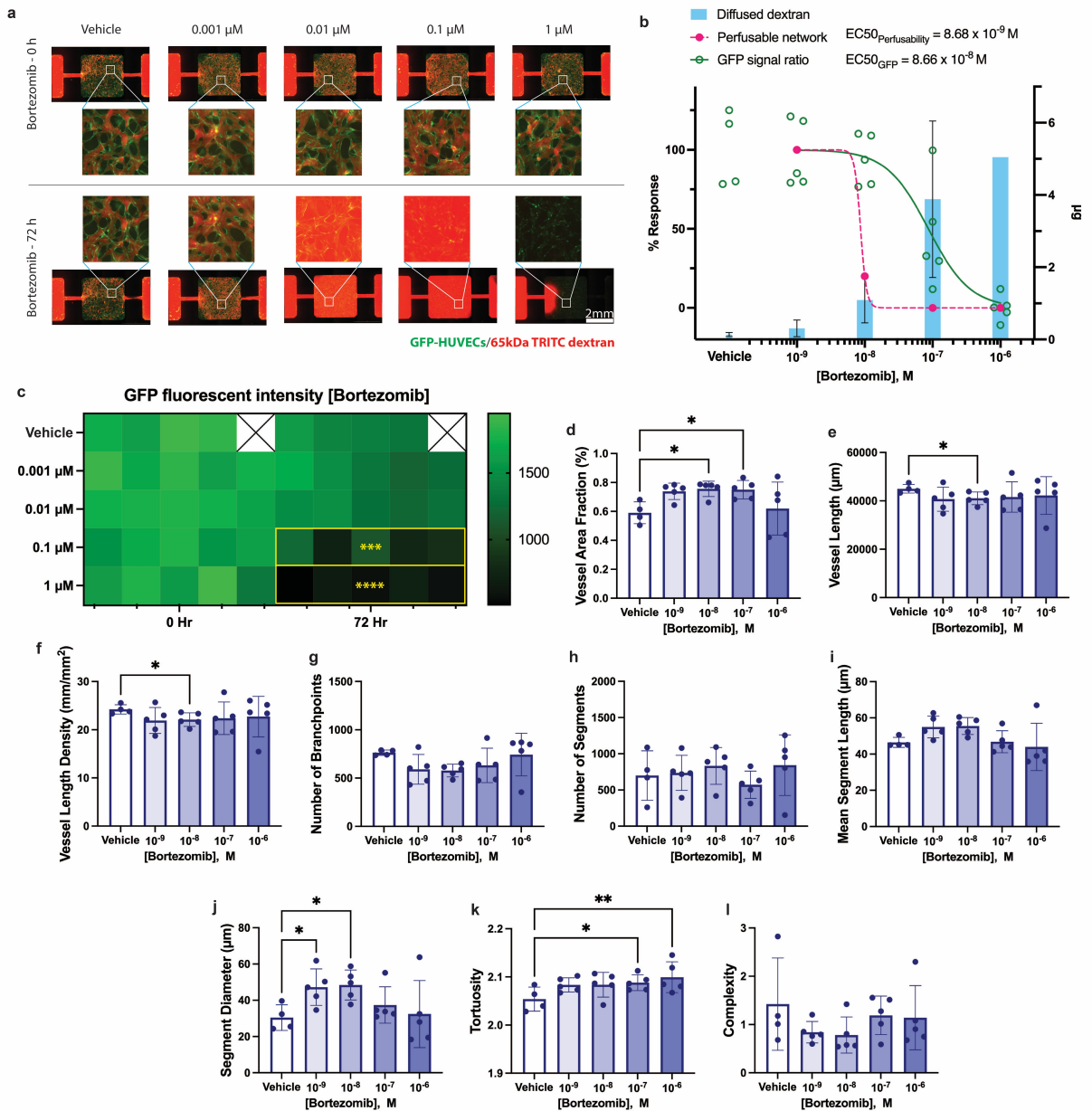


Figure 3.3: Figure 3. 3. Screening chemotherapy drug bortezomib on IFlowPlate™. (a) Representative images of microvascular networks before and after 72 h bortezomib treatment at various concentrations. $n = 4$ for the vehicle group and $n = 5$ for the rest groups. (b) Graph quantifying diffused dextran during the 1-hour permeability assay in μg , percentage change of perfusable networks, and percentage change of GFP signal ratio. $n = 4$ for the vehicle group and $n = 5$ for the other groups. (c) The heat map visualizes the GFP signal measurements of the middle wells containing microvascular networks.(continued)

Figure 3.3: (continued) (d-l) Structural analyses of the microvascular network after 72 h treatment of doses of bortezomib using REAVER [149] on day 13 for (d) the vessel area fraction (0.01 μM compared to the vehicle: * P = 0.0187, 0.1 μM compared to the vehicle: * P = 0.0261); (e) the vessel length (0.01 μM compared to the vehicle: * P = 0.0324); (f) the vessel length density (0.01 μM compared to the vehicle: * P = 0.0324); (g) the number of branchpoints; (h) the number of segments; (i) the mean segment length; (j) the mean segment diameter (0.001 μM compared to the vehicle: * P = 0.0315, 0.01 μM compared to the vehicle: * P = 0.0228); (k) the tortuosity (0.1 μM compared to the vehicle: * P = 0.0440, 1 μM compared to the vehicle: ** P = 0.0097); (l) the complexity. n = 4 for the vehicle group and n = 5 for the other groups.

We repeated the same drug screening procedure but with a different chemotherapy drug, vincristine. Vincristine is used to treat various cancers by disrupting microtubule function. Others have found that vincristine could lead to vascular toxicity [158]. In this study, we observed that vincristine affected perfusability at doses 0.01 μM and up (Figure 3.4 (a)). The GFP signal heat map revealed significant drops in GFP signal at concentrations of 0.1 μM and 1 μM (Figure 3.4 (c)). Together with the perfusability data, we determined the EC50 for the perfusability change ($1.67 \times 10^{-9}\text{M}$) and the EC50 for GFP signal loss ($2.90 \times 10^{-8}\text{M}$) (Figure 3.4 (b)). The determined EC50 values fall within the clinical range of vincristine concentrations (1 nM to 0.9 mM) previously established for cancer treatment [157]. The REAVER analysis revealed that the presence of vincristine significantly affected five vascular parameters compared to the vehicle group (Figure 3.4(d-l)). Specifically, at a concentration of 1 μM , the vessel length, the vessel length density, and the number of branchpoints decreased by 0.64-fold, 0.64-fold, and 0.50-fold, respectively (Figure 3.4(e-g)). Additionally, the number of segments exhibited a 0.55-fold decrease at both 0.1 μM and 1 μM (Figure 3.4(h)). Moreover, the complexity showed a 1.88-fold increase at 0.01

μ M (Figure 3.4(l)). The principal component analysis demonstrated clusters and distributions of bortezomib and vincristine impacted vascular architecture on day 13 (Figure 3.4(m)). In sum, we can see that bortezomib and vincristine, albeit both affected endothelial integrity, induce vascular toxicity with distinct dose-dependent patterns. These data show that we can use multi-faceted data analysis to generate a comprehensive examination of the compound screening run on these microvascular network assays.

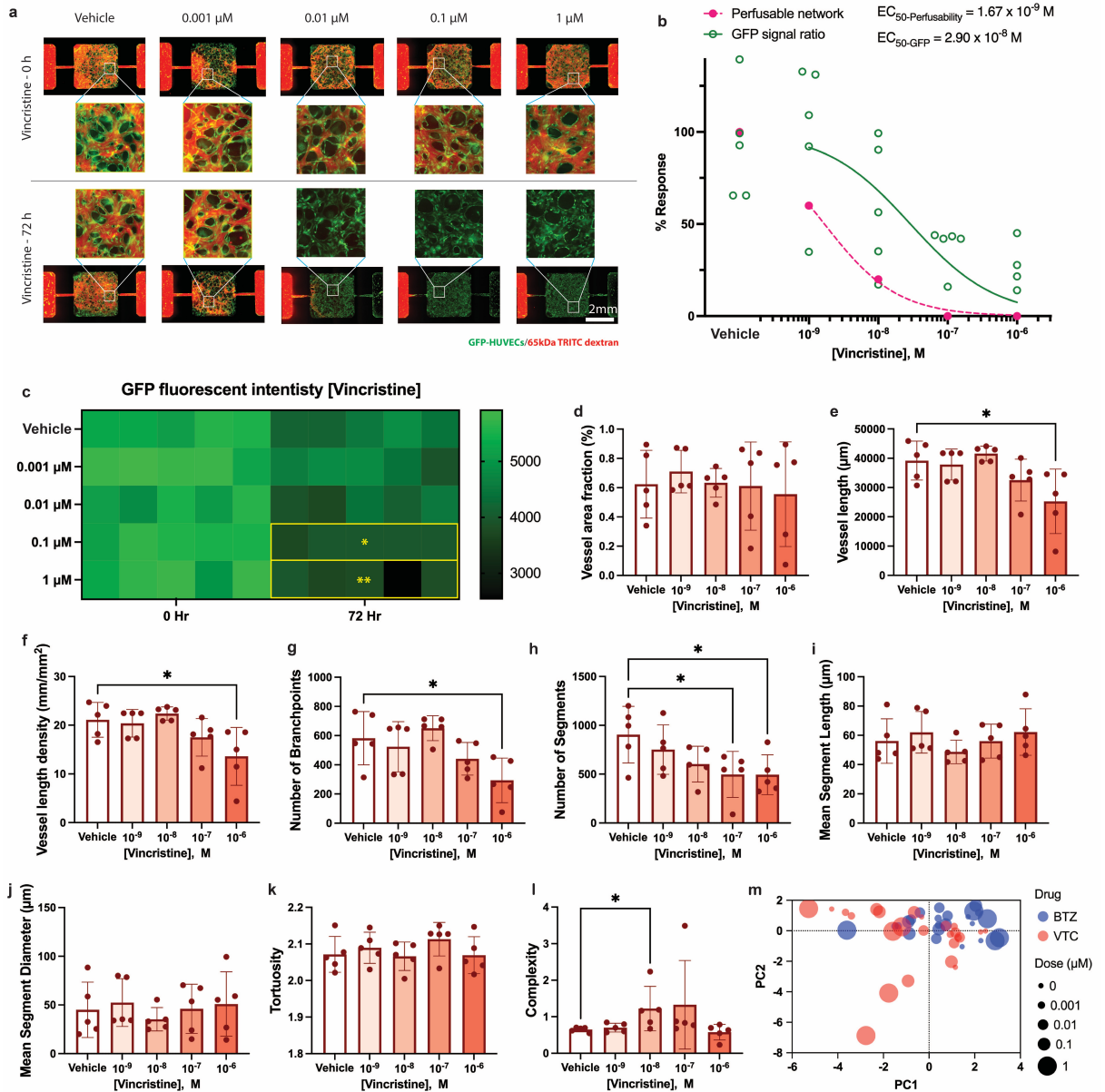


Figure 3.4: Figure 3. 4. Screening chemotherapy drug vincristine on IFlowPlate™. (a) Representative images of microvascular networks before and after 72 h vincristine treatment at various concentrations. $n = 5$ for each group. (b) Graph quantifying percentage change of perfusable networks and percentage change of GFP signal ratio. $n = 5$ for each group. (c) The heat map visualizes the GFP signal measurements of the middle wells containing microvascular networks. (continued)

Figure 3.4: (d-l) Structural analyses of the microvascular network after 72 h treatment of doses of vincristine using REAVER [149] on day 13 for (d) the vessel area fraction; (e) the vessel length (1 μM compared to the vehicle: * $P = 0.0317$); (f) the vessel length density (1 μM compared to the vehicle: * $P = 0.0317$); (g) the number of branchpoints (1 μM compared to the vehicle: * $P = 0.0203$); (h) the number of segments (0.1 μM compared to the vehicle: * $P = 0.0481$, 1 μM compared to the vehicle: * $P = 0.0203$); (i) the mean segment length; (j) the mean segment diameter; (k) the tortuosity; (l) the complexity (0.01 μM compared to the vehicle: * $P = 0.0255$). $n = 5$ for each group. (m) PCA of both bortezomib and vincristine treated microvascular networks structural analyses after 72 h treatment.(continued)

3.4 Discussion

The utilization of the IFlowPlate™, a customized 384-well device, in our study provided a unique opportunity to leverage technology in enhancing the efficiency of microvascular network assays. As previously documented, this device allows for the preparation of up to 128 microvascular network sets, facilitating high-throughput screening capabilities [145, 146]. Our current methodology builds upon the established protocols, optimizing the cell ratio and integrating advanced robotics to streamline the hydrogel casting process. This integration is pivotal as it facilitates uniformity in network formation, crucial for reliable experimental outcomes. Moreover, the strategic design of the assay timeline aligns with the dynamic nature of vascular architecture, which is influenced by various microenvironmental factors such as extracellular matrix [159], flow dynamics [160], and cell-to-cell crosstalks [161]. By initiating treatment on day 10 and monitoring through day 13, we align our observations with the critical periods of vascular adaptation mechanisms such as fusion, intussusception, sprouting, and regression, which are essential for understanding compound effects on vascular health [152]. Additionally, the application of REAVER, an image-processing

program, facilitates a detailed analysis of vascular structures, enabling us to quantify changes across multiple parameters such as vessel area fraction and vessel complexity [149]. This analytical approach is crucial for our comparative structural analyses between the manual and robotic groups of microvascular networks. Our findings indicate no significant differences in microvascular development between the manual and robotic methods, suggesting that the robotic handling system produces tissues of comparable quality to those prepared manually. This equivalence is meaningful, as it validates the scalability and standardization of robotic systems for tissue engineering applications, offering a pathway towards more reproducible and efficient production of tissue constructs [141].

Our study utilized the high-throughput microvascular network assays developed on IFlowPlate™ to evaluate the vascular toxicities of two distinct chemotherapeutic agents, bortezomib and vincristine, known for their efficacy in cancer treatment but also associated with vascular side effects. Bortezomib, a proteasome inhibitor [153], and vincristine, a microtubule-disrupting agent, were assessed for their impact on endothelial cell integrity and microvascular architecture [158]. The assays revealed that both drugs affect microvascular perfusability and endothelial viability in a dose-dependent manner. For bortezomib, we observed that microvascular networks maintained perfusability at lower concentrations but exhibited loss of perfusion starting from $0.01 \mu\text{M}$, accompanied by endothelial cell apoptosis at higher doses of 0.1 and $1 \mu\text{M}$, as indicated by significant drops in GFP signal. Similarly, vincristine affected perfusability at doses starting from $0.01 \mu\text{M}$, with notable reductions in GFP signal also at 0.1 and $1 \mu\text{M}$, reflecting severe endothelial damage with similar patterns compared to bortezomib. However, quantitative analysis using REAVER

revealed dose-dependent changes in vascular parameters varied for bortezomib and vincristine. Bortezomib resulted in an increase in vessel area fraction and segment diameter, suggesting edematous expansion at certain concentrations, whereas decreases in vessel length and density indicated a loss of structural integrity. In contrast, vincristine showed a more pronounced decrease in vessel length, density, branch points, and segments, highlighting its disruptive effect possibly leading to more fusion events (Figure 3.2(b)). The PCA demonstrated distinct patterns of vascular response for each drug, also underscoring their differential impacts on vascular architecture. The EC50 values for bortezomib and vincristine provided insights into their potency windows and potential for vascular toxicity. With both drugs' EC50 falling in the clinical range [157], it shows that the microvascular networks have the potential to be translatable for preclinical compound screening purposes. These findings illuminate the capability of using the microvascular networks on IFlowPlate™ to study the nuanced ways in which different chemotherapeutic agents can induce vascular toxicity and to provide implications for dose management of side effects.

In summary, our comparative analysis of bortezomib and vincristine using high-throughput microvascular network assays highlights the unique and shared influences with which these drugs manifest their inducing vascular toxicity. This approach not only elucidates the multi-faceted analyses of drug-induced vascular damage but also reinforces the utility of advanced microvascular assays in preclinical drug screening for optimizing chemotherapy regimens and mitigating adverse effects.

3.5 Conclusions

Our study has demonstrated the efficacy of the IFlowPlate™ system in conducting high-throughput microvascular network assays to evaluate the vascular effects of chemotherapeutic agents such as bortezomib and vincristine. By integrating advanced robotics and the REAVER image-analysis program, we have enhanced the precision and consistency of our experimental setups, streamlining the detailed quantification of vascular changes. These assays have confirmed that both drugs can induce significant vascular toxicity in a dose-dependent manner, affecting both perfusability and endothelial cell viability. The dose-dependent effects observed, alongside the EC50 values falling within clinical ranges, underscore the potential of these microvascular networks as translational models for preclinical drug screening. This approach not only aids in understanding the specific vascular impacts of different chemotherapy drugs but also provides a robust platform for optimizing treatment regimens and minimizing adverse effects. Through this work, we have illuminated the nuanced interactions between chemotherapeutic agents and vascular architecture, offering insights into the management of their vascular side effects, and advancing the field towards more effective and safer chemotherapeutic interventions.

Competing Interests

The authors declare the following competing financial interest(s): D.S.Y.L, S.R., and B.Z. are inventors of a provisional patent filed based on this work.

Acknowledgments

D.S.Y.L. was supported by the National Sciences and Engineering Research Council of Canada (NSERC, CGS-D) and B.Z. received funding from the Canadian Institute of Health Research (CIHR, PJT-166052). We thank Scott Myhal for assisting with the NIMBUS robotic handling system. Schematics were created with BioRender.com. The authors acknowledge the assistance of OpenAI’s ChatGPT for draft preparation. This research utilized the GPT-4 model, which was accessed on April 15, 2024.

Chapter 4

AngioPlate™ - Predesigned Vessels

The content of this chapter is a second revision of the manuscript text for publication under the following citation:

- Rajasekar, S.*, Lin, D. S. Y.*, Zhang, F.*, Sotra, A., Boshart, A., Clotet-Freixas, S., Liu, A., Hirota, J. A., Ogawa, S., Konvalinka, A., & Zhang, B. (2022). Subtractive manufacturing with swelling induced stochastic folding of sacrificial materials for fabricating complex perfusable tissues in multi-well plates. *Lab on a Chip*, 22(10), 1929-1942.

** These authors contributed equally to the work.*

(Obtained permission to reprint.)

Copyright © The Royal Society of Chemistry 2022

DOI: 10.1039/d1lc01141c

Subtractive manufacturing with swelling induced stochastic folding of sacrificial materials for fabricating complex perfusable tissues in multi-well plates

Author contributions

S.R., D.S.Y.L., and F.Z. performed the experiments, analyzed the results, and prepared the manuscript. A.S.pov designed and fabricated the lung mechanical actuation plate lid. A.B. and S.C. performed the Galectin-1 assay. A.L. contributed to device fabrication. J.H. edited the manuscript. S.O. performed the albumin assay and edited the manuscript. A.K. edited the manuscript. B.Z. envisioned the concept, performed the experiments, supervised the work, and edited the manuscript.

Abstract

Organ-on-a-chip systems that recapitulate tissue-level functions have been proposed to improve in vitro–in vivo correlation in drug development. Significant progress has been made to control the cellular microenvironment with mechanical stimulation and fluid flow. However, it has been challenging to introduce complex 3D tissue structures due to the physical constraints of microfluidic channels or membranes in organ-on-a-chip systems. Inspired by 4D bioprinting, we develop a subtractive manufacturing technique where a flexible sacrificial material can be patterned on a 2D surface, swell and shape change when exposed to aqueous hydrogel, and subsequently degrade to produce perfusable networks in a natural hydrogel matrix that can be populated with cells. The technique is applied to fabricate organ-specific vascular networks in a customized 384-well plate. This biofabrication method eliminates the physical constraints in organ-on-a-chip systems to incorporate complex ready-to-perfuse tissue structures in an open-well design.

4.1 Introduction

To address the limitation in existing preclinical models, there is an increasing effort towards building advanced 3D human tissues by incorporating multiple cell types, scaffolds, and dynamic forces. Advances in biofabrication are an integral part of this effort. 3D bioprinting techniques, such as Freeform Reversible Embedding of Suspended Hydrogels (FRESH) [162] and stereolithography [163], have been used to build tissues with boundless structural complexity. However, although the tissue production process is generally automated, each 3D-printed tissue construct needs to be

manually connected for media perfusion or cell seeding before tissue culture can be initiated.³ This represents a significant engineering manipulation step to transition from tissue printing to perfusion culture. On the contrary, an organ-on-a-chip system, based on microfluidic devices or microtiter plates, provides built-in perfusion connections [164, 165], but lacks the flexibility to introduce complex 3D tissue structures that are possible with 3D bioprinting [166, 167]. Although many key functional features of complex organ systems can be replicated with organ-on-a-chip systems, the physical constraints of plastic microchannels and membranes in these closed microfluidic devices limit the structural design of the tissue microenvironment that can be engineered. To integrate perfusion and complex 3D tissue structures, microfluidic chips could be pre-fabricated, and perfusable networks can be subsequently introduced in the chip with a 3D laser beam microdissection technique [168–170]. While this technique produces high-resolution features, it can be slow and difficult to scale. Hence, producing tissues with unrestrained 3D structures, built-in connection for perfusion, and high scalability is not trivial and still much needed.

4D printing, defined as “3D printing + time”, is an emerging concept where the shape of a 3D-printed structure can change as a function of time. For instance, encoded with localized swelling behavior, printed composite hydrogels can be programmed to build complex architectures that change shape over time when immersed in water [171]. We exploited this observation and further extended this concept to demonstrate that a flexible sacrificial material patterned on a 2D surface can change shape in 3D when in contact with a natural hydrogel solution. As the gel crosslinks, the structurally transformed flexible sacrificial material is locked in place. It

can subsequently be degraded to produce perfusable networks, which are then populated with human cells to emulate complex organ-specific structures. We termed this method subtractive manufacturing with swelling-induced stochastic folding due to the swellable and shape-changing property of sacrificial material. As a result, the sacrificial material initially patterned in 2D could easily integrate with a pre-designed microfluidic-based perfusion system and give rise to a 3D structure when triggered at a later stage. Furthermore, taking advantage of the scalability of 2D patterning, we adapted the technique to a high throughput format of a 384-well plate (here referred to as AngioPlate™, Figure 4.1) on which we can readily transition from tissue fabrication to perfusion culture for an array of units.

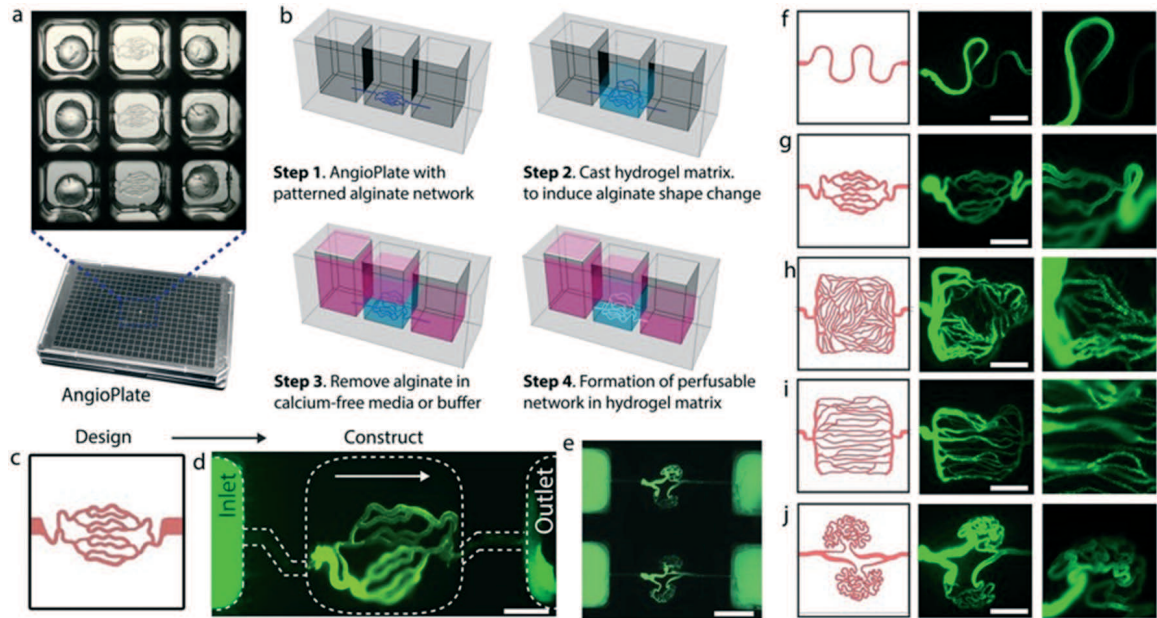


Figure 4.1: Subtractive manufacturing with swelling induced stochastic folding of sacrificial materials for fabricating complex perfusable tissues. (a) Image of encapsulated alginate fiber networks in a 384-well plate. (b) Schematic on the use of AngioPlate™, which includes gel casting, folding of the alginate network in the hydrogel, and degradation of the sacrificial alginate template. (c) Illustration of a generic bifurcating network design. (continued)

Figure 4.1: (continued) (d) Perfusion fluorescent particles ($1 \mu\text{m}$, green) through the assembled 3D network in a hydrogel matrix based on the generic bifurcation network design shown in c. Scale bar, 1 mm. (e) Perfusion of multiple networks in AngioPlate™. Scale bar, 2 mm. (f–j), Image of organ-specific networks with structural variation from different initial designs shown on the left and the resulting 3D network perfused with fluorescent particles ($1 \mu\text{m}$, green) for visualization on the right. Scale bar, 1 mm.

4.2 Materials and Methods

4.2.1 AngioPlate™ fabrication

Standard photolithography techniques were used to create each SU8 master mold. To create a negative mold, a PDMS (Ellsworth Adhesive, 4019862) mixture at a ratio of 1:30 was poured onto the SU8 master mold and cured at 47°C overnight. The cured PDMS mold was soaked in 5% w/v pluronic acid (Sigma Aldrich, P2443) for 30 minutes, washed with distilled water, dried, and then capped onto a plasma-treated polystyrene sheet ($11.5 \times 7.5 \text{ cm}$, Jerry's Artarama, V16013). Assembled PDMS mold and polystyrene sheet were then transferred to a one-well plate. To fill the entire pattern with 3% w/v alginate solution (Sigma Aldrich, A2033), 75 mL of the solution was poured into the one-well plate (VWR, 30617-594) containing assembled PDMS mold and sheet. After the alginate solution filled up the patterned microchannels, the residual solution was aspirated out. To cross-link alginate, 75 mL of 5.5% w/v calcium chloride solution (CaCl) (Sigma Aldrich, 223506) was added and left to cross-link overnight. After cross-linking, the residual CaCl solution was removed and rinsed with distilled water. Cross-linked alginate within the PDMS channels was then air-dried for 48 hours. Melted poly (ethylene glycol) dimethyl ether (PEGDM) (Sigma

Aldrich, 445908) was then injected into the channels and allowed to fill at 70 °C for 1 hour to encapsulate and preserve alginate features. Once PEGDM re-solidifies, the PDMS mold was peeled off and the alginate fibers encapsulated in PEGDM were transferred onto the polystyrene sheet. The polystyrene sheet containing the patterns was then bonded onto a bottomless 384-well plate using a high-viscosity PDMS glue (Ellsworth Adhesive, 2137054) at a ratio of 1:10. The assembled device was allowed to cure overnight at room temperature. Assembled devices were sterilized for 2.5 hours using 70% w/v ethanol and PEGDM was washed off during the sterilization process. The plates were air-dried inside a biosafety cabinet (BSC) for 12 hours and stored at 4 °C until use.

4.2.2 Cell culture

Green Fluorescent Protein-tagged Human Umbilical Vein Endothelial Cells (GFP-HUVECs, donor sex: pooled from multiple donors, Angio-Proteomie, CAP-0001GFP) were grown in Endothelial Cell Growth Media (ECGM2, (PromoCell, C-22011) in cell culture flasks coated with 0.2% w/v gelatin (Sigma Aldrich, G9391).

4.2.3 Hydrogel casting and device operation

The hydrogel used in our device was 10 mg mL⁻¹ fibrinogen (Sigma Aldrich, F3879). Before hydrogel casting, the hydrogel was aliquoted into 125 μ L aliquots, and each aliquot was mixed with 25 μ L of thrombin (7 U mL⁻¹, Sigma Aldrich, T6884). Immediately after mixing, 25 μ L of gel solution was then cast into each well. The plate was left in a BSC for 30 minutes to allow for gelation. Alternatively, neutralized rat tail collagen (2–2.5 mg mL⁻¹, Corning, CACB354249) with an extra 20% v/v D-PBS

(Thermo Scientific, 14190144) can be used as another source of natural extracellular matrix. To degrade the alginate polymers, D-PBS supplemented with 1% aprotinin was added to all wells, and the platform was placed on a rocker at 4 °C for 48 hours with daily buffer change. Alternatively, DMEM containing 10% FBS, 1% penicillin-streptomycin, 1% HEPES solution, and 1% aprotinin was added to all wells and the platform was placed in an incubator incubated at 37 °C and 5% CO₂ for 48 hours with daily media change. The device was then primed again with cell culture media and incubated at 37 °C and 5% CO₂ for 24 hours prior to cell seeding. After removing all the media, 30 μ L of fresh media was added into the middle well and 125 μ L of the cell suspension (0.6 million cells per mL) was added to the inlet and outlet wells. The plate was placed flat in the incubator for 2 hours to allow cell attachment. After cell attachment, culture media was removed, and 50 μ L fresh media was added to the middle well, and 90 μ L to the inlet and outlet wells. To initiate perfusion, the entire platform was placed on a programmable rocker that tilts at a 15° angle and alternates its tilting direction every 15 minutes. 1% v/v aprotinin (2 mg mL⁻¹, Sigma Aldrich, 616370-M) was added to all media to prevent fibrin gel degradation. Media was changed every other day.

To test alginate degradation, the networks were perfused with fluorescent FITC and/or TRITC latex beads (1.0 μ m, Sigma Aldrich, L1030 and L2778), diluted at a ratio of 1:5 in D-PBS. An image cytometer (BioTek Instruments Inc.) was used for imaging the networks.

4.2.4 Vascular variability, permeability, and drug testing

12 tissue samples were used to quantify variations in vasculature. The average diameters for each vascular tissue were measured using Image J Fiji software at 10 different locations on each sample. The numbers of branches were counted manually. To visualize the vascular permeability differences in the networks, 70 kDa FITC dextran (Sigma Aldrich, 46945) were perfused through the networks after treatments and imaged using an image cytometer (BioTek Instruments Inc.). To quantify the permeability changes in the vascular networks that were exposed to various external stimulations, vessels were treated with Triton™ X-100 (0.1% v/v), TNF- α (0.5 or 1 $\mu\text{g mL}^{-1}$, Sigma Aldrich, SRP3177) or lipopolysaccharides (LPS) from *Escherichia coli* (200 $\mu\text{g mL}^{-1}$, Sigma Aldrich, L4391) for 24 hours before the permeability test. 70 kDa FITC dextran were perfused through the networks after each treatment. The fluorescent intensities in the middle wells were measured at 0 minutes and 15 minutes after adding the dextran solution. The change in fluorescent intensity was quantified and correlated to a standard curve to calculate the amounts of dextran diffusing across the vascular barrier.

4.2.5 Immunostaining and histology

To prepare for immunostaining, culture media was first removed from all wells, and the tissues were washed with D-PBS three times. The tissues were fixed in 4% paraformaldehyde solution (Electron Microscopy Sciences, EMS 15710-S) at 4 °C overnight. Fixed tissues were washed with D-PBS, then blocked and permeated overnight at 4 °C under perfusion with 10% FBS containing 0.1% Triton™ X-100. Then the tissues were incubated in primary antibody solution for 48 hours at 4 °C

Table 4.1: List of antibodies used and their catalog numbers

Antibody	Type	Host	Dilution	Brand, Cat No.
Laminin	Primary	Rabbit	1:200	Abcam, ab11575
F-Actin	Conjugated	-	1:200	Cayman Chemical, 20553
CD31	Primary	Rabbit	1:10	Abcam, ab28364
vWF	Primary	Rabbit	1:200	Abcam, ab6994
DAPI	-	-	1:1000	Sigma-Aldrich, D9542
Anti-Mouse FITC	Secondary	Goat	1:200	Sigma-Aldrich, F0257
Anti-Rabbit Alexa Fluor 488	Secondary	Goat	1:200	Abcam, ab150077
Anti-Mouse Alexa Fluor 594	Secondary	Goat	1:200	Abcam, ab150120
Anti-Rabbit Alexa Fluor 594	Secondary	Goat	1:200	Abcam, ab150080

followed by D-PBS wash at 4 °C for 48 hours to remove residual primary antibodies from the gel. Secondary or conjugated antibodies were added along with DAPI and incubated for 48 hours at 4 °C. The tissues were then washed with D-PBS for 48 hours at 4 °C prior to imaging with an image cytometer. Dilutions used for all antibodies are shown in Table 1 below. For 3D confocal images, stained tissues were imaged using Leica SP5 confocal microscopy. The transmission electron microscope images show the subcellular features of the endothelium were imaged with the transmission electron microscope at the Electron Microscopy Facility of the Canadian Centre for Electron Microscopy at McMaster University.

4.2.6 Statistical analysis

SigmaPlot and Prism were used for all statistical analyses. All data were tested for normality and equality of variance. To determine statistical significance, one-way

ANOVA or one-way ANOVA on ranks with the Holm–Sidak method was applied. Data in all graphs were plotted as mean with standard deviation using Graphpad and at least three independent samples were used per condition for all quantitative analysis.

4.3 Results

Our objective is to develop a scalable 3D tissue culture platform (AngioPlate™) that includes built-in fluid connections as in most organ-on-a-chip systems but also a way to obtain tissues with a high level of structural complexity as made possible with 3D bioprinting. To achieve this, we proposed using a flexible sacrificial material that can be patterned in 2D so that it can be integrated into a micro channel-based device for perfusion but can also transform in 3D to produce complex structures when triggered by hydration. The flexible sacrificial material should be inert, patternable, and compatible with various natural hydrogel matrices. Most importantly, it should also degrade in response to a second trigger to carve out a 3D network inside a hydrogel. In search of a material that meets these criteria, we converged on a well-known biomaterial, alginate, which can be rapidly cross-linked and degraded in response to calcium ions. Alginate has been widely used in biological applications as tissue scaffolds [172] and drug delivery carriers [173]. Using a combination of techniques, including standard photolithography and diffusion-based calcium gelation (Supplementary Figure C.1), we patterned an array of 128 networks of branched alginate fibers on a polystyrene sheet corresponding to the format of a 384-well plate. The patterned alginate fibers were dried first (Supplementary Figure C.1) and then assembled against a bottomless 384-well plate (Figure 4.1(a)). In this format, the plate

can be packaged, sterilized with gamma radiation, and then stored. When using the plate, 25 μ L of hydrogel solution (Fibrin or Collagen) was dispensed onto the alginate network to rehydrate the alginate (Figure 4.1(b), step 1). During incubation, the dried alginate network quickly swelled, detached from the polystyrene base, and changed shape inside the hydrogel (Supplementary Video C.1). Then the hydrogel is cross-linked at 37 °C (e.g., collagen and Matrigel) or through enzymatic reaction (e.g., fibrin), locking the folded alginate structure in place (Figure 4.1(b), step 2). Finally, phosphate buffered saline (D-PBS) or culture media with low calcium and magnesium concentration ($\text{Ca}^{2+} < 200 \text{ mg mL}^{-1}$ and $\text{Mg}^{2+} < 100 \text{ mg mL}^{-1}$) was used to extract the calcium from the alginate and dissolve away the alginate network, resulting in an open perfusable network that is pre-designed to connect with the inlet/outlet wells for perfusion (Figure 4.1(b), step 3). Perfusion was initiated with gravity-driven flow by simply tilting the plate at a 15° angle on a programmable rocker (Figure 4.1(b), step 4). To ensure the stability of the tissue model over time, the fibrin gel used was highly adhesive and can attach to the polystyrene surface to form a tight seal that prevents leakage. Further, the endothelial cells can grow into the inlet/outlet channels which help in forming a continuous barrier at the transition between the plastic and the gel interface. With 1% aprotinin added fresh every other day, fibrin gel degradation was completely prevented. The hydrogel scaffolding was stable, even in the presence of fibroblasts. This feature of fibrin gels is important when compared to collagen, where gel compaction and degradation can be a major issue in long-term culture. However, extra care is needed when working with fibrin gel as the crosslinking speed needs to be fine-tuned by controlling the the concentration of thrombin used since slower gelation time caused alginate features to dissolve

resulting in incomplete network formation inside the hydrogel (Supplementary Figure C.2). Fibrin gel stiffness can also be modified by changing the concentrations of both fibrinogen and thrombin to mimic tissue-specific matrix stiffness. Previously, it has been shown that as the concentration of fibrinogen and/or thrombin increases, the structural modulus of matrices increases, yielding stiffer fibrin matrices [174].

The extent of alginate folding is determined by the crosslinking speed and viscosity of the hydrogel solution and can result in completely distinct structures from the same initial design, which adds one more dimension of control. However, even under the same gelling conditions, the exact positioning of resulting networks will vary in the 3D space (Figure 4.1(c–e) and C.3). In the native tissue, no two biological structures are identical. Hence, this degree of stochasticity is natural. Despite the stochastic behavior, distinct vessel network organizations that resemble various organs or even various parts of an organ can be captured (Figure 4.1(f–j)). The overall architectural design (i.e., the diameter, density, and location of the branches, etc.) was pre-defined in the initial design (Supplementary Figure C.3). We have built a 3D network resembling a convoluted tubule (Figure 4.1(f)), an intricately folded glomerular vessel in a kidney (Figure 4.1(h)), densely packed vessels in a liver (Figure 4.1(i)), and well-aligned vessels as in a muscle (Figure 4.1(j)). Although a significant structural transformation from the initial design is not always necessary, the detachment of alginate from the plastic base due to alginate swelling is useful to create a softer microenvironment that is away from direct contact with the hard plastic for seeded cells.

We next populated the network in the vasculature design with endothelial cells

which formed a confluent endothelium in 8 days (Figure 4.2(a)). In some areas, vascular sprouting was also observed. The numbers of branches formed vary from 13 to 19 and the vasculatures formed in the platform had average diameters ranging from $63 \mu\text{m}$ to $104 \mu\text{m}$ (Supplementary Figure C.3). The resulting vasculature is a 3D structure that contains a hollow lumen and spans the depth of the hydrogel as shown from the confocal x-z plane view (Figure 4.2(a, e)). The vascular network in the presence of a confluent endothelium was significantly less permeable and displayed barrier function to large proteins. When exposed to TritonTM X-100 and TNF- α , the vascular permeability increased significantly and showed a dose-dependent response to TNF- α . When exposed to lipopolysaccharides (LPS) from *E. coli*. to simulate infection, the networks showed no significant changes in permeability and barrier function (Figure 4.2(b, c)). The endothelial cells also deposited a basement membrane that contained laminin which was localized on the basal side of the endothelium indicating apicobasal polarity of the vessels developed (Figure 4.2(d)). Furthermore, the endothelial cells produced and distributed von Willebrand factor (vWF) both intracellularly and extracellularly, which is a key protein for regulating blood coagulation (Figure 4.2(f)). Lastly, transmission electron microscopy showed that the endothelial cells form intercellular tight junctions consistent with the vessel barrier function shown (Figure 4.2(g)).

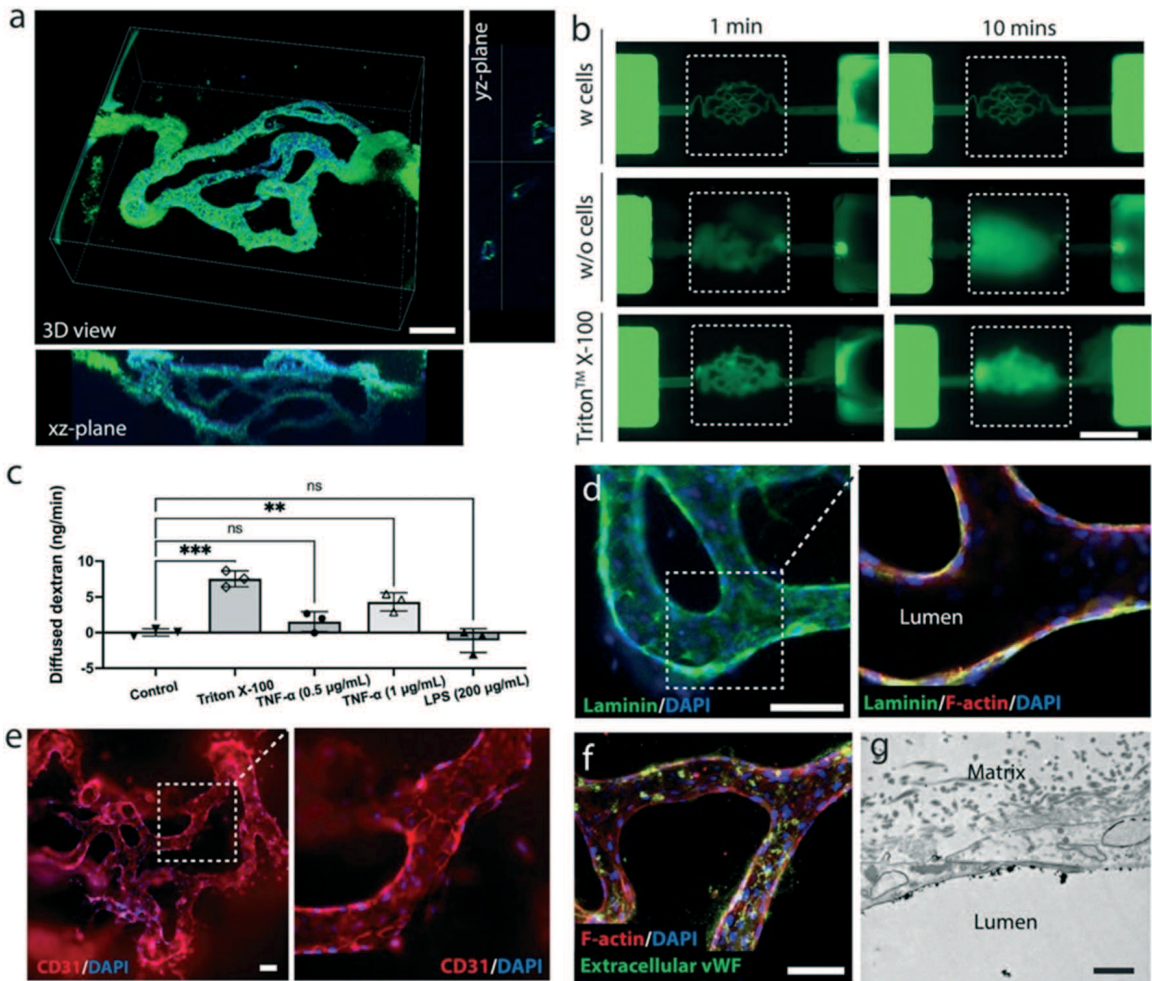


Figure 4.2: Vasculature in AngioPlate™ device. (a) 3D volumetric rendering of confocal z-stack images of a vascular network populated with human umbilical cord vein endothelial cells. View from xz-plane is maximum projection. Cells were stained for CD31 (green) and DAPI (blue). Scale bar, 500 μ m. (b) Fluorescent images of vascular networks perfused with 70 kDa fluorescein-dextran (green) with or without the presence of endothelial cells and/or Triton™ X-100 treatments. Scale bar, 2 mm. (c) Quantification of dextran (70 kDa) diffusion rates of the vascular networks in response to no treatment, Triton™ X-100 (positive control), and drug treatments, $n = 3$. Statistical significance was determined using one-way ANOVA. * $p \leq 0.05$ ** $p \leq 0.01$ *** $p \leq 0.001$. ns indicates not significantly different. (d-f) Fluorescent image of a vascular network stained for laminin (green), F-actin (red), CD31 (red), extracellular vWF (green), and DAPI (blue). Scale bar, 100 μ m. g, Transmission electron microscope image of endothelium on a vessel wall showing the tight junction between two adjacent endothelial cells. Scale bar, 1 μ m.

4.4 Discussion

For the first time, highly complex hydrogel-embedded perfusable tissues can be integrated with multi-well plates to mimic tissue specific structures and interfaces without the use of synthetic membranes or plastic channels [175, 176]. Furthermore, unlike other 3D bioprinted tissues that requires multiple steps of device assembly to introduce perfusion [177], our method provides built-in vascular and tubular connections to the biofabricated tissues directly inside a standard 384-well plate. There is no manual procedure needed to establish connection and perfusion, making the system more scalable and user-friendly. The subtractive manufacturing technique not only takes advantage of the scalability of 2D patterning to integrate with widely adopted multi-well plates for ease of use but also applies a swellable sacrificial material to transform a 2D pattern into a 3D perfusable structure for improved model complexity. Because the network structures are pre-fabricated, the time it takes to build tissues using the AngioPlate™ is just the typical duration for matrix gelation. Therefore, different from 3D printing, cells or tissues embedded within the gel matrix will experience minimal stress during the biofabrication process.

Compared to a previously published platform, IFlowPlate™, from our group, which also allows for the generation of high-throughput vascularized tissues, the AngioPlate™ provides users with the capability to create hierarchical vascular networks with a pre-defined number of vessel branches and diameters [178, 179]. AngioPlate™ also allows users to create perfusable epithelial tubes that don't easily self-assemble like endothelial cells. When compared to the previously published InVADE platform, epithelial tissues on AngioPlate™ does not contain a thick polymer wall which creates an artificial barrier that doesn't allow for mechanical actuation [180, 181]. Although

the swelling-induced stochastic folding method introduces structural variations as we have characterized (Supplementary Figure C.3(b)), these structural variations were not significant enough to prevent us from capturing significant changes to vessel permeability caused by cytokines or toxins (Figure 4.2(c)), which means the system can be used for biological studies, especially with significant experimental samples supported by the high-throughput format of this platform.

The use of fibrin is also an important aspect of the tissue fabrication process. We found fibrin strongly adhered to the polystyrene surface to form a tight seal between the inlet and outlet connection channels and the network inside the gel. Collagen on the other hand results in weaker adhesion and connection, sometimes delaminate from the polystyrene surfaces. The use of gravity driven flow provides enough pressure to perfuse the networks with various sizes to support cell growth. The networks in the 384-well version of AngioPlate™ are sufficiently perfused with gravity-driven flow. However, gravity-driven flow is not designed to achieve physiological shear stress in these vessels. The shear stress in these engineered vessels is usually below 1 dyne per cm^2 .

Another key feature of our platform is the open-well design. Different from the conventional closed microfluidic-based systems, our device allows easy tissue extraction for downstream analysis. We demonstrated that it is compatible with histopathological assessment, which is the gold standard in clinical diagnosis of disease and drug injury. Molecular analyses including RNA sequencing and proteomics are also possible experimental readouts with this system. These features could allow direct comparison of the in vitro data with human clinical data in future studies for model validation.

The open-well design also allows pre-fabricated tissue to be easily added to each well. For instance, a monolayer of organ-specific epithelial cells could be cultured on the top surface of the gel with a supporting perfusable vascular network underneath. Alternatively, tissue spheroid, organoids, or tissue explants could be vascularized by placing them on top of the gel and the supporting vascular bed. The platform could also potentially be integrated with extrusion-based 3D printing in the future to expand model complexity further. The platform becomes highly versatile by having an open-well design and by removing the geometric constrain of synthetic membranes or microfluidic channels. The tissue models, built entirely inside a natural hydrogel with no restrictive boundaries, could be seeded with stem cell-derived organoids and serve as the initial structural template to study tissue development and morphogenesis [182]. Lastly, when using our device, users need only pipetting techniques for handling all reagents. It does not require users to assemble tubes or pumps, making the platform compatible with the robotic fluid handling system for automation.

From the aspect of device fabrication, our current process uses PDMS glue to bond a bottomless well plate with a polystyrene base. PDMS is prone to drug adsorption [183] and may need to be replaced depending on the application. In addition, the spread of the PDMS glue into the middle well is not always easy to control, which could damage the patterned features and lead to device failure. Compared to our previously published platform with a simpler design, the increased complexity of AngioPlate™ with multiple inlets and outlets required for perfusion does reduce experimental throughputs. plate. However, to compensate for any loss of tissue due to quality control, around 20 tissues are usually routinely established per plate. The main point of failure we often encounter is in the plate gluing step which can be

improved with the use of pressure-sensitive adhesive, hot embossing bonding, or laser welding methods that are more accessible in industry. Because of the lack of access to these industrial techniques, PDMS glue was used to bond the plastic device which inevitably involves additional fabrication steps that are prone to failure.

From a design aspect, different from 3D printing, our current method does not provide the flexibility of changing the design on demand. However, the master molds we used for alginate patterning could be 3D printed without the time-consuming photolithography step, which would combine the scalability of the 2D patterning with the versatility of 3D printing to allow rapid design iterations. Alternatively, the patterned 2D alginate features could be directly 3D printed with an extrusion-based 3D printer without using any PDMS molds, which could significantly shorten the fabrication process while providing even more design flexibility. To avoid the use of any calcium chelating agents that could potentially damage cells, we used buffer or culture media with low calcium ion concentration for the degradation of the alginate sacrificial material. This degradation is a slower process that can last two days. But considering the overall length of a typical culture and tissue maturation process, this is a minor delay from an end-user perspective. During tissue culture, it's important to note that media perfusion is entirely driven by gravity which varies over time due to the depletion of the pressure heads. Moreover, the flow pattern is bi-directional. If a constant unidirectional flow is required, customized lids with built-in microfluidic pumps could be used to recirculate the media from outlet wells back to inlet wells to maintain fluid pressure [176].

4.5 Conclusions

The trade-off between model complexity and experimental throughputs has been a long-standing issue [184]. More studies are needed to understand the level of tissue complexity that is necessary for model systems which are likely specific to the biological question of interests. But when complex tissue structures and the use of natural extracellular matrix are needed, the subtractive manufacturing technique could offer a new way of approaching tissue production and culture to close the existing disparity between model complexity and throughputs. Moreover, the emergence of stem cell-derived organoids will require platform technology that can accommodate organoid growth with an amenable matrix and offer perfusion capability without compromising experimental throughputs [167]. In future work, the integration of organoids and the AngioPlate platform could be explored [185].

Competing Interests

A PCT application on the technology has been filed by SynoBiotech, Inc. B.Z. holds equity in the company.

Acknowledgments

We thank Dr. Samantha Slikboer for her help in performing ultrasound imaging and data processing. We thank Sonya Kouthouridis for her help in conducting histology of lung and kidney tissues. This work was made possible by the financial support of the National Sciences and Engineering Research Council of Canada (NSERC) CGS-D scholarship to S.R. and D.S.Y.L. This work was also funded by the Canadian Institute

of Health Research (CIHR) Project Grant (PJT-166052) to BZ. We also would like to acknowledge <https://BioRender.com> for its support in creating figure illustrations.

Chapter 5

AngioPlate™ - Vessel Arrays for Drug Screening

The content of this chapter is a second revision of the manuscript text for publication under the following citation:

- Lin, D. S. Y., Hashemi, H., Chakravarty, A., Jozani, K., Bonanno, J., Anvari, N., Rajasekar, S., Zhang, F., & Zhang, B. (2024). High-throughput modeling of vascular responses in human microvessel arrays using AngioPlate™

(Manuscript in preparation.)

High-throughput modeling of vascular responses in human microvessel arrays using AngioPlate™

Author contributions

D.S.Y.L. and B.Z. designed the experiments. D.S.Y.L. performed the experiments and analyzed the data. H.H. assisted with compound screening. A.C., J.B. and N.A. assisted with data analysis. K.J. performed TEM imaging and provided technical support. S.R. and F.Z. provided technical support. D.S.Y.L. and B.Z. interpreted the data. D.S.Y.L. wrote the manuscript. B.Z. supervised all aspects of the work.

Abstract

The development of new pharmaceuticals is significantly hindered by the high costs and low predictive accuracy of traditional preclinical models, which often inadequately

mimic human physiological responses. Recent advancements in organ-on-a-chip technology have ushered in sophisticated 3D vascular models and microfluidic systems that closely replicate the microarchitecture and physiology of human blood microvessels. These systems are pivotal in addressing previous limitations by integrating stromal cells such as pericytes and fibroblasts, which aid in the structural and functional maturation of endothelial cells. This paper highlights the use of the Angio-Plate™ platform, which utilizes automated preparation techniques to develop human microvessel arrays. These microvessel arrays have demonstrated high predictive accuracy in assessing vascular toxicity levels and have been instrumental in developing organ-specific models, particularly for the liver and lungs. The technological advances discussed offer insights into vascular biology and could potentially improve the translational relevance of preclinical findings. Such progress suggests possible avenues for enhancing drug development efficiency and effectiveness, with implications for future pharmaceutical research and therapy optimization.

5.1 Introduction

The development of new pharmaceuticals is constrained by high costs and low predictive accuracy in the preclinical phase. The limitations of traditional models exacerbate this challenge in accurately mimicking human physiological responses, leading to substantial inefficiencies when drugs transition to clinical trials [186, 187]. In this context, vascular models are crucial for evaluating the pharmacokinetics, pharmacodynamics, and potential vascular side effects of new drug candidates [188, 189]. Traditional in vitro models, including 2D cell cultures and animal studies, often fail to represent human vascular functions accurately. While animal models provide valuable

organism-level data, they suffer from interspecies variability that may not translate to human systems [190]. Conversely, 2D cultures lack the three-dimensional cell-cell and cell-matrix interactions that are critical in human tissues [191]. Recent advancements in organ-on-a-chip technology have led to the development of 3D vascular models and microfluidic systems that better simulate the microarchitecture and hemodynamics of human blood microvessels [192–194]. Alongside these innovations, an increasing number of vascular models have begun to integrate high-throughput capabilities essential for extensive pharmaceutical testing [195, 196], while others have emerged to more accurately recapitulate specific organ responses [197, 198]. Robotic handling systems have also been integrated into organ-on-a-chip workflows to streamline model development and enhance precision [199]. This automation allows for more consistent and efficient management of culture conditions, significantly improving the reproducibility and scalability of experiments [200].

Specifically, innovations in physiological vascular modeling have included the integration of various stromal cells, such as pericytes (PCs) and fibroblasts (FBs), which support the structural and functional maturation of endothelial cells (ECs) [201–203]. These models are instrumental in studying endothelial-stromal cell interactions in a controlled environment, providing insights into their roles in vessel stability and blood barrier integrity under physiological and pathological conditions. Moreover, research into vascular models has expanded to include the simulation of various disease states using inflammatory and fibrotic agents like $\text{TNF}\alpha$, $\text{TGF}\beta$, $\text{IFN}\gamma$, thrombin, Poly(I:C), and LPS. These studies are crucial as they reveal the complex cytokine interactions and endothelial responses that characterize different vascular diseases, improving our

understanding of disease mechanisms and the effectiveness of therapeutic interventions. In addition to modeling the disease, researchers have also investigated the endothelial responses to chemotherapy agents in vascular models [204, 205], which has been pivotal for understanding biomolecule mechanisms that underlie drug-induced vascular damage. The development of organ-specific vascular models has become increasingly important for more precise drug testing and disease modeling [206]. By mimicking the unique microenvironments of specific organs, such as the liver [207] or lungs [208], these models allow for more accurate predictions of organ-specific drug effects and disease processes, enhancing the translational relevance of preclinical findings.

In response to these needs, human microvessel arrays on the preciously developed AngioPlate™ platform [209] have been designed to provide a sophisticated candidate. We demonstrated preparation, both manually and automatedly, the utilization of these microvessel arrays, testing 670 vessels, to enable extensive and detailed studies of vascular responses under various conditions. This scale of testing is complemented by the customized 384-well plate platform's ability to accurately simulate and analyze vascular dynamics using mature vessel arrays and detailed cytokine profiling. In examining the ten chemotherapy drugs, the microvessel arrays proved to have the capability to predict the vascular toxicity level precisely. Furthermore, by incorporating specific sources of stromal cells and ECs into these models, AngioPlate™ facilitates the development of organ-specific vascular models, liver, and lung vessels, revealing the vascular microenvironments for different organs, enhancing the understanding of organ-specific vascular biology.

5.2 Materials and Methods

5.2.1 Cell culture

Original vials of Human Umbilical Vein Endothelial Cell Line (HUVEC Line, Ever-Cyte, CHT-006-0008), Human Primary Lung Fibroblasts (Lung FBs, ATCC, PCS-201-013) at passage 2 (P2), Human Pericytes from Placenta (PCs, PromoCell, C-12980) at P2, Human Primary Liver Sinusoidal Microvascular Endothelial Cells (Liver ECs, CellBiologics, H-6017) at P3, Human Primary Liver Fibroblasts (Liver FBs, CellBiologics, H-6019) at P3, and Human Primary Lung Microvascular Endothelial Cells (Lung ECs, CellBiologics, H-6011) at P3 were obtained. HUVECs, Liver ECs, Lung ECs, and Liver FBs were cultured in T75 flasks (CELLSTART, 82050-856) coated with a 0.2% w/v gelatin (Sigma-Aldrich, G9391) solution in PBS (Gibco, 14190144) for 20 minutes at 37 °C with 5% CO₂. Lung FBs and PCs were cultured in T75 flasks. HUVECs were cultured in Endothelial Cell Growth Medium2 (ECGM2, PromoCell, C-22011) supplemented with 20 µg/mL G418 (Invivogen, ant-gn-1). Liver ECs and Lung ECs were cultured in ECGM2 supplemented with an extra 3% FBS (Thermo Fisher Scientific, 12484028). Lung FBs and Liver FBs were cultured in Dulbecco's Modified Eagle Medium (DMEM, Gibco, 11995065) supplemented with 10% FBS, 1% HEPES (Gibco, 15630106), 1% Penicillin-Streptomycin (Pen-Strep, Wisent Inc., 450-201 EL). PCs were cultured in Pericyte Growth Medium2 (PGM2, PromoCell, C-28041). All ECs and FBs were harvested using Trypsin-EDTA (0.05%, Gibco, 25300054). PCs were harvested using Accutase (Gibco, A1110501). Working cell banks were prepared by expanding HUVECs to P4, Lung FBs, PCs, Liver ECs, Liver FBs, and Lung ECs to P6. HUVECs, Lung FBs, and PCs were resuspended

in a freezing medium containing 5% DMSO (Sigma-Aldrich, D2650), 20% FBS, and 75% culture media to a concentration of 7×10^5 cells/mL. Liver ECs, Liver FBs, and Lung ECs were resuspended in a freezing medium containing 10% DMSO, 50% FBS, and 40% culture media to a concentration of 5×10^5 cells/mL. Cell suspensions were aliquoted into each cryogenic vial (VWR, 66008-751) at 1 mL each. Fresh frozen vials were obtained from the working cell banks for each round of experiments.

5.2.2 Hydrogel casting

Manual preparation

To generate human microvessels the AngioPlate™ manually, on day 0, stromal cells nearing confluence in T75 flasks were harvested, counted, and added to autoclaved 1.5 mL microcentrifuge tubes (VWR, 10025-726) for centrifugation. The list of cell densities added to each microcentrifuge tube used for different setups in this study is provided in Supplementary Table D.1.

After spinning down the cells in the microcentrifuge tubes, the supernatant was removed, and 125 μL of 10 mg/mL of Fibrinogen (Sigma-Aldrich, F3879) was added to resuspend the cell pellet. Next, 25 μL of 7 U/mL Thrombin (Sigma-Aldrich, T6884, stock solution at 10 U/mL, resuspended in 0.1% w/v BSA (Sigma-Aldrich, A9418) in PBS) was added to the cell suspension in Fibrinogen and mixed by pipetting up and down five times. Right after mixing, 25 μL of the cell suspension containing Fibrinogen and Thrombin was cast into five middle wells, followed by a light tap of the plate to assist hydrogel spreading inside the wells.

Robotic preparation

To generate human microvessels on AngioPlate™ using a robotic handling system (Hamilton Company, NIMBUS4), on day 0, nearly confluent stromal cells in T75 flasks were harvested, counted, and added to four autoclaved 2.0 mL microcentrifuge tubes (VWR, 10025-738) to be spun down. The list of volumes of Fibrinogen and Thrombin needed in each microcentrifuge tube for different numbers of microvessels is provided in Supplementary Table D.2. After spinning down the cells in the microcentrifuge tubes, the supernatant was removed, and PBS was added to resuspend the cell pellet. For microvessels containing HUVEC, lung FBs, and PCs, a final concentration of 0.1 million/mL for both lung FBs and PCs was achieved. Depending on the number of columns to be set up on the AngioPlate™, four tubes containing a certain volume of 20 mg/mL Fibrinogen and another four tubes of 7U/mL Thrombin are prepared and loaded into the robotic handling system at corresponding locations (Supplementary Figure D.7). The list of volumes of Fibrinogen and Thrombin needed in each microcentrifuge tube for different number of microvessels is provided in Supplementary Table D.2. A standard non-treated 384-well flat bottom plate (VWR, 732-2906) was placed inside the robotic handling system to serve as a mixing reservoir. The AngioPlate™ was also placed inside the robotic handling system onto a shaker. Once all the tubes and plates were placed securely at designated locations (Supplementary Figure D.7), the system automated the hydrogel mixing and casting. The flowchart of the programming code is provided in Supplementary Figure D.8.

During the 30-min incubation of AngioPlate™ on a leveled surface at RT, Thrombin and Fibrinogen in the hydrogel crosslinked and formed the Fibrin gel with stromal cells suspending in its matrices. To remove the sacrificial fiber on AngioPlate™, warm

PBS was added to all wells, 100 μL to inlet and outlet wells and 50 μL to middle wells, followed by a 40-min incubation at 37 °C with 5% CO₂ on a rocker (OrganoBiotech, IFlowRocker™) set to rock at ± 15 degree, switching the angle every 5 mins. After 40 mins, the PBS was aspirated and changed to fresh PBS, followed by another 20-min incubation, then the PBS was aspirated out. Finally, ECGM2 supplemented with 8% v/v FBS, 20 $\mu\text{g}/\text{mL}$ aprotinin (Sigma-Aldrich, 616370-M) [210], and 1% Pen-Strep was added to all wells: 90 μL to inlet and outlet wells and 50 μL to middle wells. Stromal cells were cultured at 37 °C with 5% CO₂ on the rocker to maturity from day 0 to 4 with daily changes of fresh media.

5.2.3 Vessels formation

On day 4, nearly confluent ECs were harvested, counted, and added to a 50 mL Falcon tube to be spun down and resuspended to a concentration of 5×10^5 cells/mL. Media were removed from all wells and 120 μL of the ECs suspension was added to both inlet and outlet wells. This was followed by a 2-h incubation at 37 °C with 5% CO₂ on a leveled surface, allowing HUVECs to go into the hollow tubular structure in the hydrogel and attach. After 2 h, 40 μL of ECGM2 supplemented with 20 $\mu\text{g}/\text{mL}$ aprotinin and 1% Peni-Strep was added to middle wells. ECs and stromal cells were cultured at 37 °C with 5% CO₂ on the rocker to vessel maturity. Media were changed daily by adding 90 μL to inlet and outlet wells and 50 μL to middle wells. The quality of the microvessels was checked on day 11 and onwards for further studies.

5.2.4 Permeability assay

To assess the barrier function of the vessels, a permeability medium containing 1 mg/mL of 65-85 kDa TRITC dextran (Sigma-Aldrich, T1162) and 4 kDa FITC dextran (Sigma-Aldrich, 46944) in ECGM2 was used. A standard curve was prepared by serial dilution of the permeability medium, consisting of concentrations of 1 mg/mL, 0.1 mg/mL, 0.01 mg/mL, 0.001 mg/mL, 0.0001 mg/mL, and 0 mg/mL. 100 μ L of each concentration was added three times: 100 μ L to the inlet well, 100 μ L to the middle well, and another 100 μ L to the outlet well. Then all media were removed from all sample wells. 60 μ L of ECGM2 was added to each middle well, and 90 μ L of permeability medium was added to the inlet and outlet wells. Right after switching the media to the permeability medium, *AngioPlate*TM was placed into a plate reader (Agilent, BioTek Cytation 5) for intensity reading. Two-wavelengths reading was set up with excitation at 544 nm and emission at 570 nm for TRITC and at 491 nm and 516 nm for FITC. Fluorescent intensities of all sample wells were collected at $t = 0$ and $t = 60$ mins. During the 60 mins of perfusion with the permeability medium, the *AngioPlate*TM was incubated at 37 °C with CO₂, on the rocker. After the fluorescent reading at $t = 60$ mins, fluorescent imaging was also conducted with TRITC and FITC filters and the 4X objective using the same plate reader to obtain visual qualitative data. The permeability medium was aspirated, and all sample wells were washed twice using ECGM2 with 90 μ L of medium for the inlet and outlet wells, and 50 μ L of medium for the middle wells. ECGM2 supplemented with 20 μ g/mL aprotinin and 1% Peni-Strep was added back to all sample wells when continued culture was needed. The standard curve was not aspirated if further permeability testing was to be conducted on the same plate. The amount of dextran diffused from the

vessel into the hydrogel during the 60 mins interval was calculated by correlating the fluorescent intensity to the dextran mass using the standard curves. After calculating the dextran masses at the 0-mins and 60-mins, the transportation rate of the dextran in $\mu\text{g}/\text{h}$ can be determined. Data analysis was performed using Microsoft Excel, GraphPad Prism 10.2.1, and Fiji 2 software.

5.2.5 Treatments

Treatment base medium I was prepared using ECGM2 supplemented with 20 $\mu\text{g}/\text{mL}$ aprotinin and 1% Pen-Strep. Treatment base medium II was prepared using ECGM2 supplemented with 20 $\mu\text{g}/\text{mL}$ aprotinin, 1% Pen-Strep and 100 ng/mL $\text{IFN}\gamma$. Treatment base medium III was prepared using ECGM2 Kit (PromoCell, C-22111) without adding heparin, supplemented with 20 $\mu\text{g}/\text{mL}$ aprotinin and 1% Pen-Strep. In treatment base medium I, doses of $\text{IFN}\gamma$ and $\text{TNF}\alpha$, each at 1, 0.1, 0.01, 0.001, 0.0001, and 0 $\mu\text{g}/\text{mL}$; $\text{TGF}\beta$ at 0.1, 0.01, 0.001, 0.0001, 0.00001, and 0 $\mu\text{g}/\text{mL}$; thrombin at 1, 0.5, and 0.1 U/mL ; and Poly(I:C) and LPS, each at 10, 1, 0.1, 0.01, 0.001, and 0 $\mu\text{g}/\text{mL}$, were prepared. Doses of $\text{TNF}\alpha$ at 1, 0.1, 0.01, 0.001, 0.0001, and 0 $\mu\text{g}/\text{mL}$, and $\text{TGF}\beta$ at 0.1, 0.01, 0.001, 0.0001, 0.00001, and 0 $\mu\text{g}/\text{mL}$, were prepared in treatment base medium II. Doses of $\text{TGF}\beta$ at 0.1, 0.01, 0.001, 0.0001, 0.00001, and 0 $\mu\text{g}/\text{mL}$, and Thrombin at 1, 0.5, and 0.1 U/mL , were prepared in treatment base medium III. Treatment media were added to all wells, except the Thrombin group, where the media containing Thrombin was only added to the inlet and outlet wells to mimic the location of thrombosis taking place [?].

A panel of chemotherapy drugs was obtained from NIH to prepare drug treatment media using treatment base medium I. Doses of drugs including bortezomib,

vincristine, paclitaxel, axitinib, bleomycin, mitomycin, sorafenib, amifostine, imatinib, and tamoxifen were prepared at concentrations of 1×10^{-6} , 1×10^{-7} , 1×10^{-8} , 1×10^{-9} , and 0 M. Vehicle medium was prepared by adding 0.01% DMSO into treatment base media I. Quality control was conducted by conducting permeability tests for these treatments on day 11. Treatments were applied from day 14 to day 17. Fresh media were prepared on day 13 and changed daily. Cytokine samples, 80 μL from the inlet and outlet wells and 50 μL from the middle wells were collected daily from day 15 to day 17. Treatment media were applied exclusively to the inlet and outlet wells, while the middle wells were filled with drug-free media. This configuration was engineered to replicate the pharmacokinetics and pharmacodynamics observed in intravenous or oral administration of chemotherapy agents.

To study organ-specific vessels' responses to TGF β , doses of TGF β at 0.1 and 0 $\mu\text{g}/\text{mL}$, were prepared in treatment base medium II. Quality control by conducting permeability tests for these treatments was done on day 10. Treatments were applied from day 13 to day 16. Fresh media were prepared on day 12 for day 13 to day 16 daily media change. Tissues treated with TGF β were cultured with treatment base medium II without TGF β from day 16 to day 20. Fresh media were prepared on day 16 and day 18 for daily media change. Treatment media were added to all wells. The list of catalog numbers and stock concentrations of all compounds and drugs used in this study is provided in Supplementary Table D. 3.

5.2.6 Cytokine analysis

Media collected at relevant time points, 24, 48, 72 hr after treatment started, were stored at $-80\text{ }^{\circ}\text{C}$ until analysis. Media collected at different time points were pooled for

each sample and transferred to 1.5 mL microcentrifuge tubes to be spun down at 1000 RPM for 10 mins at 4 °C. 75-100 μ L of supernatants were collected and transferred into 0.65 mL microcentrifuge tubes. The supernatants were stored at -80 °C until analysis. Measurements of the cytokine concentrations in samples were performed at Eve Technologies. Human Angiogenesis & Growth Factor 17-Plex Discovery Assay were conducted for different vessel culture conditions and Human Cytokine Proinflammatory Focused 15-Plex Discovery Assay for all treatment groups. Analysis of cytokine concentrations and clustering was done using GraphPad Prism 10.2.1 and MATLAB R2023a.

5.2.7 Immunofluorescent staining and TEM imaging

Samples were washed twice with PBS and then fixed with 4% PFA (Electron Microscope Sciences, EMS 15710-S, diluted in PBS) for 1 h at RT. After fixation, samples were washed three times with PBS with 15-min intervals and blocked with 10% FBS for 1 h at RT. Next, Samples were stained with primary antibodies in 2% FBS, including anti-VE-cadherin (Abcam, ab33168, diluted 1:1000), overnight on a rocker at 4 °C. Following overnight incubation, samples were washed with PBS for two nights on a rocker at 4 °C, changing PBS once after the first night. After primary antibodies staining, samples were stained with corresponding secondary antibodies and conjugated antibodies in 2% FBS, including Alexa Fluor 488 anti-rabbit (Abcam, ab150077, diluted 1:200), Phalloidin-iFluor 594 Conjugate (Cayman Chemical, 20553, diluted 1:1000), and DAPI (Sigma-Aldrich, D9542, diluted 1:1000), overnight on a rocker at 4 °C. Following this, samples were washed again with PBS for two nights on a rocker at 4 °C, changing PBS once after the first night. Samples were

then imaged using a confocal microscope (ZEISS, 3i Marianas LightSheet).

Transmission electron microscopy (TEM) images were captured to observe the morphologies of both the vessel and the stromal cells in its vicinity. The pressure-sensitive adhesive sheet at the bottom of the samples was cut along the well walls from the back side of the AngioPlate™, and the sample was carefully removed from the device using tweezers, along with the pressure-sensitive adhesive sheet. Subsequently, the samples were sent to the Faculty of Health Sciences Electron Microscopy Facility at McMaster University for processing. The processed sections were then imaged at the Canadian Centre for Electron Microscopy (CCEM).

5.2.8 Imaging analysis

Fiji 2 was used to measure diameters at five different locations of a vessel. The average of these five measurements was used to represent the vessel diameter for each sample. The data were imported to GraphPad Prism 10.2.1 for generating a summary figure. Images of vessels' DAPI signals were imported into Fiji 2. After applying thresholds and conducting computerized measurements, data on nuclei direction, circularity, and alignment were exported to MATLAB R2023a and GraphPad Prism 10.2.1 for generating polar histogram figures and bar graphs. Nuclei with less than 10° from the vessel's centreline are considered as "aligned" with the flow direction.

5.2.9 Statistical analysis

The data were plotted with the mean and standard deviation (SD). Shapiro-Wilk normality testing was performed for all data. If all groups in the data passed the normality test, we assumed a Gaussian distribution and used ANOVA; otherwise,

a nonparametric test was used. If the ratio between the largest and smallest SDs among the tested groups was 4, equal SDs were assumed; otherwise, equal SDs were not assumed. When the data were assumed to have a Gaussian distribution and equal SDs, statistical significance was assessed using ordinary one-way ANOVA followed by Fisher's LSD test. When the data were assumed to /have a Gaussian distribution but not equal SDs, statistical significance was assessed using Brown-Forsythe and Welch ANOVA tests followed by Dunnett's T3 multiple comparisons test. When the data were not assumed to have a Gaussian distribution, statistical significance was assessed using the Kruskal-Wallis test followed by Dunn's multiple comparisons test. Significance is represented as ns for not significant, * $P < 0.05$, ** $P < 0.01$, *** $P < 0.001$, and **** $P < 0.0001$. GraphPad Prism 10.2.1 was used.

5.3 Results

In this work, we built a customized 384-well device based on previously developed technologies [209], named AngioPlate™. On this device, one can grow over 100 sets of physiologically relevant microvessels to maturity and use them to screen drugs, induce inflammation, and develop disease models. Furthermore, cell sources can be switched to establish organ-specific microvessels for organ-specific studies (Figure 5.1(a)).

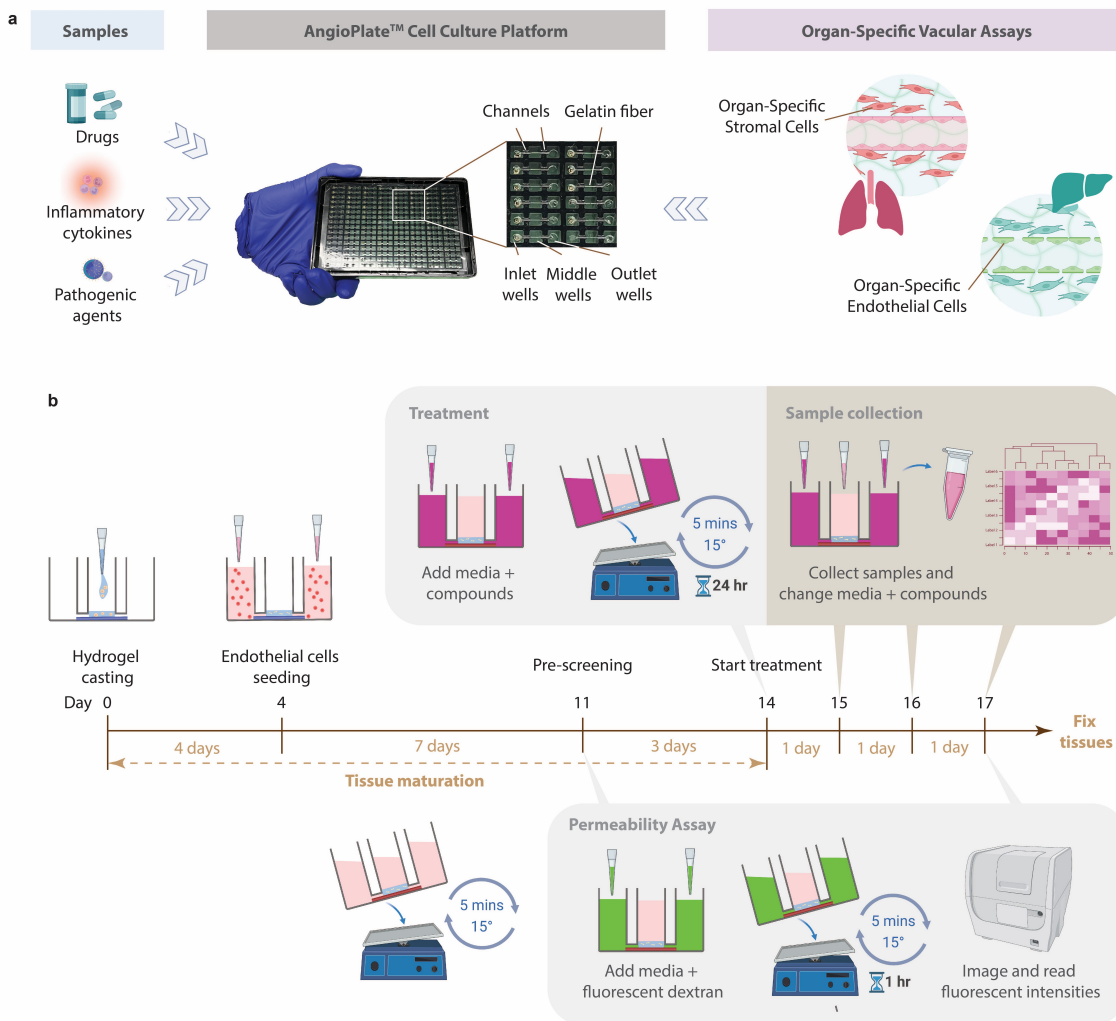


Figure 5.1: AngioPlate™ for building human microvessels assay. (a) A schematic overview of vascular assays building on AngioPlate™. Samples such as drugs, inflammatory cytokines, and pathogenic agents can be screened on AngioPlate™ through the vessels. Each AngioPlate™ contains 128 sets of tissue culture units available for building vessels. Each tissue culture unit consists of one inlet well, one middle well, and one outlet well. One channel connects the inlet and middle wells in the same tissue culture unit, while another channel connects the middle and outlet wells. Additionally, a gelatin fiber served as the sacrificial material is placed in the center of the tissue culture unit, crossing the inlet, middle, and outlet wells. Various human vessel assays can be built on AngioPlate™ using human organ-specific stromal cells and ECs, such as lung and liver-specific vessels. (continued)

Figure 5.1: (continued). Created with BioRender.com. (b) Vessel assays can be utilized for various studies with a standardized timeline and procedures. On day 0, the hydrogel with stromal cells was cast into the middle wells, and the sacrificial material was removed. After four days of stromal cell maturation, endothelial cells were seeded into the tube created by the removal of the sacrificial fiber to attach and form vessels. After seven days of culturing, on day 11, the permeability medium, containing 1 mg/mL of each TRITC 65 86 kDa and FITC 4 kDa dextran, was added to test vascular barrier function. Permeability medium was added to the inlet and outlet wells of the tissue culture unit. The fluorescent intensity of the middle well was read at $t = 0$ mins and $t = 60$ mins. During the 60 mins incubation time, the plate was placed on the IFlowRocker™ for rocking at a 15-degree angle with a directional change every 15 mins. After 60 mins, fluorescent imaging of the microvessels with dextran was also conducted. On day 14, the treatment began by adding the treatment media into the inlet and outlet wells, representing drug administration intravenously or orally. For studying systemic administration, the treatment media could be added to all the wells. From day 15 to day 17, the treatment continued, media were collected daily for later cytokine analysis, and new treatment media were added back to the culture unit. On day 17, the same permeability assay was run again to examine the vascular barrier function. Created with BioRender.com.

5.3.1 Co-culture with stromal cells improves vascular barrier function

We achieve vascular barrier function maturity through the co-culture of HUVECs with other stromal cells, including PCs and/or FBs. We selected these two stromal cell types because they have been individually reported to contribute to vascular maturation [201, 194, 211]. Additionally, the concept of a tri-culture involving both PCs and FBs together with ECs is supported by a previous study showing a synergistic effect of having both of these stromal cells [212]. We selected a total of 0.1 million stromal cells per mL to be mixed into the hydrogel, considering the cell density found in the human body and previously used in the literature [213, 214, 201]. A PCs to

FBS ratio at 1:1 was chosen based on the previous research [212]. The stromal cells, at the concentration described above, were mixed into the fibrinogen component of the hydrogel before casting and cultured from day 0 to 4 with 10% FBS in AngioPlate™ to elongate and proliferate before ECs were perfused into the device (Figure 5.1(b) and Supplementary Figure D.1, 2). The FBS concentration was strategically reduced to 2% after seeding the endothelial cells into the AngioPlate™ on day 4. We designed this protocol specifically to slow down stromal cell proliferation while promoting the health of endothelial cells.

HUVECs seeded into the hollow tube embedded in hydrogel proliferated to form a monolayer of endothelium (Supplementary Figure D.2) with and without the presence of stromal cells in the vicinity. By studying the DAPI signals from each condition, we observed that stromal cells assist HUVECs in aligning along the direction of flow (Supplementary Figure D.3(a, c)) [215] while having minimal impact on HUVECs' elongation (Supplementary Figure D.3(b)). Compared to the HUVECs-only group, confocal imaging revealed that in the presence of stromal cell co-culture, HUVECs expressed higher levels of VE-cadherin, a major endothelial molecule involved in adherens junctions. This suggests that the presence of stromal cells improves vascular formation and maturation (Figure 5.2(a)) [216]. A cross-sectional view constructed from z-stack scanning demonstrated that the vessel has an open lumen (Figure 5.2(c)). When zooming in to the level of cellular features using TEM imaging, we observed that the distance between stromal cells and endothelial cells can be closer than 1 μm (Figure 5.2(b)), comparable to the cellular distribution near microvessels [217], optimizing the crosstalk between cells [218]. We further verified the improvement in the maturity and barrier function of microvessels under the influence of stromal

cells by conducting a series of permeability tests. HUVECs cultured alone, with lung FBs, with PCs, and with both PCs and Lung FBs on AngioPlate™ were examined on days 11 and 18 using 65-85 kDa dextran and 4 kDa dextran. On day 11, significantly tighter barriers were observed in all conditions where stromal cells were present. Particularly, conditions with PCs and with both PCs and Lung FBs showed greater improvement in vascular maturity, as evidenced by a reduction of over half in the transportation rate of both dextran sizes crossing the endothelium (Figure 5.2(e, f)). However, stromal cells alone did not contribute to lowering the transportation rate of dextran. On day 18, the same permeability test was conducted again. The results showed that changes in barrier function within the same group were not significant (Supplementary Figure D.4), suggesting that the microvessels are suitable for studying at least up to day 18. We also demonstrated that the microvessels prepared on AngioPlate™ have the potential to run high-throughput assays. This was shown by our capacity to prepare a large number of microvessels (more than 50) on one plate (Figure 5.2(g)), and there was consistency between vessels, as indicated by a coefficient of variation (CV) less than 30% for 65-85 kDa dextran, less than 20% for 4 kDa dextran (Figure 5.2(h)), and less than 10% for diameters (Figure 5.2(i)).

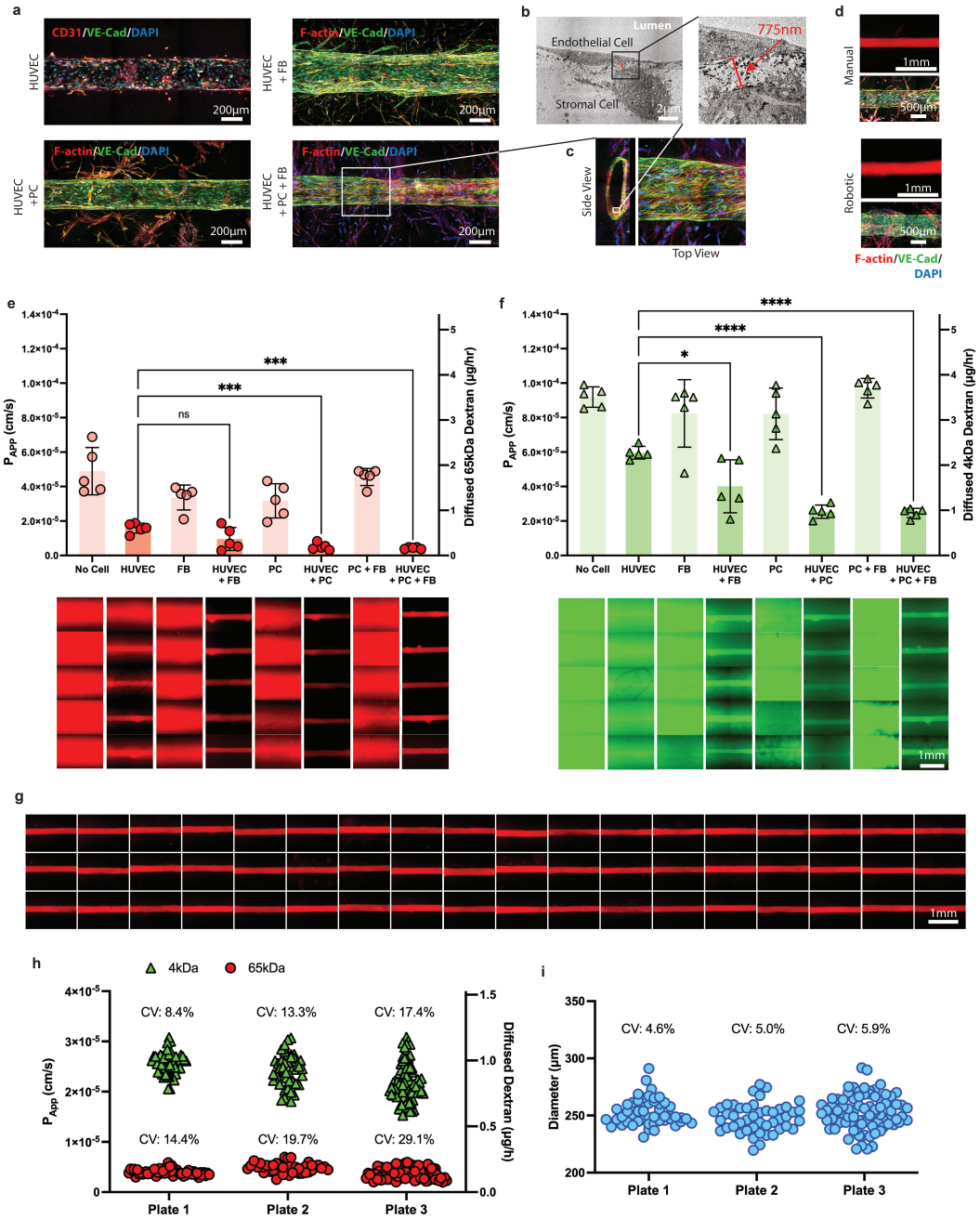


Figure 5.2: Establishment of mature microvessels with stromal cells. (continued)

Figure 5.2: (continued) (a) Representative images of microvessels built with HUVECs, with HUVECs and FBs, with HUVECs and PCs, and with HUVECs, PCs, and FBs on day 20. Stromal cells (F-actin) are embedded within the hydrogel and localized near the microvessels (VE-cadherin and F-actin). Nuclei of all cells were stained with DAPI. The white box in the HUVECs, PCs and FBs image indicates the zoom-in section used in (c). (b) TEM imaging demonstrates co-localization between ECs and stromal cells. The enlarged region indicates the distance between an EC and a stromal cell. (c) Cross-section of vessels, showing a projection onto the yz-plane. (d) Representative images of microvessels built with HUVECs, PCs, and FBs prepared manually and automatedly. TRITC 65-85 kDa dextran (red) indicates the lumen of vessels. Confocal imaging shows F-actin of the cytoskeleton, VE-cadherin of ECs, and DAPI-stained nuclei. (e, f) Quantification and visualization of TRITC 65-85 kDa (e) and FITC 4 kDa (f) dextran permeability assay. The transportation rate of diffused dextran on day 11, four conditions had no ECs seeding included no cells in hydrogel, FBs in hydrogel, PCs in hydrogel, and PCs and FBs in hydrogels; and four conditions having microvessels built with HUVECs, with HUVECs and FBs (4 kDa: * $P = 0.0450$), with HUVECs and PCs (65-85 kDa: *** $P = 0.0002$, 4 kDa: **** $P < 0.0001$), and with HUVECs, PCs and FBs (65-85 kDa: *** $P = 0.0007$, 4 kDa: **** $P < 0.0001$), $n = 5$ for each culture condition. Fluorescent images of diffused dextran after 1 h perfusion of the permeability medium. (g) Visualization of microvessels built with HUVECs, PCs and FBs on day 11 after 1 h perfusion of the permeability medium using the TRITC filter, $n = 54$. (h) Quantification of the permeability, transportation rate, and corresponding CV for 65-85 kDa and FITC 4 kDa dextran across three plates on day 11. Plate 1, $n = 52$; plate 2, $n = 45$; plate 3, $n = 78$. (i) Measurement of vascular diameters across three plates on day 20. Plate 1, $n = 50$; plate 2, $n = 46$; plate 3, $n = 81$.

To convert the transport rate - diffused dextran per hour, to the apparent permeability (P_{app}), the following equation [219, 220] was applied:

$$P_{app}(\text{cm/s}) = \frac{dQ}{dt} \cdot \frac{1}{A \cdot C_{donor}} \quad (5.3.1)$$

where dQ/dt is the transport rate in $\mu\text{g/h}$, A is the surface area of the vessel

that is in contact with the hydrogel ($1.06 \times 10^2 \text{ cm}^2$) and C_{donor} is the initial fluorescent dextran concentration (1 mg/mL) added to the inlet and outlet wells. After simplifying the equation, the relationship between dQ/dt and the P_{app} was rewritten as:

$$P_{app}(\text{cm/s}) = \frac{dQ}{dt} \cdot 2.62 \times 10^{-5} ((\text{cm} \cdot \text{h})/(\mu\text{g} \cdot \text{s})) \quad (5.3.2)$$

Thus, the data can be presented with either the design-specific transport rate in $\mu\text{g/h}$ or with the universal P_{app} in cm/s through a one-step conversion. From this conversion, we obtained an average P_{App} of $4.16 \times 10^{-6} \text{ cm/s}$ for 65-85 kDa dextran and a $2.38 \times 10^{-5} \text{ cm/s}$ for 4 kDa dextran (Figure 5.2(h)), which is about five to six times higher than the data collected in vivo, but agrees with other monolayer and 3D tubular models in vitro [221, 193].

5.3.2 Different co-cultures of stromal cells and HUVECs exhibited distinctive cytokine patterns

We examined the cytokine profiles of HUVECs-only, HUVECs with PCs, and HUVECs with both PCs and FBs culture conditions to understand the major cytokines contributing to the observed differences in EC growth shown in Figure 5.2(e, f). We plotted all cytokine data points collected on day 7 in a heat map, and the hierarchical clustering analysis revealed that the groups with PCs and both PCs and FBs were more closely similar to each other compared to the HUVECs-only group (Figure 5.3(a)). To further delve into the results, we determined the cytokines from the two groups with stromal cells that were significantly different from the HUVECs-only group and plotted them as individual bar graphs (Figure 5.3(b-k)). In HUVECs with

PCs condition, we observed significant modulation of pro-angiogenic markers, including upregulation of HGF (6.08 $\text{Log}_2(\text{FC})$) [222], G-CSF (0.95 $\text{Log}_2(\text{FC})$) [223], IL-8 (0.84 $\text{Log}_2(\text{FC})$) [224], and VEGF-C (0.63 $\text{Log}_2(\text{FC})$) [225], and downregulation of endothelin-1 (-0.29 $\text{Log}_2(\text{FC})$) [226]. Additionally, the dual-modulatory marker BMP-9 (0.26 $\text{Log}_2(\text{FC})$) [227] was upregulated (Figure 5.3 (l, m)). In the HUVECs with PCs and FBs condition, similar trends were noted with HGF (6.23 $\text{Log}_2(\text{FC})$), IL-8 (0.84 $\text{Log}_2(\text{FC})$), and VEGF-C (0.44 $\text{Log}_2(\text{FC})$) showing upregulation, while endothelin-1 (-0.39 $\text{Log}_2(\text{FC})$) exhibited a decrease (Figure 5.3 (o, p)). Other cytokines that were in the top-10 upregulated list include FGF-1 (1.52 $\text{Log}_2(\text{FC})$), VEGF-A (1.08 $\text{Log}_2(\text{FC})$), leptin (0.79 $\text{Log}_2(\text{FC})$), VEGF-D (0.58 $\text{Log}_2(\text{FC})$), and angiopoietin-2 (0.02 $\text{Log}_2(\text{FC})$) for the HUVECs with PCs condition. And VEGF-A (1.12 $\text{Log}_2(\text{FC})$), FGF-1 (0.79 $\text{Log}_2(\text{FC})$), endoglin (0.57 $\text{Log}_2(\text{FC})$), leptin (0.38 $\text{Log}_2(\text{FC})$), and EGF (0.15 $\text{Log}_2(\text{FC})$) for the HUVECs with PCs and FBs condition. Although didn't pass the significance analysis, endothelin-1 (-0.65 $\text{Log}_2(\text{FC})$) was the top-1 downregulated factor in the HUVECs with PCs condition, and VEGF-D (-0.42 $\text{Log}_2(\text{FC})$) in the HUVECs with PCs and FBs condition (Figure 5.3 (n, q)). The cytokine profiles suggest that these stromal cells play a crucial role in promoting and maintaining vascular barrier function. They achieve this by upregulating several pro-angiogenic factors, such as HGF [222], while simultaneously downregulating certain factors, including endothelin-1. Endothelin-1, renowned for its vasoconstrictive properties, possesses the capacity to induce fibrosis in endothelial cells and trigger the generation of ROS [228]. To summarize, we observed alterations in the profile of angiogenic factors specific to microvessels constructed with different compositions of stromal cells on AngioPlate™, linking cell-to-cell crosstalk to functional changes

in barrier integrity. We opted to proceed further with additional studies using compounds with the HUVECs co-cultured with PCs and FBs setup.

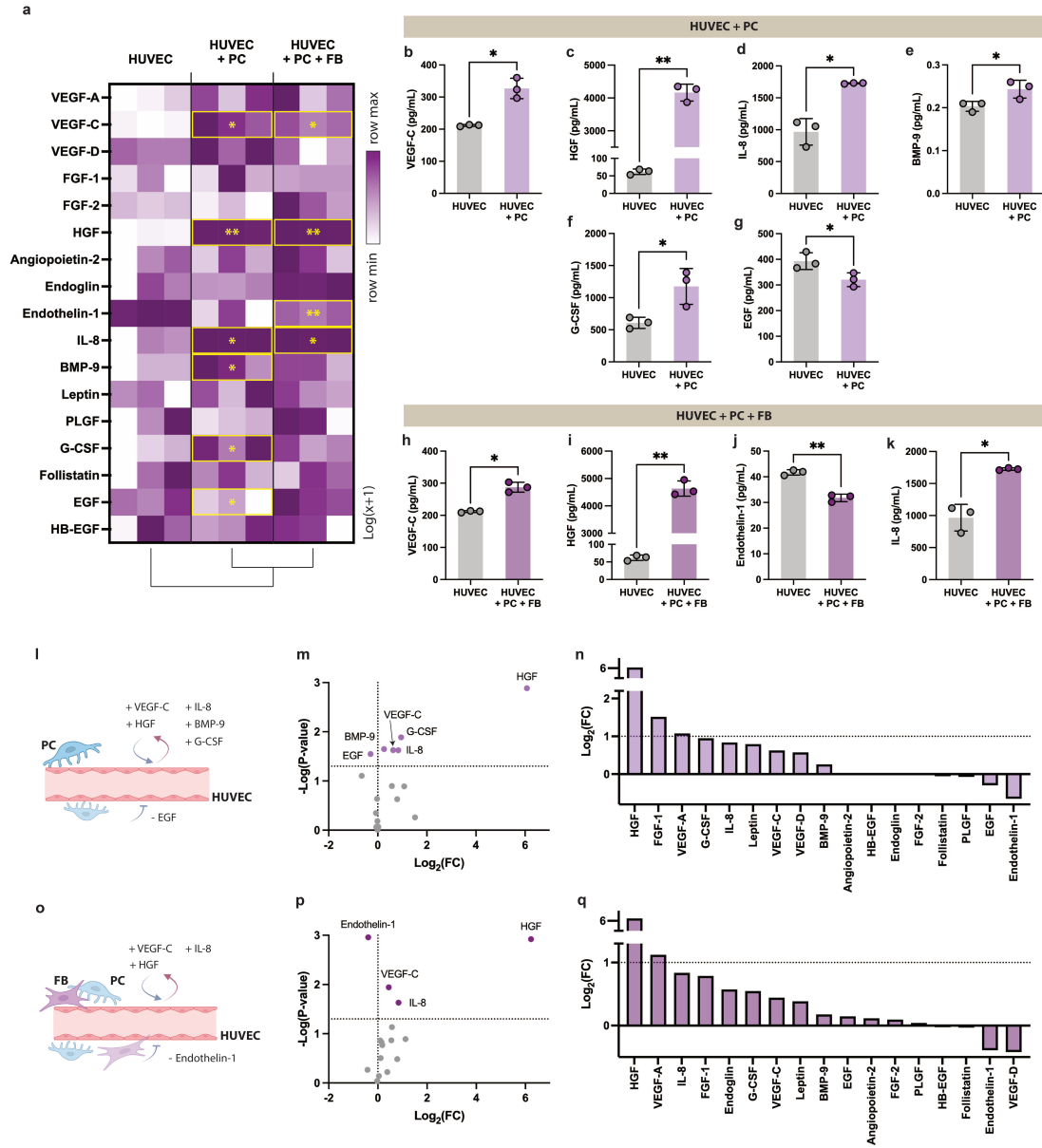


Figure 5.3: Cytokine analysis reveals the influence of stromal cells on vascular maturation. (continued)

Figure 5.3: (continued) (a) The heat map displays differential expression of human angiogenesis cytokines and growth factors in microvessels built with HUVECs alone, with HUVECs and PCs, and with HUVECs, PCs, and FBs on day 11. Supernatants were obtained from $n = 3$ independent tissue culture units. (b-g) Measurements of differential concentrations of cytokines between the group HUVECs alone and the group with HUVECs and PCs: (b) VEGF-C, * $P = 0.0235$; (c) HGF, ** $P = 0.0013$; (d) IL-8, * $P = 0.0237$; (e) BMP-9, * $P = 0.0224$; (f) G-CSF, * $P = 0.0129$; (g) EGF, * $P = 0.0283$. (h-k) Measurements of differential concentrations of cytokines between the group with HUVECs and the group with HUVECs, PCs, and FBs: (h) VEGF-C, * $P = 0.0114$; (i) HGF, ** $P = 0.0012$; (j) endothelin-1, ** $P = 0.0011$; (k) IL-8, * $P = 0.0234$. (l) Illustration of cytokines that were significantly modulated in the group with HUVECs and PCs compared to the group with HUVECs only, including VEGF-C, HGF, IL-8, BMP-9, G-CSF, and EGF. Created with BioRender.com. (m) A volcano plot of differentially expressed cytokines between the group HUVECs alone and the group of HUVECs and PCs, with the significantly upregulated and downregulated cytokines labeled ($P < 0.05$). (n) Ranking of expression of cytokines in the group of HUVECs and PCs from the most upregulated to the most downregulated compared to the HUVECs only. (o) Illustration of cytokines that were significantly modulated in the group with HUVECs, PCs, and FBs compared to the group with HUVECs only, including VEGF-C, HGF, endothelin-1, and IL-8. Created with BioRender.com. (p) A volcano plot of differentially expressed cytokines between the group HUVECs alone and the group of HUVECs, PCs, and FBs, with the significantly upregulated and downregulated cytokines labeled ($P < 0.05$). (q) Ranking of expression of cytokines in the group of HUVECs, PCs, and FBs from the most upregulated to the most downregulated compared to the HUVECs only.

5.3.3 Modeling pathophysiological microvessels with biological compounds

We were intrigued by the possibility of inducing multiple physiological states using the microvessels constructed on AngioPlate™. To validate this concept, we selected microvessels that were cultured with PCs and FBs and passed quality control ($P_{App} < 8 \times 10^{-6}$ cm/s for 65-85 kDa dextran and $P_{App} < 2.6 \times 10^{-5}$ cm/s for 4 kDa dextran)

on day 11 and subsequently administered biochemical compounds from day 14 to 17 to induce various disease states. Subsequently, we examined the corresponding dose-dependent vascular responses and the cytokines released (Figure 5.1(b)). In experimental studies, researchers frequently utilize concentrations of $\text{TNF}\alpha$ typically ranging from 0.01 to 0.1 $\mu\text{g}/\text{mL}$, and $\text{IFN}\gamma$ concentrations ranging from 0.001 to 0.01 $\mu\text{g}/\text{mL}$ to provoke vascular damage and induce inflammation [229, 230]. It has also been reported that a synergistic effect on inflammation was observed with the combination of $\text{TNF}\alpha$ and $\text{IFN}\gamma$ [231]. Thus, to induce inflammation in the vessels, we exposed them to varying doses of $\text{IFN}\gamma$ (1, 0.1, 0.01, 0.001, 0.0001, and 0 $\mu\text{g}/\text{mL}$) and $\text{TNF}\alpha$ at the same doses, both with and without 0.1 $\mu\text{g}/\text{mL}$ of $\text{IFN}\gamma$. Inflammation in the microvessels was assessed on day 17, 72 h after the initiation of treatment. Permeability tests were conducted for all groups, and confocal imaging was performed on the $\text{TNF}\alpha$ groups. After the IFN -gamma treatment, microvessels did not show significant changes in barrier function, except at the dose of 0.01 $\mu\text{g}/\text{mL}$ with 65-85 kDa dextran (Figure 5.4(a)). The cytokine profile related to the highest $\text{IFN}\gamma$ treatment revealed a 0.22-fold decrease in IL-8, a 5.41-fold increase in IL-1RA, and a 3.66-fold increase in MCP-1 compared to the vehicle group (Figure 5.4(n) and Supplementary Figure D.5(a-c)). Two of these factors, IL-8 and MCP-1, are known to increase vascular permeability [232, 233], while IL-1RA plays a protective role in maintaining vascular integrity [234]. Therefore, the minimal change observed in vascular permeability could potentially result from the combined effects of decreased IL-8 levels and increased IL-1Ra, which together counteract the impact of MCP-1. Additionally, other factors specific to this microenvironment may also contribute to the observed outcome.

The same test was conducted on the $\text{TNF}\alpha$ groups. In the $\text{TNF}\alpha$ groups without $\text{IFN}\gamma$, disruptions in vessel barrier function were determined to be significant at concentrations of 1, 0.1, and 0.01 $\mu\text{g}/\text{mL}$ with 65-85 kDa dextran, and at 1 and 0.01 $\mu\text{g}/\text{mL}$ with 4 kDa dextran (Figure 5.4(b)). The cytokine profile revealed a 6.01-fold change in IL-10, a 278.48-fold change in $\text{IFN}\gamma$, an 11.44-fold change in IL-13, and a 3.74-fold change in MCP-1 (Figure 5.4(n) and Supplementary Figure D.5(d-g)). Utilizing confocal imaging, damage to VE-cadherin was captured for all concentrations of the $\text{TNF}\alpha$ groups, and the level of damage is qualitatively proportional to the concentration of $\text{TNF}\alpha$, indicating the loss of the VE-cadherin is another major index of losing vascular barrier function (Figure 5.4(d)). In the $\text{TNF}\alpha$ groups with 0.1 $\mu\text{g}/\text{mL}$ of $\text{IFN}\gamma$, significant vascular disruptions were observed at 0.1 $\mu\text{g}/\text{mL}$ with 65-85 kDa dextran and at 1 and 0.1 $\mu\text{g}/\text{mL}$ with 4 kDa dextran (Figure 5.4(c)). Compared to the vehicle, four cytokines in this treatment group exhibited significant changes, including a 6.95-fold increase in IL-1 β , an 11.08-fold increase in IL-1RA, a 9.64-fold increase in IL-13, and a 3.65-fold increase in MCP-1 (Figure 5.4(n) and Supplementary Figure D.5(h-k)). Notably, compared to the $\text{TNF}\alpha$ -only group, both IL-1 β and IL-1RA levels are elevated, suggesting that the combination of $\text{TNF}\alpha$ and $\text{IFN}\gamma$ may have exerted a synergistic inflammatory effect on vessels, as previously reported [235].

Another compound, $\text{TGF}\beta$, has been demonstrated to promote fibrosis by stimulating the differentiation of fibroblasts into myofibroblasts [236], while also exerting a suppressive effect on immune responses [237]. Given the presence of fibroblasts in our setup, we tested various concentrations of $\text{TGF}\beta$ in the microvessels on AngioPlateTM to observe their impact on vascular functions. Additionally, a synergistic

effect of combining TGF β and IFN γ has been demonstrated, wherein they reciprocally suppress each other's activities [238]. Furthermore, it is important to note that ECGM2 contains heparin at a concentration of 22.5 $\mu\text{g}/\text{mL}$, which has been shown to bind to TGF β and alter its functions [239]. TGF β was added to microvessels at concentrations of 0.1, 0.01, 0.001, 0.0001, 0.00001, and 0 $\mu\text{g}/\text{mL}$ alone, with 0.1 $\mu\text{g}/\text{mL}$ IFN γ , and without heparin. In microvessels treated with TGF β alone in normal culture media, a significant increase in vascular permeability was observed for both 65-85 kDa and 4 kDa dextran at a concentration of 0.001 $\mu\text{g}/\text{mL}$ (Figure 5.4(e)) but not at other concentrations. Cytokine analysis revealed a 0.68-fold decrease in IL-8 and a 0.09-fold decrease in IL-12(p40) (Figure 5.4(n) and Supplementary Figure D.5(l-m)). For microvessels treated with both TGF β and IFN γ , changes in permeability for both dextran sizes were also observed at a concentration of 0.001 $\mu\text{g}/\text{mL}$. However, the microvessels became tighter instead of leakier (Figure 5.4(f)). The cytokine analysis revealed nine significant changes, including a 13.14-fold increase in IL-1 β , a 2.81-fold increase in IL-1RA, a 12.62-fold increase in IL-10, an 8.17-fold increase in IL-12(p70), a 10.97-fold increase in IL-4, a 1.93-fold increase in IL-5, an 11.44-fold increase in IL-13, and a 3.66-fold increase in MCP-1 (Figure 5.4(n) and Supplementary Figure D.5(n-u)). Among these cytokines, IL-1RA, IL-10, IL-13, and IL-4 are all known for their anti-inflammatory roles [234, 240, 241], while IL-1 β is pro-inflammatory and has been shown to increase vascular permeability [234]. The data suggest that anti-inflammatory TGF β and pro-inflammatory IFN γ had a synergistic impact through their reciprocal regulation [238, 242], as we observed numerous pro- and anti-inflammatory cytokine being upregulated, potentially by altering the TGF β /Smad signaling and JAK-STAT pathways [238, 243, 244]. The group treated

with TGF β in the absence of heparin displayed significant vascular disruptions at all concentrations except in the vehicle group (Figure 5.4(g)), accompanied by a 0.11-fold decrease in IL-6, a 0.26-fold decrease in IL-8, and a 0.53-fold decrease in MCP-1 (Figure 5.4(n) and Supplementary Figure D.5(v-x)). These results, along with those observed in other TGF β -treated groups, suggest that heparin-binding impedes TGF β 's impact on vascular [239]. We used the microvessels on AngioPlate™ to examine TGF β 's anti-inflammatory properties [238], as reflected in the cytokine profiles, as well as to mimic TGF β -induced disruptions in endothelial integrity [245, 246].

We then studied the thrombosis process using the microvessels on AngioPlate™ by increasing the level of Thrombin presented in the lumen. Notably, the presence of heparin can also hinder Thrombin's activity by binding to antithrombin III [247], which is produced by ECs. We prepared Thrombin concentrations of 1, 0.5, 0.1, and 0 U/mL with and without heparin in ECGM2. No significant change in vascular permeability was observed except at 1 U/mL without heparin for 65-85 kDa dextran, aligning with our expectation of thrombosis-induced barrier function disruption in the absence of heparin (Figure 5.4(h, i)).

We also applied Poly(I:C), a synthetic analog of double-stranded RNA [248], at concentrations of 10, 1, 0.1, 0.01, 0.001, and 0 μ g/mL to mimic viral infection in microvessels on AngioPlate™. At the highest dose, a disruption of the vascular barrier was observed with both 65 86 kDa dextran and 4 kDa dextran (Figure 5.4(j)), demonstrating our ability to capture the influence of viral infection on microvessels on AngioPlate™. Meanwhile, confocal imaging didn't show damages to VE-cadherin as severe as observed in the TNF α group (Figure 5.4(k)). The cytokine analysis also captured a 4.29-fold increase in MCP-1 (Figure 5.4(n) and Supplementary Figure

D.5(y)).

To study the impact of bacterial infection on vessels, we applied LPS at concentrations ranging from 10 $\mu\text{g}/\text{mL}$ to 0 $\mu\text{g}/\text{mL}$ [249]. However, no significant changes were observed in permeability, VE-cadherin expression, or cytokine analysis (Figure 5.4(l, m)).

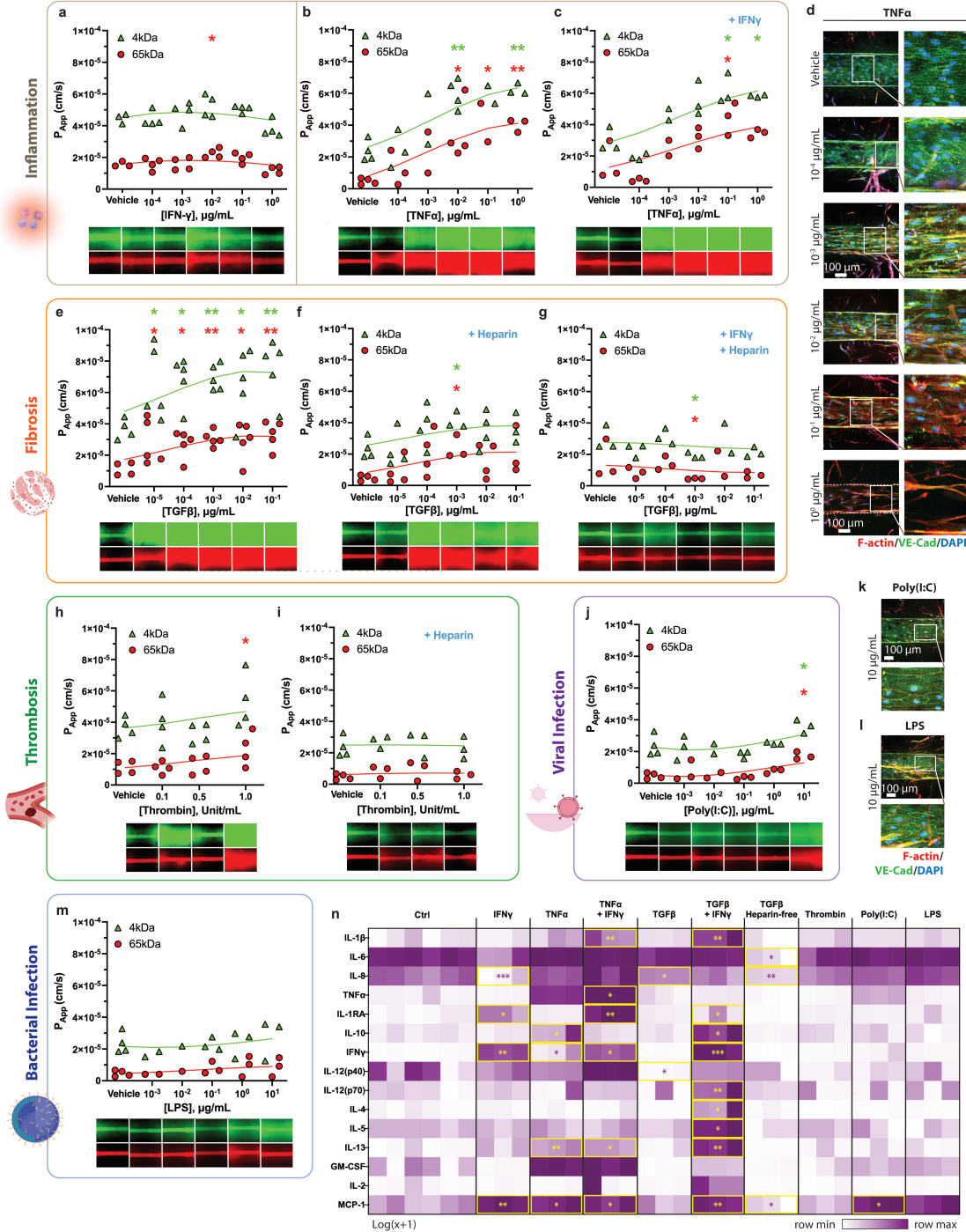


Figure 5.4: Development of microvessels that mimic pathological conditions using biological substances. (continued)

Figure 5.4: (continued) (a-c) Quantification and visualization of the dextran diffusion across multiple doses for (a) IFN γ : 65-85 kDa at 0.01 $\mu\text{g}/\text{mL}$, * P = 0.0365, n = 23 in total; (b) TNF α : 65-85 kDa at 0.01 $\mu\text{g}/\text{mL}$, * P = 0.0233, at 0.1 $\mu\text{g}/\text{mL}$, * P = 0.0191, at 1 $\mu\text{g}/\text{mL}$, ** P = 0.0069, 4 kDa at 0.01 $\mu\text{g}/\text{mL}$, ** P = 0.0062, at 1 $\mu\text{g}/\text{mL}$, ** P = 0.0078, n = 18 in total; (c) TNF α with IFN γ : 65-85 kDa at 0.1 $\mu\text{g}/\text{mL}$, * P = 0.0236, 4 kDa at 0.1 $\mu\text{g}/\text{mL}$, * P = 0.0433, at 1 $\mu\text{g}/\text{mL}$, * P = 0.0290, n = 17 in total. (d) Confocal imaging shows adherens junctions' deterioration due to the presence of TNF α . F-actin in the cytoskeleton, VE-cadherin of adherens junctions, and DAPI-labeled nuclei are shown. (e-j) Quantification and visualization of the dextran diffusion across multiple doses for (e) TGF β : 65-85 kDa at 0.001 $\mu\text{g}/\text{mL}$, * P = 0.0419, 4 kDa at 0.001 $\mu\text{g}/\text{mL}$, * P = 0.0410, n = 22 in total; (f) TGF β with IFN γ : 65-85 kDa at 0.001 $\mu\text{g}/\text{mL}$, * P = 0.0236, 4 kDa at 0.001 $\mu\text{g}/\text{mL}$, * P = 0.0475, n = 17 in total; (g) TGF β without heparin: 65-85 kDa at 0.00001 $\mu\text{g}/\text{mL}$, * P = 0.0180, at 0.0001 $\mu\text{g}/\text{mL}$, * P = 0.0212, at 0.001 $\mu\text{g}/\text{mL}$, ** P = 0.0066, at 0.01 $\mu\text{g}/\text{mL}$, * P = 0.0102, at 0.1 $\mu\text{g}/\text{mL}$, ** P = 0.0024, 4 kDa at 0.00001 $\mu\text{g}/\text{mL}$, * P = 0.0214, at 0.0001 $\mu\text{g}/\text{mL}$, * P = 0.0111, at 0.001 $\mu\text{g}/\text{mL}$, ** P = 0.0090, at 0.01 $\mu\text{g}/\text{mL}$, * P = 0.0177, at 0.1 $\mu\text{g}/\text{mL}$, ** P = 0.0028, n = 29 in total; (h) Thrombin, n = 13 in total; (i) Thrombin without heparin: 65-85 kDa at 1 U/mL, * P = 0.0318, n = 16 in total; (j) Poly(I:C): 65-85 kDa at 10 $\mu\text{g}/\text{mL}$, * P = 0.0119, 4 kDa at 10 $\mu\text{g}/\text{mL}$, * P = 0.0390, n = 18 in total; (k, l) Confocal imaging demonstrates intact adherens junctions under the influence of Poly(I:C) (k) and LPS (l). F-actin in the cytoskeleton, VE-cadherin of adherens junctions, and DAPI-labeled nuclei are shown. (m) LPS, n = 16 in total. (n) The heat map displays differential expressions of human inflammatory cytokines in microvessels both untreated and under the influence of various conditions. These conditions include IFN γ , TNF α , TNF α with IFN γ , TGF β , TGF β with IFN γ , TGF β without heparin, Thrombin, Poly(I:C), and LPS, from day 14 to day 17. Supernatants were obtained from the untreated condition (n =6) and from each treated condition (n =3) daily from day 15 to day 17. Supernatants from each culture collected were pooled.

5.3.4 Screening chemotherapy drugs and demonstrating vascular dose-dependent responses

We tested ten chemotherapy drugs on the microvessels on AngioPlate™ at five concentrations ranging from 1 to 0 μM . Six of these drugs have concentrations bracketing

the human plasma C_{max} , which is related to their active components (Figure 5.5(b)). Conventionally, drugs are active in their unbound form [250]. Since all drugs were dissolved in DMSO at a concentration of 0.01 M, the highest concentration was prepared to achieve a final concentration of DMSO at 0.01% to minimize any potential impact of DMSO on the vessels. The six drugs with concentrations bracketing their C_{max} in the testing concentrations are bortezomib, vincristine, axitinib, imatinib, and sorafenib. The four drugs with C_{max} higher than the testing concentrations include bleomycin, paclitaxel, amifostine, and mitomycin. The drugs were grouped into two categories: vasculotoxic and non-vasculotoxic, based on previous trials [251–269]. After a 72-h treatment period, drugs that increased vascular permeability while exceeding the quality control threshold, with $P_{App} < 1 \times 10^{-5}$ cm/s for 65-85 kDa dextran and $P_{App} < 3.5 \times 10^{-5}$ cm/s for 4 kDa dextran, are deemed toxic to vascular, and vice versa.

Among these ten drugs, it has been shown that bortezomib can induce apoptosis in endothelial cells [251, 252]; vincristine can damage vascular functions by elevating TNF α levels [253]; paclitaxel is toxic to ECs due to its impairment of cellular microtubule functions [254, 255]; and axitinib can cause vascular damage through its anti-VEGF properties [256, 257]. We predicted that these four drugs could damage the microvessels on AngioPlate™. On the other hand, it has been reported that bleomycin can damage DNA and halt ECs growth, with its impacts on vascular damage demonstrated through fibrosis or thrombosis processes [258–260]. Mitomycin can cross-link DNA and induce cytotoxicity, and it has been associated with inducing pulmonary veno-occlusive disease, a condition related to systematic atherosclerosis [261, 262]. Both thrombosis and fibrosis are significant events in atherosclerosis. Sorafenib, a

tyrosine kinase inhibitor, also has been shown to have vascular complications including hypertension and atherosclerosis [255, 263]. Since in our data presented above, we showed that the heparin in ECGM could hinder both fibrosis and thrombosis processes (Figure 5.4(e, g)), we anticipated attenuated damage on ECs due to these three drugs. Amifostine, a cytoprotective agent, has been shown to cause hypotension and reduce the vascular permeability [264, 265]. Imatinib, another tyrosine kinase inhibitor, has been shown to have anti-angiogenic properties by mainly targeting PCs and not ECs [266, 267]. Lastly, tamoxifen, a selective estrogen receptor modulator, has been shown to suppress angiogenesis and accelerate endothelial healing [268, 269]. Thus, for these three drugs, we expected them to have minimal impact on the microvessels on AngioPlate™.

The permeability test yielded an 100% sensitivity, in detecting vincristine, bortezomib, paclitaxel, and axitinib's potential to disrupt the vascular barrier and 100% specificity in predicting that bleomycin, mitomycin, sorafenib, amifostine, imatinib, and tamoxifen would not significantly damage the vascular barrier significantly, matching our expectations based on the literature (Figure 5.5(a-k)).

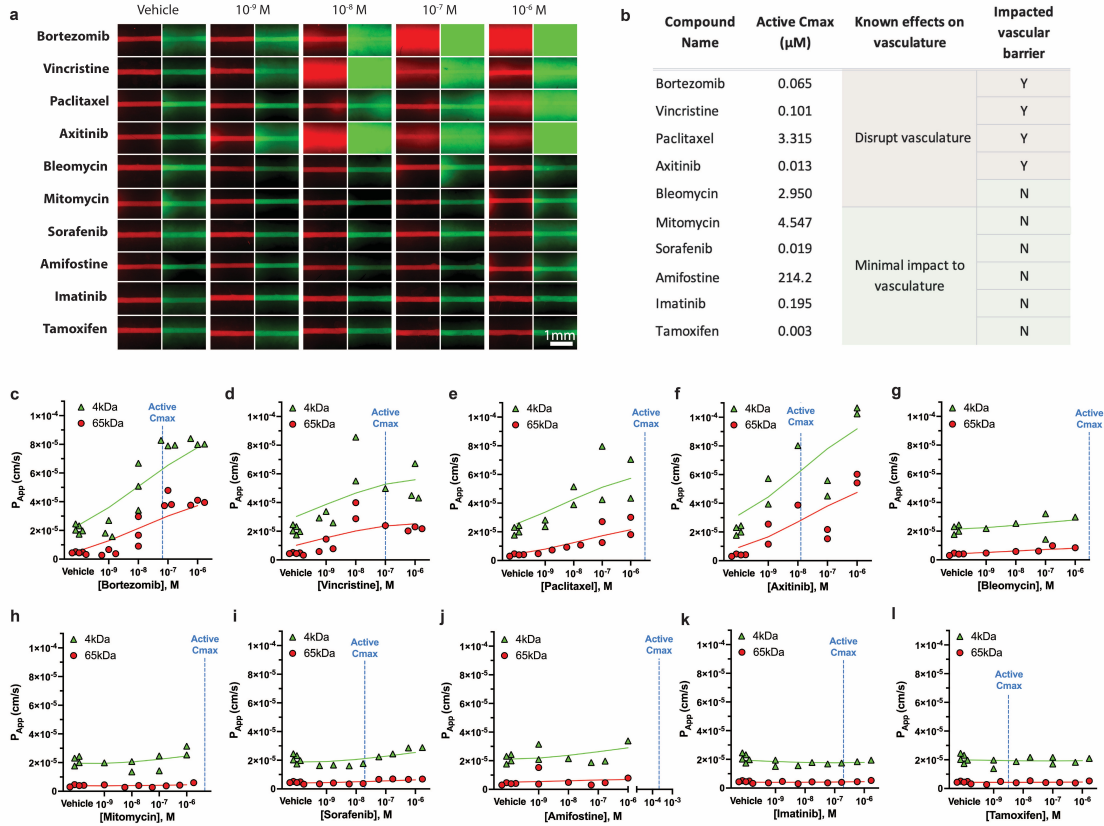


Figure 5.5: Capturing dose-dependent responses of chemotherapy drugs using microvessels assay on AngioPlate™. (a) Visualization of the dextran diffusion across various doses for bortezomib, vincristine, paclitaxel, axitinib, bleomycin, mitomycin, sorafenib, amifostine, imatinib, tamoxifen. (b) Categorization of the chemotherapy drugs tested based on their known effects on microvessels and captured impacts. (c-l) Quantification of the transportation rate for microvessels under the influence of (c) bortezomib, n = 17 in total; (d) vincristine, n = 14 in total; (e) paclitaxel, n = 12 in total; (f) axitinib, n = 11 in total; (g) bleomycin, n = 9 in total; (h) mitomycin, n = 11 in total; (i) sorafenib, n = 13 in total; (j) amifostine, n = 10 in total; (k) imatinib, n = 13 in total; (l) tamoxifen, n = 13 in total. The active C_{max} concentration for each drug is labeled.

5.3.5 Organ-specific microvessels reveal the distinctive patterns in cytokines and recovery

We then switch the stromal cells and ECs to organ-specific cell sources to develop organ-specific microvessels (Supplementary Figure D.6). Control vessels, built with HUVECs, PCs, and FBs, alongside liver microvessels built with liver ECs and liver FBs, and lung microvessels built with lung ECs and lung FBs, were examined for quality using the same permeability medium. The permeability results showed similar levels of permeability between the control and the liver vessels, while the lung microvessels formed tighter barrier functions. Particularly, in the organ-specific microvessels built on AngioPlate™, with 65-85 kDa dextran, we observed that the lung microvessels permitted 0.65-fold of dextran transported across the vascular wall compared to the control microvessels and the liver microvessels (Figure 5.6(b)). While for 4 kDa dextran, the lung microvessels permitted 0.78-fold of dextran to diffuse out of the vascular wall compared to the control vessels, and 0.74-fold compared to the liver microvessels (Figure 5.6(c)). This finding matched our expectation based on the literature, as the lung ECs typically form continuous endothelium to prevent large molecules and cells from passing through the vascular walls while permitting gases to diffuse freely [270], and liver sinusoidal ECs form fenestrated endothelium to allow for rapid exchange of substances between the blood and liver tissue [271]. Confocal imaging also indicated a lower level of VE-cadherin expression in the liver microvessels compared to the lung vessels. This implies that adherens junctions differ in the liver microvessels compared to the control microvessels and the lung vessels, which agrees with findings from previous studies (Figure 5.6(a)) [272, 273].

Next, we conducted cytokine analyses to further explore the cytokine factors contributing to the variation in barrier function. We generated a heat map plotting all cytokine data points collected on day 7, and hierarchical clustering analysis demonstrated that the liver microvessels and the lung microvessels exhibited greater similarity to each other when compared to the HUVECs group (Figure 5.6(g)). Comparing to the control group, the liver microvessels exhibited significant differences in seven cytokines: upregulation of VEGF-A ($3.53 \text{ Log}_2(\text{FC})$), IL-8 ($1.05 \text{ Log}_2(\text{FC})$), EGF ($1.00 \text{ Log}_2(\text{FC})$), and leptin ($0.66 \text{ Log}_2(\text{FC})$), and downregulation of HGF ($-2.91 \text{ Log}_2(\text{FC})$), PLGF ($-1.68 \text{ Log}_2(\text{FC})$), and VEGF-C ($-1.22 \text{ Log}_2(\text{FC})$) (Figure 5.6(h, l-r)). The lung vessels, on the other hand, exhibited only one significant difference: upregulation of leptin ($0.57 \text{ Log}_2(\text{FC})$) (Figure 5.6(j, s)). In the liver group, there were four other cytokines among the top-7 downregulated, but they did not pass the significance test. These included follistatin ($-2.91 \text{ Log}_2(\text{FC})$), endoglin ($-2.43 \text{ Log}_2(\text{FC})$), angiopoietin-2 ($-2.28 \text{ Log}_2(\text{FC})$), and G-CSF ($-0.99 \text{ Log}_2(\text{FC})$) (Figure 5.6(i)). In the lung group, besides leptin, there were two other cytokines among the top-3 upregulated factors: VEGF-A ($3.28 \text{ Log}_2(\text{FC})$) and VEGF-D ($1.21 \text{ Log}_2(\text{FC})$). Additionally, the top-5 downregulated cytokines in the lung group were G-CSF ($-2.02 \text{ Log}_2(\text{FC})$), follistatin ($-1.91 \text{ Log}_2(\text{FC})$), angiopoietin-2 ($-1.44 \text{ Log}_2(\text{FC})$), PLGF ($-1.17 \text{ Log}_2(\text{FC})$), endoglin ($-0.70 \text{ Log}_2(\text{FC})$), (Figure 5.6(k)). In the liver group, the primary downregulated factor, HGF, is primarily secreted by FBs and ECs (Figure 5.6(i)) [274–276], and it has been shown to possess protective properties for endothelial cells [277–279]. Conversely, IL-8, a proinflammatory and proangiogenic factor that can elevate endothelial permeability [280–282], emerged as the top-2 upregulated factor in the liver group (Figure 5.6(i)). These alterations in HGF and IL-8 levels relative to the control

group could potentially contribute to the differences observed in adherens junctions within the liver group (Figure 5.6(a)). In the lung groups, the contrasting regulations of HGF and IL-8 observed in the liver group were absent. This uniformity, characterized by higher levels of HGF and lower levels of IL-8 compared to the liver group, may contribute to the tighter barrier function observed in the lung vessels.

We then utilized these organ-specific microvessels and the control microvessels to investigate the impact of TGF β and the subsequent recovery processes after the removal of TGF β . This study aimed to explore the potential induction of organ-specific fibrosis [283, 284, 236, 237] and to better understand how each organ-specific vessel group responds to the TGF β signal. Following a quality control examination, TGF β at a concentration of 0.1 $\mu\text{g}/\text{mL}$ was added to the treatment group from day 13 to day 16, while the vehicle group received 0 $\mu\text{g}/\text{mL}$. Permeability tests were conducted for both groups on day 16 and the results were recorded. Subsequently, the TGF β treated group was cultured for an additional four days after the removal of TGF β to allow the microvessels to recover. On day 16, the most significant differences in permeability were observed in the lung vessels, showing a 3.23-fold increase with 65-85 kDa dextran, and a 2.70-fold increase with 4 kDa dextran. The second-largest changes due to TGF β treatment were observed in the control group, with a 2.95-fold increase in permeability with 65-85 kDa dextran, and a 1.98-fold increase with 4 kDa dextran. Lastly, a 1.54-fold increase in permeability with 65-85 kDa dextran, and a 1.75-fold increase with 4 kDa dextran were observed in the liver group. This indicates that the lung microvessels were the most susceptible to TGF β , while the liver microvessels were the least sensitive in the AngioPlateTM microenvironment (Figure 5.6(e, f)). The microvessels also showed distinctive efficiency in recovery. The highest recovery was

observed in the lung group, with 64.3% recovery with 65-85 kDa dextran and 42.7% with 4 kDa dextran. The control group showed 59.5% recovery with 65-85 kDa dextran and 26.2% with 4 kDa dextran. Meanwhile, the liver group demonstrated 51.2% recovery with 65-85 kDa dextran and 19.2% recovery with 4 kDa dextran (Figure 5.6(e, f)). In conclusion, our findings suggest potential organ-to-organ differences in vascular responses to the addition and removal of the TGF β signal were captured on AngioPlate™.

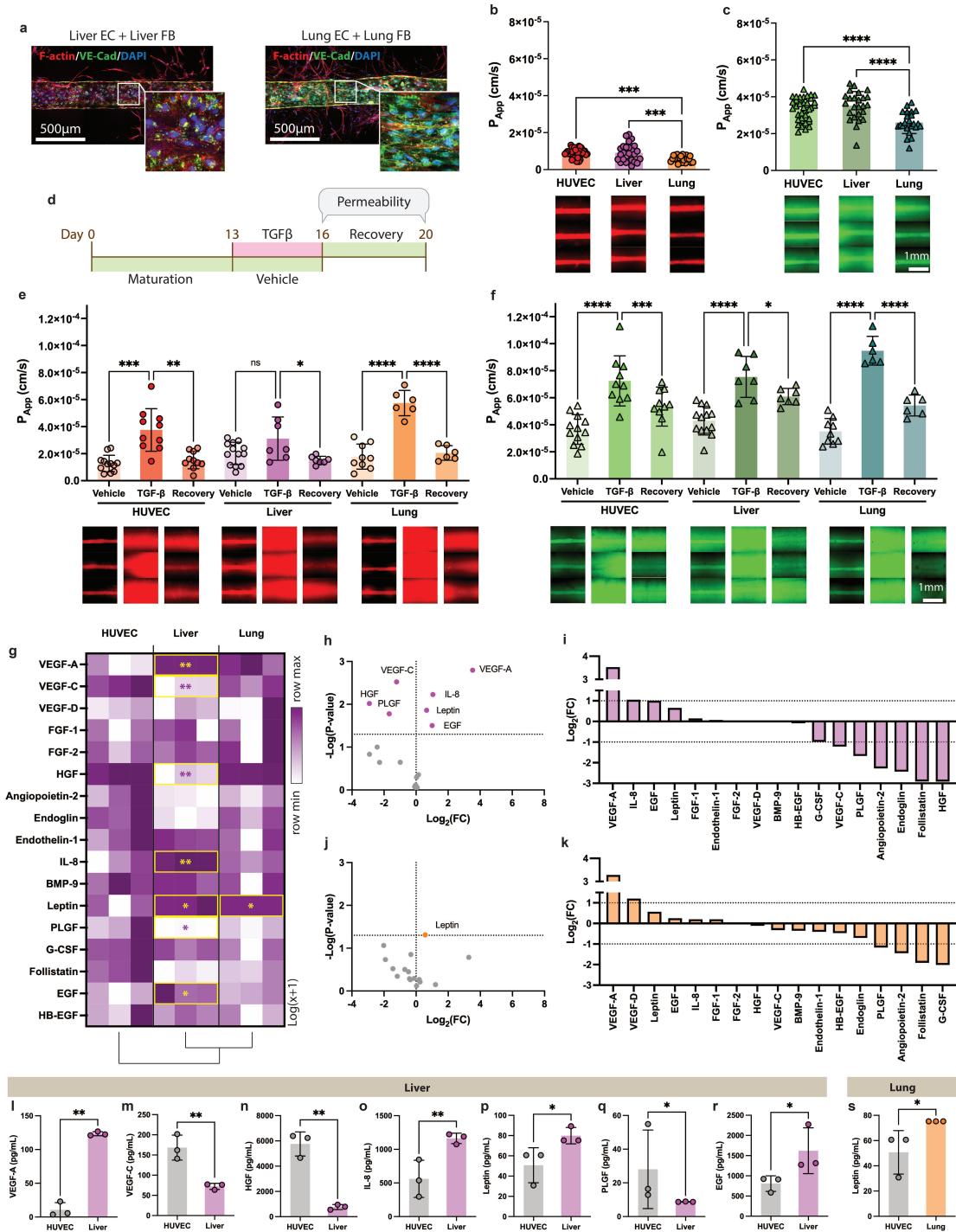


Figure 5.6: Building organ-specific microvessels and modeling organ-specific vascular responses. (continued)

Figure 5.6: (continued) (a) Confocal images featuring organ-specific stromal cells (F-actin) embedded in the hydrogel, which co-localize with the microvessels built using organ-specific endothelial cells (VE-cadherin and F-actin), along with DAPI-stained nuclei. (b, c) Quantification and visualization of TRITC 65-85 kDa (b) and FITC 4 kDa (c) dextran permeability assays applied to microvessels built with HUVECs, liver ECs, and lung ECs. The transportation rate of diffused dextran on day 11 is compared among three culture conditions: HUVECs with PCs and FBs ($n = 38$), liver ECs with liver FBs ($n = 25$), and lung ECs with lung FBs (in comparison to the HUVEC vessels: 65-85 kDa, *** $P = 0.0002$, 4 kDa, **** $P < 0.0001$; in comparison to the liver vessels: 65-85 kDa, *** $P = 0.0008$, 4 kDa, **** $P < 0.0001$, $n = 23$). Fluorescent images of diffused dextran after 1 h perfusion of the permeability medium, $n = 3$ for each culture condition. (d) Timeline for inducing pathophysiology by introducing TGF β and allowing the microvessels to recover from the diseased state. (e, f) Quantification and visualization of the barrier function changes in microvessels after TGF β treatment and recovery, with regard to TRITC 65-85 kDa (e) and FITC 4 kDa (f) dextran. Three treatment conditions are displayed for each vessel type, including HUVECs-vehicle ($n = 13$), HUVECs-TGF β (in comparison to HUVECs-vehicle: 65-85 kDa, *** $P = 0.0006$, 4 kDa, **** $P < 0.0001$, $n = 7$), HUVECs-recovery (in comparison to HUVECs-TGF β : 65-85 kDa, ** $P = 0.0014$, 4 kDa, *** $P = 0.0010$, $n = 7$), liver ECs-vehicle ($n = 9$), liver ECs-TGF β (in comparison to liver ECs-vehicle: 4 kDa, **** $P < 0.0001$, $n = 6$), liver ECs -recovery (in comparison to liver ECs-TGF β : 65-85 kDa, * $P = 0.0391$, 4 kDa, * $P = 0.0314$, $n = 6$), lung ECs-vehicle ($n = 12$), lung ECs -TGF β (in comparison to lung ECs-vehicle: 65-85 kDa, **** $P < 0.0001$, 4 kDa, **** $P < 0.0001$, $n = 10$), and lung ECs -recovery (in comparison to lung ECs-TGF β : 65-85 kDa, **** $P < 0.0001$, 4 kDa, **** $P < 0.0001$, $n = 10$). (g) The heat map displays differential expression of human angiogenesis cytokines and growth factors in microvessels built with HUVECs, PCs, and FBs, with liver ECs and liver FBs, and with lung ECs and lung FBs on day 11. Supernatants were obtained from $n = 3$ independent tissue culture units. (h) A volcano plot of differentially expressed cytokines between the HUVEC microvessels and the liver vessels, with the significantly upregulated and downregulated cytokines labeled ($P < 0.05$). (i) Ranking of expression of cytokines in the liver microvessels from the most upregulated to the most downregulated compared to the HUVEC vessels. (j) A volcano plot of differentially expressed cytokines between the HUVEC microvessels and the lung vessels, with the significantly upregulated and downregulated cytokines labeled ($P < 0.05$). (k) Ranking of expression of cytokines in the lung microvessels from the most upregulated to the most downregulated compared to the HUVEC vessels. (l-r) Measurements of differential concentrations of cytokines between the HUVEC microvessels and the liver vessels: (continued)

Figure 5.6: (continued) (l) VEGF-A, ** P = 0.0016; (m) VEGF-C, ** P = 0.0030; (n) HGF, ** P = 0.0096; (o) IL-8, ** P = 0.0059; (p) leptin, * P = 0.0138; (q) PLGF, * P = 0.0166; (r) EGF, * P = 0.0313. (s) The measurement of differential concentrations of leptin between the HUVEC microvessels and the lung vessels, * P = 0.0489.

5.4 Discussion

Vasculatures play crucial roles in cancer development and also interfere with drug delivery and metabolism. As researchers began exploring the use of organs-on-chips to improve the efficacy of drug screening, the need for sophisticated vascular models for high-throughput compound screening and vascular studies has become apparent [285]. The AngioPlate™, a 384-well device designed for building organs-on-a-chip, provides a platform for designing and studying vascular biology under physiologically relevant conditions. Due to its customized nature, which is based on a conventional 384-well design, this platform can be easily integrated with existing research tools for high-throughput analyses. Furthermore, we have demonstrated that the AngioPlate™ can be coupled with a robotic handling system for tissue preparation, improving both efficiency and consistency. This integration significantly enhances the platform's capability to streamline studies. In this study, a total of 670 microvessels were employed to investigate the impact of stromal cells on vascular maturation, compound screening, and the development of organ-specific vessels.

Our findings provide compelling evidence that co-culturing ECs with stromal cells such as PCs and FBs significantly enhances the maturity and functionality of microvessels built on the AngioPlate™. The integration of PCs and FBs with HUVECs

has been supported by prior studies indicating a synergistic effect on vascular maturation and stability [212, 201, 194, 211]. In our study, the strategic selection of stromal cell concentration and ratio—0.1 million stromal cells per mL and a 1:1 ratio of PCs to FBs—optimized the cellular interactions within the hydrogel matrix. This configuration not only supported endothelial cell health but also significantly enhanced endothelial functionality. This was evidenced by improved barrier function, as demonstrated with both 65-85 kDa and 4 kDa dextrans. Additionally, the observed improvement was characterized by an enhanced expression of VE-cadherin. The use of advanced imaging techniques such as confocal microscopy and transmission electron microscopy (TEM) revealed that the proximity between stromal cells and endothelial cells in our models was less than 1 μm . This close proximity is critical for effective cell-cell communication, which is essential for the proper formation and function of the vessels [202, 203].

The cytokine profiling conducted with the AngioPlate™ system provides valuable insights into the molecular dynamics governing vascular maturation in the presence of stromal cells. These findings underscore the complex interplay between ECs and stromal cells, highlighting the critical role of the microenvironment in vascular biology. Notably, HGF showed a substantial increase in both HUVECs with PCs and HUVECs with PCs and FBs groups, which aligns with previous *in vivo* studies that demonstrated HGF's protective effects against induced hyperpermeability [277, 286]. Although HGF is known for its angiogenic and protective roles in vascular systems, it has also been reported to increase vascular permeability *in vitro* [287]. This discrepancy in vascular responses to HGF underscores the nuanced role of cytokines

and emphasizes the importance of accurately mimicking the physiological microenvironment *in vitro*. Interestingly, endothelin-1, known for its vasoconstrictive and fibrotic effects [288–290], was consistently downregulated across tri-culture conditions involving HUVECs, PCs, and FBs. This suggests a possible protective role of the stromal cell interaction against potential endothelial dysfunction and fibrosis induced by endothelin-1 [291], likely contributing to improved vascular function and stability. The reduction in endothelin-1 levels, alongside the increase in pro-angiogenic factors like HGF, suggests a shift towards a more angiogenic and less fibrotic vascular microenvironment. Other notable cytokines that were upregulated in the co-culture and tri-culture groups include VEGF-C, IL-8, BMP-9, and G-CSF. These molecules play diverse roles in vascular health, from promoting angiogenesis to regulating vascular permeability [292, 293, 232, 294–296]. The variation in the expression of these cytokines across different tissue culture setups highlights the tailored microenvironment that these cellular interactions create.

Our study utilized the AngioPlate™ system to explore the modulation of vascular behavior under different pathological states through targeted biochemical treatments. The introduction of inflammatory cytokines $\text{TNF}\alpha$ and $\text{IFN}\gamma$, either individually or in combination, allowed us to observe their synergistic effects on vascular integrity and cytokine expression. Particularly, the combination of $\text{TNF}\alpha$ and $\text{IFN}\gamma$ revealed enhanced inflammatory responses, with significant increases in $\text{IL-1}\beta$ and IL-1RA compared to groups where each compound was introduced individually. This suggests a robust inflammatory reaction likely contributing to the observed changes in permeability, consistent with related findings [297–299, 234]. Notably, a higher ratio of $\text{IL-1}\beta$

to IL-1RA, an anti-inflammatory antagonist [300], may exacerbate vascular disruption [234]. Although the ratio of IL-1 β to IL-1RA was markedly higher at 36.20 in the TNF α group compared to 9.74 in the TNF α and IFN γ group, the TNF α group also exhibited a more significant increase in IL-10, another anti-inflammatory factor [301]. This complex balance between multiple inflammatory factors could contribute to similarly disrupted barrier functions observed in both treatment groups [231]. Conversely, IFN γ alone did not induce severe endothelial dysfunction, as indicated by significantly decreased levels of IL-8 [232], elevated levels of the anti-inflammatory factor IL-1RA [300] and the monocyte attractant MCP-1 [302]. Further investigations into the effects of TGF β , including alone, in combination with IFN γ , and alone without heparin in the media, showcased its dual role in promoting fibrosis and influencing inflammation [303]. The administration of TGF β alone resulted in slightly increased vascular permeability. This specific observation points to TGF β 's capability to alter vascular barrier properties. The cytokine profile revealed significant decreases in IL-8 and IL-12(p40), both of which are commonly known to exert a pro-fibrotic effect on tissue [304, 305]. However, researchers have also shown the depletion of IL-12(p40) could induce fibrosis [306], which supports the importance of building physiologically relevant models for recapitulating the complexity of pathways. Interestingly, when TGF β was combined with IFN γ , the effects on vascular permeability were reversed, leading to tighter microvessels at the same concentration where TGF β alone increased permeability. This paradoxical outcome was further elucidated by cytokine profiling, which showed significant increases in both pro- and anti-inflammatory cytokines, including IL-1 β , IL-1RA, IL-10, and IL-13. In this context, IL-10 and IL-13, known to

suppress pro-inflammatory cytokines such as $\text{TNF}\alpha$ [240], suggest that the upregulation of these anti-inflammatory cytokines may counterbalance the pro-inflammatory effects in the $\text{TGF}\beta$ and $\text{IFN}\gamma$ group, leading to an overall tightening of the vascular barrier. The presence of heparin in the culture medium introduced another layer of complexity. Heparin, known to bind $\text{TGF}\beta$ [239], seemed to modulate its effects on the vessels. In setups where $\text{TGF}\beta$ was administered without heparin, significant vascular disruptions were noted at all concentrations except in the vehicle control. This suggests that heparin may mitigate some of the more damaging effects of $\text{TGF}\beta$ on vascular integrity, possibly by preventing $\text{TGF}\beta$ from fully engaging its receptors or by altering its signaling pathway, i.e. $\text{TGF}\beta/\text{Smad}$ [307, 245]. However, the cytokine profiling from these experiments presented an intriguing result: despite the increased vascular leakiness, there was a marked decrease in the levels of key inflammatory cytokines such as IL-6, IL-8, and MCP-1. Given that $\text{TGF}\beta$ is known for its potent immunosuppressive effects [308], it appears capable of suppressing the production of these inflammatory cytokines within the specific microenvironment of the AngioPlate™. This occurs even as it induces systemic changes that lead to increased permeability. These findings suggest that $\text{TGF}\beta$'s role in vascular dynamics is multifaceted, involving complex interactions that influence both barrier integrity and inflammatory responses. Employing a physiological vascular model could further elucidate how $\text{TGF}\beta$ regulates these processes, enhancing our understanding of its dual role in inflammatory and fibrotic pathologies. By integrating Thrombin, the system effectively mimicked coagulation scenarios, revealing that in the absence of heparin, [247], the highest dose of Thrombin applied significantly compromised vascular integrity, critical for studying thrombosis-related permeability changes [309].

Meanwhile, the application of Poly(I:C) at various concentrations effectively replicated the impact of viral infections on vascular barriers [248], albeit with notably less damage to VE-cadherin compared to TNF α -induced changes. However, the response to LPS treatments, intended to simulate bacterial infections [] did not yield changes in vascular permeability or cytokine expression, indicating a tolerance to this treatment by the microvessels on AngioPlate™. Given that LPS can induce either an acute or a prolonged chronic effect on vascular permeability [249, 310], our results suggest that different treatment plans might be necessary. For instance, a shorter exposure time could be used to study LPS's acute effect, while a longer treatment duration may be required to observe its chronic effect. The data demonstrate that the microvessels on AngioPlate™ can be tailored to model a diverse array of vascular responses, establishing it as a versatile tool for conducting in-depth studies of vascular dynamics across various pathological conditions.

In a comprehensive evaluation using the AngioPlate™ system, ten chemotherapy drugs were tested at various dilution levels to assess their impact on vascular integrity. The study delineated drugs into vasculotoxic and non-vasculotoxic categories based on their effects on vascular permeability. Drugs such as bortezomib [251, 252], vincristine [253], paclitaxel [254, 255], and axitinib [256, 257] demonstrated significant vascular toxicity, aligning with their known cellular mechanisms such as apoptosis induction in endothelial cells and impairment of cellular microtubule functions. Conversely, drugs like bleomycin [258–260], mitomycin [261, 262], and sorafenib [255, 263], despite their association with vascular complications in systemic diseases, showed no significant endothelial damage likely due to the modulatory effects of heparin present in the culture medium [239, 247]. Similarly, cytoprotective and anti-angiogenic agents

such as amifostine [264, 265] and imatinib [266, 267] respectively showed minimal vascular impact. This precision in modeling drug effects underscores the AngioPlate™ system’s capability to accurately simulate and predict vascular responses to pharmacological agents, offering a potent tool for drug screening and vascular research.

We developed organ-specific microvessels on AngioPlate™ by switching the ECs and stromal cells to organ-specific sources, yielding insightful differences in vascular behavior. Control microvessels composed of HUVECs, PCs, and FBs were compared with liver and lung microvessels constructed from liver and lung-specific ECs and FBs respectively. The lung microvessels exhibited notably tighter barrier functions than both the control and liver vessels, consistent with the known physiological traits of lung ECs, which form continuous endothelium crucial for selective permeability [270]. This result was further quantified by reduced permeability in lung microvessels for both 65-85 kDa and 4 kDa dextrans. Conversely, liver microvessels showed similar permeability levels to control vessels, aligning with the fenestrated nature of liver sinusoidal ECs that facilitate rapid substance exchange [271]. Cytokine profiling was conducted to elucidate the differential responses in organ-specific vascular models using the AngioPlate™ system. Heat map and hierarchical clustering analysis revealed that liver and lung microvessels exhibit more similar cytokine profiles to each other than to the control group, suggesting distinct organ-specific inflammatory and growth environments. In particular, liver microvessels displayed significant cytokine modulation, with elevations in pro-angiogenic factors like IL-8 [280–282]—known to enhance vascular permeability—and a notable reduction in HGF [277–279], a protective factor against endothelial damage. These changes may explain the altered barrier properties and the distinct pattern of the liver vessels’ adherens junctions

compared to the control. Conversely, lung microvessels demonstrated a tightened barrier function, primarily characterized by relatively higher levels of HGF and lower levels of IL-8 compared to the liver group. Furthermore, when examined with TGF-beta to develop an organ-specific fibrosis model, these microvessels displayed distinct patterns in response to and recovery from the TGF-beta treatment. These findings validate the AngioPlate™ platform's capability to model organ-specific vascular characteristics, enhancing our understanding of organ-specific vascular dynamics and their implications in disease contexts.

5.5 Conclusions

In this comprehensive study utilizing the AngioPlate™ platform, we have effectively demonstrated the platform's versatility in constructing high-throughput microvessel arrays, assessing the impact of various pharmacological agents, and simulating physiological and pathological stimuli through detailed cytokine analyses and permeability studies. The integration of different stromal cells to build customized vascular models has allowed us to closely mimic the native vascular environments of different organs, as reflected in the distinct cytokine profiles and barrier functions observed in liver and lung vessels. The cytokine analysis has been instrumental in elucidating the underlying mechanisms contributing to the variation in barrier function across these models. For instance, the contrasting levels of HGF and IL-8 in liver and lung microvessels provided insights into the molecular basis of their differing vascular properties. Additionally, the application of compounds such as $\text{TNF}\alpha$, $\text{IFN}\gamma$, $\text{TGF}\beta$, and thrombin in our studies not only validated the system's capability to model disease

states but also highlighted how various cytokines modulate vascular responses to inflammation, fibrosis, and thrombosis. Drug screening on the AngioPlate™ has further emphasized its applicability in pharmacological research, with precise categorization of chemotherapy drugs based on their vasculotoxic potential. This segment of the study underlines the platform’s effectiveness in predicting the vascular side effects of drugs, thereby offering a valuable tool for preclinical drug development. Overall, the high-throughput vessel arrays on AngioPlate™ have been established as a helpful tool for multifaceted vascular research. This system’s capacity to accurately simulate and analyze various vascular conditions through mature vessel arrays and detailed cytokine profiling provides profound insights into vascular biology and disease. These capabilities not only pave the way for targeted therapeutic interventions but also enhance drug safety evaluations.

Competing Interests

A PCT application on the technology has been filed by SynoBiotech, Inc. B.Z. holds equity in the company.

Acknowledgments

D.S.Y.L. was supported by the National Sciences and Engineering Research Council of Canada (NSERC, CGS-D) and B.Z. received funding from the Canadian Institute of Health Research (CIHR, PJT-166052). We thank Scott Myhal for assisting with the NIMBUS robotic handling system, Marcia Reid for processing TEM samples, and Justin Bernar for machining. Schematics were created with BioRender.com. The authors acknowledge the assistance of OpenAI’s ChatGPT for draft preparation. This

research utilized the GPT-4 model, which was accessed on April 15, 2024.

Chapter 6

Conclusions and Recommendations for Future Work

The development and application of organ-on-a-chip technology, particularly focusing on vascular interfaces and networks, have underscored its transformative potential in revolutionizing drug development and disease modeling. This thesis systematically explores the integration of advanced microfabrication, tissue engineering, and bioprinting technologies to create dynamic, physiologically relevant vascular models that better mimic human tissue and organ functions.

In this thesis, the systematic exploration of organ-on-a-chip technology through the development and application of the IFlowPlate™ and AngioPlate™ platforms has been instrumental in advancing our capabilities for vascular modeling and drug screening. Chapter 2 details the innovation and utility of IFlowPlate™, initially focusing on its role in vascularizing liver tissues, which demonstrates its potential for creating organ-specific models. Chapter 3 discusses the capability of IFlowPlate™ in high-throughput screening of chemotherapeutic drugs, utilizing a robotic handling system to enhance efficiency and consistency. The transition to AngioPlate™ in Chapters 4 and 5 marks a shift towards a pre-designed architectural approach. Chapter 4 introduces the initial development of AngioPlate™ and sets the groundwork for its application in modeling mature, high-throughput vascular networks that are detailed in Chapter 5, crucial for various physiological studies—from disease modeling to drug screening. This progression of each platform not only highlights the technical advancements in organ-on-a-chip systems but also underscores their growing importance in more accurately mimicking human physiological responses and enhancing throughput for improved therapeutic outcomes.

6.1 Comparison of IFlowPlate™ and AngioPlate™

When evaluating and comparing the IFlowPlate™ and AngioPlate™ systems, it's crucial to understand their unique designs, applications, and how each addresses specific challenges within the realm of organ-on-a-chip technology. Each platform offers distinct advantages and is suited to different aspects of vascular modeling and biomedical research.

6.1.1 IFlowPlate™: flexibility and dynamism in vascular modeling

The IFlowPlate™ is particularly noted for its ability to facilitate the formation of self-assembled vascular beds. This capability is invaluable for studies focused on structural changes in the vascular architecture under various conditions, such as during drug treatment or under mechanical stress. The design of the IFlowPlate™, which allows for the dynamic formation and alteration of vascular networks, offers a unique advantage for experiments where the natural process of vasculogenesis or angiogenesis needs to be observed and manipulated in real-time.

Advantages:

- **Dynamic vascular modeling:** Enables the study of vascular growth and response to stimuli in a manner that closely mimics natural processes.
- **Flexibility:** Allows for various experimental setups, accommodating different types of cells and treatments to observe how they influence vascular formation and behavior.

Limitations:

- **Consistency issues:** While it offers flexibility and dynamic modeling, the IFlowPlate™ can sometimes suffer from lower sample-to-sample consistency due to the nature of self-assembly processes, which slight variations can influence in experimental conditions.

6.1.2 AngioPlate™: precision and reproducibility in high-throughput settings

In contrast, the AngioPlate™ is designed with a focus on precision and reproducibility, utilizing pre-designed, fixed vascular patterns that are embedded into each well. This approach is highly beneficial for conducting comparative studies across many samples where high consistency and standardization are required. The fixed patterns allow for uniform and reproducible vascular structures, which are crucial for high-throughput screening and detailed comparative analyses.

Advantages:

- **High consistency:** The pre-defined vascular patterns ensure that each unit within the platform is almost virtually identical, allowing for highly consistent results across experiments.
- **Suitability for high-throughput screening:** The standardization of tissue preparation and treatment processes makes AngioPlate™ ideal for large-scale drug screening and toxicity testing, where many compounds need to be evaluated under the same conditions.

Limitations:

- **Less flexibility in vascular structure:** The pre-patterned nature of the AngioPlate™ means it lacks the flexibility to study dynamic vascular mechanisms, such as fusion and intussusception, and change in the perfusability in response to emerging conditions or treatments.

6.1.3 Choosing between IFlowPlate™ and AngioPlate™

The choice between using IFlowPlate™ and AngioPlate™ largely depends on the specific requirements of the study:

IFlowPlate™ is more suited for research focusing on the mechanisms of vascular development and the effects of various treatments on these processes, where observing and manipulating the natural dynamics of vascular network formation is essential.

AngioPlate™ is ideal for applications that require high reproducibility and standardization, such as comparative drug testing and toxicity studies, where consistent and uniform vascular models are crucial.

In conclusion, both IFlowPlate™ and AngioPlate™ offer substantial contributions to the field of vascular modeling and organ-on-a-chip technology. Their applications, while overlapping in some areas, are distinctly suited to different types of vascular research, underscoring the importance of choosing the right platform based on specific experimental needs and goals.

6.2 Future Work

Looking forward, the development and application of the IFlowPlate™ and AngioPlate™ platforms present promising avenues for enhancing vascular modeling and

therapeutic screening in distinct yet complementary ways. Each system has the potential to revolutionize how we understand and treat vascular and organ-specific pathologies, especially in the context of cancer and targeted drug therapies. To upgrade the design for studying tumor progression and their responses to various drugs, we can create a compartment for tumor seeding inside the hydrogel next to the vessels using a technique we developed in the lab [311]. Additionally, we can upgrade our robotic system’s algorithm to incorporate the setup steps, including the construction of these tumor compartments. To increase the biological relevance of the tissue system, hydrogel with more complex components can be used. One such component is decellularized extracellular matrix (dECM), which has been used to improve organ-specific functions [312].

6.2.1 IFlowPlate™: advanced vascularized tumor models and organ-specific vascular mechanisms

Vascularized tumor models: Future research with the IFlowPlate™ should focus on developing sophisticated vascularized tumor models in combination with the stamping technique previously developed for IFlowPate™ [313]. These models would enable researchers to study tumor-related vascular changes dynamically and evaluate the efficacy of cancer therapy drugs against both tumors and their supporting vessels. By integrating tumor spheroids with perfusable vascular networks, this approach would allow for a more nuanced understanding of the tumor microenvironment and the complex interactions between tumor cells and blood vessels. Specifically, this model can be used to screen anti-angiogenesis agents. Since the system can be adapted to conventional facilities, the angiogenesis processes can be recorded over a long period

in a culturing chamber equipped with confocal or fluorescent imaging facilities.

Organ-specific vascular models: Another area of development for IFlowPlate™ involves creating organ-specific models to investigate unique vascular mechanisms inherent to different organs. The goal is to build self-assembled microvascular beds, possibly with distinct structural patterns and barrier functions. This could include studying the specific vascular responses and pathological changes that occur in organs such as the liver, kidneys, or lungs under various disease states or therapeutic interventions. Such models would provide valuable insights into organ-specific diseases and help tailor treatments that target these unique vascular features.

6.2.2 **AngioPlate™: organ-specific drug efficacy and mechanical actuation for disease modeling**

Organ-specific drug testing: AngioPlate™ is particularly suited for testing the efficacy of drugs within an organ-specific environment. In addition to the liver and lung vessels explored in this thesis, the platform can be adapted to construct other organ-specific vessels, such as those for the kidney and colon. By accurately mimicking the physiological conditions of specific organs, researchers can assess how drugs interact with and influence these targeted vessels. This capability is crucial for the development of more effective organ-targeted therapies, which could significantly improve patient outcomes for diseases that are currently challenging to treat. This targeted approach allows for a deeper understanding of drug behavior in different organ contexts, potentially leading to breakthroughs in personalized medicine. Cells with higher pluripotency, such as iPSC-derived endothelial cells and stromal cells, can be utilized to enhance the accuracy of cellular responses to stimuli. Compared to

primary cells, iPSC-derived cells are more sensitive to biochemical cues due to their pluripotent nature. To enhance the design of the immune microenvironment, organ-specific immune cells can be embedded into the hydrogel along with stromal cells. These resident immune cells can migrate and change their phenotype in response to biochemical cues. Two examples are microglia in the brain and Kupffer cells in the liver. [314, 315]

Mechanical actuators to model vascular diseases: Introducing mechanical actuators, such as a syringe pump, to the AngioPlate™ system offers a novel method for inducing and studying vascular diseases. These actuators can simulate disease states by altering hemodynamic forces within the microvessels, such as changes in blood flow and pressure that are typical in conditions like vascular aging or atherosclerosis. The application of the pump would alter the fluid dynamics within the vessel and induce inflammatory responses. For instance, disturbed and oscillatory flow is related to inflammatory states in vessels, while undisturbed and steady flow is associated with vessels having stable skeletal organization [316]. This approach not only adds a dynamic component to the disease modeling capabilities of AngioPlate™ but also enhances the system’s ability to replicate disease progression and respond to therapies in a controlled setting.

Bibliography

- [1] D Tsvirkun, A Grichine, A Duperray, C Misbah, and L Bureau. Microvasculature on a chip: study of the endothelial surface layer and the flow structure of red blood cells. *Sci. Rep.*, 7:45036, 2017.
- [2] C Blundell et al. A microphysiological model of the human placental barrier. *Lab Chip*, 16:3065–3073, 2016.
- [3] B Zhang and M Radisic. Organ-on-a-chip devices advance to market. *Lab Chip*, 17:2395–2420, 2017.
- [4] IFPMA. Technical report, International Federation of Pharmaceutical Manufacturers and Associations, 2017.
- [5] D Huh et al. Reconstituting organ-level lung functions on a chip. *Science*, 328:1662–1668, 2010.
- [6] S R Khetani and S N Bhatia. Microscale culture of human liver cells for drug development. *Nat. Biotechnol.*, 26:120–126, 2008.
- [7] Y Zheng, J Chen, and J A López. Flow-driven assembly of vwf fibres and webs in in vitro microvessels. *Nat. Commun.*, 6:7858, 2015.
- [8] Y S Zhang et al. Bioprinted thrombosis-on-a-chip. *Lab Chip*, 16:4097–4105, 2016.
- [9] J S Jeon et al. Human 3d vascularized organotypic microfluidic assays to study breast cancer cell extravasation. *Proc. Natl Acad. Sci.*, 112:214–219, 2015.
- [10] D T Phan et al. A vascularized and perfused organ-on-a-chip platform for large-scale drug screening applications. *Lab Chip*, 17:511–520, 2017.
- [11] A Günther et al. A microfluidic platform for probing small artery structure and function. *Lab Chip*, 10:2341–2349, 2010.

- [12] K Stevens et al. Invert molding for scalable control of tissue microarchitecture. *Nat. Commun.*, 4:1847, 2013.
- [13] S Bang et al. A low permeability microfluidic blood–brain barrier platform with direct contact between perfusable vascular network and astrocytes. *Sci. Rep.*, 7:8083, 2017.
- [14] L Wang et al. Patterning cells and shear flow conditions: convenient observation of endothelial cell remoulding, enhanced production of angiogenesis factors and drug response. *Lab Chip*, 11:4235–4240, 2011.
- [15] M Y Rotenberg, E Ruvinov, A Armoza, and S Cohen. A multi-shear perfusion bioreactor for investigating shear stress effects in endothelial cell constructs. *Lab Chip*, 12:2696–2703, 2012.
- [16] M M Thi, J M Tarbell, S Weinbaum, and D C Spray. The role of the glycocalyx in reorganization of the actin cytoskeleton under fluid shear stress: a ‘bumper-car’ model. *Proc. Natl Acad. Sci. USA*, 101:16483–16488, 2004.
- [17] L K Fiddes et al. A circular cross-section pdms microfluidics system for replication of cardiovascular flow conditions. *Biomaterials*, 31:3459–3464, 2010.
- [18] N Tousi, B Wang, K Pant, M F Kiani, and B Prabhakarpanidian. Preferential adhesion of leukocytes near bifurcations is endothelium independent. *Microvascular Res.*, 80:384–388, 2010.
- [19] G Lamberti et al. Adhesive interaction of functionalized particles and endothelium in idealized microvascular networks. *Microvascular Res.*, 89:107–114, 2013.
- [20] J M Rosano et al. A physiologically realistic in vitro model of microvascular networks. *Biomed. Microdevices*, 11:1051, 2009.
- [21] G Lamberti et al. Adhesion patterns in the microvasculature are dependent on bifurcation angle. *Microvascular Res.*, 99:19–25, 2015.
- [22] A M Smith, B Prabhakarpanidian, and K Pant. Generation of shear adhesion map using synvivo synthetic microvascular networks. *J. Vis. Exp.*, 87:e51025–e51025, 2014.
- [23] P Loskill, S G Marcus, A Mathur, W M Reese, and K E Healy. μ organo: a lego®-like plug & play system for modular multi-organ-chips. *PLoS One*, 10, 2015.
- [24] A Mathur et al. Human ipsc-based cardiac microphysiological system for drug screening applications. *Sci. Rep.*, 5:8883, 2015.

- [25] S P Deosarkar et al. A novel dynamic neonatal blood–brain barrier on a chip. *PLoS one*, 10, 2015.
- [26] B Prabhakarpanthian et al. Sym-bbb: a microfluidic blood brain barrier model. *Lab Chip*, 13:1093–1101, 2013.
- [27] G Lamberti et al. Bioinspired microfluidic assay for in vitro modeling of leukocyte–endothelium interactions. *Anal. Chem.*, 86:8344–8351, 2014.
- [28] Y Zheng et al. In vitro microvessels for the study of angiogenesis and thrombosis. *Proc. Natl Acad. Soc.*, 109:9342–9347, 2012.
- [29] B Zhang et al. Biodegradable scaffold with built-in vasculature for organ-on-a-chip engineering and direct surgical anastomosis. *Nat. Mater.*, 15:669–678, 2016.
- [30] J S Lee et al. Placenta-on-a-chip: a novel platform to study the biology of the human placenta. *J. Maternal-Fetal Neonatal Med.*, 29:1046–1054, 2016.
- [31] M Zhou et al. Development of a functional glomerulus at the organ level on a chip to mimic hypertensive nephropathy. *Sci. Rep.*, 6:31771, 2016.
- [32] R Booth and H Kim. Characterization of a microfluidic in vitro model of the blood–brain barrier (μ bbb). *Lab Chip*, 12:1784–1792, 2012.
- [33] S Srigunapalan, C Lam, A R Wheeler, and C A Simmons. A microfluidic membrane device to mimic critical components of the vascular microenvironment. *Biomicrofluidics*, 5:13409, 2011.
- [34] J Seo et al. Human blinking ‘eye-on-a-chip’. *Investigative Ophthalmol. Vis. Sci.*, 57:3872, 2016.
- [35] Y Choi et al. A microengineered pathophysiological model of early-stage breast cancer. *Lab Chip*, 15:3350–3357, 2015.
- [36] W Zhang et al. Elastomeric free-form blood vessels for interconnecting organs on chip systems. *Lab Chip*, 16:1579–1586, 2016.
- [37] D B Kolesky et al. 3d bioprinting of vascularized, heterogeneous cell-laden tissue constructs. *Adv. Mater.*, 26:3124–3130, 2014.
- [38] I Vollert et al. In vitro perfusion of engineered heart tissue through endothelialized channels. *Tissue Eng. A*, 20:854–863, 2013.

- [39] D B Kolesky, K A Homan, M A Skylar-Scott, and J A Lewis. Three-dimensional bioprinting of thick vascularized tissues. *Proc. Natl Acad. Sci.*, 113:3179–3184, 2016.
- [40] G Ligresti et al. A novel three-dimensional human peritubular microvascular system. *J. Am. Soc. Nephrol.*, 27:2370–2381, 2016.
- [41] W Wu, A DeConinck, and J A Lewis. Omnidirectional printing of 3d microvascular networks. *Adv. Mater.*, 23:H178–H183, 2011.
- [42] C J Hansen et al. Self-healing materials with interpenetrating microvascular networks. *Adv. Mater.*, 21:4143–4147, 2009.
- [43] D Therriault, R F Shepherd, S R White, and J A Lewis. Fugitive inks for direct-write assembly of three-dimensional microvascular networks. *Adv. Mater.*, 17:395–399, 2005.
- [44] D Therriault, S R White, and J A Lewis. Chaotic mixing in three-dimensional microvascular networks fabricated by direct-write assembly. *Nat. Mater.*, 2:265–271, 2003.
- [45] V V Duinen et al. 96 perfusable blood vessels to study vascular permeability in vitro. *Sci. Rep.*, 7:18071, 2017.
- [46] S J Trietsch et al. Membrane-free culture and real-time barrier integrity assessment of perfused intestinal epithelium tubes. *Nat. Commun.*, 8:262, 2017.
- [47] M J Wilmer et al. Kidney-on-a-chip technology for drug-induced nephrotoxicity screening. *Trends Biotechnol.*, 34:156–170, 2016.
- [48] E L Moreno et al. Differentiation of neuroepithelial stem cells into functional dopaminergic neurons in 3d microfluidic cell culture. *Lab Chip*, 15:2419–2428, 2015.
- [49] M Jang, P Neuzil, T Volk, A Manz, and A Kleber. On-chip three-dimensional cell culture in phaseguides improves hepatocyte functions in vitro. *Biomicrofluidics*, 9, 2015.
- [50] S J Trietsch, G D Israëls, J Joore, T Hankemeier, and P Vulto. Microfluidic titer plate for stratified 3d cell culture. *Lab Chip*, 13:3548–3554, 2013.
- [51] V Vickerman, J Blundo, S Chung, and R Kamm. Design, fabrication and implementation of a novel multi-parameter control microfluidic platform for three-dimensional cell culture and real-time imaging. *Lab Chip*, 8:1468–1477, 2008.

- [52] S Chung et al. Cell migration into scaffolds under co-culture conditions in a microfluidic platform. *Lab Chip*, 9:269–275, 2009.
- [53] Y Shin et al. Microfluidic assay for simultaneous culture of multiple cell types on surfaces or within hydrogels. *Nat. Protocols*, 7:1247–1259, 2012.
- [54] Y-H Hsu, M L Moya, C C Hughes, S C George, and A P Lee. A microfluidic platform for generating large-scale nearly identical human microphysiological vascularized tissue arrays. *Lab Chip*, 13:2990–2998, 2013.
- [55] M L Moya, Y-H Hsu, A P Lee, C C Hughes, and S C George. In vitro perfused human capillary networks. *Tissue Eng. C*, 19:730–737, 2013.
- [56] X Wang et al. An on-chip microfluidic pressure regulator that facilitates reproducible loading of cells and hydrogels into microphysiological system platforms. *Lab Chip*, 16:868–876, 2016.
- [57] W J Polacheck, A E German, A Mammoto, D E Ingber, and R D Kamm. Mechanotransduction of fluid stresses governs 3d cell migration. *Proc. Natl Acad. Sci.*, 111:2447–2452, 2014.
- [58] S Yasotharan, S Pinto, J G Sled, S-S Bolz, and A Günther. Artery-on-a-chip platform for automated, multimodal assessment of cerebral blood vessel structure and function. *Lab Chip*, 15:2660–2669, 2015.
- [59] B Zhang, C Peticone, S K Murthy, and M Radisic. A standalone perfusion platform for drug testing and target validation in micro-vessel networks. *Biomicrofluidics*, 7, 2013.
- [60] N Thavandiran et al. Design and formulation of functional pluripotent stem cell-derived cardiac microtissues. *Proc. Natl Acad. Soc.*, 110:E4698–E4707, 2013.
- [61] W R Legant et al. Microfabricated tissue gauges to measure and manipulate forces from 3d microtissues. *Proc. Natl Acad. Sci. USA*, 106:10097–10102, 2009.
- [62] W Bian. Engineered skeletal muscle tissue networks with controllable architecture. *Biomaterials*, 30:1401–1412, 2009.
- [63] M Kragl et al. The biomechanical properties of an epithelial tissue determine the location of its vasculature. *Nat. Commun.*, 7:13560, 2016.
- [64] G Majno. *Handbook of Physiology*, volume vol 3. American Physiological Society, 1965.

- [65] E Bassenge. Endothelial function in different organs. *Prog. Cardiovascular Dis.*, 39:209–228, 1996.
- [66] W Risau. Differentiation of endothelium. *FASEB J.*, 9:926–933, 1995.
- [67] D L Brutsaert et al. The cardiac endothelium: functional morphology, development, and physiology. *Prog. Cardiovascular Dis.*, 39:239–262, 1996.
- [68] R A Freitas. *Nanomedicine, Volume I: Basic Capabilities*, volume vol 1. Landes Bioscience, 1999.
- [69] A Stoehr et al. Spontaneous formation of extensive vessel-like structures in murine engineered heart tissue. *Tissue Eng. A*, 22:326–335, 2016.
- [70] L L Y Chiu, M Montgomery, Y Liang, H Liu, and M Radisic. Perfusable branching microvessel bed for vascularization of engineered tissues. *Proc. Natl Acad. Sci.*, 109:E3414–E3423, 2012.
- [71] Y S Zhang et al. Bioprinting 3d microfibrous scaffolds for engineering endothelialized myocardium and heart-on-a-chip. *Biomaterials*, 110:45–59, 2016.
- [72] S Massa et al. Bioprinted 3d vascularized tissue model for drug toxicity analysis. *Biomicrofluidics*, 11, 2017.
- [73] D L Brutsaert, P Fransen, L J Andries, G W De Keulenaer, and S U Sys. Cardiac endothelium and myocardial function. *Cardiovascular Res.*, 38:281–290, 1998.
- [74] D Meyer and C Birchmeier. Multiple essential functions of neuregulin in development. *Nature*, 378:386, 1995.
- [75] K R Stevens et al. In situ expansion of engineered human liver tissue in a mouse model of chronic liver disease. *Sci. Trans. Med.*, 9, 2017.
- [76] M Humayun, C-W Chow, and E Young. Microfluidic lung airway-on-a-chip with arrayable suspended gels for studying epithelial and smooth muscle cell interactions. *Lab Chip*, 18:1298–1309, 2018.
- [77] A Herland et al. Distinct contributions of astrocytes and pericytes to neuroinflammation identified in a 3d human blood–brain barrier on a chip. *PLoS One*, 11, 2016.
- [78] C Mandrycky, K Phong, and Y Zheng. Tissue engineering toward organ-specific regeneration and disease modeling. *MRS Commun.*, 7:332–347, 2017.

- [79] K Ronaldson-Bouchard and G Vunjak-Novakovic. Organs-on-a-chip: a fast track for engineered human tissues in drug development. *Cell Stem Cell*, 22:310–324, 2018.
- [80] E Wisse et al. Structure and function of sinusoidal lining cells in the liver. *Toxicol. Pathol.*, 24:100–111, 1996.
- [81] B E Uygun et al. Organ reengineering through development of a transplantable recellularized liver graft using decellularized liver matrix. *Nat. Med.*, 16:814, 2010.
- [82] H Itoh, M Nishino, and H Hatabu. Architecture of the lung: morphology and function. *J. Thoracic Imaging*, 19:221–227, 2004.
- [83] E R Weibel and B W Knight. A morphometric study on the thickness of the pulmonary air-blood barrier. *J. Cell Biol.*, 21:367–384, 1964.
- [84] K H Benam et al. Small airway-on-a-chip enables analysis of human lung inflammation and drug responses in vitro. *Nat. Methods*, 13:151–157, 2016.
- [85] J B West. Comparative physiology of the pulmonary blood-gas barrier: the unique avian solution. *Am. J. Physiol.-Regulatory Integr. Comparative Physiol.*, 297:R1625–R1634, 2009.
- [86] G Pocock, C D Richards, D Richards, and D A Richards. *Human Physiology*. Oxford University Press, 2013.
- [87] M H Little. *Kidney Development, Disease, Repair and Regeneration*. Academic, 2015.
- [88] S Musah et al. Mature induced-pluripotent-stem-cell-derived human podocytes reconstitute kidney glomerular-capillary-wall function on a chip. *Nat. Biomed. Eng.*, 1:0069, 2017.
- [89] L Wang et al. A disease model of diabetic nephropathy in a glomerulus-on-a-chip microdevice. *Lab Chip*, 17:1749–1760, 2017.
- [90] K A Homan et al. Bioprinting of 3d convoluted renal proximal tubules on perfusable chips. *Sci. Rep.*, 6:34845, 2016.
- [91] N J Abbott and A Friedman. Overview and introduction: the blood–brain barrier in health and disease. *Epilepsia*, 53:1–6, 2012.

- [92] Y I Wang, H E Abaci, and M L Shuler. Microfluidic blood–brain barrier model provides in vivo-like barrier properties for drug permeability screening. *Biotechnol. Bioeng.*, 114:184–194, 2017.
- [93] D T Phan et al. Blood–brain barrier-on-a-chip: microphysiological systems that capture the complexity of the blood–central nervous system interface. *Exp. Biol. Med.*, 242:1669–1678, 2017.
- [94] C Farina, F Aloisi, and E Meinl. Astrocytes are active players in cerebral innate immunity. *Trends Immunol.*, 28:138–145, 2007.
- [95] A Kovac, M A Erickson, and W A Banks. Brain microvascular pericytes are immunoactive in culture: cytokine, chemokine, nitric oxide, and lrp-1 expression in response to lipopolysaccharide. *J. Neuroinflammation*, 8:139, 2011.
- [96] E Berthier, E W Young, and D Beebe. Engineers are from pdms-land, biologists are from polystyrenia. *Lab Chip*, 12:1224–1237, 2012.
- [97] Y Wang et al. Benchtop micromolding of polystyrene by soft lithography. *Lab Chip*, 11:3089–3097, 2011.
- [98] M D Guillemette, E Roy, F A Auger, and T Veres. Rapid isothermal substrate microfabrication of a biocompatible thermoplastic elastomer for cellular contact guidance. *Acta Biomater.*, 7:2492–2498, 2011.
- [99] M D Borysiak et al. Simple replica micromolding of biocompatible styrenic elastomers. *Lab Chip*, 13:2773–2784, 2013.
- [100] M D Borysiak, E Yuferova, and J D Posner. Simple, low-cost styrene-ethylene/butylene-styrene microdevices for electrokinetic applications. *Anal. Chem.*, 85:11700–11704, 2013.
- [101] K Domansky et al. Clear castable polyurethane elastomer for fabrication of microfluidic devices. *Lab Chip*, 13:3956–3964, 2013.
- [102] E S Lippmann et al. Derivation of blood–brain barrier endothelial cells from human pluripotent stem cells. *Nat. Biotechnol.*, 30:783–791, 2012.
- [103] K. Chung et al. Structural and molecular interrogation of intact biological systems. *Nature*, 497:332–337, 2013.
- [104] M Belle et al. Tridimensional visualization and analysis of early human development. *Cell*, 169:161–173.e112, 2017.

- [105] J U Lind et al. Instrumented cardiac microphysiological devices via multimaterial three-dimensional printing. *Nat. Mater.*, 16:303–308, 2017.
- [106] R Feiner et al. Engineered hybrid cardiac patches with multifunctional electronics for online monitoring and regulation of tissue function. *Nat. Mater.*, 15:679–685, 2016.
- [107] B Tian et al. Macroporous nanowire nanoelectronic scaffolds for synthetic tissues. *Nat. Mater.*, 11:986–994, 2012.
- [108] A Junaid, A Mashaghi, T Hankemeier, and P Vulto. An end-user perspective on organ-on-a-chip: assays and usability aspects. *Curr. Opin. Biomed. Eng.*, 1:15–22, 2017.
- [109] G Adriani, D Ma, A Pavesi, R D Kamm, and E L Goh. A 3d neurovascular microfluidic model consisting of neurons, astrocytes and cerebral endothelial cells as a blood–brain barrier. *Lab Chip*, 17:448–459, 2017.
- [110] A O Stucki et al. A lung-on-a-chip array with an integrated bio-inspired respiration mechanism. *Lab Chip*, 15:1302–1310, 2015.
- [111] E J Weber et al. Development of a microphysiological model of human kidney proximal tubule function. *Kidney Int.*, 90:627–637, 2016.
- [112] B. Zhang, A. Korolj, B. F. L. Lai, and M. Radisic. Advances in organ-on-a-chip engineering. *Nat. Rev. Mater.*, 3:257, 2018.
- [113] D. Huh, B. D. Matthews, A. Mammoto, M. Montoya-Zavala, H. Y. Hsin, and D. E. Ingber. Reconstituting organ-level lung functions on a chip. *Science*, 328:1662, 2010.
- [114] D. Huh, D. C. Leslie, B. D. Matthews, J. P. Fraser, S. Jurek, G. A. Hamilton, K. S. Thorneloe, M. A. McAlexander, and D. E. Ingber. A human disease model of drug toxicity–induced pulmonary edema in a lung-on-a-chip microdevice. *Sci. Transl. Med.*, 4:159ra147, 2012.
- [115] C. Blundell, Y. S. Yi, L. Ma, E. R. Tess, M. J. Farrell, A. Georgescu, L. M. Aleksunes, and D. Huh. Placental drug transport-on-a-chip: A microengineered in vitro model of transporter-mediated drug efflux in the human placental barrier. *Adv. Healthcare Mater.*, 7:1700786, 2018.
- [116] W. Zhang, Y. Gu, Y. Hao, Q. Sun, K. Konior, H. Wang, J. Zilberberg, and W. Lee. Well plate-based perfusion culture device for tissue and tumor microenvironment replication. *Lab Chip*, 15:2854, 2015.

- [117] M. A. Redd, N. Zeinstra, W. Qin, W. Wei, A. Martinson, Y. Wang, R. K. Wang, C. E. Murry, and Y. Zheng. Patterned human microvascular grafts enable rapid vascularization and increase perfusion in infarcted rat hearts. *Nat. Commun.*, 10:1, 2019.
- [118] B. Grigoryan, S. J. Paulsen, D. C. Corbett, D. W. Sazer, C. L. Fortin, A. J. Zaita, P. T. Greenfield, N. J. Calafat, J. P. Gounley, and A. H. Ta. Multi-vascular networks and functional intravascular topologies within biocompatible hydrogels. *Science*, 364:458, 2019.
- [119] M. A. Skylar-Scott, S. G. M. Uzel, L. L. Nam, J. H. Ahrens, R. L. Truby, S. Damaraju, and J. A. Lewis. Biomanufacturing of organ-specific tissues with high cellular density and embedded vascular channels. *Science Advances*, 5:eaaw2459, 2019.
- [120] T. Osaki, V. Sivathanu, and R. D. Kamm. Crosstalk between developing vasculature and optogenetically engineered skeletal muscle improves muscle contraction and angiogenesis. *Biomaterials*, 156:65, 2018.
- [121] R. Xie, W. Zheng, L. Guan, Y. Ai, and Q. Liang. Engineering of hydrogel materials with perfusable microchannels for building vascularized tissues. *Small*, 16:1902838, 2020.
- [122] S. Kim, H. Lee, M. Chung, and N. L. Jeon. Engineering of functional, perfusable 3d microvascular networks on a chip. *Lab Chip*, 13:1489, 2013.
- [123] M. Chung, S. Kim, J. Ahn, S. Lee, and N. L. Jeon. Interstitial flow regulates angiogenic response and phenotype of endothelial cells in a 3d culture model. *Lab Chip*, 16:4189, 2016.
- [124] M. Chung, S. Lee, B. J. Lee, K. Son, N. L. Jeon, and J. H. Kim. Wet-and on a chip: Modeling outer blood-retinal barrier in vitro. *Adv. Healthcare Mater.*, 7:1700028, 2018.
- [125] D. T. Phan, X. Wang, B. M. Craver, A. Sobrino, D. Zhao, J. C. Chen, L. Y. Lee, S. C. George, A. Lee, and C. Hughes. A vascularized and perfused organ-on-a-chip platform for large-scale drug screening applications. *Lab Chip*, 17:511, 2017.
- [126] A. Sobrino, D. T. Phan, R. Datta, X. Wang, S. J. Hachey, M. Romero-López, E. Gratton, A. P. Lee, S. C. George, and C. C. Hughes. 3d microtumors in vitro supported by perfused vascular networks. *Sci. Rep.*, 6:31589, 2016.

- [127] J. S. Jeon, S. Bersini, M. Gilardi, G. Dubini, J. L. Charest, M. Moretti, and R. D. Kamm. Human 3d vascularized organotypic microfluidic assays to study breast cancer cell extravasation. *Proc. Natl. Acad. Sci. U. S. A.*, 112:214, 2015.
- [128] S. Oh, H. Ryu, D. Tahk, J. Ko, Y. Chung, H. K. Lee, T. R. Lee, and N. L. Jeon. Open-top” microfluidic device for in vitro three-dimensional capillary beds. *Lab Chip*, 17:3405, 2017.
- [129] D. S. Y. Lin, F. Guo, and B. Zhang. Modeling organ-specific vasculature with organ-on-a-chip devices. *Nanotechnology*, 30:024002, 2019.
- [130] M. P. Wiedeman. Dimensions of blood vessels from distributing artery to collecting vein. *Circ. Res.*, 12:375, 1963.
- [131] K. A. Homan, D. B. Kolesky, M. A. Skylar-Scott, J. Herrmann, H. Obuobi, A. Moisan, and J. A. Lewis. Bioprinting of 3d convoluted renal proximal tubules on perfusable chips. *Sci. Rep.*, 6:34845, 2016.
- [132] S. Chung, R. Sudo, P. J. Mack, C.-R. Wan, V. Vickerman, and R. D. Kamm. Cell migration into scaffolds under co-culture conditions in a microfluidic platform. *Lab Chip*, 9:269, 2009.
- [133] M. A. Guzzardi, F. Vozzi, and A. D. Ahluwalia. Study of the crosstalk between hepatocytes and endothelial cells using a novel multicompartamental bioreactor: a comparison between connected cultures and cocultures. *Tissue Eng., Part A*, 15:3635, 2009.
- [134] K. R. Stevens, M. A. Scull, V. Ramanan, C. L. Fortin, R. R. Chaturvedi, K. A. Knouse, J. W. Xiao, C. Fung, T. Mirabella, and A. X. Chen. In situ expansion of engineered human liver tissue in a mouse model of chronic liver disease. *Sci. Transl. Med.*, 9:eaah5505, 2017.
- [135] B. Zhang and M. Radisic. Organ-level vascularization: The mars mission of bioengineering. *J. Thorac. Cardiovasc. Surg.*, 159:2003, 2020.
- [136] A. P. McGuigan and M. V. Sefton. Vascularized organoid engineered by modular assembly enables blood perfusion. *Proc. Natl. Acad. Sci. U. S. A.*, 103:11461, 2006.
- [137] B. S. Kim, H. Kim, G. Gao, J. Jang, and D.-W. Cho. Decellularized extracellular matrix: a step towards the next generation source for bioink manufacturing. *Biofabrication*, 9:034104, 2017.

- [138] R. Marcu, Y. J. Choi, J. Xue, C. L. Fortin, Y. Wang, R. J. Nagao, J. Xu, J. W. MacDonald, T. K. Bammler, and C. E. Murry. Human organ-specific endothelial cell heterogeneity. *iScience*, 4:20, 2018.
- [139] K.-J. Jang, M. A. Otieno, J. Ronxhi, H.-K. Lim, L. Ewart, K. R. Kodella, D. B. Petropolis, G. Kulkarni, J. E. Rubins, and D. Conegliano. Reproducing human and cross-species drug toxicities using a liver-chip. *Sci. Transl. Med.*, 11:eaax5516, 2019.
- [140] Y. I. Wang and M. L. Shuler. Unichip enables long-term recirculating unidirectional perfusion with gravity-driven flow for microphysiological systems. *Lab Chip*, 18:2563, 2018.
- [141] Chao Ma, Yansong Peng, Hongtong Li, and Weiqiang Chen. Organ-on-a-chip: A new paradigm for drug development. *Trends in Pharmacological Sciences*, 42(2):119–133, 2021.
- [142] Duc TT Phan, Xiaolin Wang, Brianna M Craver, Agua Sobrino, Da Zhao, Jerry C Chen, Lilian YN Lee, Steven C George, Abraham P Lee, and Christopher CW Hughes. A vascularized and perfused organ-on-a-chip platform for large-scale drug screening applications. *Lab on a Chip*, 17(3):511–520, 2017.
- [143] Rahul Mittal, Frank W Woo, Carlo S Castro, Madeline A Cohen, Joana Karanxha, Jeenu Mittal, Tanya Chhibber, and Vasanti M Jhaveri. Organ-on-chip models: implications in drug discovery and clinical applications. *Journal of cellular physiology*, 234(6):8352–8380, 2019.
- [144] V Van Duinen, A Van Den Heuvel, SJ Trietsch, HL Lanz, JM Van Gils, AJ Van Zonneveld, P Vulto, and T Hankemeier. 96 perfusable blood vessels to study vascular permeability in vitro. *Scientific reports*, 7(1):18071, 2017.
- [145] Shravanthi Rajasekar, Dawn SY Lin, Lyan Abdul, Amy Liu, Alexander Sotra, Feng Zhang, and Boyang Zhang. Iflowplate—a customized 384-well plate for the culture of perfusable vascularized colon organoids. *Advanced materials*, 32(46):2002974, 2020.
- [146] Dawn SY Lin, Shravanthi Rajasekar, Mandeep Kaur Marway, and Boyang Zhang. From model system to therapy: scalable production of perfusable vascularized liver spheroids in “open-top “384-well plate. *ACS Biomaterials Science & Engineering*, 7(7):2964–2972, 2020.
- [147] Richard Novak, Miles Ingram, Susan Marquez, Debarun Das, Aaron Delahanty, Anna Herland, Ben M Maoz, Sauveur SF Jeanty, Mahadevabharath R Somayaji,

- Morgan Burt, et al. Robotic fluidic coupling and interrogation of multiple vascularized organ chips. *Nature biomedical engineering*, 4(4):407–420, 2020.
- [148] Jihoon Ko, Dohyun Park, Jungseub Lee, Sangmin Jung, Kyusuk Baek, Kyung E Sung, Jeeyun Lee, and Noo Li Jeon. Microfluidic high-throughput 3d cell culture. *Nature Reviews Bioengineering*, pages 1–17, 2024.
- [149] Bruce A Corliss, Richard W Doty, Corbin Mathews, Paul A Yates, Tingting Zhang, and Shayn M Peirce. Reaver: a program for improved analysis of high-resolution vascular network images. *Microcirculation*, 27(5):e12618, 2020.
- [150] Kattika Kaarj and Jeong-Yeol Yoon. Methods of delivering mechanical stimuli to organ-on-a-chip. *Micromachines*, 10(10):700, 2019.
- [151] Natalia Kosyakova, Derek D Kao, Maria Figetakis, Francesc López-Giráldez, Susann Spindler, Morven Graham, Kevin J James, Jee Won Shin, Xinran Liu, Gregory T Tietjen, et al. Differential functional roles of fibroblasts and pericytes in the formation of tissue-engineered microvascular networks in vitro. *NPJ Regenerative medicine*, 5(1):1, 2020.
- [152] Ryan S Udan, James C Culver, and Mary E Dickinson. Understanding vascular development. *Wiley Interdisciplinary Reviews: Developmental Biology*, 2(3):327–346, 2013.
- [153] Daisuke Tamura, Tokuzo Arao, Kaoru Tanaka, Hiroyasu Kaneda, Kazuko Matsumoto, Kanae Kudo, Keiichi Aomatsu, Yoshihiko Fujita, Takashi Watanabe, Nagahiro Saijo, et al. Bortezomib potentially inhibits cellular growth of vascular endothelial cells through suppression of g2/m transition. *Cancer science*, 101(6):1403–1408, 2010.
- [154] Moreau Philippe, Ievgenii Karamanesht, Natalia Domnikova, Maryna Kyselyova, Kateryna Vilchevska, Vadim Doronin, Alexander Schmidt, Cyrille Hulin, Xavier Leleu, Dixie Esseltine, Karthik Venkatakrisnan, Donna Skee, Huaibao Feng, Suzette Girgis, Andrew Cakana, Helgi Velde, William Deraedt, and Thierry Facon. Pharmacokinetic, pharmacodynamic and covariate analysis of subcutaneous versus intravenous administration of bortezomib in patients with relapsed multiple myeloma. *Clinical pharmacokinetics*, 51(12), 09 2012.
- [155] Dharminder Chauhan, Laurence Catley, Guilan Li, Klaus Podar, Teru Hideshima, Mugdha Velankar, Constantine Mitsiades, Nicolas Mitsiades, Hiroshi Yasui, Anthony Letai, et al. A novel orally active proteasome inhibitor induces apoptosis in multiple myeloma cells with mechanisms distinct from bortezomib. *Cancer cell*, 8(5):407–419, 2005.

- [156] Julian Adams, Vito J Palombella, Edward A Sausville, Jill Johnson, Antonia Destree, Douglas D Lazarus, Jochen Maas, Christine S Pien, Samuel Prakash, and Peter J Elliott. Proteasome inhibitors: a novel class of potent and effective antitumor agents. *Cancer research*, 59(11):2615–2622, 1999.
- [157] Wanjian Yang, Jorge Soares, Patricia Greninger, Elena J Edelman, Howard Lightfoot, Simon Forbes, Nidhi Bindal, Dave Beare, James A Smith, I Richard Thompson, et al. Genomics of drug sensitivity in cancer (gdsc): a resource for therapeutic biomarker discovery in cancer cells. *Nucleic acids research*, 41(D1):D955–D961, 2012.
- [158] Esperanza Herradón, Cristina González, Antonio González, Jose Antonio Uranga, and Visitación López-Miranda. Cardiovascular toxicity induced by chronic vincristine treatment. *Frontiers in Pharmacology*, 12:692970, 2021.
- [159] Johannes Eble and Stephan Niland. The extracellular matrix of blood vessels. *Current pharmaceutical design*, 15:1385–400, 02 2009.
- [160] Elizabeth Jones, Ferdinand Noble, and Anne Eichmann. What determines blood vessel structure? genetic prespecification vs. hemodynamics. *Physiology (Bethesda, Md.)*, 21:388–95, 01 2007.
- [161] Mark Sweeney and Gabor Foldes. It takes two: Endothelial-perivascular cell cross-talk in vascular development and disease. *Frontiers in Cardiovascular Medicine*, 5, 2018.
- [162] A Lee, AR Hudson, DJ Shiwarski, JW Tashman, TJ Hinton, S Yerneni, JM Bliley, PG Campbell, and AW Feinberg. 3d bioprinting of collagen to rebuild components of the human heart. *Science (New York, N.Y.)*, 365(6452):482—487, August 2019.
- [163] Bagrat Grigoryan, Samantha J Paulsen, Daniel C Corbett, Daniel W Sazer, Chelsea L Fortin, Alexander J Zaita, Paul T Greenfield, Nicholas J Calafat, John P Gounley, Anderson H Ta, Fredrik Johansson, Amanda Randles, Jessica E Rosenkrantz, Jesse D Louis-Rosenberg, Peter A Galie, Kelly R Stevens, and Jordan S Miller. Multivascular networks and functional intravascular topologies within biocompatible hydrogels. *Science (New York, N.Y.)*, 364(6439):458—464, May 2019.
- [164] Richard Novak, Miles Ingram, Susan Marquez, Debarun Das, Aaron Delahanty, Anna Herland, Ben M Maoz, Sauveur S F Jeanty, Mahadevabharath R Somayaji, Morgan Burt, Elizabeth Calamari, Angeliki Chalkiadaki, Alexander Cho, Youngjae Choe, David Benson Chou, Michael Counce, Stephanie Dauth,

- Toni Divic, Jose Fernandez-Alcon, Thomas Ferrante, John Ferrier, Edward A FitzGerald, Rachel Fleming, Sasan Jalili-Firoozinezhad, Thomas Grevesse, Josue A Goss, Tiama Hamkins-Indik, Olivier Henry, Chris Hinojosa, Tessa Huffstater, Kyung-Jin Jang, Ville Kujala, Lian Leng, Robert Mannix, Yuka Milton, Janna Nawroth, Bret A Nestor, Carlos F Ng, Blakely O'Connor, Tae-Eun Park, Henry Sanchez, Josiah Sliz, Alexandra Sontheimer-Phelps, Ben Swenor, Guy Thompson, George J Touloumes, Zachary Tranchemontagne, Norman Wen, Moran Yadid, Anthony Bahinski, Geraldine A Hamilton, Daniel Levner, Oren Levy, Andrzej Przekwas, Rachelle Prantil-Baun, Kevin K Parker, and Donald E Ingber. Robotic fluidic coupling and interrogation of multiple vascularized organ chips. *Nature biomedical engineering*, 4(4):407–420, April 2020.
- [165] Sebastiaan J Trietsch, Elena Naumovska, Dorota Kurek, Meily C Setyawati, Marianne K Vormann, Karlijn J Wilschut, Henriëtte L Lanz, Arnaud Nicolas, Chee Ping Ng, Jos Joore, Stefan Kustermann, Adrian Roth, Thomas Hanke-meier, Annie Moisan, and Paul Vulto. Membrane-free culture and real-time barrier integrity assessment of perfused intestinal epithelium tubes. *Nature communications*, 8(1):262, August 2017.
- [166] Neil Y C Lin, Kimberly A Homan, Sanlin S Robinson, David B Kolesky, Nathan Duarte, Annie Moisan, and Jennifer A Lewis. Renal reabsorption in 3d vascularized proximal tubule models. *Proceedings of the National Academy of Sciences of the United States of America*, 116(12):5399–5404, March 2019.
- [167] Jonathan A Brassard, Mike Nikolaev, Tania Hübscher, Moritz Hofer, and Matthias P Lutolf. Recapitulating macro-scale tissue self-organization through organoid bioprinting. *Nature materials*, 20(1):22–29, January 2021.
- [168] Mikhail Nikolaev, Olga Mitrofanova, Nicolas Broguiere, Sara Geraldo, Devanjali Dutta, Yoji Tabata, Bilge Elci, Nathalie Brandenberg, Irina Kolotuev, Nikolce Gjorevski, Hans Clevers, and Matthias P Lutolf. Homeostatic mini-intestines through scaffold-guided organoid morphogenesis. *Nature*, 585(7826):574–578, September 2020.
- [169] Christopher Arakawa, Celina Gunnarsson, Caitlin Howard, Maria Bernabeu, Kiet Phong, Eric Yang, Cole A DeForest, Joseph D Smith, and Ying Zheng. Biophysical and biomolecular interactions of malaria-infected erythrocytes in engineered human capillaries. *Science advances*, 6(3):eaay7243, January 2020.
- [170] Samuel G Rayner, Caitlin C Howard, Christian J Mandrycky, Stefan Stamenkovic, Jonathan Himmelfarb, Andy Y Shih, and Ying Zheng. Multiphoton-guided creation of complex organ-specific microvasculature. *Advanced healthcare materials*, 10(10):e2100031, May 2021.

- [171] A Sydney Gladman, Elisabetta A Matsumoto, Ralph G Nuzzo, L Mahadevan, and Jennifer A Lewis. Biomimetic 4d printing. *Nature materials*, 15(4):413–418, April 2016.
- [172] Lian Leng, Arianna McAllister, Boyang Zhang, Milica Radisic, and Axel Günther. Mosaic hydrogels: one-step formation of multiscale soft materials. *Advanced materials (Deerfield Beach, Fla.)*, 24(27):3650–3658, July 2012.
- [173] Hanne Hjorth Tønnesen and Jan Karlsen. Alginate in drug delivery systems. *Drug development and industrial pharmacy*, 28(6):621–630, July 2002.
- [174] Haison Duong, Benjamin Wu, and Bill Tawil. Modulation of 3d fibrin matrix stiffness by intrinsic fibrinogen-thrombin compositions and by extrinsic cellular activity. *Tissue engineering. Part A*, 15(7):1865–1876, July 2009.
- [175] A Nicolas, F Schavemaker, K Kosim, D Kurek, M Haarmans, M Bulst, K Lee, S Wegner, T Hankemeier, J Joore, K Domansky, HL Lanz, P Vulto, and SJ Trietsch. High throughput transepithelial electrical resistance (teer) measurements on perfused membrane-free epithelia. *Lab on a chip*, 21(9):1676–1685, May 2021.
- [176] H Azizgolshani, JR Coppeta, EM Vedula, EE Marr, BP Cain, RJ Luu, MP Lech, SH Kann, TJ Mulhern, V Tandon, K Tan, NJ Haroutunian, P Keegan, M Rogers, AL Gard, KB Baldwin, JC de Souza, BC Hoefler, SS Bale, LB Kratchman, A Zorn, A Patterson, ES Kim, TA Petrie, EL WIELLETTE, C Williams, BC Isenberg, and JL Charest. High-throughput organ-on-chip platform with integrated programmable fluid flow and real-time sensing for complex tissue models in drug development workflows. *Lab on a chip*, 21(8):1454–1474, April 2021.
- [177] Ian S Kinstlinger, Gisele A Calderon, Madison K Royse, A Kristen Means, Bagrat Grigoryan, and Jordan S Miller. Perfusion and endothelialization of engineered tissues with patterned vascular networks. *Nature protocols*, 16(6):3089–3113, June 2021.
- [178] Shravanthi Rajasekar, Dawn S Y Lin, Lyan Abdul, Amy Liu, Alexander So-tra, Feng Zhang, and Boyang Zhang. Iflowplate-a customized 384-well plate for the culture of perfusable vascularized colon organoids. *Advanced materials (Deerfield Beach, Fla.)*, 32(46):e2002974, November 2020.
- [179] Dawn S Y Lin, Shravanthi Rajasekar, Mandeep Kaur Marway, and Boyang Zhang. From model system to therapy: Scalable production of perfusable vascularized liver spheroids in ”open-top” 384-well plate. *ACS biomaterials science & engineering*, 7(7):2964–2972, July 2021.

- [180] Benjamin Fook Lun Lai, Rick Xing Ze Lu, Locke Davenport Huyer, Sachiro Kakinoki, Joshua Yazbeck, Erika Yan Wang, Qinghua Wu, Boyang Zhang, and Milica Radisic. A well plate-based multiplexed platform for incorporation of organoids into an organ-on-a-chip system with a perfusable vasculature. *Nature protocols*, 16(4):2158–2189, April 2021.
- [181] Benjamin Fook Lun Lai, Locke Davenport Huyer, Rick Xing Ze Lu, Stasja Drecun, Milica Radisic, and Boyang Zhang. Invade: integrated vasculature for assessing dynamic events. *Advanced functional materials*, 27(46):1703524, 2017.
- [182] Pinak Samal, Clemens van Blitterswijk, Roman Truckenmüller, and Stefan Giselbrecht. Grow with the flow: When morphogenesis meets microfluidics. *Advanced materials (Deerfield Beach, Fla.)*, 31(17):e1805764, April 2019.
- [183] Scott B Campbell, Qinghua Wu, Joshua Yazbeck, Chuan Liu, Sargol Okhovatian, and Milica Radisic. Beyond polydimethylsiloxane: Alternative materials for fabrication of organ-on-a-chip devices and microphysiological systems. *ACS biomaterials science & engineering*, 7(7):2880–2899, July 2021.
- [184] Jonathon Parrish, Khoon Lim, Boyang Zhang, Milica Radisic, and Tim B F Woodfield. New frontiers for biofabrication and bioreactor design in microphysiological system development. *Trends in biotechnology*, 37(12):1327–1343, December 2019.
- [185] Takanori Takebe, Boyang Zhang, and Milica Radisic. Synergistic engineering: Organoids meet organs-on-a-chip. *Cell stem cell*, 21(3):297–300, September 2017.
- [186] John G Moffat, Fabien Vincent, Jonathan A Lee, Jörg Eder, and Marco Prunotto. Opportunities and challenges in phenotypic drug discovery: an industry perspective. *Nature reviews Drug discovery*, 16(8):531–543, 2017.
- [187] Jack W Scannell and Jim Bosley. When quality beats quantity: decision theory, drug discovery, and the reproducibility crisis. *PloS one*, 11(2):e0147215, 2016.
- [188] Nelita T Elliott and FAN Yuan. A review of three-dimensional in vitro tissue models for drug discovery and transport studies. *Journal of pharmaceutical sciences*, 100(1):59–74, 2011.
- [189] Eric W Esch, Anthony Bahinski, and Dongeun Huh. Organs-on-chips at the frontiers of drug discovery. *Nature reviews Drug discovery*, 14(4):248–260, 2015.
- [190] Paul McGonigle and Bruce Ruggeri. Animal models of human disease: challenges in enabling translation. *Biochemical pharmacology*, 87(1):162–171, 2014.

- [191] Sigrid A Langhans. Three-dimensional in vitro cell culture models in drug discovery and drug repositioning. *Frontiers in pharmacology*, 9:334617, 2018.
- [192] Boyang Zhang, Miles Montgomery, M Dean Chamberlain, Shinichiro Ogawa, Anastasia Korolj, Aric Pahnke, Laura A Wells, Stéphane Massé, Jihye Kim, Lewis Reis, et al. Biodegradable scaffold with built-in vasculature for organ-on-a-chip engineering and direct surgical anastomosis. *Nature materials*, 15(6):669–678, 2016.
- [193] Ying Zheng, Junmei Chen, Michael Craven, Nak Won Choi, Samuel Totorica, Anthony Diaz-Santana, Pouneh Kermani, Barbara Hempstead, Claudia Fischbach-Teschl, José A López, et al. In vitro microvessels for the study of angiogenesis and thrombosis. *Proceedings of the national academy of sciences*, 109(24):9342–9347, 2012.
- [194] Sudong Kim, Hyunjae Lee, Minhwan Chung, and Noo Li Jeon. Engineering of functional, perfusable 3d microvascular networks on a chip. *Lab on a Chip*, 13(8):1489–1500, 2013.
- [195] V Van Duinen, A Van Den Heuvel, SJ Trietsch, HL Lanz, JM Van Gils, AJ Van Zonneveld, P Vulto, and T Hankemeier. 96 perfusable blood vessels to study vascular permeability in vitro. *Scientific reports*, 7(1):18071, 2017.
- [196] Nienke R Wevers, Dhanesh G Kasi, Taylor Gray, Karlijn J Wilschut, Benjamin Smith, Remko van Vught, Fumitaka Shimizu, Yasuteru Sano, Takashi Kanda, Graham Marsh, et al. A perfused human blood–brain barrier on-a-chip for high-throughput assessment of barrier function and antibody transport. *Fluids and Barriers of the CNS*, 15:1–12, 2018.
- [197] Thomas L Maurissen, Alena J Spielmann, Gabriella Schellenberg, Marc Bickle, Jose Ricardo Vieira, Si Ying Lai, Georgios Pavlou, Sascha Fauser, Peter D Westenskow, Roger D Kamm, et al. Modeling early pathophysiological phenotypes of diabetic retinopathy in a human inner blood-retinal barrier-on-a-chip. *Nature Communications*, 15(1):1372, 2024.
- [198] Samuel G Rayner, Caitlin C Howard, Christian J Mandrycky, Stefan Stamenkovic, Jonathan Himmelfarb, Andy Y Shih, and Ying Zheng. Multiphoton-guided creation of complex organ-specific microvasculature. *Advanced healthcare materials*, 10(10):2100031, 2021.
- [199] Richard Novak, Miles Ingram, Susan Marquez, Das Debarun, Aaron Delahanty, Anna Herland, Ben Maoz, Sauveur Jeanty, Mahadevabharath Somayaji, Morgan Burt, Elizabeth Calamari, Angeliki Chalkiadaki, Alexander Cho, Young-jae Choe, David Chou, Michael Cronce, Stephanie Dauth, Toni Divic, Jose

- Fernandez-Alcon, and Donald Ingber. Robotic fluidic coupling and interrogation of multiple vascularized organ chips. *Nature Biomedical Engineering*, 4, 04 2020.
- [200] Jihoon Ko, Dohyun Park, Jungseub Lee, Sangmin Jung, Kyusuk Baek, Kyung E Sung, Jeeyun Lee, and Noo Li Jeon. Microfluidic high-throughput 3d cell culture. *Nature Reviews Bioengineering*, pages 1–17, 2024.
- [201] Natalia Kosyakova, Derek D Kao, Maria Figetakis, Francesc López-Giráldez, Susann Spindler, Morven Graham, Kevin J James, Jee Won Shin, Xinran Liu, Gregory T Tietjen, et al. Differential functional roles of fibroblasts and pericytes in the formation of tissue-engineered microvascular networks in vitro. *NPJ Regenerative medicine*, 5(1):1, 2020.
- [202] Annika Armulik, Alexandra Abramsson, and Christer Betsholtz. Endothelial/pericyte interactions. *Circulation research*, 97(6):512–523, 2005.
- [203] Andrew C Newman, Martin N Nakatsu, Wayne Chou, Paul D Gershon, and Christopher CW Hughes. The requirement for fibroblasts in angiogenesis: fibroblast-derived matrix proteins are essential for endothelial cell lumen formation. *Molecular biology of the cell*, 22(20):3791–3800, 2011.
- [204] Duc TT Phan, Xiaolin Wang, Brianna M Craver, Agua Sobrino, Da Zhao, Jerry C Chen, Lilian YN Lee, Steven C George, Abraham P Lee, and Christopher CW Hughes. A vascularized and perfused organ-on-a-chip platform for large-scale drug screening applications. *Lab on a Chip*, 17(3):511–520, 2017.
- [205] David Caballero, Sophie M Blackburn, Mar De Pablo, Josep Samitier, and Lorenzo Albertazzi. Tumour-vessel-on-a-chip models for drug delivery. *Lab on a Chip*, 17(22):3760–3771, 2017.
- [206] Raluca Marcu, Yoon Jung Choi, Jun Xue, Chelsea L. Fortin, Yuliang Wang, Ryan J. Nagao, Jin Xu, James W. MacDonald, Theo K. Bammler, Charles E. Murry, Kimberly A. Muczynski, Kelly R. Stevens, Jonathan Himmelfarb, Stephen M Schwartz, and Ying Zheng. Human organ-specific endothelial cell heterogeneity. *iScience*, 4:20 – 35, 2018.
- [207] Lorna Ewart, Athanasia Apostolou, Skyler A. Briggs, Christopher V. Carman, Jake T. Chaff, Anthony R. Heng, Sushma Jadalannagari, Jeshina Janardhanan, Kyung-Jin Jang, Sannidhi R. Joshipura, Mahika M. Kadam, Marianne Kanelias, Ville J. Kujala, Gauri Kulkarni, Christopher Y. Le, Carolina Lucchesi,

- Dimitris V. Manatakis, Kairav K. Maniar, Meaghan E. Quinn, Joseph S. Ravan, Ann Catherine Rizos, John F. K. Sauld, Josiah D. Sliz, William Tien-Street, Dennis Ramos Trinidad, James Velez, Max Wendell, Onyi Irrechukwu, Prathap Kumar Mahalingaiah, Donald E. Ingber, Jack W. Scannell, and Daniel Levner. Performance assessment and economic analysis of a human liver-chip for predictive toxicology. *Communications Medicine*, 2(1), December 2022.
- [208] Longlong Si, Haiqing Bai, Melissa Rodas, Wuji Cao, Crystal Oh, Amanda Jiang, Rasmus Moller, Daisy Hoagland, Kohei Oishi, Shu Horicuhi, Skyler Uhl, Daniel Blanco-Melo, Randy Albrecht, Wen-Chun Liu, Tristan Jordan, Benjamin Nilsson-Payant, Ilona Golynker, Justin Frere, James Logue, and Donald Ingber. A human-airway-on-a-chip for the rapid identification of candidate antiviral therapeutics and prophylactics. *Nature Biomedical Engineering*, 5:1–15, 08 2021.
- [209] Shravanthi Rajasekar, Dawn S.Y. Lin, Feng Zhang, Alexander Sotra, Alex Boshart, Sergi Clotet-Freixas, Amy Liu, Jeremy Alexander Hirota, Shinichiro Ogawa, Ana Konvalinka, and Boyang Zhang. Subtractive manufacturing with swelling induced stochastic folding of sacrificial materials for fabricating complex perfusable tissues in multi-well plates. 12 2021.
- [210] Qing Ye, Gregor Zünd, Peter Benedikt, Stefan Jockenhoevel, Simon P Hoerstrup, Shelly Sakyama, Jeffrey A Hubbell, and Marko Turina. Fibrin gel as a three dimensional matrix in cardiovascular tissue engineering. *European Journal of Cardio-Thoracic Surgery*, 17(5):587–591, 2000.
- [211] Miles T Rogers, Ashley L Gard, Robert Gaibler, Thomas J Mulhern, Rivka Strelnikov, Hesham Azizgolshani, Brian P Cain, Brett C Isenberg, Nerses J Haroutunian, Nicole E Raustad, et al. A high-throughput microfluidic bilayer co-culture platform to study endothelial-pericyte interactions. *Scientific reports*, 11(1):12225, 2021.
- [212] Kristina Haase, Mark R Gillrie, Cynthia Hajal, and Roger D Kamm. Pericytes contribute to dysfunction in a human 3d model of placental microvasculature through vegf-ang-tie2 signaling. *Advanced Science*, 6(23):1900878, 2019.
- [213] David Shepro and Nicole ML Morel. Pericyte physiology. *The FASEB Journal*, 7(11):1031–1038, 1993.
- [214] CC Miller, G Godeau, C Lebreton-DeCoster, A Desmouliere, B Pellat, L Dubertret, and B Coulomb. Validation of a morphometric method for evaluating fibroblast numbers in normal and pathologic tissues. *Experimental dermatology*, 12(4):403–411, 2003.

- [215] Chong Wang, Brendon M Baker, Christopher S Chen, and Martin Alexander Schwartz. Endothelial cell sensing of flow direction. *Arteriosclerosis, thrombosis, and vascular biology*, 33(9):2130–2136, 2013.
- [216] Daniel Vittet, Marie-Helene Prandini, Rolande Berthier, Annie Schweitzer, Herve Martin-Sisteron, Gerges Uzan, and Elissabeta Dejana. Embryonic stem cells differentiate in vitro to endothelial cells through successive maturation steps. 1996.
- [217] David E Sims. The pericyte—a review. *Tissue and Cell*, 18(2):153–174, 1986.
- [218] A Enzerink and A Vaheri. Fibroblast activation in vascular inflammation. *Journal of Thrombosis and Haemostasis*, 9(4):619–626, 2011.
- [219] V Van Duinen, A Van Den Heuvel, SJ Trietsch, HL Lanz, JM Van Gils, AJ Van Zonneveld, P Vulto, and T Hankemeier. 96 perfusable blood vessels to study vascular permeability in vitro. *Scientific reports*, 7(1):18071, 2017.
- [220] Katrin Palm, Krishna Luthman, Anna-Lena Unge, Gert Strandlund, and Per Artursson. Correlation of drug absorption with molecular surface properties. *Journal of pharmaceutical sciences*, 85(1):32–39, 1996.
- [221] CC Michel and FE Curry. Microvascular permeability. *Physiological reviews*, 1999.
- [222] Eliot M Rosen, Katrin Lamszus, John Laterra, Peter J Polverini, Jeffrey S Rubin, and Itzhak D Goldberg. Hgf/sf in angiogenesis. In *Ciba Foundation Symposium 212-Plasminogen-Related Growth Factors: Plasminogen-Related Growth Factors: Ciba Foundation Symposium 212*, pages 215–229. Wiley Online Library, 2007.
- [223] Takeshi Natori, Masataka Sata, Miwa Washida, Yasunobu Hirata, Ryozo Nagai, and Masatoshi Makuuchi. G-csf stimulates angiogenesis and promotes tumor growth: potential contribution of bone marrow-derived endothelial progenitor cells. *Biochemical and biophysical research communications*, 297(4):1058–1061, 2002.
- [224] Daniel J Brat, Anita C Bellail, and Erwin G Van Meir. The role of interleukin-8 and its receptors in gliomagenesis and tumoral angiogenesis. *Neuro-oncology*, 7(2):122–133, 2005.
- [225] Bernhard Witzenbichler, Takayuki Asahara, Toyooki Murohara, Marcy Silver, Ioakim Spyridopoulos, Meredith Magner, Nicole Principe, Marianne Kearney,

- Jing-Shan Hu, and Jeffrey M Isner. Vascular endothelial growth factor-c (vegfc/vegfc-2) promotes angiogenesis in the setting of tissue ischemia. *The American journal of pathology*, 153(2):381–394, 1998.
- [226] Pia Wulfing, Christian Kersting, Joke Tio, Rudolph-Josef Fischer, Christian Wulfing, Christopher Poremba, Raihanatou Diallo, Werner Bocker, and Ludwig Kiesel. Endothelin-1-, endothelin-a-, and endothelin-b-receptor expression is correlated with vascular endothelial growth factor expression and angiogenesis in breast cancer. *Clinical cancer research*, 10(7):2393–2400, 2004.
- [227] Laurent David, Jean-Jacques Feige, and Sabine Bailly. Emerging role of bone morphogenetic proteins in angiogenesis. *Cytokine & growth factor reviews*, 20(3):203–212, 2009.
- [228] Agata Kowalczyk, Paulina Kleniewska, Michal Kolodziejczyk, Beata Skibska, and Anna Goraca. The role of endothelin-1 and endothelin receptor antagonists in inflammatory response and sepsis. *Archivum immunologiae et therapeuticae experimentalis*, 63:41–52, 2015.
- [229] Haley Ehlers, Arnaud Nicolas, Frederik Schavemaker, Jeroen PM Heijmans, Martin Bulst, Sebastiaan J Trietsch, and Lenie J van den Broek. Vascular inflammation on a chip: a scalable platform for trans-endothelial electrical resistance and immune cell migration. *Frontiers in Immunology*, 14:1118624, 2023.
- [230] Stella Alimperti, Teodelinda Mirabella, Varnica Bajaj, William Polacheck, Dana M Pirone, Jeremy Duffield, Jeroen Eyckmans, Richard K Assoian, and Christopher S Chen. Three-dimensional biomimetic vascular model reveals a rhoa, rac1, and n-cadherin balance in mural cell–endothelial cell-regulated barrier function. *Proceedings of the National Academy of Sciences*, 114(33):8758–8763, 2017.
- [231] Jean-Marc Cavaillon. Pro-versus anti-inflammatory cytokines: myth or reality. *Cellular And Molecular Biology-Paris-Wegmann-*, 47(4):695–702, 2001.
- [232] Melissa L Petreaca, Min Yao, Yan Liu, Kathryn DeFea, and Manuela Martins-Green. Transactivation of vascular endothelial growth factor receptor-2 by interleukin-8 (il-8/cxcl8) is required for il-8/cxcl8-induced endothelial permeability. *Molecular biology of the cell*, 18(12):5014–5023, 2007.
- [233] Amita Yadav, Vandana Saini, and Sarika Arora. Mcp-1: chemoattractant with a role beyond immunity: a review. *Clinica chimica acta*, 411(21-22):1570–1579, 2010.

- [234] Erin Fahey and Sarah L Doyle. Il-1 family cytokine regulation of vascular permeability and angiogenesis. *Frontiers in Immunology*, 10:462450, 2019.
- [235] Rajendra Karki, Bhesh Raj Sharma, Shraddha Tuladhar, Evan Peter Williams, Lillian Zalduondo, Parimal Samir, Min Zheng, Balamurugan Sundaram, Balaji Banoth, RK Subbarao Malireddi, et al. Synergism of $\text{tnf-}\alpha$ and $\text{ifn-}\gamma$ triggers inflammatory cell death, tissue damage, and mortality in sars-cov-2 infection and cytokine shock syndromes. *Cell*, 184(1):149–168, 2021.
- [236] Laia Caja, Francesco Dituri, Serena Mancarella, Daniel Caballero-Diaz, Aristidis Moustakas, Gianluigi Giannelli, and Isabel Fabregat. $\text{Tgf-}\beta$ and the tissue microenvironment: Relevance in fibrosis and cancer. *International journal of molecular sciences*, 19(5):1294, 2018.
- [237] Shomyseh Sanjabi, Soyoungh A Oh, and Ming O Li. Regulation of the immune response by $\text{tgf-}\beta$: from conception to autoimmunity and infection. *Cold Spring Harbor perspectives in biology*, 9(6):a022236, 2017.
- [238] Akihiko Yoshimura and Go Muto. $\text{Tgf-}\beta$ function in immune suppression. *Negative co-receptors and ligands*, pages 127–147, 2011.
- [239] Jonathan Lee, Sheena Wee, Jayantha Gunaratne, RJE Chua, Raymond AA Smith, Ling Ling, David G Fernig, Kunchithapadam Swaminathan, Victor Nurcombe, and Simon M Cool. Structural determinants of heparin–transforming growth factor- β 1 interactions and their effects on signaling. *Glycobiology*, 25(12):1491–1504, 2015.
- [240] Alex B Lentsch and Peter A Ward. Regulation of inflammatory vascular damage. *The Journal of pathology*, 190(3):343–348, 2000.
- [241] Piyali Chatterjee, Valorie L Chiasson, Kelsey R Bounds, and Brett M Mitchell. Regulation of the anti-inflammatory cytokines interleukin-4 and interleukin-10 during pregnancy. *Frontiers in immunology*, 5:253, 2014.
- [242] Chun-Jung Chang, Chiou-Feng Lin, Chih-Hsin Lee, Hsiao-Chi Chuang, Fu-Chia Shih, Shu-Wen Wan, Chi Tai, and Chia-Ling Chen. Overcoming interferon ($\text{ifn-}\gamma$) resistance ameliorates transforming growth factor ($\text{tgf-}\beta$)-mediated lung fibroblast-to-myofibroblast transition and bleomycin-induced pulmonary fibrosis. *Biochemical Pharmacology*, 183:114356, 2021.
- [243] Hiromi Takaki, Yasumasa Minoda, Keiko Koga, Giichi Takaesu, Akihiko Yoshimura, and Takashi Kobayashi. $\text{Tgf-}\beta$ 1 suppresses $\text{ifn-}\gamma$ -induced no production in macrophages by suppressing stat1 activation and accelerating inos protein degradation. *Genes to Cells*, 11(8):871–882, 2006.

- [244] Colin Reardon and Derek M McKay. Tgf- β suppresses ifn- γ -stat1-dependent gene transcription by enhancing stat1-pias1 interactions in epithelia but not monocytes/macrophages. *The Journal of Immunology*, 178(7):4284–4295, 2007.
- [245] Marie-José Goumans, Zhen Liu, and Peter Ten Dijke. Tgf- β signaling in vascular biology and dysfunction. *Cell research*, 19(1):116–127, 2009.
- [246] Anna A Birukova, Djanibek Adyshev, Boris Gorshkov, Konstantin G Birukov, and Alexander D Verin. Alk5 and smad4 are involved in tgf- β 1-induced pulmonary endothelial permeability. *FEBS letters*, 579(18):4031–4037, 2005.
- [247] Steven T Olson and Ingemar Björk. Regulation of thrombin activity by antithrombin and heparin. In *Seminars in Thrombosis and Hemostasis*, volume 20, pages 373–409. Copyright© 1994 by Thieme Medical Publishers, Inc., 1994.
- [248] Silvia Fischer, Tibo Gerriets, Carina Wessels, Maureen Walberer, Sawa Kostin, Erwin Stolz, Kirila Zheleva, Andreas Hocke, Stefan Hippenstiel, and Klaus T Preissner. Extracellular rna mediates endothelial-cell permeability via vascular endothelial growth factor. *Blood, The Journal of the American Society of Hematology*, 110(7):2457–2465, 2007.
- [249] Alina Grylls, Karin Seidler, and James Neil. Link between microbiota and hypertension: Focus on lps/tlr4 pathway in endothelial dysfunction and vascular inflammation, and therapeutic implication of probiotics. *Biomedicine & Pharmacotherapy*, 137:111334, 2021.
- [250] Stephan T Stern, Marilyn N Martinez, and David M Stevens. When is it important to measure unbound drug in evaluating nanomedicine pharmacokinetics? *Drug Metabolism and Disposition*, 44(12):1934–1939, 2016.
- [251] Daisuke Tamura, Tokuzo Arao, Kaoru Tanaka, Hiroyasu Kaneda, Kazuko Matsumoto, Kanae Kudo, Keiichi Aomatsu, Yoshihiko Fujita, Takashi Watanabe, Nagahiro Saijo, et al. Bortezomib potentially inhibits cellular growth of vascular endothelial cells through suppression of g2/m transition. *Cancer science*, 101(6):1403–1408, 2010.
- [252] Alexandra Flemming. Proteasome inhibitor unleashes three-pronged attack. *Nature Reviews Drug Discovery*, 7(9):731–731, 2008.
- [253] Esperanza Herradón, Cristina González, Antonio González, Jose Antonio Uranga, and Visitación López-Miranda. Cardiovascular toxicity induced by chronic vincristine treatment. *Frontiers in Pharmacology*, 12:692970, 2021.

- [254] Aspasia Soultati, Giannis Mountzios, Chrysoula Avgerinou, George Papaxoinis, Dimitrios Pectasides, Meletios-Athanassios Dimopoulos, and Christos Papadimitriou. Endothelial vascular toxicity from chemotherapeutic agents: preclinical evidence and clinical implications. *Cancer treatment reviews*, 38(5):473–483, 2012.
- [255] Alan C Cameron, Rhian M Touyz, and Ninian N Lang. Vascular complications of cancer chemotherapy. *Canadian Journal of Cardiology*, 32(7):852–862, 2016.
- [256] Veronica J Shi, Anjela Galan, Ian D Odell, and Jennifer N Choi. Cutaneous vasculopathy as an adverse effect of the anti-vascular endothelial growth factor agent axitinib. *JAMA dermatology*, 152(2):222–223, 2016.
- [257] Masashi Kimura, Sentaro Kusuhara, Mizuki Tagami, and Makoto Nakamura. Impaired retinal circulation during axitinib treatment for metastatic renal cell carcinoma. *Case Reports in Ophthalmology*, 10(1):5–10, 2019.
- [258] IY Adamson. Pulmonary toxicity of bleomycin. *Environmental health perspectives*, 16:119–125, 1976.
- [259] Toshiyuki Yamamoto, Ichiro Katayama, et al. Vascular changes in bleomycin-induced scleroderma. *International journal of rheumatology*, 2011, 2011.
- [260] A Burkhardt, W J Hölftje, and J O Gebbers. Vascular lesions following perfusion with bleomycin: electron-microscopic observations. *Virchows Archiv A*, 372:227–236, 1976.
- [261] Frédéric Perros, Sven Günther, Benoit Ranchoux, Laurent Godinas, Fabrice Antigny, Marie-Camille Chaumais, Peter Dorfmueller, Aurélie Hautefort, Nicolas Raymond, Laurent Savale, et al. Mitomycin-induced pulmonary venoocclusive disease: evidence from human disease and animal models. *Circulation*, 132(9):834–847, 2015.
- [262] Marie-Caroline Certain, Marie-Camille Chaumais, Xavier Jaïs, Laurent Savale, Andrei Seferian, Florence Parent, Marjolaine Georges, Nicolas Favrolt, Arnaud Bourdin, Clément Boissin, et al. Characteristics and long-term outcomes of pulmonary venoocclusive disease induced by mitomycin c. *Chest*, 159(3):1197–1207, 2021.
- [263] Toni K Choueiri, FA Schutz, Youjin Je, Jonathan E Rosenberg, and Joaquim Bellmunt. Risk of arterial thromboembolic events with sunitinib and sorafenib: a systematic review and meta-analysis of clinical trials. *Database of Abstracts of Reviews of Effects (DARE): Quality-assessed Reviews [Internet]*, 2010.

- [264] Sean V Ryan, Stephen L Carrithers, Scott J Parkinson, Carsten Skurk, Charles Nuss, Patricia M Pooler, Charles S Owen, Allan M Lefer, and Scott A Waldman. Hypotensive mechanisms of amifostine. *The Journal of Clinical Pharmacology*, 36(4):365–373, 1996.
- [265] Panfeng Fu, Anna A Birukova, Junjie Xing, Saad Sammani, Jeffrey S Murley, Joe GN Garcia, David J Grdina, and Konstantin G Birukov. Amifostine reduces lung vascular permeability via suppression of inflammatory signalling. *European Respiratory Journal*, 33(3):612–624, 2009.
- [266] Elisabeth Buchdunger, Terence O’Reilley, and Jeanette Wood. Pharmacology of imatinib (sti571). *European journal of cancer*, 38:S28–S36, 2002.
- [267] Jia Ruan, Min Luo, Chunjie Wang, Lei Fan, Shao Ning Yang, Mariano Cardenas, Huimin Geng, John P Leonard, Ari Melnick, Leandro Cerchietti, et al. Imatinib disrupts lymphoma angiogenesis by targeting vascular pericytes. *Blood, The Journal of the American Society of Hematology*, 121(26):5192–5202, 2013.
- [268] LP Marson, KM Kurian, WR Miller, and JM Dixon. The effect of tamoxifen on breast tumour vascularity. *Breast cancer research and treatment*, 66:9–15, 2001.
- [269] Rana Zahreddine, Morgane Davezac, Natalia Smirnova, Melissa Buscato, Emeline Lhuillier, Adrien Lupieri, Romain Solinhac, Alexia Vinel, Emilie Vessieres, Daniel Henrion, et al. Tamoxifen accelerates endothelial healing by targeting *era* in smooth muscle cells. *Circulation Research*, 127(12):1473–1487, 2020.
- [270] Judy King, Tray Hamil, Judy Creighton, Songwei Wu, Priya Bhat, Freda McDonald, and Troy Stevens. Structural and functional characteristics of lung macro-and microvascular endothelial cell phenotypes. *Microvascular research*, 67(2):139–151, 2004.
- [271] Johanne Poisson, Sara Lemoine, Chantal Boulanger, François Durand, Richard Moreau, Dominique Valla, and Pierre-Emmanuel Rautou. Liver sinusoidal endothelial cells: Physiology and role in liver diseases. *Journal of hepatology*, 66(1):212–227, 2017.
- [272] Bo Xu, Ulrika Broome, Mehmet Uzunel, Silvia Nava, Xupeng Ge, Makiko Kumagai-Braesch, Kjell Hultenby, Birger Christensson, Bo-Göran Ericzon, Jan Holgersson, et al. Capillarization of hepatic sinusoid by liver endothelial cell-reactive autoantibodies in patients with cirrhosis and chronic hepatitis. *The American journal of pathology*, 163(4):1275–1289, 2003.

- [273] Cyrill Geraud, Konstantin Evdokimov, Beate K Straub, Wiebke K Peitsch, Alexandra Demory, Yvette Dörflinger, Kai Schledzewski, Astrid Schmieder, Peter Schemmer, Hellmut G Augustin, et al. Unique cell type-specific junctional complexes in vascular endothelium of human and rat liver sinusoids. *PLoS one*, 7(4):e34206, 2012.
- [274] Jacquelyn J Maher et al. Cell-specific expression of hepatocyte growth factor in liver. upregulation in sinusoidal endothelial cells after carbon tetrachloride. *The Journal of clinical investigation*, 91(5):2244–2252, 1993.
- [275] Bruno Crestani, Sylvain Marchand-Adam, Christophe Quesnel, Laurent Plantier, Keren Borensztajn, Joelle Marchal, Arnaud Mailleux, Paul Soler, and Monique Dehoux. Hepatocyte growth factor and lung fibrosis. *Proceedings of the American Thoracic Society*, 9(3):158–163, 2012.
- [276] Kimihiko Yanagita, Mika Nagaike, Hiromi Ishibashi, Yoshiyuki Niho, Kunio Matsumoto, and Toshikazu Nakamura. Lung may have an endocrine function producing hepatocyte growth factor in response to injury of distal organs. *Biochemical and biophysical research communications*, 182(2):802–809, 1992.
- [277] Anna A Birukova, Elena Alekseeva, Arsen Mikaelyan, and Konstantin G Birukov. Hgf attenuates thrombin-induced endothelial permeability by tiam1-mediated activation of the rac pathway and by tiam1/rac-dependent inhibition of the rho pathway. *The FASEB Journal*, 21(11):2776–2786, 2007.
- [278] Yi Yang, Qi-hong Chen, Ai-ran Liu, Xiu-ping Xu, Ji-bin Han, and Hai-bo Qiu. Synergism of msc-secreted hgf and vegf in stabilising endothelial barrier function upon lipopolysaccharide stimulation via the rac1 pathway. *Stem cell research & therapy*, 6:1–14, 2015.
- [279] Eric Sulpice, Shunli Ding, Béatrice Muscatelli-Groux, Mathieu Bergé, Zhong Chao Han, Jean Plouet, Gérard Tobelem, and Tatyana Merkulova-Rainon. Cross-talk between the vegf-a and hgf signalling pathways in endothelial cells. *Biology of the Cell*, 101(9):525–539, 2009.
- [280] Hongchi Yu, Xianliang Huang, Yunlong Ma, Min Gao, Ou Wang, Ting Gao, Yang Shen, and Xiaoheng Liu. Interleukin-8 regulates endothelial permeability by down-regulation of tight junction but not dependent on integrins induced focal adhesions. *International journal of biological sciences*, 9(9):966, 2013.
- [281] Walter L Biffi, Ernest E Moore, Frederick A Moore, Virginia S Carl, Reginald J Franciose, and Anirban Banerjee. Interleukin-8 increases endothelial permeability independent of neutrophils. *Journal of Trauma and Acute Care Surgery*, 39(1):98–103, 1995.

- [282] JUN Shi and Pin-Kang Wei. Interleukin-8: A potent promoter of angiogenesis in gastric cancer. *Oncology letters*, 11(2):1043–1050, 2016.
- [283] Kelly L Walton, Katharine E Johnson, and Craig A Harrison. Targeting $\text{tgf-}\beta$ mediated smad signaling for the prevention of fibrosis. *Frontiers in pharmacology*, 8:461, 2017.
- [284] Steven Dooley and Peter Ten Dijke. $\text{Tgf-}\beta$ in progression of liver disease. *Cell and tissue research*, 347(1):245–256, 2012.
- [285] Sangeeta N Bhatia and Donald E Ingber. Microfluidic organs-on-chips. *Nature biotechnology*, 32(8):760–772, 2014.
- [286] Anna A Birukova, Nurgul Moldobaeva, Junjie Xing, and Konstantin G Birukov. Magnitude-dependent effects of cyclic stretch on hgf-and vegf-induced pulmonary endothelial remodeling and barrier regulation. *American Journal of Physiology-Lung Cellular and Molecular Physiology*, 295(4):L612–L623, 2008.
- [287] Tracey A Martin, Robert E Mansel, and Wen G Jiang. Antagonistic effect of nk4 on hgf/sf induced changes in the transendothelial resistance (ter) and paracellular permeability of human vascular endothelial cells. *Journal of cellular physiology*, 192(3):268–275, 2002.
- [288] Steven K Nishiyama, Jia Zhao, D Walter Wray, and Russell S Richardson. Vascular function and endothelin-1: tipping the balance between vasodilation and vasoconstriction. *Journal of Applied Physiology*, 122(2):354–360, 2017.
- [289] Jeffrey J Swigris and Kevin K Brown. The role of endothelin-1 in the pathogenesis of idiopathic pulmonary fibrosis. *BioDrugs*, 24:49–54, 2010.
- [290] Fernando Rodríguez-Pascual, Oscar Busnadiago, and José González-Santamaría. The profibrotic role of endothelin-1: is the door still open for the treatment of fibrotic diseases? *Life sciences*, 118(2):156–164, 2014.
- [291] Marc Iglarz and Martine Clozel. Mechanisms of et-1-induced endothelial dysfunction. *Journal of cardiovascular pharmacology*, 50(6):621–628, 2007.
- [292] Renhai Cao, Anna Eriksson, Hajime Kubo, Kari Alitalo, Yihai Cao, and Johan Thyberg. Comparative evaluation of fgf-2- , vegf-a- , and vegf-c- induced angiogenesis, lymphangiogenesis, vascular fenestrations, and permeability. *Circulation research*, 94(5):664–670, 2004.

- [293] Bernhard Witzendichler, Takayuki Asahara, Toyooki Murohara, Marcy Silver, Ioakim Spyridopoulos, Meredith Magner, Nicole Principe, Marianne Kearney, Jing-Shan Hu, and Jeffrey M Isner. Vascular endothelial growth factor-c (vegfc/vegfc-2) promotes angiogenesis in the setting of tissue ischemia. *The American journal of pathology*, 153(2):381–394, 1998.
- [294] Yuka Suzuki, Noritaka Ohga, Yasuyuki Morishita, Kyoko Hida, Kohei Miyazono, and Tetsuro Watabe. Bmp-9 induces proliferation of multiple types of endothelial cells in vitro and in vivo. *Journal of cell science*, 123(10):1684–1692, 2010.
- [295] Naoufal Akla, Claire Viallard, Natalija Popovic, Cindy Lora Gil, Przemyslaw Sapielha, and Bruno Larrivée. Bmp9 (bone morphogenetic protein-9)/alk1 (activin-like kinase receptor type i) signaling prevents hyperglycemia-induced vascular permeability. *Arteriosclerosis, thrombosis, and vascular biology*, 38(8):1821–1836, 2018.
- [296] Kwee Yong. Granulocyte colony-stimulating factor (g-csf) increases neutrophil migration across vascular endothelium independent of an effect on adhesion: comparison with granulocyte-macrophage colony-stimulating factor (gm-csf). *British journal of haematology*, 94(1):40–47, 1996.
- [297] Danica Stanimirovic and Kei Satoh. Inflammatory mediators of cerebral endothelium: a role in ischemic brain inflammation. *Brain pathology*, 10(1):113–126, 2000.
- [298] Markus Puhlmann, David M Weinreich, Jeffrey M Farma, Nancy M Carroll, Ewa M Turner, and H Richard Alexander. Interleukin-1 β induced vascular permeability is dependent on induction of endothelial tissue factor (tf) activity. *Journal of translational medicine*, 3:1–7, 2005.
- [299] Sid Kerkar, Mallory Williams, Jason M Blocksom, Robert F Wilson, James G Tyburski, and Christopher P Steffes. Tnf- α and il-1 β increase pericyte/endothelial cell co-culture permeability. *Journal of Surgical Research*, 132(1):40–45, 2006.
- [300] William P Arend. The balance between il-1 and il-1ra in disease. *Cytokine & growth factor reviews*, 13(4-5):323–340, 2002.
- [301] Carol A Gunnnett, Donald D Heistad, Daniel J Berg, and Frank M Faraci. Il-10 deficiency increases superoxide and endothelial dysfunction during inflammation. *American Journal of Physiology-Heart and Circulatory Physiology*, 279(4):H1555–H1562, 2000.

- [302] Amita Yadav, Vandana Saini, and Sarika Arora. Mcp-1: chemoattractant with a role beyond immunity: a review. *Clinica chimica acta*, 411(21-22):1570–1579, 2010.
- [303] Mary H Branton and Jeffrey B Kopp. Tgf- β and fibrosis. *Microbes and infection*, 1(15):1349–1365, 1999.
- [304] BRUCE D Car, Federica Meloni, MAURIZIO Luisetti, GIAMPIERO Semenzato, G Gialdroni-Grassi, and A Walz. Elevated il-8 and mcp-1 in the bronchoalveolar lavage fluid of patients with idiopathic pulmonary fibrosis and pulmonary sarcoidosis. *American journal of respiratory and critical care medicine*, 149(3):655–659, 1994.
- [305] Francois Huaux, Mohammed Arras, David Tomasi, Virginie Barbarin, Monique Delos, Jean-Paul Coutelier, Anne Vink, Sem H Phan, Jean-Christophe Renauld, and Dominique Lison. A profibrotic function of il-12p40 in experimental pulmonary fibrosis. *The Journal of Immunology*, 169(5):2653–2661, 2002.
- [306] Yuan Yao, Wei Yang, Yan-Qing Yang, Hong-Di Ma, Fang-Ting Lu, Liang Li, Yan-Yan Tao, Koichi Tsuneyama, Weici Zhang, Scott Friedman, et al. Distinct from its canonical effects, deletion of il-12p40 induces cholangitis and fibrosis in interleukin-2 α -/- mice. *Journal of autoimmunity*, 51:99–108, 2014.
- [307] Ju-Hee Lee, Hyunseung Lee, Yoon Ki Joung, Kyung Hee Jung, Jong-Hoon Choi, Don-Haeng Lee, Ki Dong Park, and Soon-Sun Hong. The use of low molecular weight heparin–pluronic nanogels to impede liver fibrosis by inhibition the tgf- β /smad signaling pathway. *Biomaterials*, 32(5):1438–1445, 2011.
- [308] Rosemary J Akhurst. Tgf β signaling in health and disease. *Nature genetics*, 36(8):790–792, 2004.
- [309] Asrar B Malik and John W Fenton. Thrombin-mediated increase in vascular endothelial permeability. In *Seminars in thrombosis and hemostasis*, volume 18, pages 193–199. Copyright© 1992 by Thieme Medical Publishers, Inc., 1992.
- [310] Martin J Page, Douglas B Kell, and Etheresia Pretorius. The role of lipopolysaccharide-induced cell signalling in chronic inflammation. *Chronic Stress*, 6:24705470221076390, 2022.
- [311] Alexander Sotra, Kimia Asadi Jozani, and Boyang Zhang. A vascularized crypt-patterned colon model for high-throughput drug screening and disease modelling. *Lab on a Chip*, 23(15):3370–3387, 2023.

-
- [312] Xuewei Zhang, Xi Chen, Hua Hong, Rubei Hu, Jiashang Liu, and Changsheng Liu. Decellularized extracellular matrix scaffolds: Recent trends and emerging strategies in tissue engineering. *Bioactive materials*, 10:15–31, 2022.
- [313] Alexander Sotra, Kimia Asadi Jozani, and Boyang Zhang. A vascularized crypt-patterned colon model for high-throughput drug screening and disease modelling. *Lab on a Chip*, 23(15):3370–3387, 2023.
- [314] Marco Colonna and Oleg Butovsky. Microglia function in the central nervous system during health and neurodegeneration. *Annual review of immunology*, 35:441–468, 2017.
- [315] Manfred Bilzer, Frigga Roggel, and Alexander L Gerbes. Role of kupffer cells in host defense and liver disease. *Liver International*, 26(10):1175–1186, 2006.
- [316] Claire A Dessalles, Claire Leclech, Alessia Castagnino, and Abdul I Barakat. Integration of substrate-and flow-derived stresses in endothelial cell mechanobiology. *Communications Biology*, 4(1):764, 2021.

Appendix A

Supplemental Information for

Chapter 2

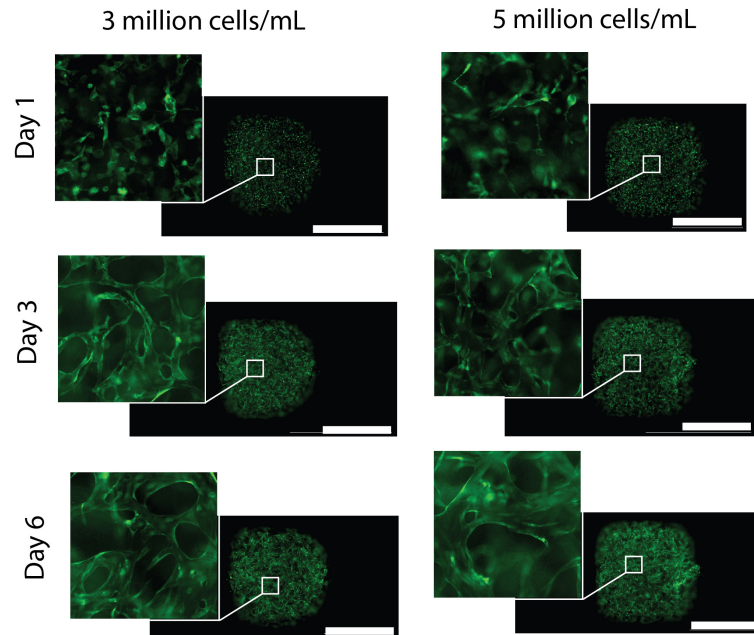


Figure A.1: Fluorescent images of GFP-endothelial cells (green) self-assemble into microvascular networks at different initial cell seeding densities. Scale bar, 3mm.

Video A.1: Nanoparticle perfusion in self-assembled vasculature on IFlowPlate™.

(Click here to download)

Video A.2: Intravascular nanoparticle delivery and accumulation in liver spheroids on IFlowPlate™. (Click here to download)

Appendix B

Supplemental Information for

Chapter 3

Table B.1: Reagents for establishing different numbers of columns using the NIMBUS system

Number of columns	Number of sample tubes containing cells	Volume of Fibrinogen (μ L)	Volume of Thrombin (μ L)	Volume of water (mL)
1	4	190	140	1
2	8	255	170	1.2
3	12	320	200	1.4
4	16	385	230	1.8
5	20	450	260	2
6	24	515	290	2.2
7	28	580	320	2.4
8	32	645	350	2.6

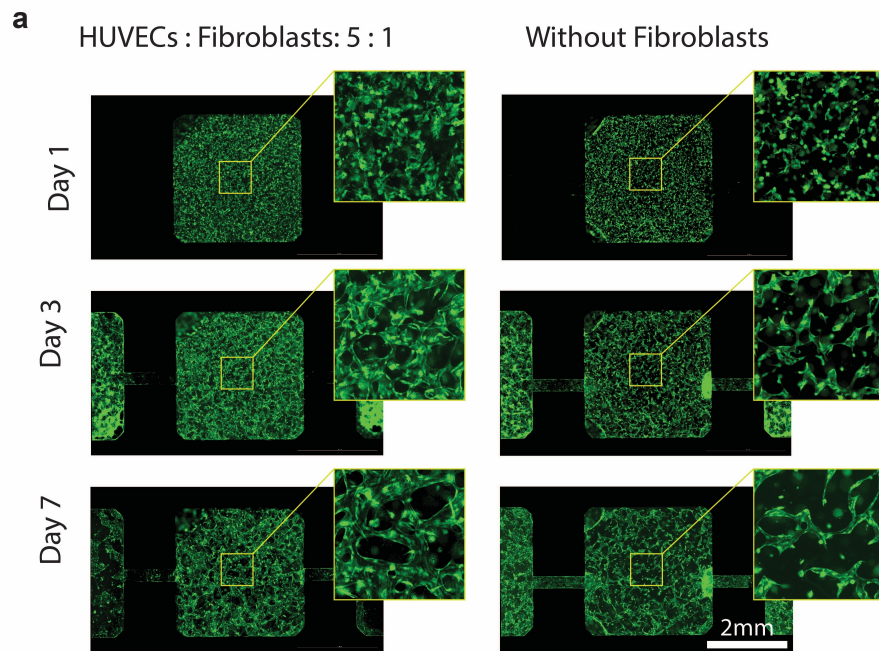


Figure B.1: Fluorescent images taken with the FITC filter and 4X objective of self-assembled microvascular networks with and without fibroblasts on day 1, day 3, and day 7.

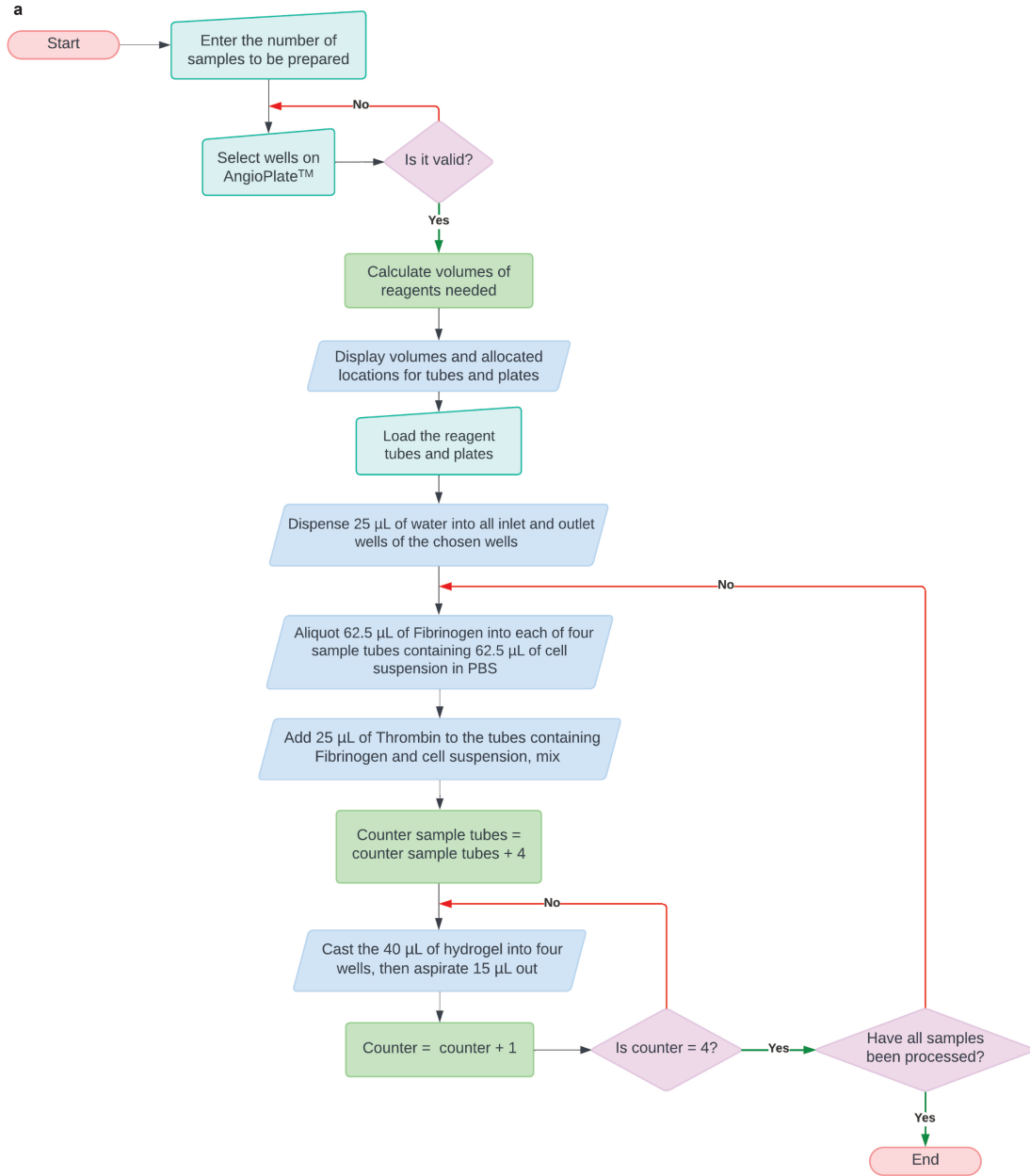


Figure B.2: The flowchart describing the major processes in code to control the robotic handling system for preparing microvascular networks on IFlowPlate™. Created in Lucid (lucid.co)

Appendix C

Supplemental Information for

Chapter 4

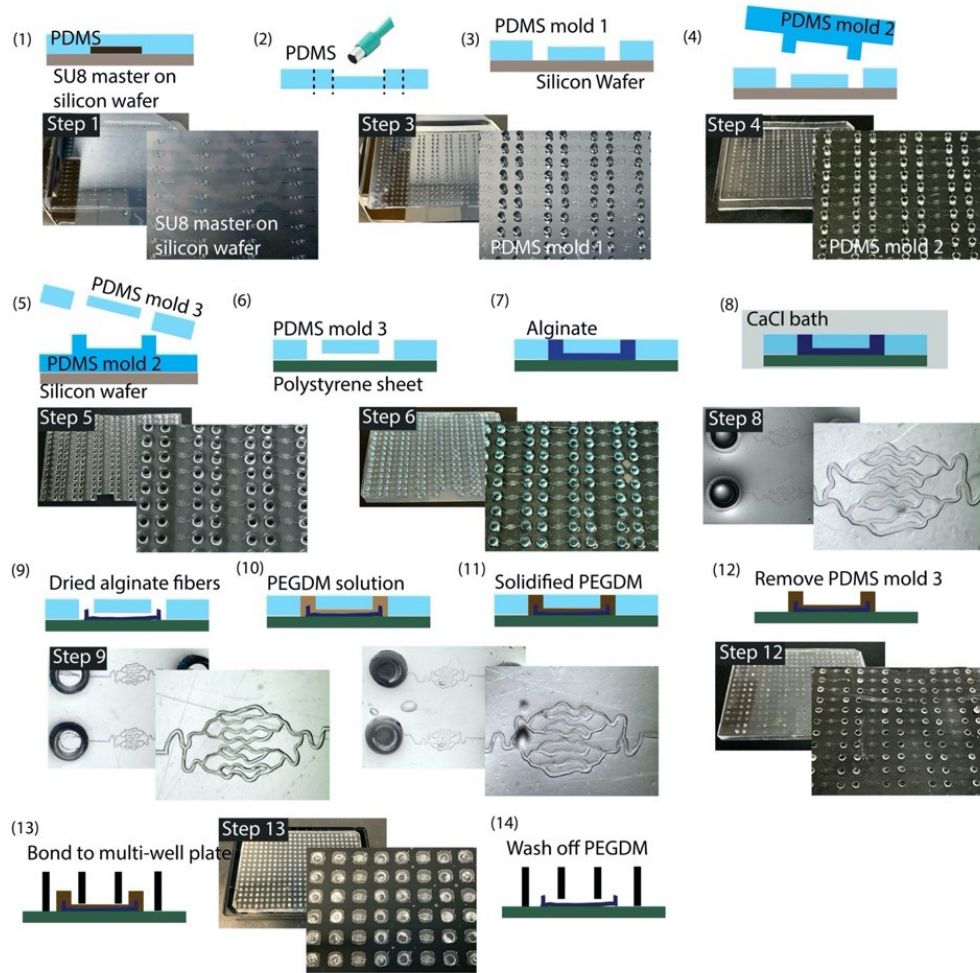


Figure C.1: Step-by-step fabrication of AngioPlate-384™. First, using standard photolithography, we fabricated a PDMS mold with various patterns connected to an inlet and outlet well. The mold was then capped onto a polystyrene sheet to form an array of micro-channel networks. The networks were loaded with 3 wt.% alginate solution. Next, the entire mold was immersed in a calcium bath (1 mM), where calcium ions gradually diffused from the inlet and outlet wells into the alginate solution within the network, cross-linking the alginate overnight. With this approach, we were able to pattern 128 independent alginate fiber networks in the format of a 384-well plate. PEGDM solution was injected into the channels in the same way to encapsulate the alginate fiber to facilitate alginate release and to create the inlet/outlet channels. Finally, the polystyrene sheet patterned with alginate and PEGDM was assembled onto the base of a bottomless 384-well plate, encasing and sealing the alginate networks with a high-viscosity PDMS glue.

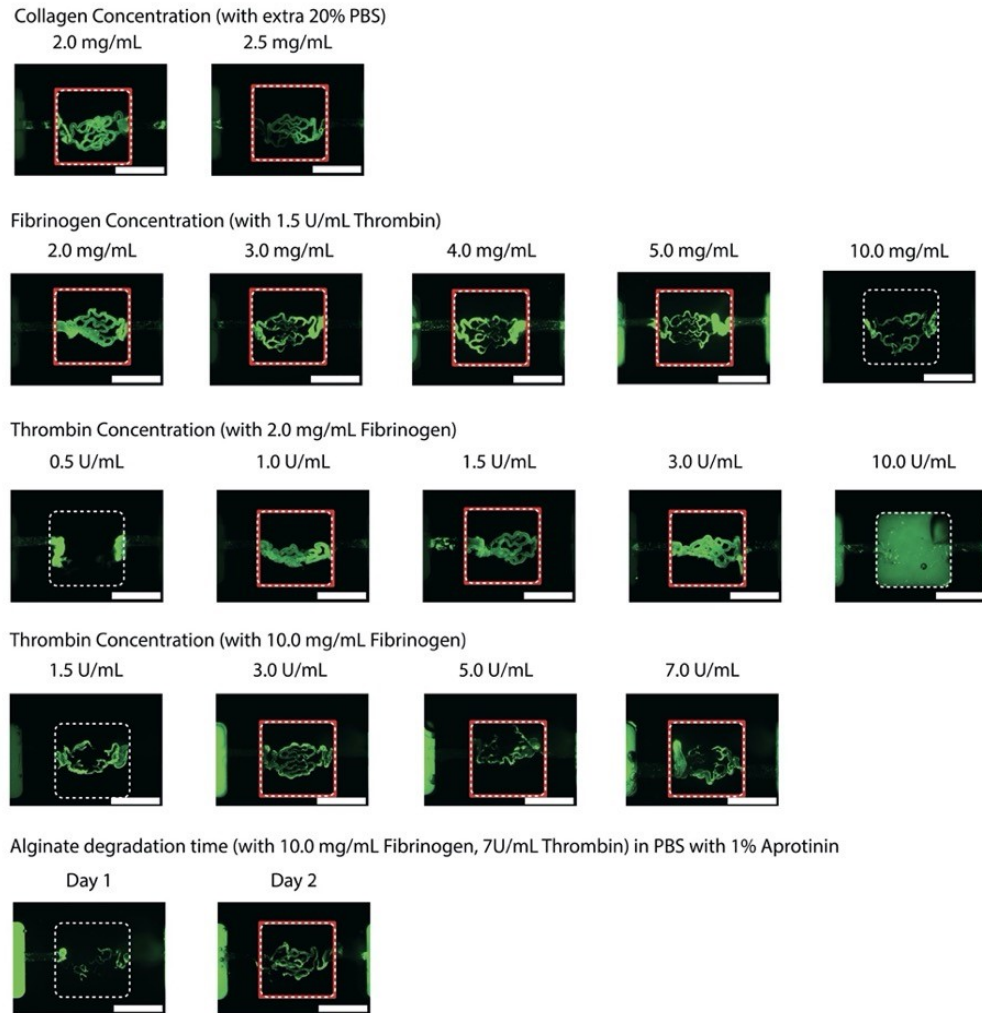


Figure C.2: Optimization of hydrogel matrix cross-linking condition for network formation. Fluorescent images of networks perfused with $1 \mu\text{m}$ fluorescent particles (green) under various gelling conditions in both the collagen-based gel and fibrin-based gel. Red boxes label the good conditions that resulted in the formation of complete perfusable networks. Scale bar, 2mm.

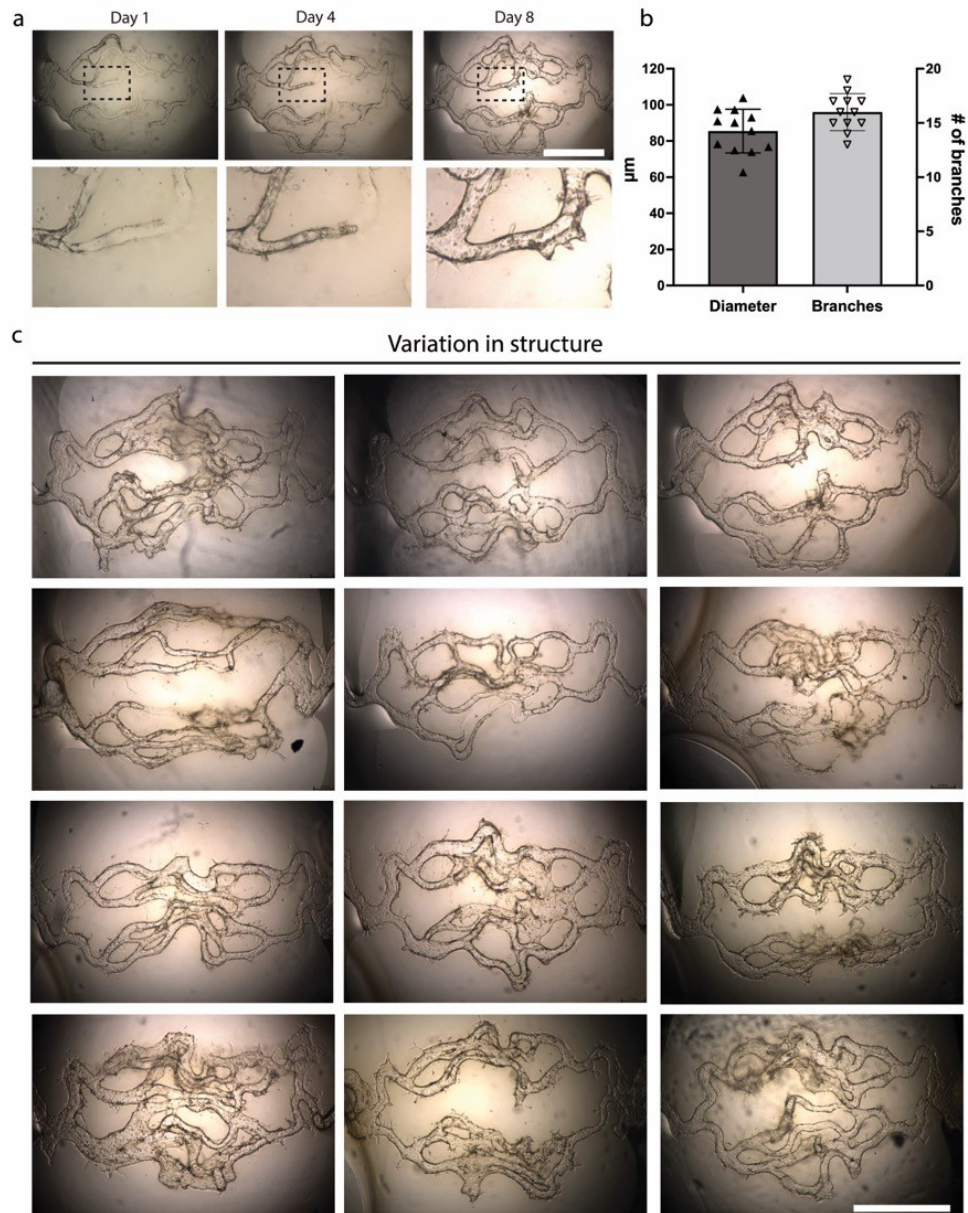


Figure C.3: Structural variation of vasculature in AngioPlate™. (a) Brightfield time-lapse images of networks seeded with human endothelial cells. Scale bar 1mm. (b) Quantification of variation in vasculature structure. $n=12$. (c) Variation in the network structures from 12 different wells. Scale bar 1mm.

Video C.1: Shape changing alginate fibers on AngioPlate™. (Click here to open)

Appendix D

Supplemental Information for

Chapter 5

Table D.1: Cell suspension preparation for setting up different experimental manually

Conditions	Stromal cells added	Final cell density in 125 μ L Fibrinogen to 1.5 mL tubes
HUVEC	-	-
HUVEC + FB	0.0125 million	FB: 0.1 million/mL
HUVECs + PC	0.0125 million	PC: 0.1 million/mL
HUVEC + PC + FB	0.00625 million each	PC & FB: 0.05 million/mL each
Liver EC + Liver FB	0.0125 million	FB: 0.1 million/mL
Lung EC + Lung FB	0.00625 million	FB: 0.05 million/mL

Table D.2: Reagents preparation for setting up various number of columns using the NIMBUS system

Number of columns	Volume of cell suspension* (μ L)	Volume of Fibrinogen (μ L)	Volume of Thrombin (μ L)
1	195	195	140
2	270	270	170
3	345	345	200
4	420	420	230
5	495	495	260
6	570	570	290
7	645	645	320
8	720	720	350

* For HUVEC + PC + FB condition: 0.1 million/mL of PCs and FBs each in PBS.

Table D.3: Compounds' catalog numbers and stock concentrations

Compound name	Company, Cat No.	Stock solution
IFN γ	Sigma-Aldrich, I17001	100 $\mu\text{g}/\text{mL}$ in water
TNF α	Sigma-Aldrich, SRP3177	10 $\mu\text{g}/\text{ml}$ in PBS
TGF β	R & D Systems, 240-B/CF	2 $\mu\text{g}/\text{ml}$ in 0.1% BSA in PBS
Thrombin	Sigma-Aldrich, T6884	10 U/mL in 0.1% BSA in PBS
Poly(I:C)	Invivogen, tlrl-pic	1 mg/mL in physiological water
LPS	Sigma-Aldrich, L4391	1 mg/ml in PBS
Vincristine		
Bortezomib		
Bleomycin		
Paclitaxel		
Axitinib	NIH, Approved Oncology Drugs Set X, plates	0.01 M in DMSO
Imatinib	4893-4894	
Amifostine		
Mitomycin		
Sorafenib		
Tamoxifen		

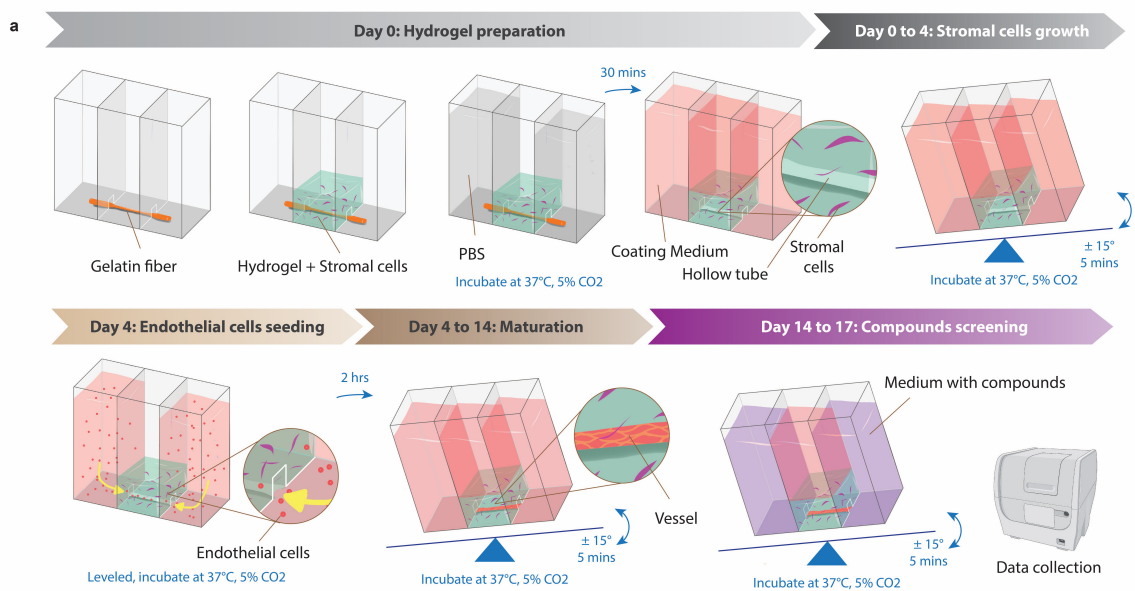


Figure D.1: Illustration of vessel development on AngioPlate™. Hydrogel casting and sacrificial material removal are performed on day 0. Stromal cells are cultured from day 0 to day 4 for maturation, and ECs are seeded on day 4 and cultured until day 14 for further vascular maturation. Treatments and data collection occur from day 14 to day 17. Created with BioRender.com.

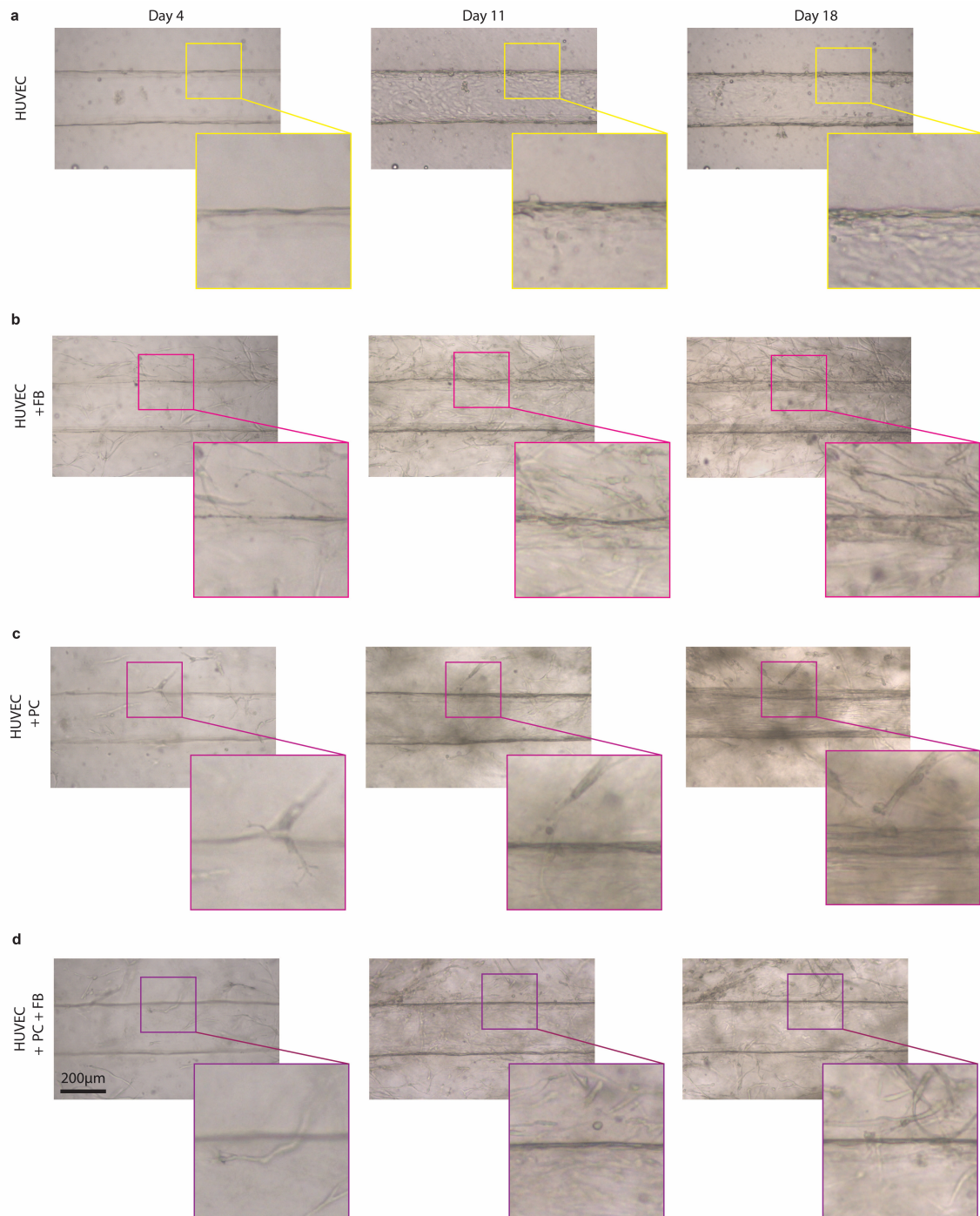


Figure D.2: Brightfield images of vessels built with different stromal cell conditions on day 4, day 11, and 18 (continued)

Figure D.2: (continued) Brightfield images taken with the 4x objective and enlarged regions for (a) HUVECs only group; (b) HUVECs with FBs; (c) HUVECs with PCs; (d) HUVECs with PCs and FBs.

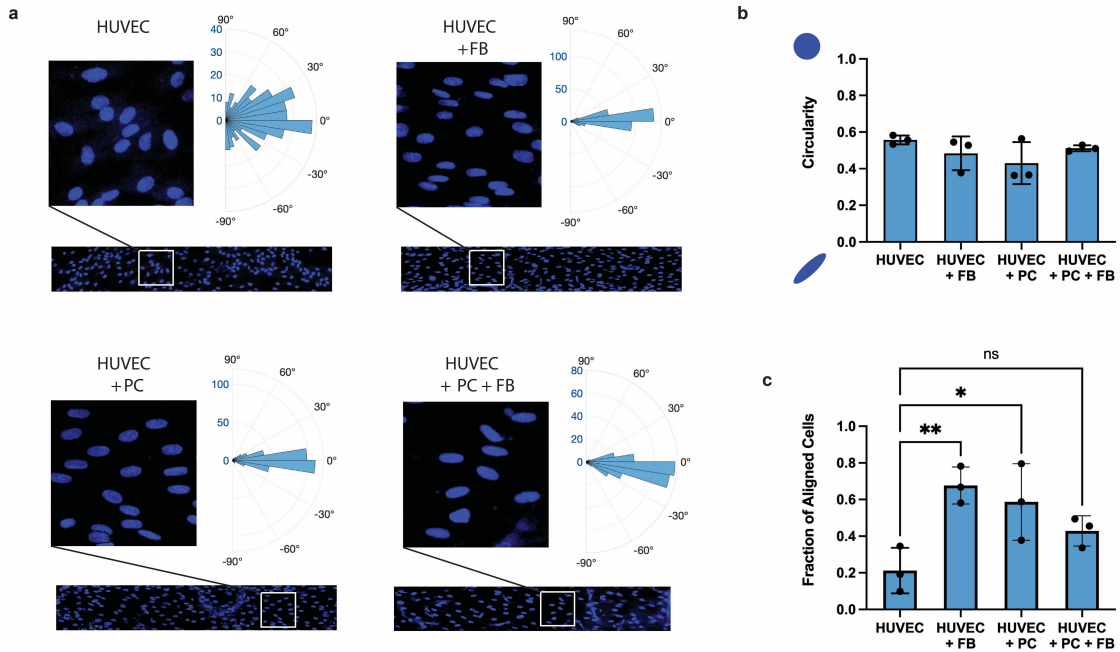


Figure D.3: DAPI analyses of vessels cultured with different stromal cell conditions. (a) Visualization of the DAPI from vessel images and quantification demonstrated as polar histogram for each nuclei identified from each vessel. Three vessels from each condition were used: vessels built with HUVECs (vessel 1: $n = 141$, vessel 2: $n = 84$, vessel 3: $n = 111$), HUVECs with FBs (vessel 1: $n = 136$, vessel 2: $n = 142$, vessel 3: $n = 69$), HUVECs with PCs (vessel 1: $n = 127$, vessel 2: $n = 155$, vessel 3: $n = 93$), and HUVECs with PCs and FBs (vessel 1: $n = 101$, vessel 2: $n = 93$, vessel 3: $n = 101$). (b) The average circularity of the nuclei identified in each vessel for vessels built with HUVECs only, with HUVECs and FBs, with HUVECs and PCs, and with HUVECs, PCs, and FBs. $n = 3$. (c) The fraction of cells that are aligned with the flow direction, having DAPI centre line direction within 10° away from the vessel centre line. The fraction of aligned cells for each condition was compared to the HUVECs only group ($n = 3$): HUVECs with FBs (** $P = 0.0033$, $n = 3$); HUVECs with PCs (* $P = 0.0104$, $n = 3$); HUVECs with PCs and FBs ($n = 3$).

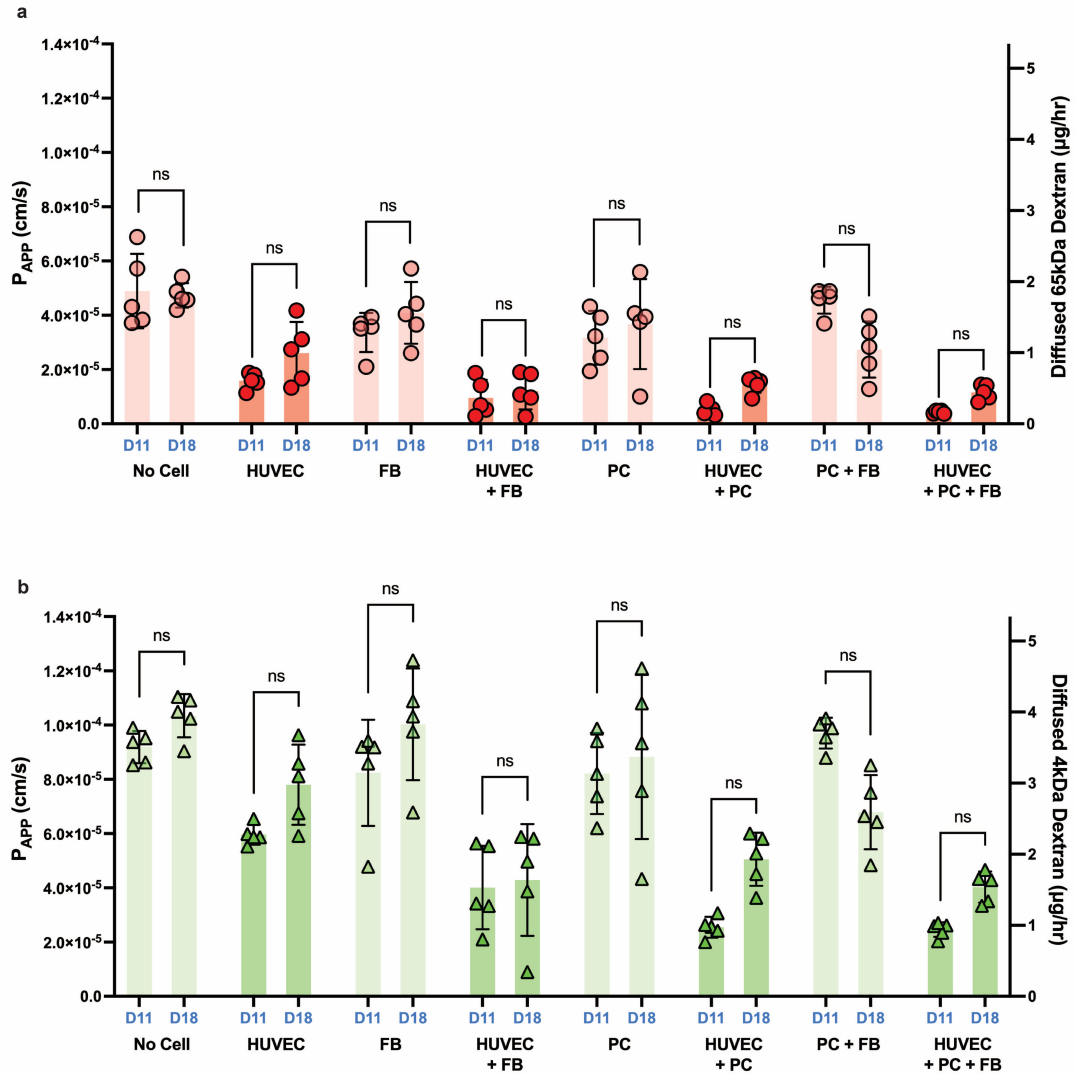


Figure D.4: (a, b) Quantification of TRITC 65-85 kDa (a) and FITC 4 kDa (b) dextran diffusion in the vessels on day 11 and day 18 for conditions developed without cells, with HUVECs, with FBs, with HUVECs and FBs, with PCs, with HUVECs and PCs, with PCs and FBs, and with HUVECs, PCs, and FBs.

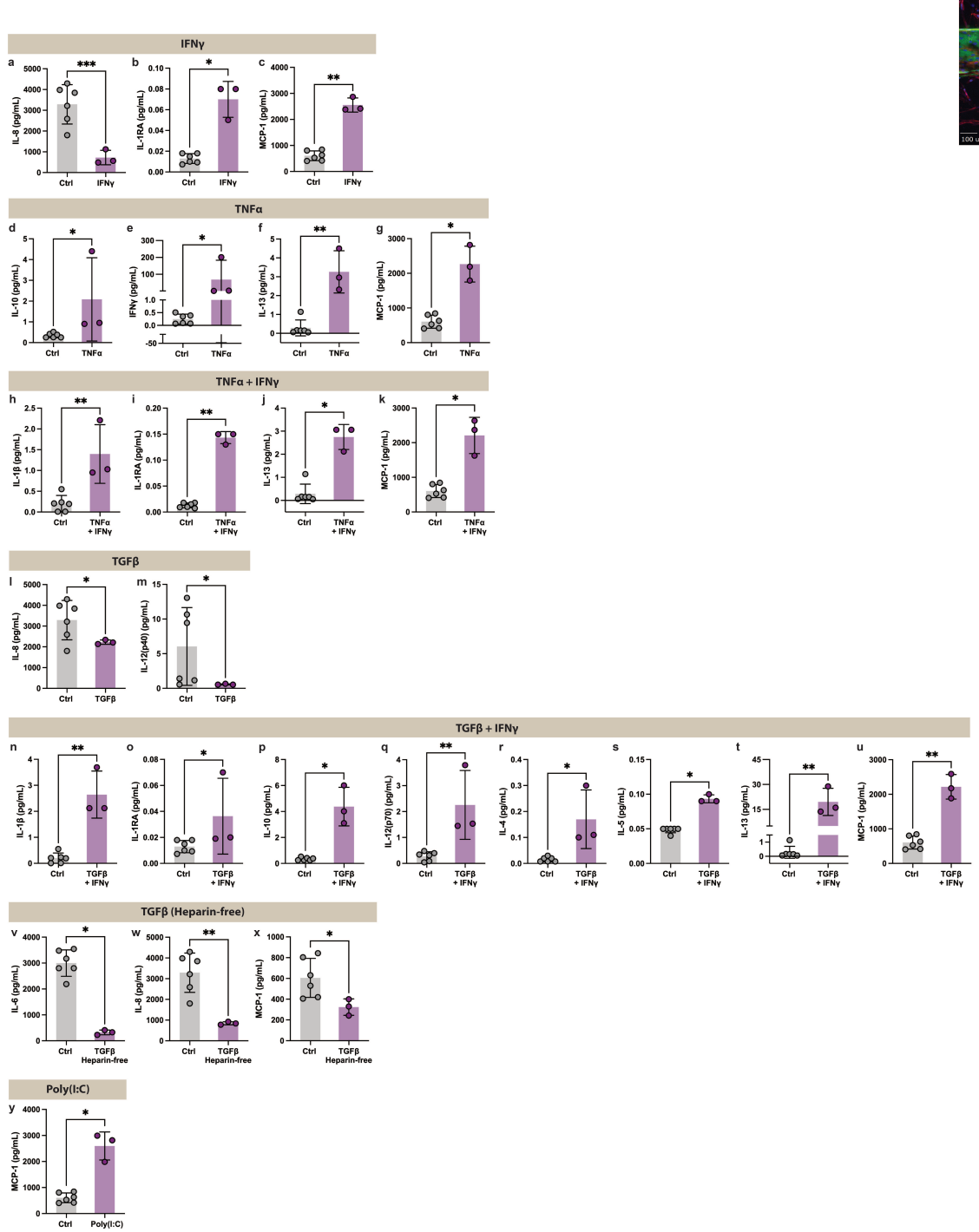


Figure D.5: (a-c) Measurements of differential concentrations of cytokines between the control group (n = 6) and the IFN γ group (n = 3). (continued)

Figure D.5: (continued) (a) IL-8: *** P = 0.0007; (b) IL-1RA: * P = 0.0119; (c) MCP-1: * P = 0.0015. (d-g) Measurements of differential concentrations of cytokines between the control group (n = 6) and the TNF α group (n = 3). (d) IL-10: * P = 0.0362; (e) IFN γ : * P = 0.0430; (f) IL-13: ** P = 0.0086; (g) MCP-1: * P = 0.0248. (h-k) Measurements of differential concentrations of cytokines between the control group (n = 6) and the TNF α with IFN γ group (n = 3). (h) IL-1 β : ** P = 0.0075; (i) IL-1RA: ** P = 0.0027; (j) IL-13: * P = 0.0114; (k) MCP-1: * P = 0.0273. (l, m) Measurements of differential concentrations of cytokines between the control group (n = 6) and the TGF β group (n = 3). (l) IL-8: * P = 0.0406; (m) IL-12(p40): * P = 0.0253. (n-u) Measurements of differential concentrations of cytokines between the control group (n = 6) and the TGF β with IFN γ group (n = 3). (n) IL-1 β : ** P = 0.0035; (o) IL-1RA: * P = 0.0382; (p) IL-10: * P = 0.0193; (q) IL-12(p70): ** P = 0.0090; (r) IL-4: * P = 0.0289; (s) IL-5: * P = 0.0452; (t) IL-13: ** P = 0.0011; (u) MCP-1: ** P = 0.0085. (v-x) Measurements of differential concentrations of cytokines between the control group (n = 6) and the TGF β without heparin group (n = 3). (v) IL-6: * P = 0.0234; (w) IL-8: ** P = 0.0014; (x) MCP-1: * P = 0.0162. (y) The measurement of differential concentrations of cytokines between the control group (n = 6) and the Poly(I:C) group (n = 3). MCP-1: * P = 0.0185.

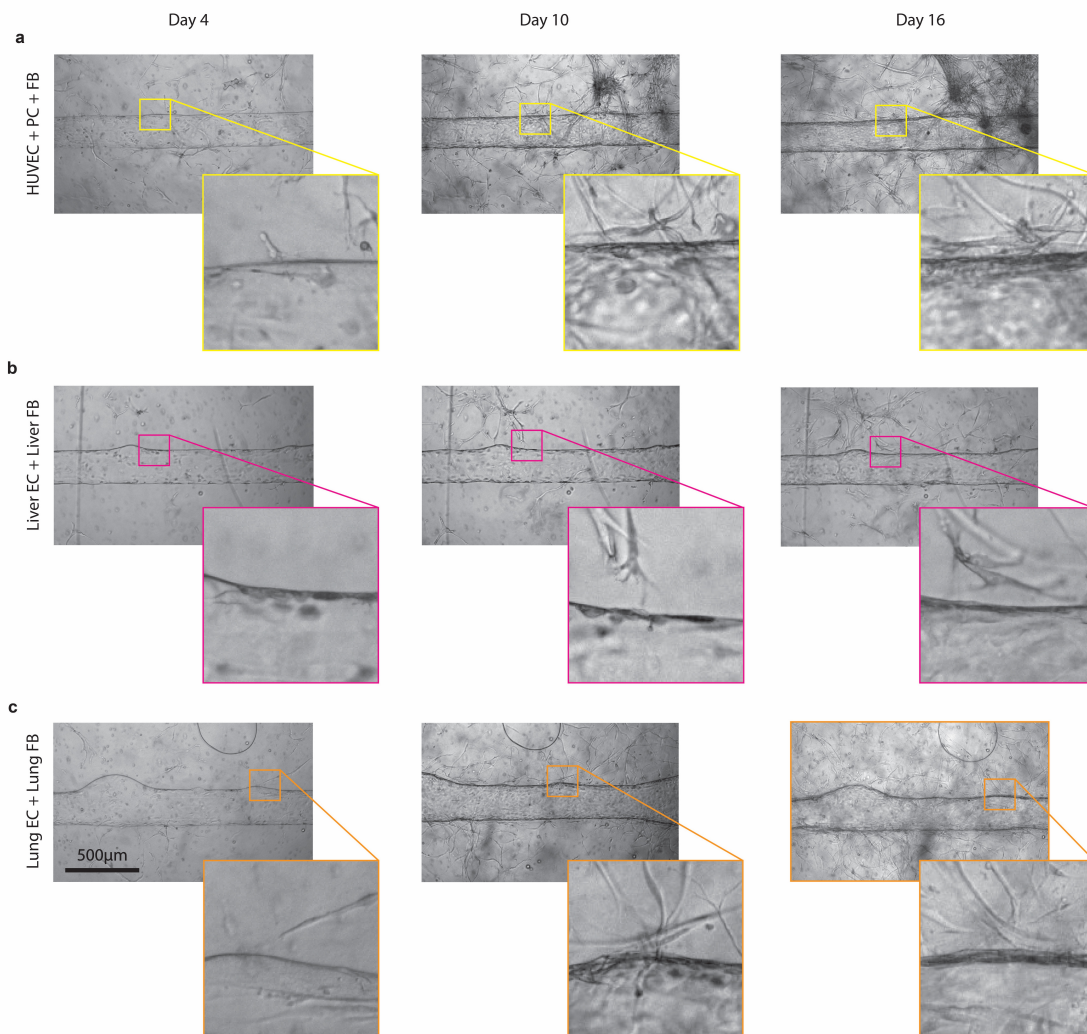


Figure D.6: (a-c) Brightfield images of vessels taken with 4x objectives and enlarged regions for vessels built with different organ specific cells on day 4, day 10, and day 16: (a) HUVECs and Lung FBs; (b) liver ECs and liver FBs; (c) lung ECs and lung FBs.

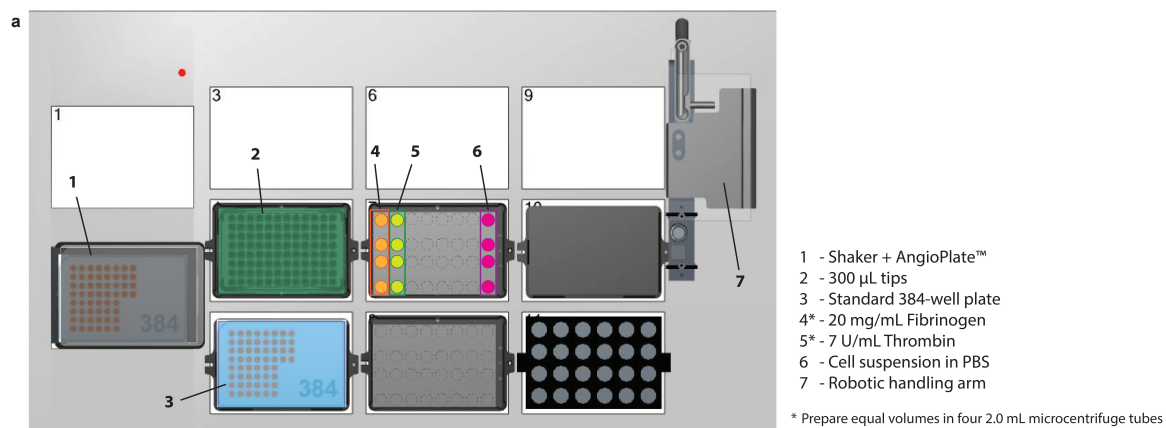


Figure D.7: The illustration of the sterile reagents and devices loading locations on the robotic handling system.

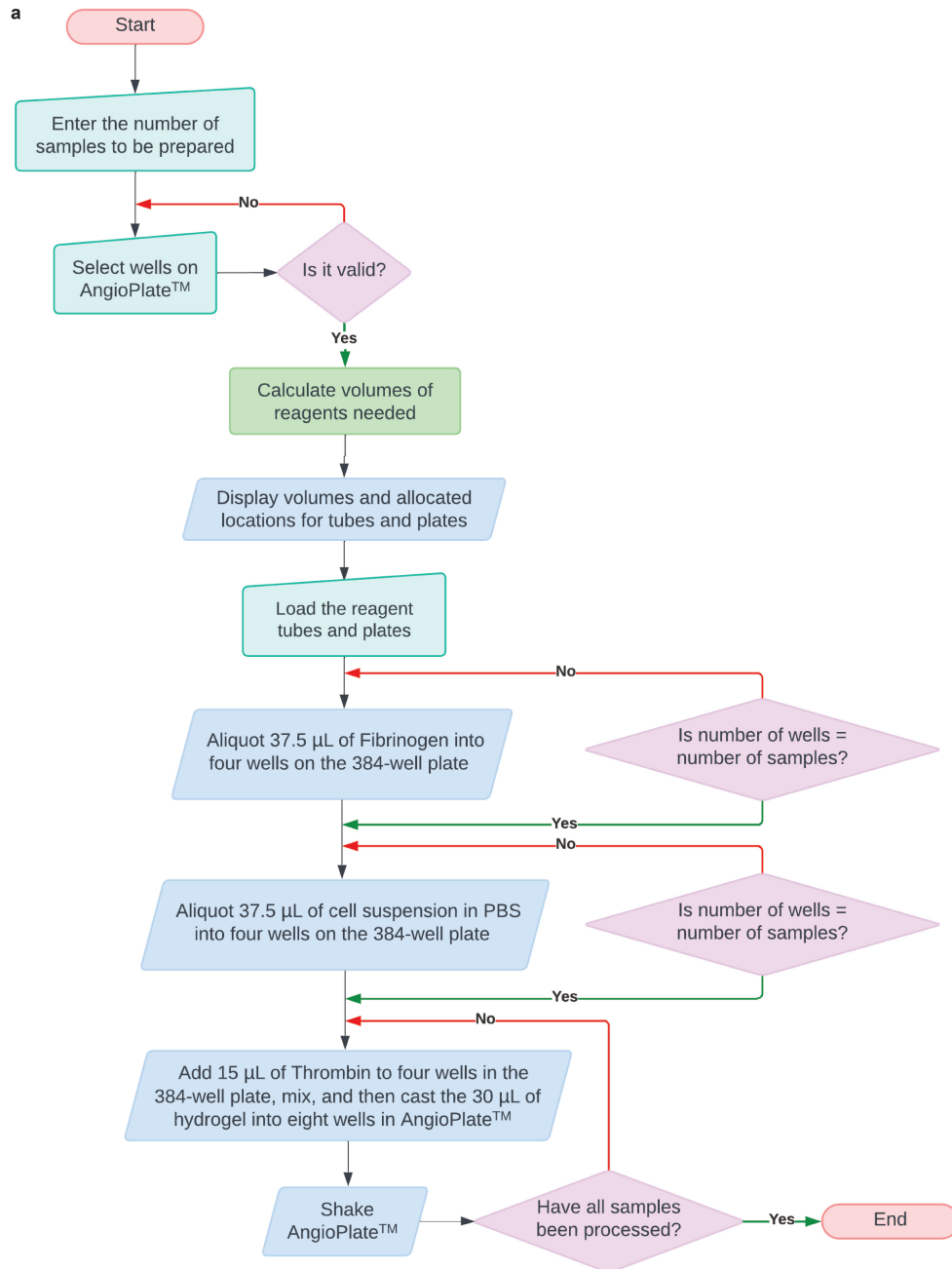


Figure D.8: The flowchart describing the major processes in code to control the robotic handling system for preparing vessels on AngioPlate™. Created in Lucid (lucid.co)